

Characterization of cell and matrix ultrastructure, composition and function of elasmobranch skeletal cartilage: integrating 3D visual data analysis, material science, and label-free imaging techniques

D I S S E R T A T I O N

zur Erlangung des akademischen Grades

Doctor of Philosophy

(Ph. D)

eingereicht an der

Lebenswissenschaftlichen Fakultät der Humboldt-Universität zu Berlin

von

Júlia Chaumel Cerdà

Präsidentin

der Humboldt-Universität zu Berlin

Prof. Dr. –Ing. Dr. Sabine Kunst

Dekanin/Dekan der Lebenswissenschaftlichen Fakultät
der Humboldt-Universität zu Berlin

Prof. Dr. Dr. Christian Ulrichs

Gutachter/innen

1. Prof. Dr. Mason N. Dean
2. Prof. Dr. John A. Nyakatura
3. Prof. Dr. Ron Shahar

Tag der mündlichen Prüfung:

29. September. 2021

TABLE OF CONTENTS

I. ABSTRACT.....	7
II. INTRODUCTION & STATE OF THE ART.....	13
1. WHAT IS CARTILAGE?.....	15
2. CARTILAGE VARIATIONS ACROSS TAXA.....	16
3. CARTILAGE IN CHONDRICHTHYANS.....	17
4. THE SKELETON OF ELASMOBRANCHS.....	18
4.1. THE UNMINERALIZED CARTILAGE.....	18
4.2. THE TESSERAE.....	19
5. COMMON TECHNIQUES USED TO IMAGE CARTILAGE.....	22
5.1. LABELED IMAGING TECHNIQUES.....	22
5.2. LABEL-FREE IMAGING TECHNIQUES.....	26
6. IMAGING ELASMOBRANCH CARTILAGE.....	32
III. AIMS & OUTLINE OF DISSERTATION.....	37
REFERENCES.....	39
IV. METHODS FOR SAMPLE PREPARATION.....	51
1. PRE-PLANNING AND DISSECTION.....	52
2. SAMPLE PREPARATION.....	55
2.1. FIXATION.....	55
2.1.1. ETHANOL – ORGANIC SOLVENT.....	56
2.1.2. PARAFORMALDEHYDE 4% PBS – CROSS-LINKING FIXATIVE.....	57
2.1.3. GLUTARALDEHYDE 2% + 2% PFA – CROSS-LINKING FIXATIVE.....	59
2.1.4. OSMIUM TETROXIDE.....	61
2.1.5. NON – FIXED SAMPLES.....	61

2.2. EMBEDDING.....	62
2.2.1. PMMA EMBEDDING.....	63
2.2.2. EPON EMBEDDING.....	64
2.2.3. CRYO-EMBEDDING.....	64
2.2.4. CLARIFICATION.....	65
2.3. CUTTING, POLISHING AND MOUNTING.....	67
2.3.1. MICROTOME CUTTING AND MOUNTING.....	67
2.3.2. CRYO-MICROTOME CUTTING AND MOUNTING.....	70
2.3.3. BLOCK POLISHING.....	72
2.4. STAININGS.....	73
2.4.1. CLASSICAL HISTOLOGY.....	74
2.4.2. FLUORESCENT DYES.....	77
2.4.3. IMMUNOHISTOCHEMISTRY.....	78
2.4.4. STAININGS FOR ELECTRON MICROSCOPY.....	79
REFERENCES.....	81
V. PUBLISHED PAPERS.....	83
PAPER 1.....	83
PAPER 2.....	123
PAPER 3.....	141
VI. DISCUSSION.....	199
1. ADVANCES IN CARTILAGE IMAGING TECHNIQUES.....	200
2. ADVANCES IN CARTILAGE BIOLOGY.....	203
REFERENCES.....	211
APPENDIX.....	215

ACKNOWLEDGMENTS

All research work contained in this dissertation would not have been possible without the contribution of colleagues/friends from the academic area as well as from my personal environment. They know that I am very bad writing acknowledgements, however, I will do my best in this case, since they really deserve it.

I would like to start by thanking my supervisor, Mason Dean, who has been the most important person during my doctoral degree. We worked hard together to have all projects done and, in most of the cases, he had to be very patient with me like, for example, explaining a thousands of times the concepts that were not easy for me to understand, as well as correcting all my grammar spellings, especially “*specially*”, “*allow to*” and during the times when I could not believe that the word “*tesserae*” is plural, not single. He also became a good friend for me, which allowed us to have good times enjoying beers and coffees in Barcelona, Alicante, Banyuls and Berlin. I also hope he does not forget our agreement where, if one day one of us wins the Nobel Prize, we will dedicate a few words to each other.

In addition to Mason, I had the luck to work with people that were both personally and scientifically outstanding. Among them, I would especially like to thank to Michael Blumer, the best histologist but the worst clapping at high speeds; to Mélanie Debiais-Thibaud, who has been a role model for me as a scientist woman, but also as a generous and funny person with who you can eat 1 m long sandwiches, drink the best French wines and analyze gene expression in elasmobranch skeleton, all of it in the same day; to Maria Marsal, who teach me how to use confocal, but also that it is ok to speak English interleaving Spanish words (¿vale?). I would also like to thank to all my colleagues from the Biomaterials department of Max Planck Institute, including Hubert Taieb, Oliver Späker, Anna Maria Tsigoni, Toni Tang, Nikolai Rosenthal, Daniel Werner, Elena Macías, Sarah Young, Victoria Schemenz, Inés Moreno, Alex Van Tol, Jeannette Steffen, Birgit Schonert, Laura Zorzetto, Aravind Jayasankar and Ronald Seidel. All of them helped me with tons of stuff, including my experiments, discussion of ideas and helping me out with the German bureaucracy, which is not easy at all. I also would like to thank to Peter Fratzl, the head of Biomaterials department, and Kerstin Gabbe; both make us feel like we are part of a big family.

I am also very thankful to all people from my close environment. First, thanks to my closest friends Elisa Cerdá Doñate, José Ángel Danglad Flores, Nieves López Salas and Patricia López García. They also are wonderful scientist who have always listened to my infinite theories and “desvaríos” about elasmobranch chondrocytes and cartilage. To Nuria Serna and Susana Calles for collecting and dissecting specimens for me altruistically during my master and doctoral period. I also want to thank to my aunt Anna María Cerdá Ferrándiz, my uncles Andrés Gisbert Pérez and Josep Gabriel Cerdá Ferrándiz, my grandma Maruja Pérez Jimeno, my cousins Andreu, Nere e Isel and, of course, my dogs Coco and Pitu, who are the queens of the family. They are the reason why I am here today, supporting me during each single year of my career.

Finally, last but not least, I am really thankful to my life partner Alejandro Campos Falcones and his car Audi Fabia. He always helped me with all my scientific stuff, taking specimens for me, driving me to the harbors to recollect samples, supporting all my stressing moments and, at the end, making my life a better place to live (te quiero!).

Thank you all! It was a fun run!

I | ABSTRACT (ENGLISH)

The vast majority of vertebrates have skeletons formed from bone, a mineralized tissue that supports body shape, acts as a surface for muscle attachment, and regulates the body's mineral homeostasis. In contrast to the hard material that bone offers to deal with skeletal demands, elasmobranchs (sharks and rays) have skeletons formed entirely of cartilage, a flexible and softer material, composed mainly of water. Elasmobranch cartilage, however, is stiffened by a surrounding mineralized layer, formed of abutting tiles called tesserae; this distinct skeletal crust is thought to be a major factor in the evolutionary success of the elasmobranch lineage. The cells in elasmobranch cartilage (chondrocytes) show a similar morphology and ultrastructure to chondrocytes of other vertebrates, but are responsible for forming the complex architectures of this tessellated cartilage, that combine both mineralized and unmineralized tissues. Moreover, elasmobranch chondrocytes appear to perform different functions than chondrocytes in other vertebrates by, for example, surviving the mineralization process and apparently exerting finescale control over where mineralization does and doesn't occur (e.g. in the complex joints between tesserae). And yet, although the particular interactions of cell and matrix appear to dictate the formation of this unique cartilage type, the factors that distinguish these cells and their surrounding cartilage matrix have not been deeply explored nor compared to other vertebrate cartilages. In this dissertation, I characterize cell and matrix structure and organization in elasmobranch skeletal cartilage using a variety of imaging and materials characterization tools, including two label-free imaging and analysis techniques customized for this tissue. To characterize the anatomies and roles of tesserae chondrocytes, thousands of tesserae lacunae (cell spaces) were imaged in 3D using high-resolution synchrotron microCT, and morphometrics and arrangements of lacunae quantified in a high-throughput workflow. The results showed that tesserae lacunae have zonal variation in their morphology and orientation, as well as connections through passages (canaliculi) that link cells throughout the tesserae. This organization may permit long-distance fluid transport within and between tesserae, allowing for tesserae growth and biomechanics, as well as providing an integrated cellular connectivity throughout the mineralized tissue, a role typically attributed to bone cells rather than chondrocytes in other vertebrates. To further explore the interactions and physiological roles of hard and soft tissue components (matrix and cells) in both tesserae and the unmineralized matrix, I imaged and characterized cell morphology and matrix

composition by taking novel advantage of the tissue's native fluorophores, applying a customized label-free imaging technique based on exciting the inherent autofluorescence of the tissue. Autofluorescence imaging revealed a rich diversity of different signals associated to specific tissue locations and cell populations, indicating untapped potential of this label-free tool for imaging tessellated cartilage. The autofluorescence signals that could be linked to specific tissue architectures (e.g. chondrocyte pericellular envelopes) and compositions (e.g. collagen type II, a common cartilage protein) suggest deeply conserved features among vertebrate cartilages; however, the many components that could not be identified from their spectral signatures suggest there may still be taxon-specific features of tessellated cartilage yet to be discovered. The combined works in this dissertation illustrate that the cells in tesserae and the unmineralized matrix, although all considered 'chondrocytes', exhibit distinguishing morphological and organizational features and, therefore, likely different functions (e.g. in mineralization, matrix turnover), suggesting that elasmobranch chondrocytes are plastic cells able to form and maintain different skeletal structures by adapting their morphology to cope with elasmobranch-specific skeletal demands. Furthermore, the finescale variations in tissue architecture, evidenced by the complex arrays of native fluorophores in the tissue, argue that the mineralized architectures of tessellated cartilage are not formed by a direct mineralization of a hyaline cartilage matrix, but perhaps result from local variation and/or reorganization of matrix properties, probably through cellular action. Given the variety of cartilage types across vertebrates and the diversity of skeletal structures they form, the plasticity of elasmobranch chondrocytes may be just one example of plasticity in this cell type, a topic that has been deeply overlooked in cellular biology and cartilage evolution research (whereas cell fates and variation are heavily studied in bone biology). Further studies should characterize whether the diversity of chondrocyte function in elasmobranchs and in other vertebrates is genetically encoded (which may suggest multiple cell types), or whether all chondrocytes are the same cell type whose function is triggered by varying environmental factors (e.g. chemical and mechanical). This will help to clarify the roles that chondrocytes and cartilage played in the evolution of skeletal tissues, but also lineage diversification (e.g. into different habitats) and key anatomical adaptations in animal evolution, both in invertebrate body support and the origin of vertebrate endoskeleton.

ABSTRAKT (DEUTSCH)

Die große Mehrheit unter den Vertebrata besitzen ein Skelett aus Knochen, ein mineralisiertes Gewebe, welches die Körperform stützt, als Ansatzstelle für Muskeln fungiert und die Mineral-Homöostase des Körpers reguliert. Im Gegensatz zu dem harten Material, welches Knochen bereitstellt, um die Anforderungen an ein Skelett zu erfüllen, besitzen Elasmobranchii (Haie und Rochen) ein Skelett welches vollständig aus Knorpel gebildet ist, ein flexibles und weiches Material, das hauptsächlich aus Wasser besteht. Der Knorpel der Elasmobranchii wird allerdings durch eine umgebende mineralisierte Schicht, gebildet aus nebeneinanderliegenden Kacheln - den Tesseræ - versteift; es wird angenommen, dass diese distinkte Skelett-Schicht einen wesentlichen Faktor für den evolutionären Erfolg der Klasse der Elasmobranchii darstellt. Die Zellen (Chondrozyten) im Knorpel der Elasmobranchii weisen eine ähnliche Morphologie und Ultrastruktur wie die Chondrozyten anderer Vertebrata auf, sind aber verantwortlich für die Bildung der komplexen Architektur des ‚tessellated cartilage‘ Gewebes (Mosaik-Knorpels), welches sowohl mineralisiertes als auch unmineralisiertes Gewebe in sich vereint. Darüber hinaus scheinen die Chondrozyten der Elasmobranchii andere Funktionen zu erfüllen als die Chondrozyten anderer Vertebrata, in dem sie zum Beispiel den Mineralisierungsprozess überleben und scheinbar feinskalige Kontrolle darüber ausüben, wo Mineralisierung stattfindet und wo nicht (z. B. in den komplexen Fugen zwischen den Tesseræ). Obwohl die spezielle Interaktion von Zelle und Matrix scheinbar die Bildung dieses einzigartigen Knorpeltyps bestimmt, wurden die Faktoren, welche diese Zellen und deren umgebende Knorpelmatrix ausmachen weder weitergehend untersucht noch mit dem Knorpel anderer Vertebrata verglichen. Im Rahmen dieser Dissertation charakterisiere ich Zell- und Matrixstruktur und die Organisation im Skelettknorpel der Elasmobranchii unter Verwendung einer Vielzahl von Bildgebungs- und Materialcharakterisierungs-Methoden, inklusive zweier marker-freier Bildgebungs- und Analysetechniken, die für dieses Gewebe speziell angepasst wurden. Um die Anatomie und Rolle der Tesseræ Chondrozyten zu charakterisieren, wurden tausende Tesseræ Lacunæ (Zellzwischenräume) mittels hochauflösendem Synchrotron micro-CT in 3D aufgenommen und die Morphometrie und Anordnung der Lacunæ durch einen Hochdurchsatz-Workflow quantifiziert. Die Ergebnisse haben gezeigt, dass die Lacunæ der Tesseræ zonale Variationen in ihrer Morphologie und Orientierung aufweisen, sowie Verbindungskanäle (Canaliculi) welche die Zellen der Tesseræ miteinander

verbinden. Diese Anordnung erlaubt möglicherweise Flüssigkeitstransport über größere Distanz innerhalb und zwischen Tesseræ und spielt damit nicht nur eine Rolle für Wachstum und Biomechanik der Tesseræ, sondern stellt auch eine integrierte zelluläre Verbindung durch das mineralisierte Gewebe dar, eine Funktion die in anderen Vertebrata typischerweise Knochenzellen zugeschrieben wird und nicht Chondrozyten. Um die Wechselwirkungen und physiologische Bedeutung von harten und weichen Gewebekomponenten (Matrix und Zellen) in Tesseræ und unmineralisierter Matrix weitergehend zu untersuchen, habe ich die Zellmorphologie und die Matrixzusammensetzung bildgebend untersucht und charakterisiert. Hierfür verfolgte ich den neuen Ansatz die nativen Fluorophore des Gewebes durch Verwendung einer maßgeschneiderten marker-freien Bildgebungstechnik, die auf der Anregung der inhärenten Autofluoreszenz des Gewebes basiert, zu nutzen. Die Autofluoreszenz-Bildgebung zeigte eine großer Diversität an unterschiedlichen Signalen, die mit spezifischen Gewebestellen und Zellpopulationen assoziiert sind, ein Hinweis auf das ungenutzte Potenzial dieser marker-freien Methode für die Bildgebung von ‚tessellated cartilage‘. Die Autofluoreszenzsignale, die mit spezifischen Gewebearchitekturen (z. B. die perizelluläre Chondrozytenkapsel) und Zusammensetzungen (z. B. Kollagen Typ II, ein häufiges Knorpelprotein) in Verbindung gebracht werden konnten, deuten auf stark konservierte Merkmale unter den Knorpeln der Vertebrata hin; die vielen Komponenten, die anhand ihrer spektralen Signaturen nicht identifiziert werden konnten, lassen jedoch vermuten, dass es noch taxonspezifische Merkmale des ‚tessellated cartilage‘ gibt, die noch zu identifizieren sind. Die kombinierten Arbeiten in dieser Dissertation zeigen, dass die Zellen in den Tesseræ und der unmineralisierten Matrix, obwohl sie alle als "Chondrozyten" angesehen werden, unterschiedliche morphologische und organisatorische Merkmale aufweisen und daher wahrscheinlich unterschiedliche Funktionen haben (z. B. bei der Mineralisierung, dem Matrixumbau). Dies deutet darauf hin, dass Chondrozyten der Elasmobranchii plastische Zellen sind, die in der Lage sind, verschiedene Skelettstrukturen zu bilden und zu erhalten, indem sie ihre Morphologie an die für Elasmobranchii spezifischen Anforderungen des Skeletts anpassen. Darüber hinaus sprechen die kleinskaligen Variationen in der Gewebearchitektur, die durch die komplexen Anordnungen von nativen Fluorophoren im Gewebe belegt sind, dafür, dass die mineralisierten Architekturen des ‚tessellated cartilage‘ nicht durch eine direkte Mineralisierung einer hyalinen Knorpelmatrix gebildet werden, sondern möglicherweise durch lokale Variation und/oder Reorganisation der Matrixeigenschaften, hier wiederum vielleicht durch zelluläre Aktivität. Angesichts der Vielfalt der Knorpeltypen bei den Vertebrata und der Vielfalt der Skelettstrukturen, die sie bilden,

könnte die Plastizität der Chondrozyten der Elasmobranchii nur ein Beispiel für die Plastizität dieses Zelltyps sein, ein Thema, das in der Zellbiologie und der Knorpel-Evolutions-Forschung stark vernachlässigt wurde (während das Schicksal der Zellen und Zellvariationen in der Knochenbiologie intensiv untersucht werden). Weitere Studien sollten charakterisieren, ob die Diversität der Chondrozytenfunktion bei den Elasmobranchii und anderen Vertebrata genetisch kodiert ist (was auf mehrere Zelltypen hindeuten könnte), oder ob alle Chondrozyten derselbe Zelltyp sind, dessen Funktion durch unterschiedliche Umgebungsfaktoren (z. B. chemische und mechanische) ausgelöst wird. Dies wird dazu beitragen zu klären, welche Rolle die Chondrozyten und Knorpel bei der Evolution von Skelettgewebe, aber auch bei der Diversifizierung von Abstammungslinien (z. B. in verschiedene Lebensräume) und bei wichtigen anatomischen Anpassungen in der Evolution von Tieren gespielt haben, sowohl bei dem Skelett der Invertebrata als auch bei der Entstehung des Endoskeletts von Vertebrata.

II | INTRODUCTION & STATE OF THE ART

Cartilage is an ancient skeletal tissue, previously thought to be exclusive to jawed vertebrates (gnathostomes) and considered a key in the evolution of vertebrate endoskeletons, together with bone [1,2,3]. In the past several decades, however, cartilage and cartilage-like tissues have been found to occur incredibly broadly, in jawless vertebrates (cyclostomes: hagfishes and lampreys), chordates (lancelets), hemichordates, and even a variety of invertebrate protostome taxa (e.g. cephalopods, horseshoe crabs, sabellid worms) (Fig. 1) [4,5,6,7]. Yet, despite cartilage being a support tissue shared among diverse animals, its definition has always been based on cartilages from mammals, the most studied group among vertebrates with regard to skeletal biology.

The work in this dissertation focuses on characterizing cellular organization and matrix composition of elasmobranch (shark and ray) skeletal cartilage by customizing and applying, through a collaboration with scientists from multiple disciplines, two imaging techniques that capitalize on intrinsic properties of the tissue using X-rays and light. For context, in the next pages, I describe the state of the art with regard to cartilage biology in animals, detailing the current knowledge of elasmobranch skeletal cartilage, describing similarities and differences in organization, composition and function relative to mammalian cartilage, the tissue considered the 'gold standard' in cartilage biology research. Then, I describe the common imaging techniques used in cartilage biology, classifying them based on whether or not they use external reagents ('labeled imaging techniques' and 'label-free imaging techniques', respectively). Finally, I summarize which techniques have been used to image elasmobranch skeletal cartilage matrix and cells, the limitations that these present in imaging and characterizing this tissue, and the need to develop new imaging techniques using physical principles such as autofluorescence or X-rays to avoid the use of external reagents.

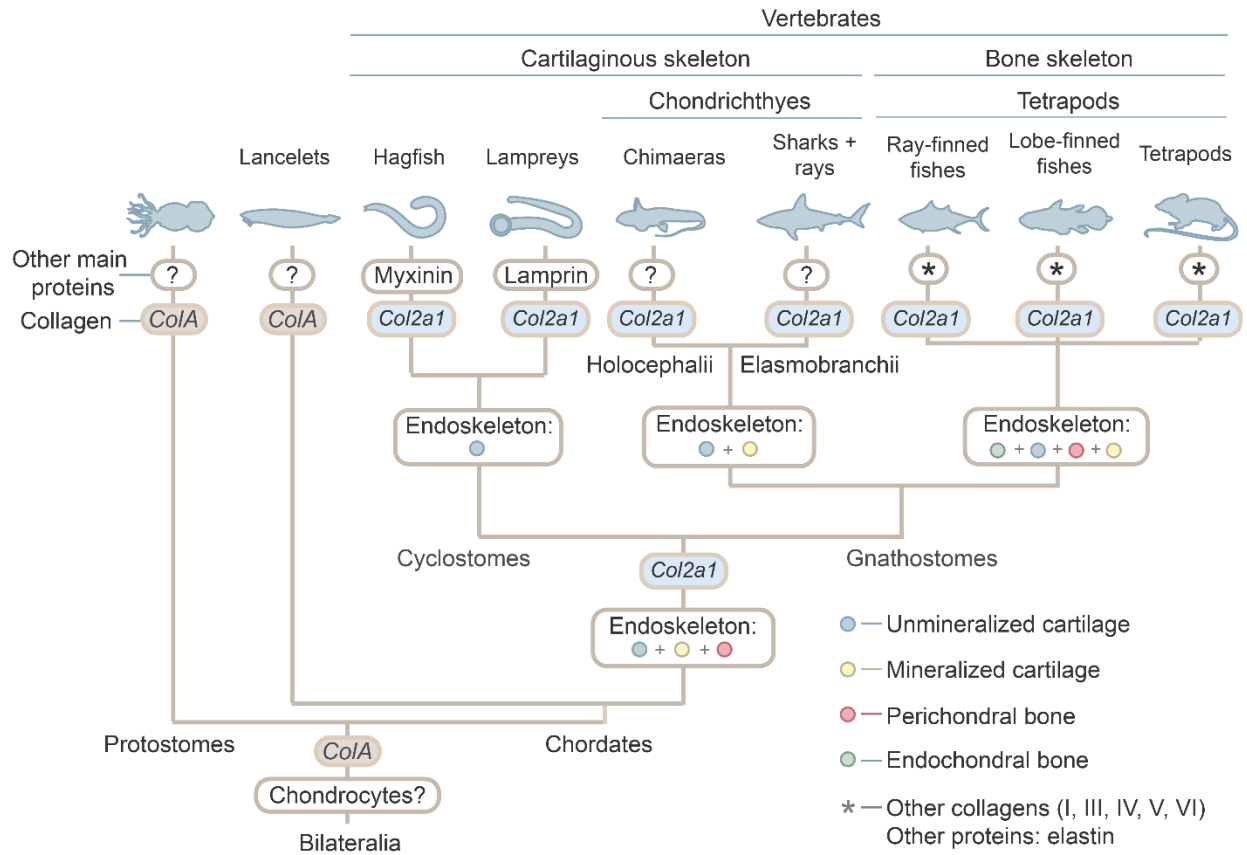


Fig. 1. Phylogenetic distribution of cartilage in bilaterians with special focus on vertebrates. The compiled information indicates that, a cartilage-like tissue based on class-A fibrillar collagen (encoded by the *ColA* gene) and a proto-chondrocyte may have been present in the last common ancestor of bilaterians. In protostomes and lancelets, cartilage cells synthesize a cartilage matrix based on class-A fibrillar collagen, which may be forming the cartilage matrix together with other unknown structural proteins (indicated with a question mark). Vertebrates have an endoskeleton which, depending on the taxonomic group, is composed of various skeletal materials (indicated in the figure with different colors). Vertebrate cartilage is synthesized by chondrocytes and the matrix is composed of fibrillar type II collagen (encoded by *Col2a1* gene), which can be combined with other structural proteins (*) such as myxinin (hagfishes), lamprin (lampreys) or elastin (tetrapods). Similar taxon-specific structural proteins have not been described in chondrichthyan cartilage. The oldest vertebrates (cyclostomes and chondrichthyans) have skeletons composed entirely of cartilage, while in more recent vertebrate groups (fishes and tetrapods), whereas bone is the predominant skeletal tissue, cartilage in adult animals is sparsely distributed and only associated with specific body functions. For further details see [5,6,7,8,9].

1. What is cartilage?

Cartilage is a connective tissue that, together with tendon and bone, forms the skeleton of vertebrates [10]. The dominance in the skeleton of each of these tissues varies according to developmental stages: during the embryonic stages of vertebrates, the entire skeleton is formed by cartilage (denominated embryonic primary cartilage), which allows comparatively fast growth and gives flexibility to the skeleton. Cartilage also provides a scaffold for skeletal development, in that in most vertebrates, embryonic primary cartilage is replaced by bone during development. In contrast, in adult stages, cartilage is associated only with specific body locations such as joints, noses, ears and parts of the respiratory system [10,11].

According to classical (mammal-centric) textbook definitions, adult cartilage: 1) is a stiff, gel-like tissue with copious amounts of extracellular matrix (ECM) composed mainly of water (~70%), collagen type II (Col2) and proteoglycans (PGs, core proteins with branched glycosaminoglycans = GAGs); 2) is devoid of vascularisation; and 3) has only one resident cell type (the chondrocyte), which occupies little of the tissue compared to the ECM [3,9,10,12]. The interplay of these characteristics dictates the specific physiological and biomechanical aspects of cartilage. For example, the biophysical properties of the ECM are conferred by the interplay of Col2 (the most dominant collagen in cartilage), aggrecan (the most abundant PG in cartilage) and water: Col2 fibrils form a tensile network that resists swelling pressure from the huge amount of water trapped by PGs, highly hydrophilic due to the presence of GAGs [10,13–15]. Additionally, the lack of resident vasculature in adult cartilage means chondrocytes must rely on diffusion for nutrient and waste exchange with surrounding connective tissues, resulting in chondrocyte metabolism being mainly anaerobic and cartilage typically having hypoxic oxygen tensions (10% in peripheral areas adjacent to connective tissues, but <1% in regions more distant) [3,10,12,16,17]. The associations of matrix components and their resultant biomechanics are a major focus of cartilage research, particularly with regard to biomedical interests (e.g. for cartilage grafts and joint repair) (e.g. [14,18,19]). As a result, the majority of research has centered on cartilage from humans or from model mammalian systems (e.g. rodents) [20–23].

2. Cartilage variations across taxa

The synergistic effects of cartilage cellular and matrix components mean that compositional variations can have pronounced structure-function implications. However, the functional and physiological implications of the wide natural variation among cartilages from different animal groups —or even among mammals— have barely been explored (but see [24] for differences during cartilage ossification between mice and humans). For example, volume ratios between ECM and cells are highly variable: some cartilages are more cell- than ECM-rich, such as elastic cartilages in mouse, rabbits, rats and bats [25,26]; several cartilage types in fishes [27,28]; several skeletal cartilages in lampreys [10,29] and lingual cartilage in hagfishes [30,31]. On the contrary, cartilages can also be acellular —entirely devoid of chondrocytes— for example the pharyngeal cartilages of hemichordates and lancelets [4,32]. In vertebrates, acellular cartilage has only been described in the heart valve of a freshwater stingray [33], but this has not been deeply studied. The composition of the ECM is also variable, with Col2 and PGs not always being the dominant structural molecules. For example, taxon-specific non-collagenous proteins can serve as primary structural molecules, such as the elastin-like lamprin in lamprey cartilage [10,29] or myxinin in hagfishes [5,7,30].

This natural diversity indicates the little-appreciated variability of cartilage structure and composition in animals, demonstrating that not all descriptions for mammalian cartilage are accurate for other taxa. Cartilage diversification also illustrates how skeletal systems have adapted through evolution to cope with different skeletal demands to survive. For example, chondrichthyans are the only jawed vertebrates that lack bones, with a skeleton completely formed by cartilage. With a cartilaginous skeleton, chondrichthyans became a successful evolutionary group for more than 400 million years, including the world's largest living fish (the whale shark, *Rhincodon typus*), the vertebrate with the longest lifespan, reaching 400 years old (Greenland shark, *Somniosus microcephalus*) and a high variety of life history strategies (from top predators to filter feeders) [34–38].

3. Cartilage in chondrichthyans

Chondrichthyes (sharks, rays, and chimaeras; Fig. 2) represent an important model for understanding cartilage evolution as well as the extant functional diversity of cartilage, in being the only group of jawed vertebrates (gnathostomes) with a skeleton composed solely of cartilage throughout life, not replaced by bone during ontogeny [39,40]. As a result, the cartilage of these fishes must serve the roles expected for cartilage in vertebrates —flexible contour filler (e.g. in noses), scaffold for skeletal growth— but also some usually attributed to bone, for example organ protection, support and muscle attachment. Cartilage is a flexible and gel-like tissue and, to cope with these skeletal demands, the skeleton needs to be stiff at the same time as flexible.

One hypothesis is that the cartilaginous skeleton of chondrichthyes has adapted to be stiff enough by surrounding the skeleton with a thin mineralized layer, made up of tiles called tesserae [41–43]. The particular architecture of the tessellated layer (formed by abutting tiles joined together) results in a sheath around the flexible cartilaginous core, stiffening it enough to cope with the skeletal mechanical demands. The tesserae and the underlying unmineralized cartilage matrix constitute the main skeletal tissues of chondrichthyans, comprising nearly the entirety of the skeleton, excepting just a small region of the vertebral column (Fig. 2.) [44–46]. However, their structure and composition have been mainly studied in model species of sharks and rays (elasmobranchs), and are less known in chimaeras, the elasmobranch's sister group. The lack of information in chimaeras is due to the difficulty to obtain samples, as many species live in deep sea water (below 2000 m), and arguably the general broader interest in sharks and rays (chimaera are little-studied in general). In fact, the skeleton organization of chimaera has only recently been described in depth for the first time [47,48]. These works showed that the skeleton in chimaeras presents a skeletal structure similar to elasmobranchs, based on a cartilaginous matrix surrounded by tesserae, however, with substantial differences such as, for example, a lack of cells living inside of the tesserae [47]. Therefore, due to the chimaera skeleton being still not well characterized, in the following sections and projects of this dissertation, I will be referring exclusively to the elasmobranch group (sharks and rays).

4. The skeleton of elasmobranchs

4.1. *The unmineralized cartilage*

As stated above, the bulk of the elasmobranch skeleton is composed of an unmineralized cartilaginous matrix (probably ~80% of the volume of the tessellated cartilage elements; [49]) with chondrocytes embedded, similar to the hyaline cartilage that forms articular joints and embryonic skeleton in mammals (Fig. 2). Histologically, elasmobranch skeletal cartilage and mammalian hyaline cartilage present a similar glassy appearance, huge amounts of ECM composed mainly of water, Col2 and PG, and sparse chondrocytes [39,40,42,43].

However, despite this grossly similar histological organization, elasmobranchs cartilage is suggested to differ in composition from mammalian hyaline cartilage in a variety of ways. For example, elasmobranchs cartilage contains urea (nitrogenous protein breakdown product) that, in mammals and fishes, is only present in the urine but not in the skeleton. The effect of urea in the cartilage is unknown, but it is thought to contribute to the high swelling ratios [50]. Similar to mammalian cartilages, PGs have been identified as the major non-collagenous molecules forming the cartilaginous matrix of elasmobranch cartilage [51], with the GAGs chondroitin sulfate and keratan sulfate attached to the PG's protein core. However, in elasmobranch cartilage, these GAGs differ in size, structure and concentration from their counterparts in mammalian hyaline cartilage. This confers larger hydrodynamic sizes to elasmobranch cartilage PGs, which increases their hydrophilic interactions with water, resulting as well in an increase in the swelling ratio compared to those for mammal and bony fish cartilage; this in turn should also make the elasmobranch cartilaginous matrix stiffer [50–54]. Additionally, elasmobranch lack the GAG hyaluronan and, thus, the ability to form PG aggregates, suggesting that the observed compositional variations could translate to profound structural differences between elasmobranch and mammalian hyaline cartilage [51].

Together with PGs and GAGs, collagen type-II (Col2) has been identified as the main structural protein forming the unmineralized elasmobranch cartilaginous matrix [49] which indicates that, despite the compositional differences listed above, the elasmobranch cartilage matrix has the same dominant structural protein as other vertebrate cartilages [7,10,55]. Beyond these primary

components, the composition of elasmobranch cartilage is largely uncharacterized. In other vertebrates, a variety of secondary components can be found in cartilage, depending on the cartilage's function and mechanics. These can include other collagens (e.g. collagen type 5, 9; [3]), other proteins (e.g. elastin, myxinin, lamprin; [30,56,57]) and other cells like large adipocytes (lipohyaline-cell cartilage in fishes; [28]). Due to the unique performance demands of the elasmobranch skeleton, molecules other than Col2, PGs and GAGs could be expected to form the unmineralized cartilaginous matrix. However, these have yet to be identified.

4.2. *The tesserae*

Surrounding the unmineralized cartilage are the tesserae, forming a permanent, apparently ever-growing, and tessellated ring of mineralized tissue (Fig. 2.) [42–44]. Unlike in mammals, where permanent calcified cartilage represents a small portion of the adult skeleton (only located at the base of the articular cartilage), in the elasmobranch skeleton, tesserae are one of the main components. In fact, tesserae are considered a synapomorphy of the entire chondrichthyan group, appearing in the 400 million years-old fossil record of stem species such as the extinct shark *Mcmurdodus* and shark-like *Doliodus* [35,47,58].

The distinct polygonal pattern of the tesserae is thought to have crucial roles in skeletal growth and biomechanics (Fig. 2) [39,43,59,60]. Tesserae first appear during embryonic development as isolated platelets at the outer borders of the unmineralized matrix [59,61]. These platelets continue growing throughout the animal's life, eventually growing into contact with one another [39,61]. The constant growth of the tesserae is an exclusive attribute of elasmobranchs, differing with what is known for mammals, where calcified cartilage growth during adult stages is only associated with pathological conditions (e.g. osteoarthritis, [62,63]).

During growth, tesserae add mineral to all edges, increasing their size and volume in all directions through the unmineralized matrix [39,64]. In this process, the chondrocytes in the unmineralized matrix adjacent tesserae are also surrounded by the accreting mineral, ending permanently trapped within the tesserae where they are maintain alive within spaces in the mineral, called

lacunae [42,43,65]. In mammals and birds, cartilage mineralization is led by chondrocytes (e.g. endochondral ossification) which become larger (hypertrophic chondrocytes), synthesize specific matrix products (e.g. Collagen type 10) and, once their surrounding matrix is mineralized, undergo programmed death (apoptosis) or transdifferentiation into bone cells [66–68]. It is unknown whether these cells change their function during this process or whether they are involved in the mineralization process itself, but neither during the mineralization process nor once enclosed within tesserae, do these chondrocytes appear to suffer any variation in morphology, volume or shape [49,69], differing from what is known for chondrocytes in other vertebrates. These differences in chondrocyte function between mammals and elasmobranchs suggest that elasmobranch chondrocytes differ cell function during the skeletal mineralization process, performing specific functions to form and maintain the cartilaginous matrix as well as the tesserae.

The growth process of tesserae —their accretion of mineral, their apparent lack of remodeling, their eventual growth into contact with each other— determines tesserae architecture and ultrastructure [59,61], which are likely directly related with their biomechanical function [60,70]. In this sense, mathematical models have shown that a structure that plays crucial roles in tesserae growth and biomechanics are the regions where the tesserae abut, the intertesseral joints (Fig. 2) [59,60,70–72]. In the intertesseral joint region, there are zones where tesserae are in direct contact and zones where tesserae are separated by gaps filled with unmineralized cartilage and fibers connecting the tesserae [45,49,59]. It is hypothesized that this unmineralized area between tesserae neighbours allows continuous space for mineral deposition at tesserae margins, also increasing versatility of the mineralized layer by introducing regions of flexibility [60,70–72]. In contrast, in the areas where tesserae are in direct contact with their neighbours with no gap between them, the continuous mineral accretion appears to densify the mineralized tissue, producing areas of high mineral concentration denominated spokes, that radiate from the center to the edge of tesserae, like spokes in a wheel [59]. It is believed that spoke regions provide mechanical protection to the center of the tesserae (especially the central cells) by dispersing the energy and redirecting cracks [60]. However, the biomechanical function of spokes and intertesseral joints has only been theorized using mathematical models and simulations, never experimentally tested *in situ*.

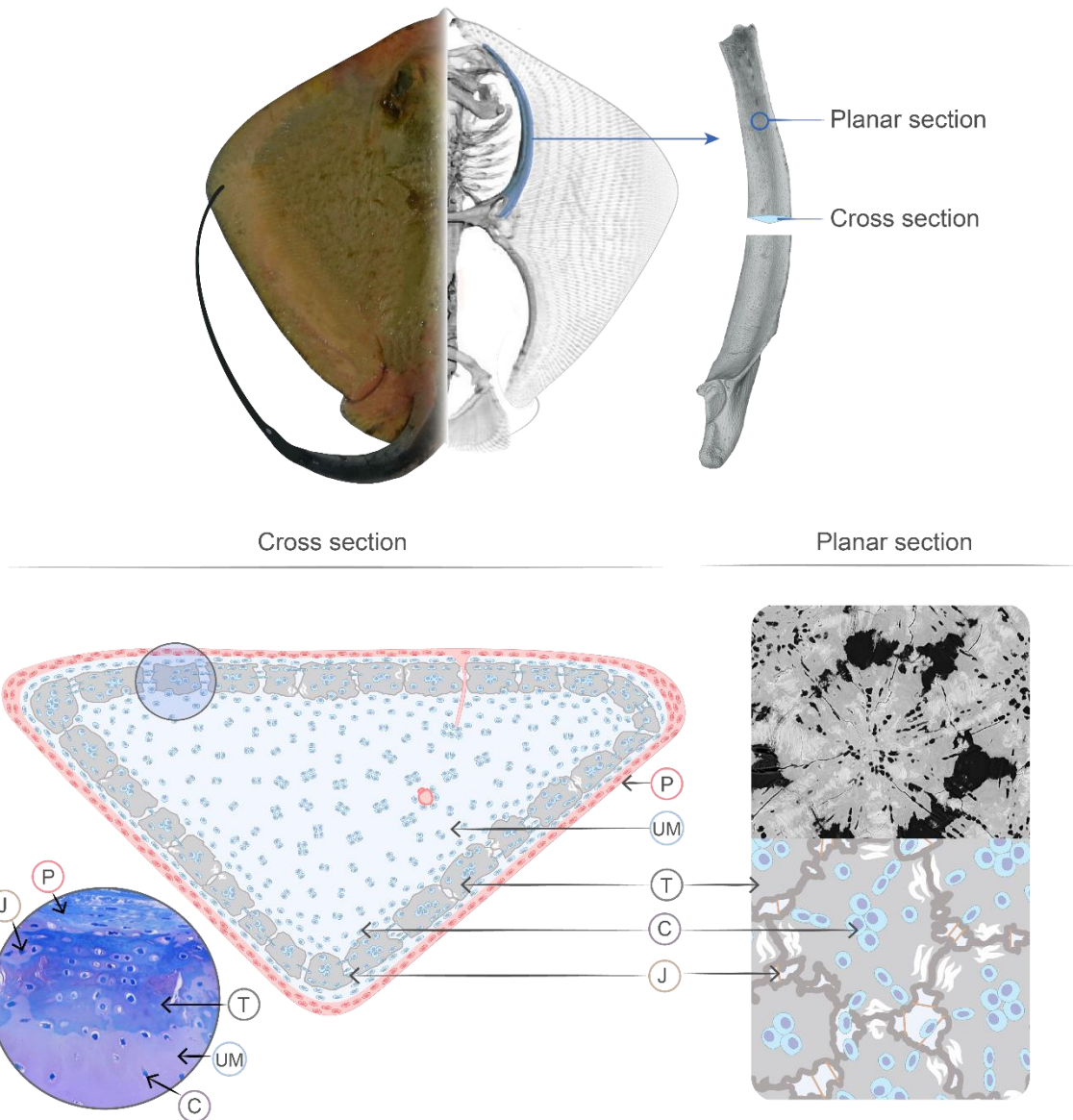


Fig. 2. The tessellated cartilaginous skeleton of elasmobranchs. A photograph of the stingray *Dasyatis pastinaca* (left) combined with a microCT scan of the skeleton (right). The enlarged propterygium shows the unmineralized cartilaginous matrix (UM) entirely covered by tesserae (T). Bottom: The schematic view of a cross section of the skeleton shows the distribution and organization of the UM, T and perichondrium (P). Enclosed in the circle, tesserae cross section stained with toluidine blue can be observed, showing a tessera with two intertesseral joints (J) at each side, the P located at the upper part and the UM at the lower part. Note that the UM occupies the majority of the skeleton. A planar section of the tesserae, shown with an SEM image and a schema, illustrates the tesserae architecture, involving polygonal tiles joined together by (J). Spokes (high-mineral density features) are indicated by white lines in the regions where two tesserae are in direct contact. Both planar and cross section images show the distribution of chondrocytes (C) and their differences in organization between the tesserae and the UM. **Abbreviations:** Chondrocytes (C), Intertesseral Joints (J), Perichondrium (P), Tesserae (T), Unmineralized Matrix (UM).

5. Common techniques used to image cartilage

To understand how cartilage (or any other tissue) has adapted to cope with different biomechanical demands, it is necessary to study its anatomical arrangement, matrix composition and cell type, organization and function. Nearly all the knowledge in cartilage research comes from mammals and few other well-established animal models (e.g. zebrafish), from which the resulting information is usually extrapolated to define cartilage in other vertebrates. To study cartilage, a variety of imaging techniques are typically used (most of them optimized to those model species), allowing the characterization of specific cartilage components from different perspectives, depending on the technique. For example, to analyze composition and ultrastructure, techniques based on tissue staining with external reagents (e.g. histology) and a posterior imaging with light microscopy (e.g. optical microscopy) or electron microscopy (e.g. TEM) are used. To study, instead, 3D structure and organization of tissues and cells, techniques based on computed tomography (e.g. CT-scans), magnetic resonances and light (e.g. polarized microscopy) are commonly used. Therefore, depending on whether or not these techniques use external reagents to highlight specific tissue components and structures, they can be divided into two groups: labeled imaging techniques and label-free imaging techniques. In the following paragraphs I outline some of the more commonly used techniques and their advantages and disadvantages, particularly with regard to cartilage imaging.

5.1. Labeled imaging techniques

Labeled imaging techniques use reagents that bind to specific molecules, highlighting their location in the tissue and making them visible under the microscope. They are broadly applied to study morphology, structures and composition of cells and tissues and so are the techniques most often taught in anatomy and physiology courses. Depending on the microscope used, these techniques can be classified as: 1) histology (including immunohistochemistry); 2) *In situ* hybridization, both relying on light microscopy, and 3) electron microscopy.

The term histology refers to a variety of techniques based on imaging the stained tissue under the light microscope (e.g. confocal microscope, optical microscope). Several staining agents can be used to stain tissue and cellular structures [3,73], with histology techniques typically classified into either classical histology and immunohistochemistry (IHC), depending on the specificity of the dyes used and how they bind to target tissues. Classical histology colours tissue using dyes (which can also be fluorescent) that have affinity to specific chemical properties of the molecules. For example, basic dyes (positively charged) bind to cell and tissue components that are negatively charged such as DNA and GAGs. Since GAGs are one of the main components in cartilage, several basic dyes (e.g. alcian blue and toluidine blue) are used in cartilage histology [21,74,75]. On the contrary, acidic dyes (negatively charged) bind to cell and tissue components that are positively charged, such as proteins like collagens. Thus, acidic dyes like sirius red are also widely applied to study cartilage, since proteins are important to cartilage structure (e.g. Col2) [76,77]. Due to their basic and relatively non-specific function, histological dyes have been applied to anatomical and comparative biology studies in a broad range of tissues from a huge diversity of organisms [5,78]. The result of the long-standing, standard application of such stains for histology of particular tissues (e.g. cartilage or bone) means that staining function is often casually (or even erroneously) attributed to particular tissue types (e.g. Col1), rather than to general qualities of those tissues (e.g. their charge). Other histological techniques use dyes (usually fluorescent) that bind to specific molecules such as, for example, the enzyme alkaline phosphatase, the cell nucleus (DAPI staining) and the actin fibers of the cytoplasm (phalloidin staining) [79,80]. As these techniques bind specific components, they require testing and optimization of protocols for different tissue preparations (fixation, embedding) and tissue types [79,81–83].

An even more specific histology technique, immunohistochemistry, relies on the use of antibodies to localize specific proteins (antigens), providing information about expression, distribution and localization of target proteins (e.g. a particular collagen) in a tissue [84,85]. To detect the antibodies (and, therefore, the antigens they bind to) under the light microscope, the antibodies need to be labeled with a visible marker, either directly or indirectly in the form of a labelled secondary antibody [84,86,87]. The latter is more common, since it enables the amplification of the signal, as more than one secondary antibody binds to each primary. Several labels can be used

as markers, such as fluorochromes like rhodamine, enzymes like alkaline phosphatase or biotin [73]. In cartilage biology, IHC is mainly used to characterize matrix composition like, for example, identifying different collagens such as Col2 (cartilage matrix, Fig.3) and Col6 (pericellular matrix), as well as chondrocyte- and gene-products that give information about cell function and cartilage development, such as Sox9 [6,73,88,89].

In contrast to the gene products stained in tissues by immunohistochemistry, *in situ* hybridization (ISH) involves the identification of a specific DNA or RNA sequence in the tissue and, therefore, is a tool used to understand the regulation, expression and function of genes and cells. Labelled DNA or RNA probes (counterparts of the target sequence) are used to identify and quantify the position of the genetic sequences *in situ* (in their natural position within the chromosome) [90,91]. To ensure the correct attachment, there should be a high specificity between the labelled sequences and the target sequence and, for that, the nucleotide sequence of the mRNA or the DNA of the desired cell must be known beforehand [92]. In cartilage, ISH has been mainly used to target the expression of cartilage and chondrocyte-specific genes such as *Col2a1*, *Sox9* or *Runx2* [93,94].

Whereas histological techniques rely on light microscopy, electron microscopy uses a beam of accelerated electrons to image tissues. The short wavelengths of the electrons result in images of high resolution (of nanometers), allowing imaging of matrix and cellular ultrastructure [95]. Depending on how the electrons are detected, two types of electron microscopes are used: scanning electron microscope (SEM) and transmitted electron microscope (TEM). SEM images tissues by detecting reflected or scattered electrons, giving information about the surface of the sample and its composition. In contrast, TEM creates an image detecting the transmitted electrons (electrons that passed through the sample), offering information on the inner structure of ultrathin samples (50 - 70 nm) [95–97]. Depending on their electron density, the biological structures interact differently with the electron beam, scattering or absorbing the electrons. The differences in electron density generate contrast in the resulting images, making it possible to distinguish between biological structures [98–100]. However, non-mineralized biological tissues like cartilage and chondrocytes are low-contrast materials and, therefore, their resolution is lower (~100nm) than high-contrast materials (which can reach 10 nm) [98]. To increase the resolution

of low-contrast materials, electron-dense markers such as heavy metals (e.g. lead citrate and uranyl acetate) or gold nanoparticles (immunogold technique) are used, giving enough contrast to distinguish cell ultrastructure (e.g. organelles) and aspects of extracellular matrix composition (e.g. GAGs, Col2) [101–104]. Based on TEM and SEM principles, other microscopy arrays have been developed to cope with specific imaging demands, such as, for example, FIB-SEM, which images the surface of the sample using an ion beam, or cryoSEM, which images the surface of hydrated and cryogenically fixed samples (frozen below -127°C) [105,106].

The information given by classical histology, IHC, ISH and electron microscopy can be complemented in order to obtain a broad picture of the tissue at different scales (Fig. 3). For example, histology is frequently used to study the morphological organization and composition of the tissue at large scales (mm - cm), such as the arrangement of chondrocytes in the cartilage matrix, to compare cartilages among species or to differentiate cartilage from bone (e.g. [21,107,108]). To identify specific components in the tissue, IHC and ISH can be used, allowing the characterization of tissue composition and cellular function. However, histology, IHC and ISH are indirect techniques, where the components are identified and imaged using vectors (antibodies, dyes or genetic material) and, therefore, several inaccuracies can result such as cross-reactivity (binding to non-target antigens) or false negatives (no staining because the protein is in low concentration or not enough antibody bound to the protein). To help verify the presence of components in such cases, their ultrastructure (nm - μm) can be imaged using electron microscopy, also allowing the study of their morphology and organization within the tissue (e.g. the cartilage matrix network formed by GAGs and Col2). However, the high resolution images obtained by electron microscopy are limited to image small areas of the sample (of μm^2), being only possible to image discrete structures of the tissue.

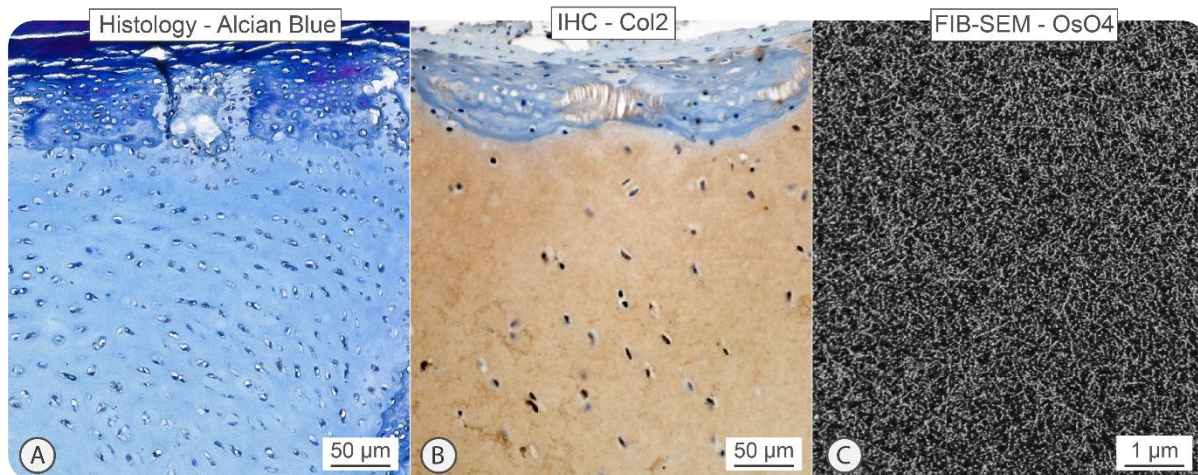


Fig. 3. Comparison of elasmobranch tessellated cartilage imaged using labeled imaging techniques. All images show cross sections of *Raja clavata*'s tessellated cartilage. **A)** Section stained with alcian blue (classical histology), which highlights the negatively charged molecules like the glycosaminoglycans and cell nuclei. **B)** Section immunohistochemically stained (IHC) for Col2 (yellow-brown regions). Both the unmineralized cartilaginous matrix and spokes are stained, while no staining is observed in the perichondrium and the tesserae. **C)** FIB-SEM image of the cartilage matrix ultrastructure, with Col2 fibers visible, stained with heavy metals.

5.2. Label-free imaging techniques

Label-free imaging techniques involve imaging the tissue without the need of external reagents. Instead, they cause a reaction in specific biological molecules using electromagnetic radiation such as light (UV, visible light, X-rays), magnetic fields or electron beams to image the tissue. Biological molecules react differently when excited with these sources and, based on the molecular physical properties (e.g. chemical composition, structure, density), they will emit a specific signal that is collected by the detector. Although the physical properties of the different sources are known for decades, some of them have only in the last 10-15 years started being applied to image biological tissues, especially non-mineralized tissues like cartilage [109–111]. In cartilage research, several label-free imaging techniques have been used in order to image the matrix and cell ultrastructure and composition. These techniques differ in the excitation source and the technology utilized (e.g. confocal microscopy, laser surface scanning, polarized light microscopy) and, therefore, they can be classified as: light-based techniques, computed tomography, electron beams and magnetic resonance.

Light-based label-free imaging techniques use light to excite different photonic properties of molecules. Polarized light imaging distinguishes between singly refracting materials (light refraction is direction independent) and double refracting materials (light refraction is direction dependent) (Fig. 4) [112,113]. This allow us to define the prefer orientation of birefringence fibers present in the tissue like, for example, collagen Polarized light microscopy has been used in cartilage research to localize fibrial collagens in the tissue (which have positive birefringence), however, it is not possible to distinguish between collagen types [114,115]. Autofluorescence is the capacity of certain biological molecules with aromatic rings (endogenous fluorophores) to emit light (Fig. 4) [116,117]. There are several biological fluorophores in the cartilage matrix such as Col1, Col2, Col3 and elastin, as well as in cells, like flavins, DNA or NADH (e.g. [116,118–120]. Depending on the molecular structure, fluorophores react and emit light with different wavelengths (different colors), meaning that, once standardized, they can be distinguished based on their emission and excitation spectra [116,119,121].

Like autofluorescence, two-photon excitation fluorescence (TPEF) and second harmonic generation (SHG) are nonlinear optical processes based on the excitation of an endogenous fluorophore (biological molecules that react to light), resulting in the emission of light [122–126]. TPEF excites the fluorophore when two photons from high wavelengths (near infrared) hit the fluorophore simultaneously. These photons are absorbed by the fluorophore, resulting in an emission of light (Fig. 4) [123,127]. As longer wavelengths are used, they have the advantage of penetrating deeply in the tissue producing less damage than lower wavelengths. In cartilage, TPEF has been mainly applied in mammalian articular cartilage for imaging elastin networks and chondrocytes [128–130]. Lastly, SHG is the capacity of specific molecules (nonlinear materials) to interact with two photons with the same energy, and emit one photon with twice the energy of the excitation photons (Fig. 4) [122,131]. In cartilage, Col2 can generate second harmonic generation properties due to their molecular structure [130,132,133].

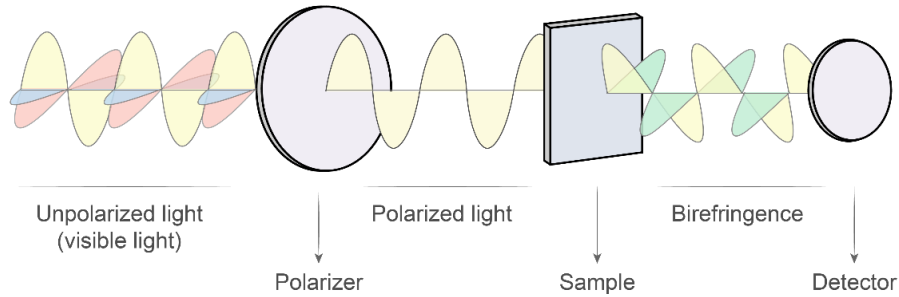
Rather than light, computed tomography uses X-rays for sample imaging [134,135]. The sample is placed between a source and a detector and, as the X-ray beam crosses the sample, the constituent sample materials attenuate the passage of X-rays differently depending on their

density (Fig. 5). The resulting signal is collected by the detector, creating a projection image, a 2D radiograph. In the late twentieth century, the detector was often a physical X-ray-sensitive film, but in modern machines (e.g. laboratory microCTs) are digital flat panel detectors. In computed tomography, either the sample or the source-detector pair are then rotated to direct the X-rays through the sample from different angular positions, generating a series of 2D projection images that can then be used to reconstruct a 3D volumetric dataset (showing the sample's interior structure) (Fig. 5) [135–137]. As this technique is non-destructive, it is particularly valuable to obtain 3D data sets of the outer and inner materials without losing the sample. Several computed tomography techniques are used in biology, which vary in the maximum sample size they can support, their X-ray energy, and the geometry of their scanning chambers (e.g. how close samples can be brought to the source, how far the detector can be moved from the sample) [138]. These factors decide the resulting image resolution, which ranges over four orders of magnitude, from sub-millimeter down to sub-micron, with inherent trade-offs between sample size and resolution:

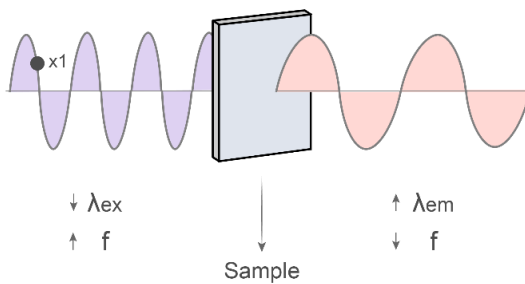
1. Medical computed tomography, which can be used for larger patients/specimens (up to ~60 cm wide), but has comparatively low resolution ($\geq 600 \mu\text{m}$) and so is useful largely only for overview scans of larger animals.
2. Micro-computed tomography (μCT), which can be used to image smaller samples (like skulls or small animals, Fig. 6A) with a voxel size typically one to two orders of magnitude better than medical CT ($\sim 100 \mu\text{m}$ down to $\sim 5 \mu\text{m}$). In the last decade, this technique has become far more accessible: laboratory μCT s now are common in research laboratories, varying from desktop machines that accommodate small bones/animals (e.g. Bruker) to stand-alone cabinet devices that can scan items the size of a volleyball and weighing kilograms (e.g. RX Solutions, YXLON).
3. Nano-computed tomography (nCT), which can be used to image even smaller samples (Fig. 6B) with a higher resolution, with voxel size values ranging from $\sim 5 \mu\text{m}$ down to $0.4 \mu\text{m}$ (i.e. an order of magnitude better than μCT).
4. Synchrotron radiation micro-computed tomography (SR- μCT), which also allows imaging samples at resolutions similar to nCT, but using beams with a single X-ray wavelength, which

results in higher beam intensities and, therefore, higher contrast in order to image structures of interest (Fig. 6C).

Polarized light microscopy



Autofluorescence $\lambda_{ex} < \lambda_{em}$

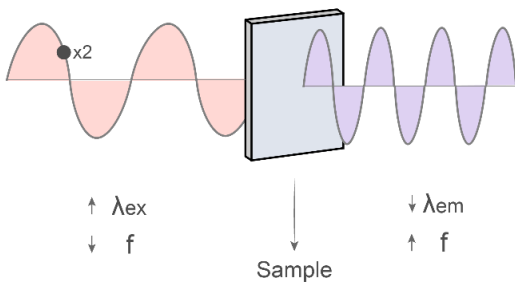


λ = wavelength

f = frequency

● = photon

Two-Photons $\lambda_{ex} > \lambda_{em}$



SHG $\lambda_{em} = 1/2\lambda_{ex}$

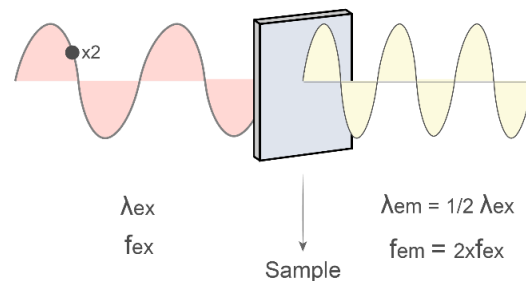


Fig. 4. Light-based label-free imaging techniques. Schematic visualizations of the different label-free imaging techniques based on light, showing how the sample interacts when excited with an excitation wavelength (λ_{ex}) by emitting a specific wavelength (λ_{em}). Light polarization and autofluorescence are techniques based on linear properties of light, while Two-Photons and SHG are based on non-linear properties of light (i.e. responding non-linearly to the light electric field). Among several differences between linear and non-linear principles, one visible example is the inconsistency of the non-linear techniques between the number of photons excited (2) and emitted (1).

Two ‘next generation’ directions in computed tomography, under development currently, are particularly relevant for biological and medical research, namely the scanning of moving objects and the imaging of soft tissues. With regard to the former, true “4D”- μ CT —scanning moving objects in real-time, without having to move the sample in a stepwise fashion— is especially sought-after for scanning tissues and organs *in vivo*. Although this technique is highly technically challenging due to its requirement of high temporal resolution (i.e. rapid acquisition of multiple 3D datasets, in order to capture biological motion), systems are in development and in use in industry (e.g. TESCAN) and synchrotron facilities for application in, for example, biomechanics and fluid transport in geological materials [139,140].

With regard to soft tissue imaging, cartilage, as a non-mineralized tissue, offers poor contrast to be clearly imaged using computed tomography. Therefore, computed tomography techniques are mainly used to image mineralized tissues (e.g. calcified cartilage, bone) and less used to image soft tissues. Where soft tissues are of interest, staining reagents (e.g. PTA, PMA, iodine) have been used to increase contrast, for example, between matrix and cells; with its high water content, however, cartilage does not respond well to contrast enhancement and most images allow only gross evaluation of structural features in CT [141–144].

X-rays - Computed Tomography

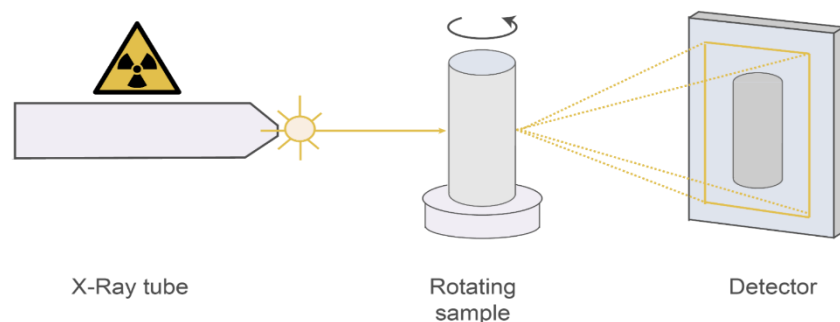


Fig. 5. Schema of the computed tomography scan set up. X-rays (in yellow) are emitted from a X-ray tube towards a rotating sample, and the transmitted electrons are recorded by a detector as a 2D projection image. 2D projections, recorded from multiple sample rotation angles, are then used to reconstruct a 3D volumetric dataset.

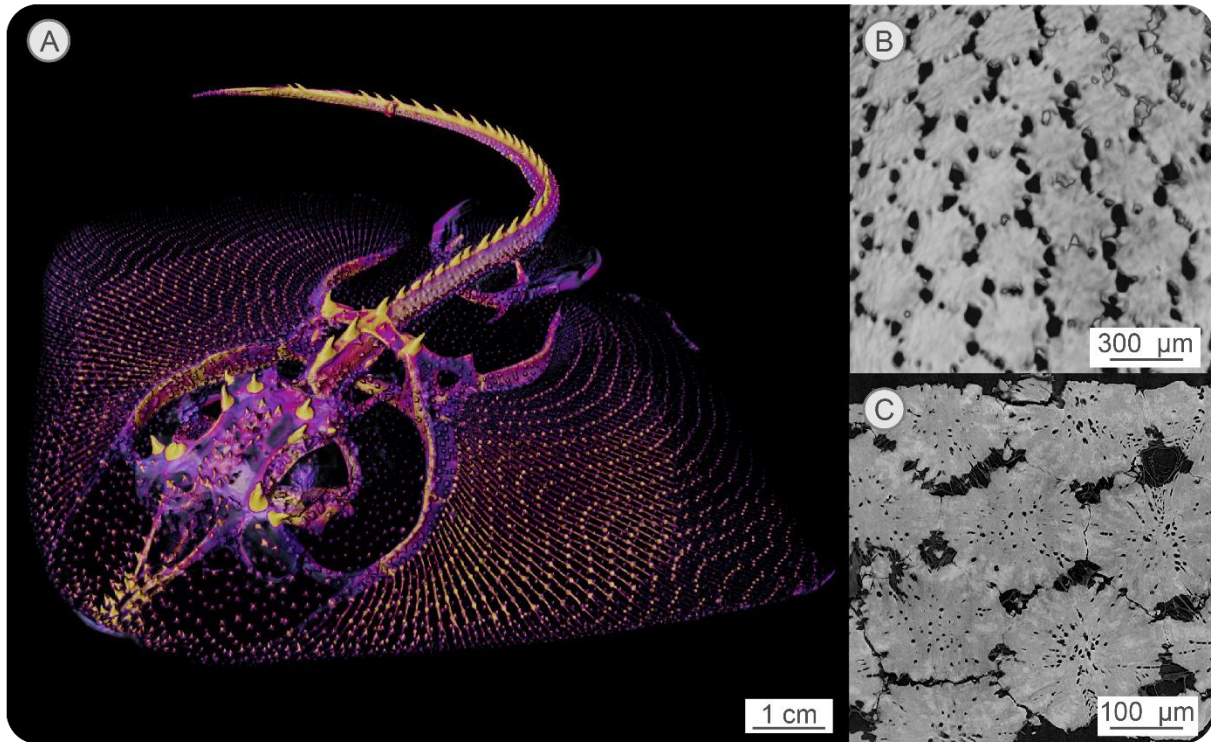


Fig. 6. Computed tomography scans of batoid's mineralized skeleton. **A)** μ CT scan of *Raja clavata*'s skeleton rendered in Amira. Yellow areas correspond to higher mineralized structures, such as scales located on the dorsal side of the animal, whereas purple areas correspond to lower mineralized structures. **B)** nanoCT scan of tesserae surface, where the morphology of tesserae and the joint areas (non-mineralized black gaps) can be appreciated. **C)** Cross section of tesserae SR- μ CT image, where several features can be distinguished such as spokes laminae (highly mineralized regions), the lacunae spaces where chondrocytes reside and the fibrous material characteristic of the intertesseral joints.

Magnetic resonance combines high magnetic fields with radiofrequency pulses to image tissues at large scales (cm-m). This technique involves exposing the biological sample to powerful magnets, which align the positively charged atoms (mainly hydrogen) in the direction of the magnetic field generated. Once the atoms are aligned, a radiofrequency pulse is applied, pushing the atoms to be aligned to the radiofrequency field instead of to the magnetic field. Then, the atoms emit their own radiofrequency radiation, which is detected by the scanner. After a certain amount of time, the atoms stop emitting a radiofrequency signal and realign again with the magnetic field. The times to stop emitting a radiofrequency signal (T2 relaxation) and to realign (T1 relaxation) vary within different tissues in the body and, therefore, can be used to generate

images with different contrast [145–147]. For example, tissues with low T2 are bones and lungs, and high T2 include more fluid-filled tissues such as synovial fluid and the gray matter of the brain [148]. Although magnetic resonance is a label-free technique, sometimes contrast agents like gadolinium can be used to identify specific components such as GAGs and Col2 in cartilage [149]. Due to the fact that magnetic resonance is safe to be used in living specimens and can generate images of entire organs (e.g. brains, lungs, joints) it is widely used in clinical assays [150–154]. However, this technique cannot achieve enough resolution to image tissue ultrastructure and, therefore, it is not suitable for cellular and matrix characterization.

The fact that these techniques do not require the use of reagents offers a variety of advantages. First, external reagents can interfere with the organization and structure of molecules, so tissues can be imaged in a closer native state. Second, they are easier to use in non-model organisms, since there is no need to optimize the reactivity of reagents to ensure staining of specific tissue structures (e.g. not all antibodies for mammalian IHC work for the tissues of other taxonomic groups).

6. Imaging elasmobranch cartilage

Although the imaging approaches applied to elasmobranch skeletal cartilage are not nearly as diverse as those applied to mammalian tissues, tessellated cartilage has been studied since the 19th century, being especially of interest to paleontologists and comparative anatomists [155–158]. Since the mineralized parts are the structures that fossilize and are easier to fix and preserve, there was an interest during the 20th century in studying the structure, composition and arrangement of the hard parts of the elasmobranch skeleton, including teeth, denticles, vertebra and tesserae (e.g. [41,159–162]). The study of hard parts, especially tesserae, has increased in the last 40 years, addressing new topics such as growth and biomechanics [59,60,70]. However, the soft parts of the skeleton, like the cartilage matrix and cells, have been far less studied. This is probably because 1) the cells and matrix are more difficult to preserve than mineralized tissues and 2) the techniques to image them are mainly label-based, and require a thorough optimization of, for example, staining protocols. Regarding fixation, cells are especially difficult to preserve and

prepare to be imaged under the microscope and, until now, no study has succeeded in obtaining an optimal preservation of elasmobranch cellular ultrastructure and morphology, especially regarding the cells enclosed within the tesserae.

In general, the techniques used to study elasmobranch cartilage matrix and cells are mainly labeled imaging techniques (e.g. classical histology, IHC; *see section 5.1*). These techniques have allowed the identification of different tissue types forming the elasmobranch skeleton (e.g. tesserae, cartilage matrix, intertesseral joints), the characterization of their anatomical organization, and the description of several matrix components and cell products (e.g. [40,46,49,163]). However, the information obtained with these techniques is also limited, since they can be, depending on the technique, unspecific and/or biased toward the study of proteins already described in mammals and other model-organisms.

Classical histology techniques have been the most used techniques to image elasmobranch cartilage, as they are highly useful to quickly obtain a broad sense of tissue anatomy and organization (e.g. [40,49,61,164,165]). However, since the composition of elasmobranch cartilage is largely unidentified, the components that bind to stainings have yet to be verified. Indeed, some histological results for tessellated cartilage do not correspond to their mammalian supposed counterparts (see Table 2 in [49]). For example, as stated in the *section 5.1.*, alcian blue and toluidine blue are positively-charged dyes that bind to negatively-charged components like GAGs. When these stains are used in elasmobranch cartilage, it is assumed that they are bound to GAGs, leading to the conclusion that elasmobranch cartilage is similar in composition to mammalian cartilage [40,49,61]. However, other negatively charged structures or elasmobranch-specific GAGs may be reacting to the stainings in elasmobranch cartilage. Actually, studies based on cartilage matrix characterization have demonstrated that elasmobranch GAGs differ from other vertebrate GAGs, as showcased by their lack of hyaluronan [50,53,166]. Therefore, classical histology cannot be used for fine comparison of elasmobranch cartilage with other vertebrate cartilages, requiring support from other techniques, such as chemical composition analyses or electron microscopy. However, such systematic, multi-technique correlative characterizations of unmineralized elasmobranch cartilage have yet to be tackled.

For more specific localization of gene expression or products (proteins), several different techniques have been successfully applied to elasmobranch cartilage, identifying the expression or presence of several components crucial for understanding the development, composition and function of the elasmobranch skeleton. For example, using histological dyes, the identification of alkaline phosphatase (enzyme related with mineralization) in cells prior to tesserae formation and surrounding tesserae borders, demonstrating that 1) cells are involved in the mineralization process and 2) mineralization is accomplished using an enzyme conserved through evolution, since alkaline phosphatase is involved during mineralization in both prokaryotes and eukaryotes [61,64,167–169]. Similarly, immunohistochemistry (IHC) has been used to identify several tissue components such as Col1, Col2, and *in situ* hybridization (ISH) to localize the genes for *Col1a1* (Col1), *Col2a1* (Col2), *Col10a1* (Col10), *Agc* (Aggrecan), as well as genes from the *Sox* family related with cartilage development and growth (*Sox5*, *Sox6* and *Sox9*) [40,46,49,61,163,170]. The presence of these components in elasmobranch cartilage indicates a shared cartilage composition and chondrocyte function with mammals, demonstrating that the basal cartilage structure is apparently conserved across evolution. However, similar to classical histology, the applications of these techniques and their resulting information present several limiting factors. First, ensuring result accuracy in elasmobranch cartilage requires protocols more difficult to optimize and apply than classical histology due to the specificity of antibodies and genetic material, which also are more expensive than dyes used in classical histology. Second, the information obtained is limited to the identification of genes and proteins already described in mammals, not allowing further identification of specific components of elasmobranch cartilage, which still remain unidentified.

To characterize the ultrastructure of elasmobranch cartilage matrix and cells, electron microscopy techniques such as SEM and TEM have been used in multiple studies. SEM has been mostly used to image the ultrastructure of mineralized tissues (e.g. tesserae), some non-mineralized structures such as cells and cartilage matrix, and the morphological interactions between them [39,42,43,47,59,171]. On the other hand, TEM has been used to image, with a resolution of nanometers, the ultrastructure of both mineralized and non-mineralized tissues, being especially useful for imaging cells and matrix components. Therefore, TEM images have been effective in supporting results obtained by histology, such as the verification of Col1 in the perichondrium and

tesserae, Col2 in the unmineralized matrix [42,49,172], the characterization of cell ultrastructure and morphology [39,42,171], and to identify unknown fibers not detected by histology techniques, such as the parallel organized fibers of the intertesseral joints [49]. Although electron microscopy techniques have proved powerful for describing ultrastructural components, –especially those specific for elasmobranchs–, sample preparation for these techniques can be technically very complex, requiring several steps that, in most of the cases, cannot be achieved for elasmobranch cartilage like, for example, the difficulty of getting fresh samples to fix the tissue as closer as possible to its native stage.

Due to the difficulty of applying labeled imaging techniques to image elasmobranch cartilage, other techniques should be developed and optimized to study and characterize elasmobranch skeletal cartilage, especially techniques able to distinguish and identify distinct features of the elasmobranch skeleton. Among the battery of label-free imaging techniques, only polarized light has been used to image elasmobranch cartilage [43,59,173,174]. These studies were able to illustrate how the organization of fibers (e.g. collagen) vary depending on the tissue region where they are located. For example, while the intertesseral joints are composed of well aligned fibers that link tesserae [59], the cartilage matrix appears to be composed of fibers with a far more random organization [43,59]. However, polarized light does not give information about the composition of the tissue and, therefore, this technique needs to be complemented with information from other techniques.

III | AIMS & OUTLINE OF DISSERTATION

In this dissertation, through three consecutive and highly multidisciplinary projects, I characterize aspects of elasmobranch skeletal cartilage structure and biology, with particular emphasis on the use of label-free imaging techniques based on X-rays and light; these were specifically developed and optimized for this tissue through collaborations with scientists with a broad range of backgrounds. These techniques allowed us to describe for the first time several tissue structures from elasmobranch skeletal cartilage, as well as to provide insights into the physiology of the tissues, especially the cells. The dissertation tackles these research questions through the following structure:

- **Protocols and Methods.** For all techniques, I firstly developed and optimized sample preparation protocols (e.g. fixation, embedding), tailored to the particular material properties and composition of tessellated cartilage. These allowed the analysis of elasmobranch skeletal cartilage using a variety of different techniques and microscopes.
- **Paper 1.** This study describes quantitatively the three-dimensional organization and orientation of chondrocytes living in tesserae, by the analysis of high-resolution synchrotron scans using a custom workflow in AMIRA software. Quantification of chondrocyte organization allowed understanding of the role cells play in tesserae growth and biomechanics.
- **Paper 2.** This study builds a flexible workflow for high-throughput processing of large tomographic datasets with repeating structural elements. The approach has broad utility—this structural motif is very common in nature and 3D (e.g. μ CT) datasets are ever larger— also demonstrating the value of multi-disciplinary approaches for tissue analyses and enriching collaborations. The developed workflow was used to analyze the data set of the chondrocytes enclosed in the tesserae from Paper 1.
- **Paper 3.** This study explores the use of a native fluorescence signal (autofluorescence) to image elasmobranch skeletal cartilage. We demonstrate that, without the need of external

reagents, the autofluorescence signal can be used to obtain high-quality images of elasmobranch skeletal cartilage at different scales (from cells to entire skeletal pieces) and, with a posterior hyperspectral image analysis, identify different tissue components (e.g. Coll2, mineralization fronts, cell membranes) and their location in the tissue.

The combined results of these works demonstrate how, within the same skeleton, chondrocytes can develop species-specific functions and structures, as in the case of the tesserae, but also maintain the basic tissue structure and composition characteristic of deuterostome and protostome cartilage, as is the case with chondrocytes of the unmineralized matrix. In addition, the techniques developed here provide the possibility to explore cartilages from non-model species, offering foundations for a comparative approach to explore the diversity of cartilaginous skeletal structures across a massive evolutionary scope (i.e. bilaterian animals).

References

- [1] Ørving T. Histologic studies of Placoderms and fossil Elasmobranchs. 1951.
- [2] Donoghue PC, Sansom IJ, Downs JP. Early evolution of vertebrate skeletal tissues and cellular interactions, and the canalization of skeletal development. *Journal of Experimental Zoology Part B: Molecular and Developmental Evolution*. 2006 May 15;306(3):278-94.
- [3] Pawlina W, Ross MH. *Histology: a text and atlas: with correlated cell and molecular biology*. Lippincott Williams & Wilkins; 2018 Dec 7.
- [4] Cole AG, Hall BK. The nature and significance of invertebrate cartilages revisited: distribution and histology of cartilage and cartilage-like tissues within the Metazoa. *Zoology*. 2004 Dec 15;107(4):261-73.
- [5] Zhang G, Cohn MJ. Hagfish and lancelet fibrillar collagens reveal that type II collagen-based cartilage evolved in stem vertebrates. *Proceedings of the National Academy of Sciences*. 2006 Nov 7;103(45):16829-33.
- [6] Zhang G, Miyamoto MM, Cohn MJ. Lamprey type II collagen and Sox9 reveal an ancient origin of the vertebrate collagenous skeleton. *Proceedings of the National Academy of Sciences*. 2006 Feb 28;103(9):3180-5.
- [7] Zhang G, Eames BF, Cohn MJ. Evolution of vertebrate cartilage development. *Current topics in developmental biology*. 2009 Jan 1;86:15-42.
- [8] Tarazona OA, Slota LA, Lopez DH, Zhang G, Cohn MJ. The genetic program for cartilage development has deep homology within Bilateria. *Nature*. 2016 May;533(7601):86-9.
- [9] Gillis JA. *The development and evolution of cartilage*. Elsevier Reference Module in Life Sciences: Developmental Biology. 2018.
- [10] Hall BK. *Bones and cartilage: developmental and evolutionary skeletal biology*. Elsevier; 2005 Jun 20.
- [11] Hall BK, Miyake T. All for one and one for all: condensations and the initiation of skeletal development. *Bioessays*. 2000 Feb;22(2):138-47
- [12] Archer CW, Francis-West P. The chondrocyte. *The international journal of biochemistry & cell biology*. 2003 Apr 1;35(4):401-4.
- [13] Mow VC, Holmes MH, Lai WM. Fluid transport and mechanical properties of articular cartilage: a review. *Journal of biomechanics*. 1984 Jan 1;17(5):377-94.
- [14] Wayne JS, Kraft KA, Shields KJ, Yin C, Owen JR, Disler DG. MR imaging of normal and matrix-depleted cartilage: correlation with biomechanical function and biochemical composition. *Radiology*. 2003 Aug;228(2):493-9.
- [15] Bertassoni LE, Swain MV. The contribution of proteoglycans to the mechanical behavior of mineralized tissues. *Journal of the mechanical behavior of biomedical materials*. 2014 Oct 1;38:91-104.
- [16] Prydz K, Dalen KT. Synthesis and sorting of proteoglycans. *Journal of cell science*. 2000 Jan 15;113(2):193-205.

- [17] Luderman LN, Unlu G, Knapik EW. Zebrafish developmental models of skeletal diseases. *Current topics in developmental biology*. 2017 Jan 1;124:81-124.
- [18] Julkunen P, Harjula T, Iivarinen J, Marjanen J, Seppänen K, Närhi T, Arokoski J, Lammi MJ, Brama PA, Jurvelin JS, Helminen HJ. Biomechanical, biochemical and structural correlations in immature and mature rabbit articular cartilage. *Osteoarthritis and Cartilage*. 2009 Dec 1;17(12):1628-38.
- [19] Kuroda S, Tanimoto K, Izawa T, Fujihara S, Koolstra JH, Tanaka E. Biomechanical and biochemical characteristics of the mandibular condylar cartilage. *Osteoarthritis and Cartilage*. 2009 Nov 1;17(11):1408-15.
- [20] Stockwell RA. The interrelationship of cell density and cartilage thickness in mammalian articular cartilage. *Journal of anatomy*. 1971 Sep;109(Pt 3):411.
- [21] Hunziker EB, Quinn TM, Häuselmann HJ. Quantitative structural organization of normal adult human articular cartilage. *Osteoarthritis and cartilage*. 2002 Jul 1;10(7):564-72.
- [22] Sophia Fox AJ, Bedi A, Rodeo SA. The basic science of articular cartilage: structure, composition, and function. *Sports health*. 2009 Nov;1(6):461-8.
- [23] Cooper KL, Oh S, Sung Y, Dasari RR, Kirschner MW, Tabin CJ. Multiple phases of chondrocyte enlargement underlie differences in skeletal proportions. *Nature*. 2013 Mar;495(7441):375-8.
- [24] Cole HA, Yuasa M, Hawley G, Cates JM, Nyman JS, Schoenecker JG. Differential development of the distal and proximal femoral epiphysis and physis in mice. *Bone*. 2013 Jan 1;52(1):337-46.
- [25] Naumann A, Dennis JE, Awadallah A, Carrino DA, Mansour JM, Kastenbauer E, Caplan AI. Immunochemical and mechanical characterization of cartilage subtypes in rabbit. *Journal of Histochemistry & Cytochemistry*. 2002 Aug;50(8):1049-58.
- [26] Kostović-Knežević L, Bradamante Ž, Švajger A. Ultrastructure of elastic cartilage in the rat external ear. *Cell and tissue research*. 1981 Jun;218(1):149-60.
- [27] Benjamin MI. The cranial cartilages of teleosts and their classification. *Journal of Anatomy*. 1990 Apr;169:153.
- [28] Witten PE, Huysseune A, Hall BK. A practical approach for the identification of the many cartilaginous tissues in teleost fish. *Journal of Applied Ichthyology*. 2010 Apr;26(2):257-62.
- [29] Wright GM, Armstrong LA, Jacques AM, Youson JH. Trabecular, nasal, branchial, and pericardial cartilages in the sea lamprey, *Petromyzon marinus*: fine structure and immunohistochemical detection of elastin. *American journal of anatomy*. 1988 May;182(1):1-5
- [30] Wright GM, Keeley FW, Youson JH, Babineau DL. Cartilage in the Atlantic hagfish, *Myxine glutinosa*. *American journal of anatomy*. 1984 Apr;169(4):407-24.
- [31] Jørgensen JM, Lomholt JP, Weber RE, Malte H, editors. *The biology of hagfishes*. Springer Science & Business Media; 2012 Dec 6.
- [32] Rychel AL, Swalla BJ. Development and evolution of chordate cartilage. *Journal of Experimental Zoology Part B: Molecular and Developmental Evolution*. 2007 May 15;308(3):325-35.

- [33] Junqueira LC, Toledo OM, Montes GS. Histochemical and morphological studies on a new type of acellular cartilage. *Basic and applied histochemistry*. 1983 Jan 1;27(1):1-8.
- [34] Maisey JG. The diversity of tessellated calcification in modern and extinct chondrichthyans. *Revue de Paléobiologie*. 2013;32(2):355-71.
- [35] Long JA, Burrow CJ, Ginter M, Maisey JG, Trinajstić KM, Coates MI, Young GC, Senden TJ. First shark from the Late Devonian (Frasnian) Gogo Formation, Western Australia sheds new light on the development of tessellated calcified cartilage. *PLoS One*. 2015 May 28;10(5):e0126066.
- [36] Nielsen J, Hedeholm RB, Heinemeier J, Bushnell PG, Christiansen JS, Olsen J, Ramsey CB, Brill RW, Simon M, Steffensen KF, Steffensen JF. Eye lens radiocarbon reveals centuries of longevity in the Greenland shark (*Somniosus microcephalus*). *Science*. 2016 Aug 12;353(6300):702-4.
- [37] Pierce SJ, Norman B. *Rhincodon typus*. The IUCN red list of threatened species. 2016:e-T19488A2365291.
- [38] Boisvert CA, Johnston P, Trinajstić K, Johanson Z. Chondrichthyan evolution, diversity, and senses. In: *Heads, Jaws, and Muscles 2019* (pp. 65-91). Springer, Cham.
- [39] Dean MN, Mull CG, Gorb SN, Summers AP. Ontogeny of the tessellated skeleton: insight from the skeletal growth of the round stingray *Urolophus halleri*. *Journal of Anatomy*. 2009 Sep;215(3):227-39.
- [40] Egerbacher M, Helmreich M, Mayrhofer E, Böck P. Mineralisation of hyaline cartilage in the small-spotted dogfish *Scyliorhinus canicula* L. *Scripta Medica (BRNO)*. 2006 Aug;79:199-212.
- [41] Applegate SP. A survey of shark hard parts. *Sharks, skates and rays*. 1967:37-67.
- [42] Kemp NE, Westrin SK. Ultrastructure of calcified cartilage in the endoskeletal tesserae of sharks. *Journal of Morphology*. 1979 Apr;160(1):75-101.
- [43] Clement JG. Re-examination of the fine structure of endoskeletal mineralization in chondrichthyans: implications for growth, ageing and calcium homeostasis. *Marine and Freshwater Research*. 1992;43(1):157-81.
- [44] Dean MN, Summers AP. Mineralized cartilage in the skeleton of chondrichthyan fishes. *Zoology*. 2006 May 22;109(2):164-8.
- [45] Dean MN. Cartilaginous Fish Skeletal Tissues. In: Farrell AP, ed. *Encyclopedia of fish physiology: from genome to environment*. Academic press; 2011 Jun 1.
- [46] Debais-Thibaud M. The evolution of endoskeletal mineralization in chondrichthyan fish. *Evolution and development of fishes*. 2019 Jan 10:110-25.
- [47] Seidel R, Blumer M, Chaumel J, Amini S, Dean MN. Endoskeletal mineralization in chimaera and a comparative guide to tessellated cartilage in chondrichthyan fishes (sharks, rays and chimaera). *Journal of the Royal Society Interface*. 2020 Oct 28;17(171):20200474.
- [48] Pears JB, Johanson Z, Trinajstić K, Dean MN, Boisvert CA. Mineralization of the *Callorhynchus* Vertebral Column (Holocephali; Chondrichthyes). *Frontiers in Genetics*. 2020 Nov 26;11:1477.

- [49] Seidel R, Blumer M, Pechriggl EJ, Lyons K, Hall BK, Fratzi P, Weaver JC, Dean MN. Calcified cartilage or bone? Collagens in the tessellated endoskeletons of cartilaginous fish (sharks and rays). *Journal of structural biology*. 2017 Oct 1;200(1):54-71.
- [50] Mathews MB, Decker L. Comparative studies of water sorption of hyaline cartilage. *Biochimica et Biophysica Acta (BBA)-General Subjects*. 1977 Mar 29;497(1):151-9.
- [51] Michelacci YM, Horton DS. Proteoglycans from the cartilage of young hammerhead shark *Sphyrna lewini*. *Comparative Biochemistry and Physiology Part B: Comparative Biochemistry*. 1989 Jan 1;92(4):651-8.
- [52] Doyle J. Ageing changes in cartilage from *squalus acanthias* L. *Comparative biochemistry and physiology*. 1968 Apr 1;25(1):201-6.
- [53] Seno N, Anno K, Yaegashi Y, Okuyama T. Microheterogeneity of chondroitin sulfates from various cartilages. *Connective tissue research*. 1975 Jan 1;3(1):87-96.
- [54] Porter ME, Beltrán JL, Koob TJ, Summers AP. Material properties and biochemical composition of mineralized vertebral cartilage in seven elasmobranch species (Chondrichthyes). *Journal of Experimental Biology*. 2006 Aug 1;209(15):2920-8.
- [55] Eyre D. Articular cartilage and changes in arthritis: collagen of articular cartilage. *Arthritis Research & Therapy*. 2001 Oct;4(1):1-6.
- [56] Robson P, Wright GM, Sitarz E, Maiti A, Rawat M, Youson JH, Keeley FW. Characterization of lamprin, an unusual matrix protein from lamprey cartilage. Implications for evolution, structure, and assembly of elastin and other fibrillar proteins. *Journal of Biological Chemistry*. 1993 Jan 15;268(2):1440-7.
- [57] Green EM, Peter Winlove C. The structure and mechanical properties of the proteins of lamprey cartilage. *Biopolymers*. 2015 Apr;103(4):187-202.
- [58] Maisey JG, Denton JS, Burrow C, Pradel A. Architectural and ultrastructural features of tessellated calcified cartilage in modern and extinct chondrichthyan fishes. *Journal of Fish Biology*. 2021 Apr;98(4):919-41.
- [59] Seidel R, Lyons K, Blumer M, Zaslansky P, Fratzi P, Weaver JC, Dean MN. Ultrastructural and developmental features of the tessellated endoskeleton of elasmobranchs (sharks and rays). *Journal of Anatomy*. 2016 Nov;229(5):681-702.
- [60] Jayasankar AK, Seidel R, Hosny A, Weaver JC, Fratzi P, Chen J, Dean MN. Multi-scale modeling and mechanical performance characterization of stingray skeleton-inspired tessellations. *Journal of the Mechanics and Physics of Solids*. 2020 May 1;138:103906.
- [61] Eames BF, Allen N, Young J, Kaplan A, Helms JA, Schneider RA. Skeletogenesis in the swell shark *Cephaloscyllium ventriosum*. *Journal of anatomy*. 2007 May;210(5):542-54.
- [62] Mitsuyama H, Healey RM, Terkeltaub RA, Coutts RD, Amiel D. Calcification of human articular knee cartilage is primarily an effect of aging rather than osteoarthritis. *Osteoarthritis and cartilage*. 2007 May 1;15(5):559-65.

- [63] Fuerst M, Niggemeyer O, Lammers L, Schäfer F, Lohmann C, Rütger W. Articular cartilage mineralization in osteoarthritis of the hip. *BMC Musculoskeletal Disorders*. 2009 Dec;10(1):1-8
- [64] Omelon S, Georgiou J, Variola F, Dean MN. Colocation and role of polyphosphates and alkaline phosphatase in apatite biomineralization of elasmobranch tesserae. *Acta biomaterialia*. 2014 Sep 1;10(9):3899-910.
- [65] Dean MN, Socha JJ, Hall BK, Summers AP. Canaliculi in the tessellated skeleton of cartilaginous fishes. *Journal of Applied Ichthyology*. 2010 Apr;26(2):263-7.
- [66] Mackie EJ. The skeleton: a multi-functional complex organ: the growth plate chondrocyte. *International Journal of Biochemistry & Cell Biology*. 2011;40:46-62.
- [67] Yang G, Zhu L, Hou N, Lan Y, Wu XM, Zhou B, Teng Y, Yang X. Osteogenic fate of hypertrophic chondrocytes. *Cell research*. 2014 Oct;24(10):1266-9.
- [68] Park J, Gebhardt M, Golovchenko S, Perez-Branguli F, Hattori T, Hartmann C, Zhou X, deCrombrugge B, Stock M, Schneider H, Von Der Mark K. Dual pathways to endochondral osteoblasts: a novel chondrocyte-derived osteoprogenitor cell identified in hypertrophic cartilage. *Biology open*. 2015 May 15;4(5):608-21.
- [69] Chaumel J, Schotte M, Bizzarro JJ, Zaslansky P, Fratzl P, Baum D, Dean MN. Co-aligned chondrocytes: zonal morphological variation and structured arrangement of cell lacunae in tessellated cartilage. *Bone*. 2020 May 1;134:115264.
- [70] Jayasankar AK, Seidel R, Naumann J, Guiducci L, Hosny A, Fratzl P, Weaver JC, Dunlop JW, Dean MN. Mechanical behavior of idealized, stingray-skeleton-inspired tiled composites as a function of geometry and material properties. *Journal of the mechanical behavior of biomedical materials*. 2017 Sep 1;73:86-101.
- [71] Liu X, Dean MN, Summers AP, Earthman JC. Composite model of the shark's skeleton in bending: a novel architecture for biomimetic design of functional compression bias. *Materials Science and Engineering: C*. 2010 Oct 12;30(8):1077-84.
- [72] Fratzl P, Kolednik O, Fischer FD, Dean MN. The mechanics of tessellations—bioinspired strategies for fracture resistance. *Chemical Society Reviews*. 2016;45(2):252-67.
- [73] An YH, Martin KL, editors. *Handbook of histology methods for bone and cartilage*. Totowa, NJ: Humana Press; 2003 May 1.
- [74] Mallinger R, Geleff S, Böck P. Histochemistry of glycosaminoglycans in cartilage ground substance. *Histochemistry*. 1986 Mar;85(2):121-7.
- [75] Blumer MJ. Bone tissue and histological and molecular events during development of the long bones. *Annals of Anatomy-Anatomischer Anzeiger*. 2021 Feb 16:151704.
- [76] Rosenberg L. Chemical basis for the histological use of safranin O in the study of articular cartilage. *JBJS*. 1971 Jan 1;53(1):69-82.
- [77] Hyllested JL, Veje K, Ostergaard K. Histochemical studies of the extracellular matrix of human articular cartilage—a review. *Osteoarthritis and cartilage*. 2002 May 1;10(5):333-43.

- [78] Cattell M, Lai S, Cerny R, Medeiros DM. A new mechanistic scenario for the origin and evolution of vertebrate cartilage. *PloS one*. 2011 Jul 22;6(7):e22474.
- [79] Jacoby F, Martin BF. The histochemical test for alkaline phosphatase. *Nature*. 1949 Jun;163(4153):875-6.
- [80] Kapuscinski J. DAPI: a DNA-specific fluorescent probe. *Biotechnic & Histochemistry*. 1995 Jan 1;70(5):220-33.
- [81] Osawa S. Histochemical studies of alkaline phosphatase in the oogenesis and the early embryogenesis of the amphibia. *Embryologia*. 1951 Dec;2(1):1-20.
- [82] Van Goor H, Gerrits PO, Hardonk MJ. Enzyme histochemical demonstration of alkaline phosphatase activity in plastic-embedded tissues using a Gomori-based cerium-DAB technique. *Journal of Histochemistry & Cytochemistry*. 1989 Mar;37(3):399-403.
- [83] Miao D, Scutt A. Histochemical localization of alkaline phosphatase activity in decalcified bone and cartilage. *Journal of Histochemistry & Cytochemistry*. 2002 Mar;50(3):333-40.
- [84] Lin F, Prichard J, editors. *Handbook of practical immunohistochemistry: frequently asked questions*. Springer; 2015 Feb 21.
- [85] Kalyuzhny AE. Immunohistochemistry. *Nature*, S. ed. 2016:978-3.
- [86] Liddell E. Antibodies. In: *The immunoassay handbook 2013* Jan 1 (pp. 245-265). Elsevier.
- [87] Renshaw, S. Immunohistochemistry and Immunocytochemistry. In: *The immunoassay handbook 2013* Jan 1 (pp. 245-265). Elsevier.
- [88] Poole CA. Articular cartilage chondrons: form, function and failure. *Journal of anatomy*. 1997 Jul;191(1):1-3.
- [89] Guilak F, Alexopoulos LG, Upton ML, Youn I, Choi JB, Cao L, Setton LA, Haider MA. The pericellular matrix as a transducer of biomechanical and biochemical signals in articular cartilage. *Annals of the New York Academy of Sciences*. 2006 Apr;1068(1):498-512.
- [90] Gall JG, Pardue ML. Formation and detection of RNA-DNA hybrid molecules in cytological preparations. *Proceedings of the National Academy of Sciences*. 1969 Jun 1;63(2):378-83.
- [91] Parra I, Windle B. High resolution visual mapping of stretched DNA by fluorescent hybridization. *Nature genetics*. 1993 Sep;5(1):17-21.
- [92] Jensen E. Technical review: In situ hybridization. *The Anatomical Record*. 2014 Aug;297(8):1349-53.
- [93] Oshima O, Leboy PS, McDonald SA, Tuan RS, Shapiro IM. Developmental expression of genes in chick growth cartilage detected by in situ hybridization. *Calcified tissue international*. 1989 May;45(3):182-92.
- [94] Shibata S, Suda N, Suzuki S, Fukuoka H, Yamashita Y. An in situ hybridization study of Runx2, Osterix, and Sox9 at the onset of condylar cartilage formation in fetal mouse mandible. *Journal of Anatomy*. 2006 Feb;208(2):169-77.
- [95] Hawkes PW, Spence JC, editors. *Springer handbook of microscopy*. Springer Nature; 2019 Nov 2.

- [96] Winey M, Meehl JB, O'Toole ET, Giddings Jr TH. Conventional transmission electron microscopy. *Molecular biology of the cell*. 2014 Feb 1;25(3):319-23.
- [97] Amelinckx S, Van Dyck D, Van Landuyt J, van Tendeloo G, editors. *Electron microscopy: principles and fundamentals*. John Wiley & Sons; 2008 Sep 26.
- [98] Thiberge S, Nechushtan A, Sprinzak D, Gileadi O, Behar V, Zik O, Chowars Y, Michaeli S, Schlessinger J, Moses E. Scanning electron microscopy of cells and tissues under fully hydrated conditions. *Proceedings of the National Academy of Sciences*. 2004 Mar 9;101(10):3346-51.
- [99] Kourkoutis LF, Plitzko JM, Baumeister W. Electron microscopy of biological materials at the nanometer scale. *Annual review of materials research*. 2012 Aug 4;42:33-58.
- [100] Zuo JM, Spence JC. *Advanced transmission electron microscopy*. *Advanced Transmission Electron Microscopy*, ISBN 978-1-4939-6605-9. Springer Science+ Business Media New York. 2017.
- [101] Itani TS, Kanai KA, Watanabe J, Ogawa RY, Kanamura SH. Quantitative analysis of rough endoplasmic reticulum in chondrocytes of articular and tracheal cartilage of rabbits following the systemic administration of hydrocortisone. *Journal of anatomy*. 1992 Oct;181(Pt 2):357.
- [102] Kouri JB, Jiménez SA, Quintero M, Chico A. Ultrastructural study of chondrocytes from fibrillated and non-fibrillated human osteoarthritic cartilage. *Osteoarthritis and cartilage*. 1996 Jun 1;4(2):111-25.
- [103] Keene DR, Tufa SF. Transmission electron microscopy of cartilage and bone. *Methods in cell biology*. 2010 Jan 1;96:443-73.
- [104] Hunziker EB, Lippuner K, Shintani N. How best to preserve and reveal the structural intricacies of cartilaginous tissue. *Matrix biology*. 2014 Oct 1;39:33-43.
- [105] Orloff J, Swanson L, Utlaut M. High resolution focused ion beams: FIB and its applications: Fib and its applications: the physics of liquid metal ion sources and ion optics and their application to focused ion beam technology. Springer Science & Business Media; 2003.
- [106] Briggman KL, Bock DD. Volume electron microscopy for neuronal circuit reconstruction. *Current opinion in neurobiology*. 2012 Feb 1;22(1):154-61.
- [107] Amizuka N, Hasegawa T, Oda K, Luiz de Freitas PH, Hoshi K, Li M, Ozawa H. Histology of epiphyseal cartilage calcification and endochondral ossification. *Front Biosci (Elite Ed)*. 2012 Jan 1;4(6):2085-100.
- [108] Malda J, de Grauw JC, Benders KE, Kik MJ, van de Lest CH, Creemers LB, Dhert WJ, van Weeren PR. Of mice, men and elephants: the relation between articular cartilage thickness and body mass. *PloS one*. 2013 Feb 21;8(2):e57683.
- [109] König K, Schenke-Layland K, Riemann I, Stock UA. Multiphoton autofluorescence imaging of intratissue elastic fibers. *Biomaterials*. 2005 Feb 1;26(5):495-500
- [110] Mansfield JC, Winlove CP, Moger JJ, Matcher SJ. Collagen fiber arrangement in normal and diseased cartilage studied by polarization sensitive nonlinear microscopy. *Journal of biomedical optics*. 2008 Jul;13(4):044020.

- [111] Lutz V, Sattler M, Gallinat S, Wenck H, Poertner R, Fischer F. Impact of collagen crosslinking on the second harmonic generation signal and the fluorescence lifetime of collagen autofluorescence. *Skin Research and Technology*. 2012 May;18(2):168-79.
- [112] Carlton RA. *Pharmaceutical microscopy*. Springer Science & Business Media; 2011 May 4.
- [113] Tuchin VV. Polarized light interaction with tissues. *Journal of biomedical optics*. 2016 Apr;21(7):071114
- [114] Wolman M, Kasten FH. Polarized light microscopy in the study of the molecular structure of collagen and reticulin. *Histochemistry*. 1986 Jan;85(1):41-9.
- [115] Rich L, Whittaker P. Collagen and picosirius red staining: a polarized light assessment of fibrillar hue and spatial distribution. *Journal of morphological sciences*. 2017 Jan 16;22(2):0-
- [116] Monici M. Cell and tissue autofluorescence research and diagnostic applications. *Biotechnology annual review*. 2005 Jan 1;11:227-56.
- [117] Haug JT, Haug C, Kutschera V, Mayer G, Maas A, Liebau S, Castellani C, Wolfram U, Clarkson EN, Waloszek D. Autofluorescence imaging, an excellent tool for comparative morphology. *Journal of Microscopy*. 2011 Dec;244(3):259-72.
- [118] Gibson GJ, Verner JJ, Nelson FR, Lin DL. Degradation of the cartilage collagen matrix associated with changes in chondrocytes in osteoarthritis. Assessment by loss of background fluorescence and immunodetection of matrix components. *Journal of Orthopaedic Research*. 2001 Jan;19(1):33-42
- [119] Korol RM, Finlay HM, Josseau MJ, Lucas AR, Canham PB. Fluorescence spectroscopy and birefringence of molecular changes in maturing rat tail tendon. *Journal of biomedical optics*. 2007 Mar;12(2):024011.
- [120] Manning HB, Nickdel MB, Yamamoto K, Lagarto JL, Kelly DJ, Talbot CB, Kennedy G, Dudhia J, Lever J, Dunsby C, French P. Detection of cartilage matrix degradation by autofluorescence lifetime. *Matrix Biology*. 2013 Jan 1;32(1):32-8.
- [121] Laifer LI, O'Brien KM, Stetz ML, Gindi GR, Garrand TJ, Deckelbaum LI. Biochemical basis for the difference between normal and atherosclerotic arterial fluorescence. *Circulation*. 1989 Dec;80(6):1893-901.
- [122] Kleinman DA. Theory of second harmonic generation of light. *Physical Review*. 1962 Nov 15;128(4):1761.
- [123] Denk W, Strickler JH, Webb WW. Two-photon laser scanning fluorescence microscopy. *Science*. 1990 Apr 6;248(4951):73-6.
- [124] Gannaway JN, Sheppard CJ. Second-harmonic imaging in the scanning optical microscope. *Optical and Quantum Electronics*. 1978 Sep;10(5):435-9.
- [125] Williams RM, Piston DW, Webb WW. Two-photon molecular excitation provides intrinsic 3-dimensional resolution for laser-based microscopy and microphotochemistry. *The FASEB journal*. 1994 Aug;8(11):804-13.
- [126] Campagnola PJ, Loew LM. Second-harmonic imaging microscopy for visualizing biomolecular arrays in cells, tissues and organisms. *Nature biotechnology*. 2003 Nov;21(11):1356-60.

- [127] König K, So PC, Mantulin WW, Tromberg BJ, Gratton E. Two-photon excited lifetime imaging of autofluorescence in cells during UV A and NIR photostress. *Journal of microscopy*. 1996 Sep;183(3):197-204.
- [128] Wong BJ, Wallace V, Coleno M, Benton HP, Tromberg BJ. Two-photon excitation laser scanning microscopy of human, porcine, and rabbit nasal septal cartilage. *Tissue engineering*. 2001 Oct 1;7(5):599-606.
- [129] Yeh AT, Hammer-Wilson MJ, Van Sickle DC, Benton HP, Zoumi A, Tromberg BJ, Peavy GM. Nonlinear optical microscopy of articular cartilage. *Osteoarthritis and cartilage*. 2005 Apr 1;13(4):345-52.
- [130] Mansfield J, Yu J, Attenburrow D, Moger J, Tirlapur U, Urban J, Cui Z, Winlove P. The elastin network: its relationship with collagen and cells in articular cartilage as visualized by multiphoton microscopy. *Journal of anatomy*. 2009 Dec;215(6):682-91.
- [131] Gauderon R, Lukins PB, Sheppard CJ. Optimization of second-harmonic generation microscopy. *Micron*. 2001 Oct 1;32(7):691-700.
- [132] Cox G, Kable E, Jones A, Fraser I, Manconi F, Gorrell MD. 3-dimensional imaging of collagen using second harmonic generation. *Journal of structural biology*. 2003 Jan 1;141(1):53-62.
- [133] Werkmeister E, De Isla N, Netter P, Stoltz JF, Dumas D. Collagenous extracellular matrix of cartilage submitted to mechanical forces studied by second harmonic generation microscopy. *Photochemistry and photobiology*. 2010 Mar;86(2):302-10.
- [134] Hounsfield GN. Computerized transverse axial scanning (tomography): Part 1. Description of system. *The British journal of radiology*. 1973 Dec;46(552):1016-22.
- [135] Buzug TM. Computed tomography. In: *Springer handbook of medical technology 2011* (pp. 311-342). Springer, Berlin, Heidelberg.
- [136] Hsieh J. *Computed tomography: principles, design, artifacts, and recent advances*. SPIE press; 2003.
- [137] Orhan K, editor. *Micro-computed Tomography (micro-CT) in Medicine and Engineering*. Berlin: Springer; 2020.
- [138] Rawson SD, Maksimcuka J, Withers PJ, Cartmell SH. X-ray computed tomography in life sciences. *BMC biology*. 2020 Dec;18(1):1-5.
- [139] Guo X, Johnston SM, Qi Y, Johnson GA, Badea CT. 4D micro-CT using fast prospective gating. *Physics in Medicine & Biology*. 2011 Dec 9;57(1):257.
- [140] Bultreys T, Boone MA, Boone MN, De Schryver T, Masschaele B, Van Hoorebeke L, Cnudde V. Fast laboratory-based micro-computed tomography for pore-scale research: Illustrative experiments and perspectives on the future. *Advances in water resources*. 2016 Sep 1;95:341-51.
- [141] Metscher BD. MicroCT for comparative morphology: simple staining methods allow high-contrast 3D imaging of diverse non-mineralized animal tissues. *BMC physiology*. 2009 Dec;9(1):1-4.
- [142] Descamps E, Sochacka A, De Kegel B, Van Loo D, Van Hoorebeke L, Adriaens D. Soft tissue discrimination with contrast agents using micro-CT scanning. *Belgian Journal of Zoology*. 2014;144(1).

- [143] Gignac PM, Kley NJ, Clarke JA, Colbert MW, Morhardt AC, Cerio D, Cost IN, Cox PG, Daza JD, Early CM, Echols MS. Diffusible iodine-based contrast-enhanced computed tomography (diceCT): an emerging tool for rapid, high-resolution, 3-D imaging of metazoan soft tissues. *Journal of anatomy*. 2016 Jun;228(6):889-909.
- [144] Haimov H, Shimoni E, Brumfeld V, Shemesh M, Varsano N, Addadi L, Weiner S. Mineralization pathways in the active murine epiphyseal growth plate. *Bone*. 2020 Jan 1;130:115086.
- [145] Edelman RR, Warach S. Magnetic resonance imaging. *New England Journal of Medicine*. 1993 Mar 18;328(11):785-91.
- [146] Huettel SA, Song AW, McCarthy G. *Functional magnetic resonance imaging*. Sunderland, MA: Sinauer Associates; 2004 Apr 1.
- [147] Morris SA, Slesnick TC. Magnetic resonance imaging. *Visual Guide to Neonatal Cardiology*. 2018 Apr 16:104-8.
- [148] Bojorquez JZ, Bricq S, Acquitter C, Brunotte F, Walker PM, Lalande A. What are normal relaxation times of tissues at 3 T?. *Magnetic resonance imaging*. 2017 Jan 1;35:69-80.
- [149] Trattng S, Mlynarik V, Huber M, Ba-Ssalamah A, Stefan PU, Imhof H. Magnetic resonance imaging of articular cartilage and evaluation of cartilage disease. *Investigative radiology*. 2000 Oct 1;35(10):595-601.
- [150] Hatabu H, Chen Q, Stock KW, Gefter WB, Itoh H. Fast magnetic resonance imaging of the lung. *European journal of radiology*. 1999 Feb 1;29(2):114-32.
- [151] Burstein D, Gray M. New MRI techniques for imaging cartilage. *JBJS*. 2003 Apr 1;85(suppl_2):70-7.
- [152] Kozel FA, Revell LJ, Lorberbaum JP, Shastri A, Elhai JD, Horner MD, Smith A, Nahas Z, Bohning DE, George MS. A pilot study of functional magnetic resonance imaging brain correlates of deception in healthy young men. *The Journal of Neuropsychiatry and Clinical Neurosciences*. 2004 Aug;16(3):295-305.
- [153] Eckstein F, Charles HC, Buck RJ, Kraus VB, Remmers AE, Hudelmaier M, Wirth W, Evelhoch JL. Accuracy and precision of quantitative assessment of cartilage morphology by magnetic resonance imaging at 3.0 T. *Arthritis & Rheumatism: Official Journal of the American College of Rheumatology*. 2005 Oct;52(10):3132-6.
- [154] Borthakur A, Reddy R. Imaging cartilage physiology. *Topics in Magnetic Resonance Imaging*. 2010 Oct;21(5):291.
- [155] Hasse JC. Über den Bau und über die Entwicklung des Knorpels bei den Elasmobranchiern. *Zoologischer Anzeiger*. 1879;2:325-74.
- [156] Woodward AS. *Catalogue of the Fossil Fishes in the British Museum (Natural History): Elasmobranchii*. order of the Trustees; 1889.
- [157] Dean B. Contributions to the morphology of Cladoselache (Cladodus). *Journal of Morphology*. 1894 Jan;9(1):87-114.
- [158] Fürbringer, K. Beiträge zur Kenntnis des Visceralskelets der Selachier. *Morph.Jahrb*. 1903 31(2-3):360-445

- [159] Budker, P. Les cryptes sensorielles et les denticules cutanés des plagiostomes. *Annales de L'Institut Oceanographique*, 1938 Paris 18, 207-288
- [160] Ridewood WG, MacBride EW. VIII.—On the calcification of the vertebral centra in sharks and rays. *Philosophical Transactions of the Royal Society of London. Series B, Containing Papers of a Biological Character*. 1921 Jan 1; 210(372-381):311-407.
- [161] James WW. The succession of teeth in elasmobranchs. In: *Proceedings of the Zoological Society of London* 1953 Aug (Vol. 123, No. 2, pp. 419-474). Oxford, UK: Blackwell Publishing Ltd.
- [162] Applegate SP. Tooth terminology and variation in sharks with special reference to the sand shark *Carcharias taurus* Rafinesque.
- [163] Marconi A, Hancock-Ronemus A, Gillis JA. Adult chondrogenesis and spontaneous cartilage repair in the skate, *Leucoraja erinacea*. *Elife*. 2020 May 12; 9:e53414.
- [164] Atake OJ, Cooper DM, Eames BF. Bone-like features in skate suggest a novel elasmobranch synapomorphy and deep homology of trabecular mineralization patterns. *Acta biomaterialia*. 2019 Jan 15; 84:424-36.
- [165] Berio F, Evin A, Goudemand N, Debiais-Thibaud M. The intraspecific diversity of tooth morphology in the large-spotted catshark *Scyliorhinus stellaris*: insights into the ontogenetic cues driving sexual dimorphism. *Journal of Anatomy*. 2020 Nov; 237(5):960-78.
- [166] Takagi M, Parmley RT, Denys FR, Yagasaki H, Toda Y. Ultrastructural cytochemistry of proteoglycans associated with calcification of shark cartilage. *The Anatomical Record*. 1984 Feb; 208(2):149-58.
- [167] Libbin RM, Hirschman A, Person P, Blumenthal NC. Alkaline phosphatase and peptidase levels in invertebrate cartilage. *Calcified tissue international*. 1992 Jul; 51(1):62-6.
- [168] Golub EE, Boesze-Battaglia K. The role of alkaline phosphatase in mineralization. *Current opinion in Orthopaedics*. 2007 Sep 1; 18(5):444-8.
- [169] Dean MN, Ekstrom L, Monson-Ornan E, Ballantyne J, Witten PE, Riley C, Habraken W, Omelon S. Mineral homeostasis and regulation of mineralization processes in the skeletons of sharks, rays and relatives (Elasmobranchii). In: *Seminars in Cell & Developmental Biology* 2015 Oct 1 (Vol. 46, pp. 51-67). Academic Press.
- [170] Enault S, Muñoz DN, Silva WT, Borday-Birraux V, Bonade M, Oulion S, Ventéo S, Marcellini S, Debiais-Thibaud M. Molecular footprinting of skeletal tissues in the catshark *Scyliorhinus canicula* and the clawed frog *Xenopus tropicalis* identifies conserved and derived features of vertebrate calcification. *Frontiers in genetics*. 2015 Sep 15; 6:283.
- [171] Dean MN, Gorb SN, Summers AP. A cryoSEM method for preservation and visualization of calcified shark cartilage (and other stubborn heterogeneous skeletal tissues). *Microscopy Today*. 2008 Nov; 16(6):48-51.
- [172] Peignoux-Deville J, Lallier F, Vidal B. Evidence for the presence of osseous tissue in dogfish vertebrae. *Cell and tissue research*. 1982 Feb; 222(3):605-14.

[173] Schmidt WJ. Über die Verkalkung des Knorpelgewebes der Haie. Zeitschrift für Zellforschung und Mikroskopische Anatomie. 1952a Jul;37(4):377-88.

[174] Schmidt WJ. Zur Polarisationsoptik des Knorpelgewebes. Zeitschrift für Zellforschung und Mikroskopische Anatomie. 1952b Nov;37(6):534-46.

IV | METHODS FOR SAMPLE PREPARATION

Cartilage is challenging to prepare for imaging and analysis, due its high water content; shared borders with mineralized tissues with different swelling properties (e.g. subchondral bone); and its cells (chondrocytes), which are very sensitive to osmotic variations, losing their structure when hydration fluctuates even minutely. As such, it has been argued that the only method that adequately preserves tissue and cellular architectures is high-pressure freezing, a technique that involves ultra-rapidly freezing the tissue below -128°C under high pressure conditions to avoid the formation of ice crystals [1]. While the imaging results from fresh, high-pressure frozen cartilage samples do indeed show a near-ideal level of tissue structure preservation [2,3], high-pressure freezing is not available to all laboratories. In particular, in the study of non-model species (e.g. those rarely maintained in the laboratory), specimens are often captured in the field (e.g. boats, ports) out of controlled conditions, making complicated, device-driven sample preparation unrealistic. These sampling restrictions for cartilage have surely limited the understanding of how cartilage structure and composition vary, especially at fine tissue scales, outside of well-known model species.

During my dissertation, I developed and optimized several protocols for sample preparation of elasmobranch skeletal cartilage, adapted to different imaging modalities (e.g. light-, electron- and x-ray based imaging) and analysis techniques. Moreover, these straightforward and efficient protocols are suitable for field sampling, providing a high level of preservation of tissue and cellular ultrastructure, without the hardware-intensive aspects of high-pressure freezing. However, although the resulting preservation is not as pristine as that obtained with high-pressure freezing (especially regarding cell ultrastructure), these protocols allow an optimal sample preservation in situations where high-pressure freezing is not available or cannot be used (e.g. field work; separated animal facilities and high-pressure device).

Protocols developed to study elasmobranch skeletal cartilage:

Independently of the technique, all protocols developed during this doctoral period follow a basic structure:

1. Pre-planning and dissection
2. Sample preparation (e.g. fixation, staining)
3. Sample imaging (e.g. electron microscopy, histology, fluorescence microscopy, μ CT)
4. Image processing (e.g. AMIRA segmentation; autofluorescence signal deconvolution)

This chapter describes the dissection and sample preparation protocols developed to study elasmobranch skeletal cartilage, while also acting as a primer for aspects to consider when designing experiments to investigate this tissue. The downstream, specific posterior sample imaging and image processing techniques are described in each manuscript, for example, the AMIRA segmentation workflow in Paper 1 and 2, and the autofluorescence signal deconvolution in Paper 3. The protocols are designed and optimized to prepare mineralized samples since we aim to study mineralized structures and to keep the tissue as less altered as possible by avoiding tissue demineralization treatments (e.g. demineralization with EDTA). Therefore, any protocol related with demineralized or non-mineralized tissues (e.g. paraffin embedded) is included.

1. Pre-planning and dissection

For optimal preparation of elasmobranch skeletal cartilage, the following recommendations should be considered before dissection, as some will play decisive roles in tissue preservation quality, especially with regard to soft tissues (e.g. cells, extracellular matrix):

- **Specimen morphometrics.** Record relevant specimen morphometrics such as total length (TL), disc width (DW, for batoid fishes) and sex (determined by the presence or absence of claspers). Take photos of the animal next to a ruler to later verify measurements (see Fig. 1A).

- **Localize the skeletal piece of interest and plan out the dissection.** The more exposed samples are to the environment, the more quickly they degrade, so planning incisions for more rapid processing is helpful. Especially in batoids (rays and skates), some skeletal elements such as the propterygium and metapterygium are large and close to the skin and can be easily localized by palpating the animal (Fig. 1B-C).
- **Process specimens quickly.** In case the samples need to be fixed, the time between the animal's death and fixation should be kept as short as possible (< 5 minutes). Hydration is particularly important for cartilage structure: never let the sample dry.
- **Plan specimen size in advance.** If the planned imaging or analysis is geared toward tissue ultrastructure (e.g. preservation of cell structures, analysis with electron microscopy), samples should be as small as possible for better fixation, with a maximum size of 1x1x1 cm. Tessellated cartilage can be cut quite easily with double-edged safety razor blades, but also a variety of other medical or craft tools work well for standardizing sample extraction (e.g. biopsy or leather punches).
- **Remove all unnecessary tissue.** Fixative permeates smaller samples more rapidly, resulting in higher quality preservation. For optimal fixation, remove muscle and connective tissue attached to skeletal pieces to help fixative penetrate faster into the deeper areas of the tissue (Fig. 1B). We have found this particularly important for adequate fixation of cells in the tissue.

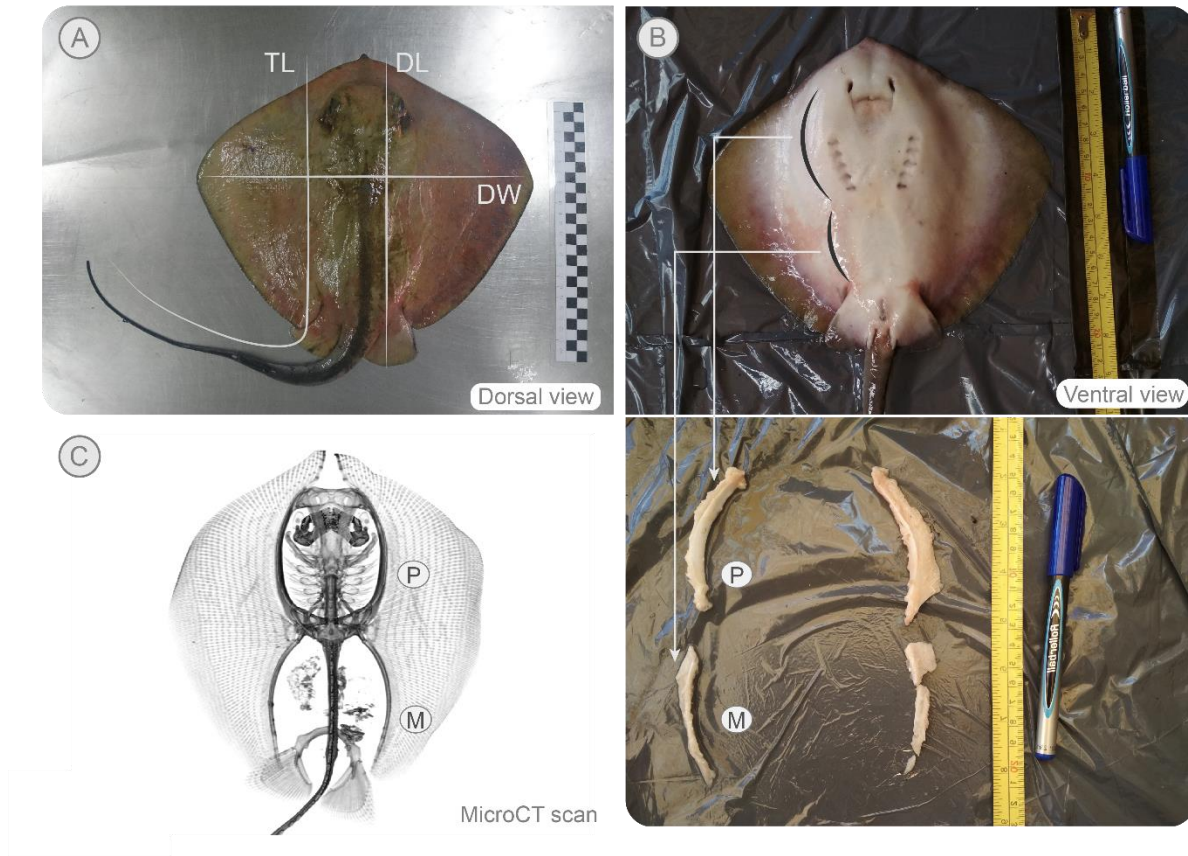


Fig. 1. Morphometrics and dissection of *Dasyatis pastinaca*. A) Dorsal view of the stingray *D. pastinaca*, with relevant specimen morphometrics indicated, such as total length (TL), the distance from the rostrum to the end of the tail; disc length (DL), from the rostrum to the caudal end of the body disc; and disc width (DW), which measure the distance between the tips of both wings. Sex is determined by the presence or absence of claspers. B) Ventral view of *D. pastinaca*; the larger skeletal pieces (propterygium and metapterygium) can be located by palpating the animal prior to its dissection. C) μ CT scan of the animal's skeleton, where the propterygium (P) and metapterygium (M) can be recognized in the skeleton as the largest skeletal pieces.

2. Sample preparation

2.1. Fixation

Fixation is the preservation of biological tissues, to avoid decay due to autolysis or putrefaction and therefore, preserve tissue structure and composition. In addition to the factors for consideration for fixation of mammalian cartilage (e.g. quick sample fixation, small sample size), elasmobranch skeletal cartilage fixation requires additional steps (e.g., because of the higher content of water and swelling ratios [4,5]). Therefore, for an optimal fixation of elasmobranch skeletal cartilage, the following points need to be considered:

- **Reduce time between animal death and fixation.** As tissue degradation begins when the animal dies, for high-quality histology and ultrastructure imaging, it is critical that tissue be fixed as soon as possible after the animal's death; we have found that if fixation can be performed within 5 minutes, it makes a large difference to resultant tissue quality. If this requirement cannot be reached, the tissue should at least be maintained at low temperatures ($\sim 4^{\circ}\text{C}$) to slow down tissue degradation, but not frozen, as ice crystals can severely damage cell membranes.
- **Avoid dehydration.** Additionally, once the biological sample has been removed from the animal, exposure with air should be limited to avoid dehydration. Water is a large proportion of tessellated cartilage volume [6,7] and so dehydration can result in extreme distortions and catastrophic collapse of samples; the collapse of the unmineralized cartilage in air-dried specimens is why museum collection specimens often present cracks in the tesseral layer. Although specimens can be rehydrated to some degree if placed back in water or physiologic saline, considerable structural damage can be caused in dehydration/rehydration. Hence, samples are best kept hydrated, either in chilled seawater or PBS. If fixation cannot be performed immediately, it is useful to delay specimen dissection as well: the muscle surrounding the cartilage appears to act as a buffer against large temperature and hydration changes, with resultant tissue preparations being of higher quality the shorter the time between dissection and fixation.

- **Fixative volume should be ~20 times the volume of the sample.** With this ratio, it is ensured that there is enough fixative (e.g. enough PFA molecules) to react with the tissue. Specific fixatives are discussed below.
- **Smaller samples are better.** We have found that cutting samples into blocks of $\leq 1 \times 1 \times 1$ cm is optimal for adequate fixation of elasmobranch skeletal cartilage (denser tissue may require smaller samples). The importance of the sample size is based on the penetration rate by diffusion of formaldehyde reagents, which is ~ 1 mm/h [8]. Thus, if the sample is too large, it will take several hours until the reagent reaches the inner areas of the sample (it will take ~ 25 h for the fixative to reach to the center of a 10 mm thick sample) and, by this time, the biological structures in these areas (especially cells) may have degraded.
- **Use a fixative that fits your imaging goals.** There is no universal fixative optimized to fix all tissue structures for all imaging techniques and so, depending on the structure or technique of interest, a different fixation protocol should be used (see Table 1). We discuss common fixatives below, outlining their advantages, disadvantages and other considerations (e.g. with regard to imaging):

2.1.1. Ethanol - Organic solvent

- **Fixation:** Replacement of water (dehydration) by ethanol, precipitation and denaturation of proteins in situ.
- **Advantages:** Cheap, easy to come by, non-toxic and easy to dispose of.
- **Disadvantages:** It extracts lipids and aqueous-soluble proteins, altering the cartilage extracellular matrix and shrinking the chondrocytes.
- **Recommended structures:** Mineralized structures (e.g. tesserae, areolar cartilage) and genetic material analyses.

- **Suitable techniques:** Computed tomography (CT-scan, synchrotron), SEM, Raman, histology, some immunohistochemistry (IHC), DNA and RNA.
- **Reagent considerations:** Flammable.

Protocol:

Due to the potentially damaging effect of dehydration on structure, samples should be stepped gradually through increasing ethanol concentration in 20 minute steps until reaching 100% (see Appendix, protocol *Fixatives*).

Considerations:

1. The buffer solution used (e.g. for rinsing and hydrating samples) should be PBS 0.1M. To avoid impurities that can have an effect in our sample (e.g. osmolarity variations), it is recommended to prepare the PBS solution fresh everytime. For that, solid PBS tablets can be dissolved in distilled water prior to use (we used *PBS tablets Thermofisher, catalog number: 18912014*).
2. All the steps should be performed on the rotator to facilitate the fixative reaching all tissue areas.
3. After each step, it is recommendable to leave the sample 10 min in the desiccator under vacuum to facilitate the infiltration of the fixative. We have found this step particularly important to preserving cells located within mineralized areas (e.g. tesseræ).
4. All steps can be performed at room temperature. If some of the steps need to be done overnight, the sample should be kept at 4°C (fridge).

2.1.2. Paraformaldehyde 4% in PBS – cross-linking fixative

Paraformaldehyde (PFA) is the most-used fixative in histology because it is a monoaldehyde (i.e. its molecules are small), which allows rapid diffusion into tissue, and therefore, an efficient fixation. However, there are indications that PFA does not adequately preserve cell membranes

and organelles and, as a consequence, it is not used for ultrastructural analyses (see section below) [8,9].

- **Fixation:** PFA establishes covalent links with the side-chains of several molecules such as unsaturated lipids (particularly if calcium ions are present), groups on lysine, arginine, cysteine, tyrosine, threonine, serine and glutamine to form reactive complexes. These reactive complexes can also react with each other forming cross-links, which results in a stable meshwork. PFA does not react with carbohydrates [8,10].
- **Advantages:** Fast, optimal for cartilage matrix preservation and cell morphology analysis at non-high resolution scales (e.g. for histology, rather than electron microscopy).
- **Disadvantages:** Toxic. Oxidates with time. Masks some epitopes for certain antibodies through the generation of a dense cross-linked meshwork (excessive cross-linking). Not recommended for cell ultrastructure analysis with electron microscopy imaging (TEM, FIB-SEM) due to destruction of organelles.
- **Recommended structures:** Cartilage extracellular matrix, cells (gross morphology), mineralized tissues.
- **Suitable techniques:** Computed tomography (μ CT, synchrotron- μ CT), SEM, Raman, histology, most IHC, DNA and RNA.
- **Hazard statements:** Toxic (skin contact and inhalation). Manipulate under the hood with adequate protection (lab coat, goggles). Dispose of properly.

Protocol:

The fixation solution 4% PFA is buffered with PBS 0.1M. Samples should be maintained in this solution during 6 hours at room temperature (RT) or overnight at 4°C. Once the sample has been fixed, the fixative should be washed by soaking three times the sample in PBS (see Appendix, protocol *Fixatives*).

Considerations:

1. All the steps should be performed on the rotator to facilitate the fixative reaching all tissue areas.
2. After each step, it is recommendable to leave the sample 10 min in the desiccator under vacuum to facilitate the infiltration of the fixative. We have found this step particularly important to preserving cells located within mineralized areas (e.g. tesserae).
3. We recommend purchasing a pre-mixed stock solution of buffered 4% PFA (we used *Paraformaldehyde solution 4% PBS, Santa Cruz Biotechnology, catalog number: sc-281692*). This can then be divided into separate vials (e.g. 15 ml vials) and frozen until time for use. PFA oxidizes to formic acid with time; older (less reactive) PFA has an obvious yellow tint. Our method ensures that the PFA is fresh for each sample preparation.
4. The fixation time cannot exceed 48 hours. Otherwise, the fixative will create excessive cross-linking (mask of epitopes and proteins that produces a weak histology staining) [11].
5. Once fixed, samples can be stored in PBS at 4°C, although it is recommended to continue with the ensuing procedures (e.g. embedding) as soon as possible.

2.1.3. Glutaraldehyde 2% + 2% PFA – cross-linking fixative

Glutaraldehyde (GA) is a crucial fixative for electron microscopy due to its effectiveness in stabilizing cell ultrastructure and morphology. However, it is composed of larger molecules than PFA and, as a consequence, has a lower penetration rate into the tissue. To ensure the optimal tissue and cell ultrastructure preservation, a combination of GA and PFA is used to analyze samples in electron microscopy [12,13].

- **Fixation:** GA (similar to PFA) establishes covalent links with tissue molecules creating a stable meshwork. GA can react with the same chemical groups as PFA (see above), however, GA has a higher potential to produce cross-links, due to the presence of an extra aldehyde group: while PFA has only one aldehyde group at the end of its molecule, GA contains two. The extra aldehyde group of GA also reacts with the protein, resulting in a

higher cross-linking than PFA. The excessive cross-linking results in better preservation of the tissue ultrastructure, although it negatively affects other techniques such as immunohistochemistry (reacting with the epitopes of the antibodies) and slows the penetration of the fixative (due to the higher size of the molecule). GA does not react with lipids, unless they contain free amino groups (e.g. phospholipids) [10].

- **Advantages:** Fast, optimal for cartilage matrix and cell ultrastructure fixation.
- **Disadvantages:** Toxic. Oxidates with time. Masks some epitopes for certain antibodies through the generation of a dense cross-linked meshwork (excessive cross-linking).
- **Recommended structures:** Ultrastructure of cartilage extracellular matrix and cells.
- **Suitable techniques:** Electron microscopy (SEM, ESEM, TEM, FIB-SEM).
- **Hazard statements:** Toxic (skin contact and inhalation). Manipulate under the hood, with adequate protection. Dispose of properly.

Protocol:

The fixation solution 2% GA + 2% PFA can be buffered with PBS 0.1M or sodium cacodylate buffer (see Appendix, protocol *Fixatives*).

Considerations:

1. The fixative solution needs to be prepared fresh every time, ideally immediately prior to fixation. Usually, GA is stored in a stock solution of 25% GA and PFA can be obtained from a frozen stock solution or prepared from scratch (see section above).
2. To preserve cell ultrastructure it is crucial to fix the tissue immediately after the animal's death.
3. The sample should be maintained at 4°C (fridge) in the fixative until the embedding procedure. However, the storage time should be minimized to avoid excessive cross-linking.

2.1.4. Osmium tetroxide

Osmium tetroxide (OsO_4) is used after the samples have been fixed with GA 2% + PFA 2% and prior to electron microscopy analysis, acting as a post-fixation reagent (second-fixation step) as well as a staining reagent.

- **Fixation:** OsO_4 reacts with amino and sulphydryl groups, binding unsaturated acyl chains of membrane lipids (stabilizing cell membranes) and staining them black, which provides contrast with cellular structures.
- **Advantages:** Optimal to preserve and visualize cell and matrix ultrastructure, particularly for soft tissues with low native electron-contrast.
- **Disadvantages:** Highly toxic and difficult to dispose of.
- **Recommended structures:** Ultrastructure of cartilage extracellular matrix and cells
- **Suitable techniques:** Electron microscopy (SEM, ESEM, TEM, FIB-SEM).
- **Hazard statements:** Highly volatile. Severe irritant for eyes and respiratory tract, can cause irreversible eye damage including blindness with direct contact. Can cause long-term toxicity in liver and kidneys.

Considerations:

1. OsO_4 is photosensitive. Both the reagent and post-fixed samples should be maintained in dark conditions until embedding (see Appendix, protocol *TEM+FIB-SEM sample preparation*).

2.1.5. Non-fixed samples

For some applications, it should be noted that cartilage can also be preserved to some degree by freezing (e.g. in traditional -20° or -80° freezers). To a point, this allows the study of the tissue closer to its native state, in avoiding some artifacts produced by fixatives (e.g. excessive cross-linking). However, depending on the freezing temperature and rate of cooling, artifacts and tissue disruption related to water vitrification and crystallization can appear. These can be avoided using

cryofixation techniques, which involve rapid cooling of tissues to temperatures below the “safe temperature” (-127.41°C) [14]. By cooling extremely rapidly (e.g. by plunge-freezing in liquid nitrogen or ethane) and especially at high pressures (~2100 bars, as in *high-pressure freezing*), artifacts from ice crystal formation (vitrification) can be avoided [2,3,16,17,18]. Whereas cryofixation techniques render the best cartilage and cell ultrastructure preservation, however, they could not be used during this dissertation to prepare elasmobranch skeletal samples since the needed laboratory equipment and reagents (e.g. liquid nitrogen) were not available when the specimens were fixed.

2.2. Embedding

Embedding involves encasing a tissue sample within a block of material, to provide a stabilizing matrix for sample sectioning and imaging. Just as the surrounding banana bread helps you slice through walnuts, embedding samples allows tissues to be sectioned in uniform, oriented and thin slices (in the range of mm to μm), that can then be polished to expose and smooth desired regions of interest.

The properties of the supporting matrix must match those of the sample in order to stabilize sectioning (i.e. the bread cannot be too soft compared to the walnut or the knife will drag it through the bread); as a result, the hardness of the embedding block is crucial for precise sectioning. Thus, if we want to accurately section tissues containing mineralized materials (e.g. tesserae), the embedding media should match the hardest material (e.g. a hard plastic resin like PMMA should be used). If, on the contrary, our tissue lacks mineralized areas or has been demineralized, we can use softer embedding media (e.g. paraffin). We are especially interested in preserving the mineralized tesserae and therefore all embedding techniques below are based on hard embedding media.

2.2.1. PMMA Embedding

PMMA is a hard plastic material (polymer) used to embed mineralized tissues. The exact material properties of PMMA are adjustable, depending on the combination of reagents used to prepare it and the polymerization protocol. We have used two PMMA protocols with different polymerization temperatures: “cold PMMA embedding” (performed at 4°C) and “hot PMMA embedding” (performed at 30-60°C).

The two protocols have different advantages and disadvantages. The hot PMMA embedding process is considerably faster than the cold PMMA embedding process (1 week vs. 1 month); however, as sample blocks tend to fracture when cut in a microtome, hot embedding is only suitable for thick sectioning of sample blocks (e.g. with low-speed saw) for resultant sections tens to hundreds of microns thick. This is useful for imaging and analyses where sample thickness is not particularly relevant (e.g. surface imaging techniques like SEM). In contrast, cold-embedded sample blocks can be sectioned considerably more thinly, allowing the production of samples of microns thick, and therefore more suitable for techniques that require serial sectioning such as, for example, histology. For this reason, only cold PMMA embedding was used to prepare the samples for this dissertation (see *PMMA embedding* protocol).

- **Embedding media:** Polymethylmethacrylate (PMMA).
- **Advantages:** Transparent embedding blocks, optimal for cutting by microtome or low-speed saw (e.g. Isomet precision saw).
- **Disadvantages:** Toxic, long embedding process (1 month), not functional for IHC.
- **Suitable techniques:** CT-scan, histology, light microscopy (confocal, polarized), SEM.
- **Hazard statements:** Toxic (skin contact and inhalation). Manipulate under the hood, with adequate protection. Dispose of properly.

2.2.2. EPON Embedding

EPON is a resin widely used to embed samples for electron microscopy, since it allows sectioning ultra-thin cuts [19].

- **Embedding media:** Glycid ether 100 (aka EPON 812).
- **Advantages:** The best embedding media for ultrastructure imaging of cartilage matrix and cells in electron microscopy.
- **Disadvantages:** Highly toxic, medium-long embedding process (2 weeks), not functional for IHC.
- **Suitable techniques:** Electron microscopy (TEM, FIB-SEM, SEM, ESEM), CT-scan and histology.
- **Hazard statements:** Toxic, produces eye and respiratory tract damage, skin corrosion and irritation, skin sensitization, carcinogenic. However, the resin is not toxic once it has polymerized.

Considerations:

1. EPON must be prepared freshly for each embedding session (see protocol). The proportions of combined reagents results in differing degrees of hardness, which can be tuned to the type of sample being embedded.

2.2.3. Cryo-embedding

The primary advantage of cryo-embedding/microtomy is time: samples can be embedded, sectioned and imaged in <1 day. Cryo-embedding is commonly used to embed non-fixed samples, although it can also be used with fixed tissue. This process involves embedding samples in OCT (a water-soluble medium of resins and glycols) at low temperatures (~-10°C). OCT-embedded blocks can be stored frozen, but typically are immediately cut into slices using the cryo-microtome on the same cold stage where embedding is performed (see *Cryo-microtomy* below). Once slices have

been cut, the OCT media is easily removed with distilled water. The protocol from cryo-embedding to cryo-microtomy is described under *Cryo-microtomy* below.

- **Embedding media:** OCT reagent.
- **Advantages:** Optimal for rapid preparation of unfixed tissues, fast embedding (<1 day), allows sectioning of both hard and soft materials, the embedding media is removed with water, and is non-toxic.
- **Disadvantages:** Requires the cryo-microtome, only used to cut thin samples, permanent blocks are not possible (only short storage), fresh samples remain unfixed.
- **Suitable techniques:** Histology, IHC, Raman.
- **Hazard statements:** Not toxic.

2.2.4. Clarification

Although not an embedding technique, clarification is also used to prepare samples for imaging and so we will discuss it briefly here. Clarification functions by rendering bulk tissues transparent to permit imaging of deeper structures (e.g. for confocal microscopy). The tissue is submerged in a reagent with a higher refraction index than the sample's tissues; once the clarification reagent permeates the tissue, the sample and the reagent have the same refractive index, allowing light to pass through without being refracted, making the tissue transparent [20]. Comparatively large samples, several centimeters in each dimension, can be cleared effectively, allowing imaging of macroscopic tissue features.

As no published protocols exist for clarification of tessellated cartilage, we compared two clearing agents: ethyl cynamate (ECi) [21] and BABB (BenzyAlcohol-BenylBenzoate) [22]. We found that ECi cleared the tissue more completely (e.g. in BABB-cleared samples, blood vessels were often not completely cleared), while also being faster, cheaper and non-toxic. Protocols for ECi clarification are found in Appendix, *ECi clarification*.

- **Embedding media:** Ethyl cinnamate (ECi).
- **Advantages:** Optimal to visualize large pieces of samples, on the order of centimeters thick (e.g. entire skeletal elements), to penetrate deeply into tissues and obtain 3D images of whole structures.
- **Disadvantages:** To be transparent, the tissue needs to be submerged within the clarification media.
- **Suitable techniques:** Raman, confocal microscopy (autofluorescence, fluorescent-stained samples), light sheet microscopy.
- **Hazard statements:** Not toxic.

Considerations:

1. The tissue can be kept submerged in the clarification media for months without degradation.

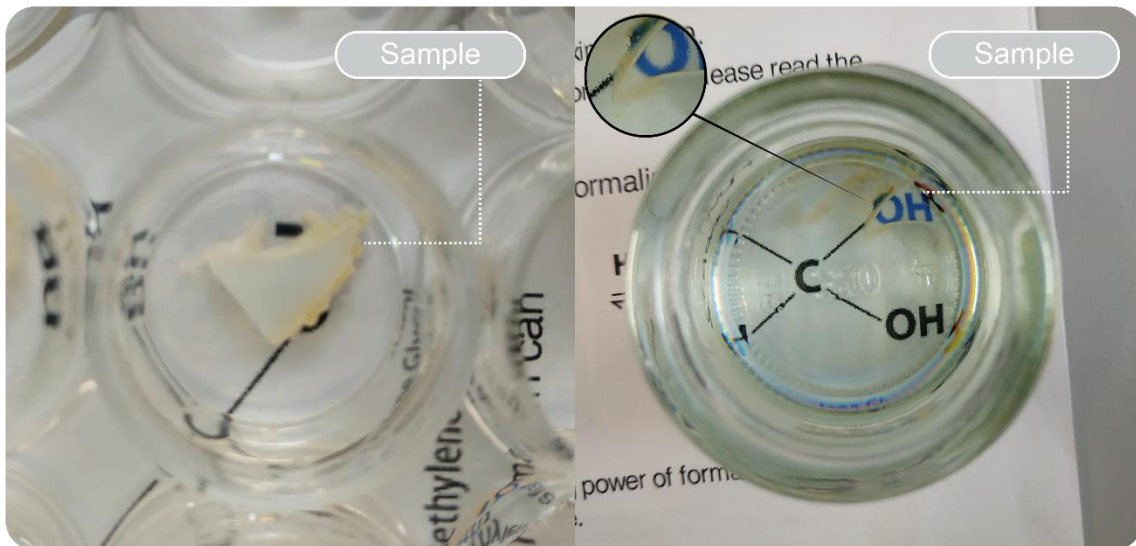


Fig.2. Proterrygium cross-section before and after being clarified with ECi. Note that, in the clarified sample (right), the tesserae and the cartilage matrix became transparent, however, the perichondrium (yellow elements at top of image) remained opaque.

2.3. Cutting, polishing and mounting

Once the samples are embedded in blocks —whether PMMA, Epon or some other technique— the blocks need to be prepared for the visualization technique of interest. The preparation methods are listed as follows:

2.3.1. Microtome cutting and mounting

Microtome cutting and mounting is suitable for histology, IHC, Polarized microscope, Confocal microscope.

Microtome cutting and mounting is suitable for histology, IHC, Polarized and confocal microscopy.

1. Using a saw, trim the excess embedding media from the block. It is recommended to leave some embedding media surrounding the sample, in order to make the slices more stable when cut with the microtome.
2. Superglue the sample block to a piece of PMMA (Fig. 3) that fits into the microtome holder; we made a mold so the PMMA base piece could be easily reproduced. Once the sample and block are clamped in the microtome, rotate and orient the sample according to the desired cutting orientation.
3. Use a D-knife (diamond knife) to trim into the block face until reaching (Fig. 4) the region of interest. For this trimming step, an older/duller D-knife can be used and thicker cuts (~20-30 μm) can be made to remove tissue more quickly.
4. When cutting sample slices, to make cutting smoother, it is useful to wet the sample surface before each slice, using a brush dipped in 0.25% Triton X-100 (detergent) in distilled water.
5. Once the desired region of interest is reached, change for the sharpest/newest D-knife for more precision in cutting (Fig. 3).

6. Reduce the speed and adjust the thickness of the cut. The optimal thickness for tessellated cartilage is between 7 and 10 μm . Thicker than that, the tesserae are pulled away from the soft tissue and out of the sample block (Fig. 5). To generate sections of more uniform thickness and to avoid damage, it is recommended to cut the block at low speeds.
7. Prepare Dako slides (special glass slides with a glue on them, which facilitates the adhesion of the tesserae) on a flat surface with a drop of 70% ETOH on them. It is important to hydrate cut samples at all times with 70% ETOH. Never with 100% ETOH, as this will dissolve the PMMA.
8. Once a section is cut, take it carefully with tweezers and place it in the previously prepared drop of 70% ETOH on top of a Dako glass slide. The section should be soaked all time with 70% ETOH.
9. Cover the sections with a plastic cover slip (Kisol) and pass a roller or brush over the covered samples to flatten them out. The cover slip should cover the sample completely, without jutting beyond the borders of the glass slide, otherwise air may leak into the sample space.
10. Cover the samples with a filter paper to absorb the remaining 70% ETOH.
11. Once all slide sections have been prepared, stack the slides together with filter paper between them, Add empty glass slides (5 of each) on top and below the pile of slide-sections containing the samples and place them in the pressing device.
12. Tighten the pressing device without breaking any glass slides and place the pressing device with the slides in the oven at 60°C for 48h.
13. After 48h in the oven, take out the slides and wait until they cool and reach RT. The sections are ready to use or store.

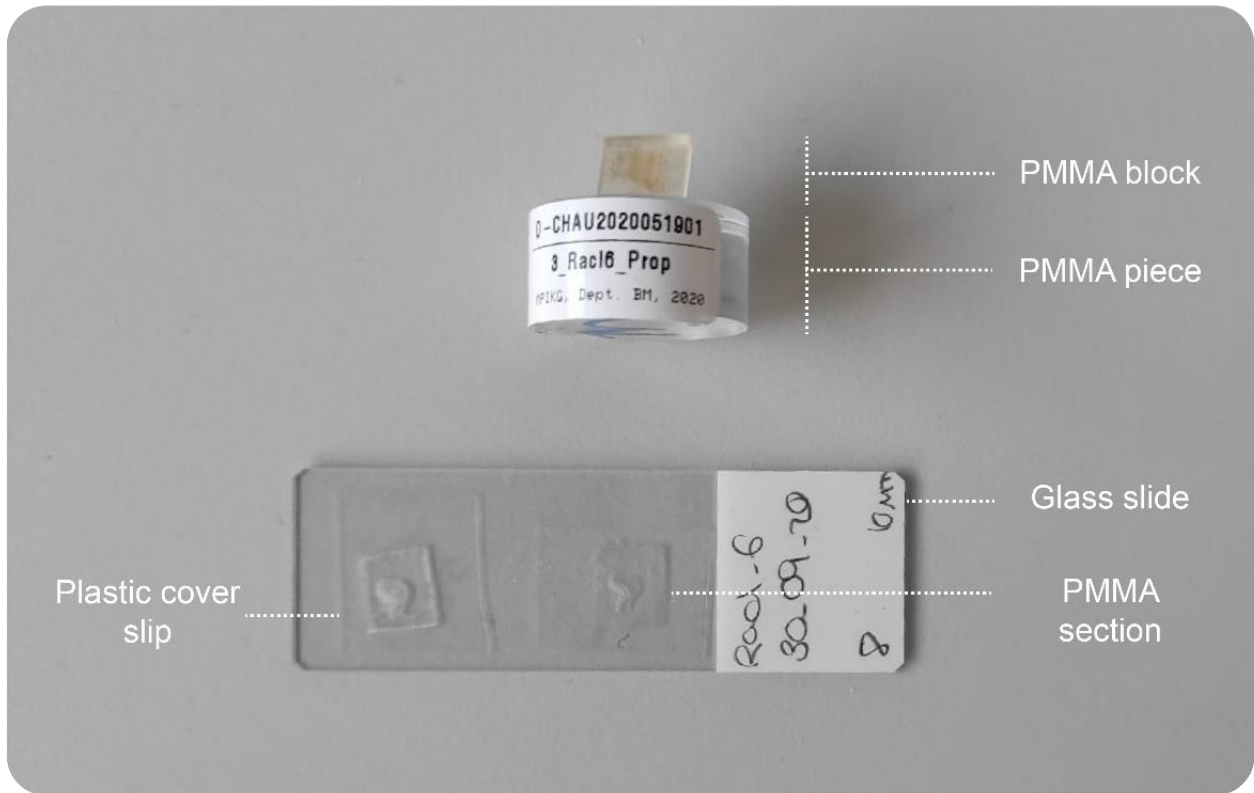


Fig. 3. Sample embedded in PMMA and cut sections. Above: A sample embedded in a PMMA block superglued in a piece of PMMA. Below: a Dako glass slice with PMMA cut sections covered with a plastic cover slip (Kisol).

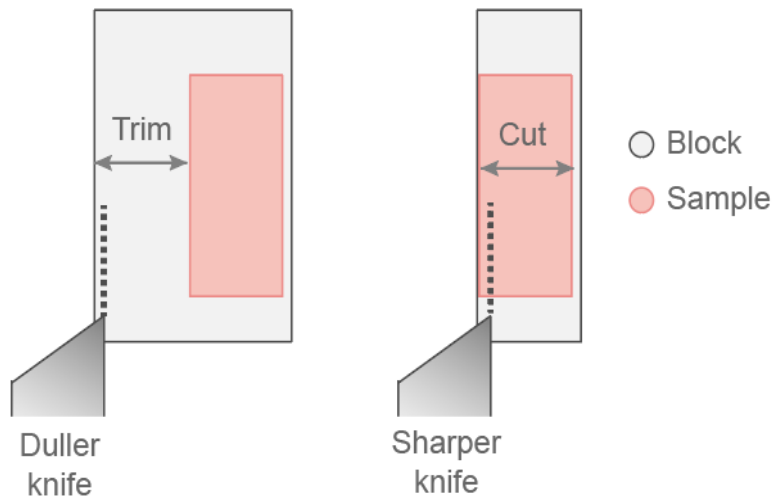


Fig. 4. Difference between trimming and cutting steps.

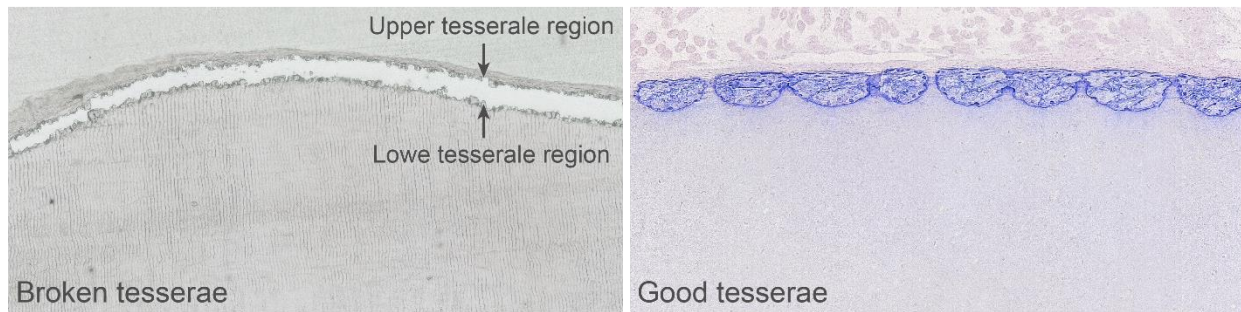


Fig. 5. Difference between sections showing broken tesseræ and well-sectioned tesseræ. In non-demineralized samples, when tesseræ are not sectioned properly (left), the tesseræ layer tends to tear in two parts like a zipper, making impossible any analysis and imaging. In the well-sectioned tesseræ (right), the tesseræ morphology is maintained.

2.3.2. Cryo-microtome cutting and mounting

Cryosectioning can be performed with formalin-fixed, fresh or frozen tissue samples. Suitable techniques include light microscopy (Raman, confocal and polarized microscopy), histology and IHC.

1. Cut the sample in small pieces that can fit into silicone flat embedding molds.
2. Place the samples into the molds, with the regions of interest oriented to the tip (where the block will be cut).
3. Slowly fill the molds with OCT medium, avoiding the formation of bubbles.
4. Place the molds inside the cryo-microtome chamber on the metal plate at -7°C . Wait until the OCT medium turns white, indicating that the sample has frozen.
5. Affix the sample block to the cutting plate by placing a drop of OCT medium between block and plate, freezing them together.
6. Cut the block with the cryo-microtome in a manner generally similar to the process described for the microtome above (*Microtome cutting + mounting* section): First, trim the block with thick cuts ($\sim 60\ \mu\text{m}$) and, once the region of interest is reached, make cuts thinner ($\sim 10 - 50\ \mu\text{m}$). In fresh, cryo-prepared samples, we have found that thicker samples ($50\ \mu\text{m}$) maintain structures better than thinner samples.

7. The cut sections can be lifted off with a paintbrush and placed on a glass slide. As above, Dako glass slides are recommended, as they have a special coating that helps the section adhere to the glass slide.
8. The tissue sections on the glass slides can be stored in the freezer indefinitely. When ready for use, the glass slides can be removed from the freezer and thawed, but then should be mounted as soon as possible to avoid sample damage.
9. Once thawed, check tissue slices under the microscope (some may be broken or destroyed) and select samples of interest.
10. To eliminate the OCT medium, take the desired tissue slices with tweezers (being careful not to break them) and place them on a separate glass slide with a drop of PBS and wait ~5 minutes. Then, place the sections in a new drop of PBS
11. While the sample is in PBS, prepare a glass slide with a gene frame on it, with one new drop of PBS inside the frame (Fig. 6).
12. Place the tissue slice inside the gene frame in the PBS drop (Fig. 6).
13. Cover it with a cover slip (Fig. 6).
14. The sample can be kept in this configuration until it starts degrading; how long depends on whether the sample is fixed or not and whether anti-bacterial solution has been added to the PBS.

Considerations:

1. The tissue slices can be stored in the freezer. However, once thawed, slices should be processed/imaged immediately, as multiple freeze-thaw cycles can damage tissue structure, particular for cartilage.
2. Once cut and the embedding media removed, slices are mounted using aqueous media (usually PBS, see below). Therefore, they have a limited storage time (~2 weeks) until bacteria starts growing on the tissue.

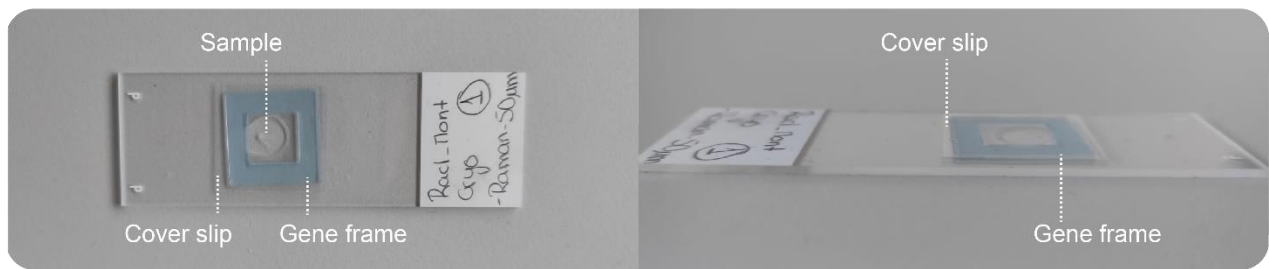


Fig. 6. Cryosectioned samples mounted and maintained in wet conditions. To keep cryosectioned samples hydrated, they are kept in aqueous media (usually PBS) inside of a gene frame (blue square), which is covered with a cover slip to avoid evaporation.

2.3.3. Block polishing

Block polishing is suitable for SEM, FIB-SEM, confocal and polarized microscopy.

1. If possible, perform a μ CT scan of the sample block to have an image of the sample orientation and localize the regions of interest.
2. If the region of interest is far from the surface, the sample can be trimmed down using a cutting saw, using the reconstructed μ CT data as a guide (if available).
3. Once the region of interest is close to the surface, the sample is polished with decreasing grain size (e.g. grinding paper or diamond spray) to expose a smoothed region of interest at the surface. Start polishing with higher grain size (4000) until the region of interest is exposed to the surface. Then, continue polishing using smaller grain size (2000 and diamond size) to polish the sample surface (Fig. 7).
4. If a sub-surface imaging technique is planned (e.g. FIB-SEM, confocal microscopy, Raman spectroscopy), perform a second μ CT scan to localize subsurface regions of interest according to surface landmarks.
5. For FIB-SEM and SEM, place the sample on carbon conductive tabs and coat them with 3X carbon and 1X platinum.

Considerations:

1. Samples prepared for SEM need to be polished carefully to create a perfectly smooth block face, as the regions of interest are located on the surface of the sample.
2. In contrast, samples prepared for FIB-SEM do not need to be polished carefully, as the regions of interest are usually located beneath the surface.

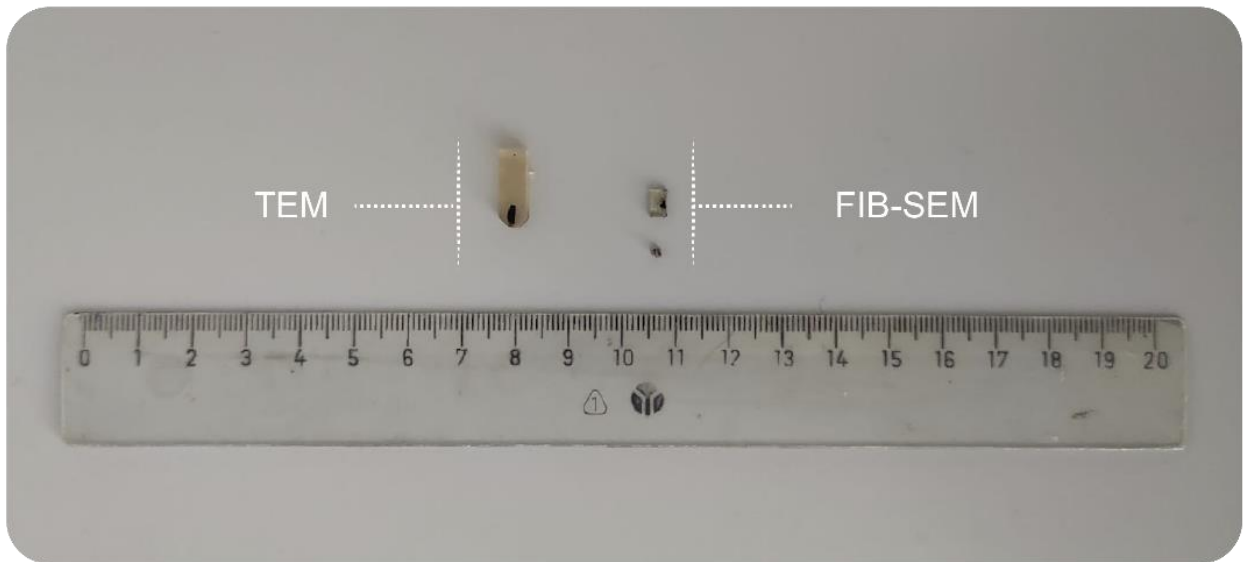


Fig. 7. Samples embedded in EPON for electron microscopy imaging. For TEM (left), the sample is positioned facing and against the cut surface of the tip (at the bottom of the sample block in the image) for ultra-thin (nm) sectioning using an ultramicrotome. The rest of the block, containing only EPON, is needed to hold the sample in the ultramicrotome while cutting. For FIB-SEM (right), the sample block needs to be as small as possible, again with the sample positioned on the surface of the block.

2.4. Stainings

In this section are summarized the techniques based on histology, fluorescent dyes and IHC used and optimized during the doctoral period. Protocols can be found in Appendix, pages 227-244.

2.4.1. Classical histology

Alcian blue

Alcian blue is a positively charged dye (cationic) with an affinity for anionic groups (negatively charged) such as glycosaminoglycans in cartilage (Fig. 8).

Results:

- Blue: Cartilage extracellular matrix, pericellular matrix, territorial matrix, tesserae matrix, spokes.

Toluidine blue

Similar to alcian blue, toluidine blue is a positively charged dye (cationic) with an affinity for anionic groups (negatively charged) such as glycosaminoglycans in cartilage (Fig. 8). It is often used to stain samples prepared for electron microscopy, in order to have a broad image of the section before imaging it under the electron microscope.

Results:

- Blue: Cartilage extracellular matrix, pericellular matrix, territorial matrix, tesserae matrix, spokes.

Safranin O

Safranin O is a positively charged dye (cationic) that binds to polyanions (several anionic groups, negatively charged), having an affinity for glycosaminoglycans (Fig. 8). Safranin O is usually combined with fast green (negatively charged) as a counterstaining.

Results:

- Red: Cartilage extracellular matrix, pericellular matrix, territorial matrix, spokes.

References: [23]

Hematoxylin & Eosin

Hematoxylin & Eosin is used to have an overview of the tissue, as it stains different structures (Fig. 8). This staining is a combination of two dyes: (1) Eosin (pink), which is acidic (negatively charged) with affinity for basic structures, and (2) hematoxylin (purple), which is used in a combination with aluminum salts (mordant) and interacts with acidic structures.

Result:

- Red-pink: cartilage matrix
- Purple-blue: Nucleus

Sirius red

Sirius red is a negatively charged dye (anionic) containing sulfonic acids groups that increase the birefringence when bound parallel to basic proteins such as collagens or proteins containing basic aminoacids (positively charged). In cartilage, it has an affinity for collagen fibers, where the staining intensity corresponds to the abundance or degree of packing of collagen fibers.

Results:

- Red: Cartilage extracellular matrix, perichondrium, tesserae.

References: [24,25]

Classical histology

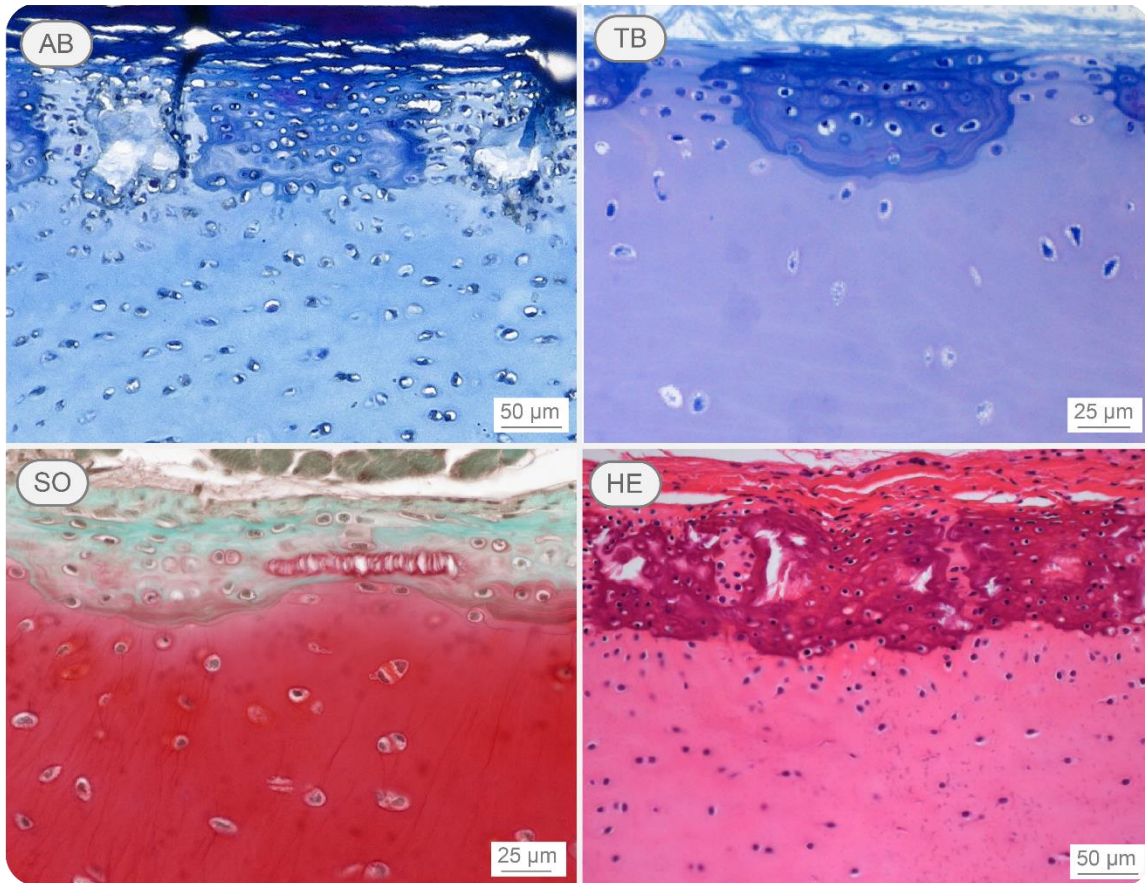


Fig. 8. Tessellated cartilage stained using classical histology dyes. Alcian blue (AB), toluidine blue (TB) and safranin O (SO) are cationic dyes with an affinity for glycosaminoglycans, located mainly in the cartilage matrix, tesserae and spokes. Unlike AB and TB, SO shows a better contrast between the cartilage matrix and spokes, since this stain is used in combination with fast green (counterstrain). Hematoxylin-Eosin (HE) is a combination of eosin (which stains positively-charged structures such as collagens in pink) and hematoxylin (which stains negatively-charged structures such as nucleus and GAGs in purple). Note that the unmineralized cartilage matrix is stained with pink, showing the dominance of collagens over GAGs.

2.4.2. Fluorescent dyes

Phalloidin

Phalloidin is a toxin with an affinity for the actin fibers present in the cytoplasm of the cells. For its visualization under the microscope, phalloidin is labelled with a fluorescent analog. Several fluorescent analogs can be used, differing on their excitation and emission spectra such as, for example, Alexa Fluor 488 phalloidin (green) or rhodamine phalloidin (red). Both phalloidins were tested in elasmobranch skeletal cartilage, and none of them gave satisfactory results. Red phalloidin did not bind to the cellular actin fibers, but to the mineralized matrix of the tesserae (Fig. 9). Instead, green phalloidin bound to the cellular actin fibers, but also to the nucleus and cellular membrane.

Rhodamine 6G

Rhodamine 6G is a fluorescent dye with an affinity for soft tissues, not binding to mineralized tissues. As the soft tissues are stained with bright red and mineralized tissues are seen in black, it offers an optimal contrast to segment and visualize soft tissues, especially those that are small such as canaliculi passages in bone or tesserae (Fig. 9).

DAPI

DAPI is a fluorescent dye with an affinity for the DNA and, therefore, it is used to visualize cell nuclei (Fig. 9A-B).

2.4.3 Immunohistochemistry

Sox9

Sox9 is a transcription factor exclusive for chondrocytes, as it regulates the genes *Agc* and *Col2a1*, which encode the production of aggrecan and Col2 (Fig. 9B).

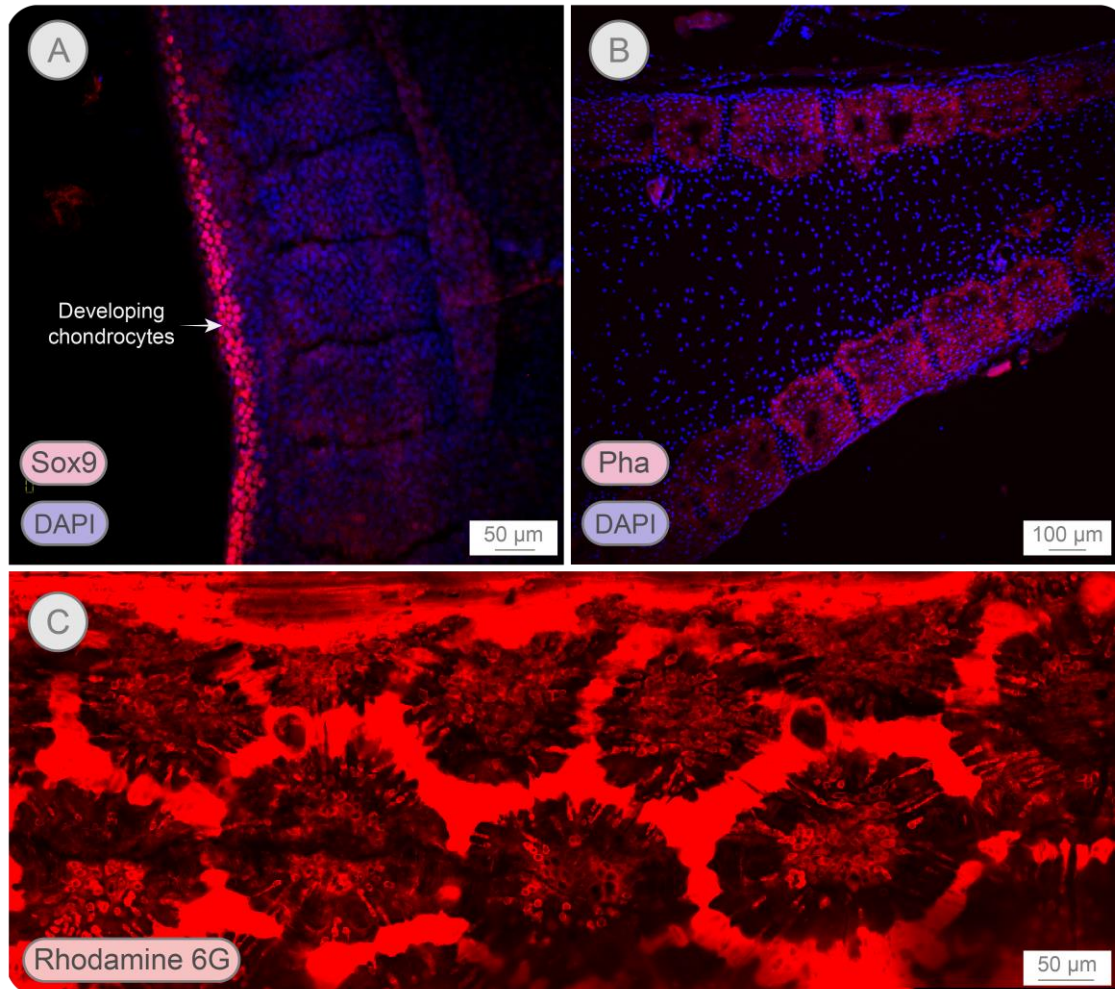


Fig. 9. Elasmobranch skeletal cartilage stained with fluorescent labels. **A)** Chondrocytes from a catshark embryo notochord stained with Sox9 antibody (red) and DAPI (blue) to highlight the cell nuclei. **B)** Cross section of the (juvenile) tessellated skeleton stained with rhodamine phalloidin (red) and DAPI (blue). Note that although rhodamine phalloidin is typically used to stain the actin cytoskeleton, here, it stained the mineralized matrix of the tesserae, instead of the cell cytoplasm. **C)** Planar view of tesserae stained with rhodamine (red). Rhodamine stains soft tissues, including the joint spaces and the cell lacunae. Mineralized structures are unstained (black in this image).

2.4.4. Stainings for electron microscopy

Uranyl acetate

Uranyl acetate (UA) is a staining used to enhance the contrast in biological tissues that are analyzed in electron microscopy (Fig. 10). In particular, the uranyl ions of UA enhance the contrast by binding with lipids and proteins with sialic acid carboxyl groups such as glycoproteins as well as with the nucleic acid phosphate groups of the genetic materials (DNA and RNA).

Lead citrate

Lead citrate is a staining used to enhance the contrast in biological tissues for electron microscopy (Fig.10). Lead citrate reacts with several cellular structures such as ribosomes, lipid membranes and cytoskeleton.

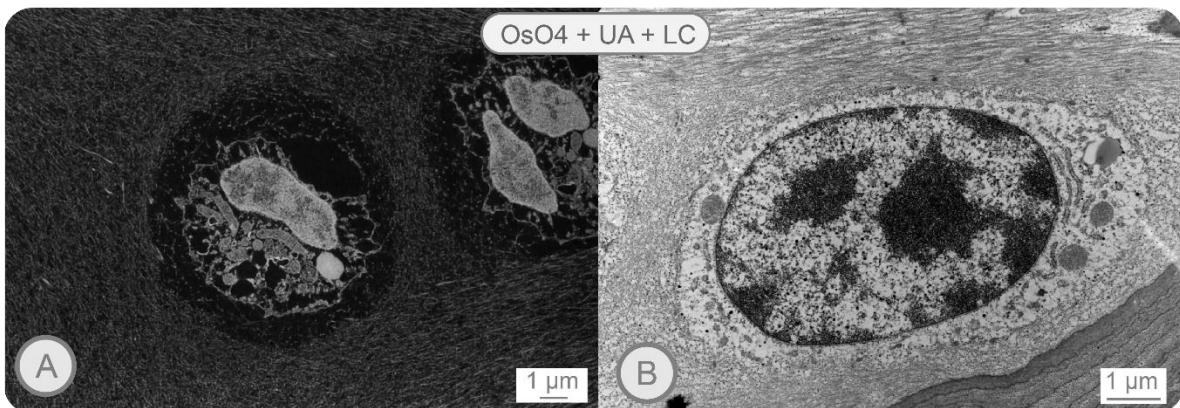


Fig. 10. Elasmobranch skeletal cartilage stained with heavy metals for electron microscopy imaging. **A)** A pair of twin chondrocytes from the same chondron imaged with FIB-SEM. **B)** A chondrocyte from the tesserae imaged with TEM. In both cases, samples were stained with osmium tetroxide (OsO_4), uranyl acetate (UA) and lead citrate (LC), which allowed imaging cellular and matrix ultrastructure such as matrix Col1 and Col2 fibers and cell organelles such as the nucleus, the mitochondria and the rough endoplasmic reticulum.

Table 1. Summary of the sample preparation protocols required for each technique and the image types obtained.

Technique	Biological structure	Scale range	Fixative	Post-fixation	Staining	Embedding	Polishing	Microtome cutting	Time
FIB-SEM	3D tissue ultras	nm - μm	2%GA + 2% PFA	2% OsO ₄	2% UA + lead citrate	EPON	Yes	-	3 weeks
SEM	2D cells + matrix	nm - μm	2%GA + 2% PFA / 4% PFA / ETOH 70%	Optional	Optional	EPON/PMMA	Yes	-	4 weeks
TEM	2D cells + matrix	nm - μm	2%GA + 2% PFA	2% OsO ₄	2% UA + lead citrate	EPON	Yes	-	3 weeks
BSEM	2D mineralized tissue	nm - μm	Without / ETOH 70%	-	-	EPON/PMMA/ Without	Yes	-	1 week
Histology	2D cells + matrix + mineralized tissue	μm - mm	4% PFA / ETOH 70%	-	-	PMMA/Paraffin / OCT	-	Yes	4 weeks
IHC	2D cells + matrix	μm - mm	4% PFA / ETOH 70%	-	-	PMMA/Paraffin / OCT	-	Yes	3 days - 3 weeks
Dyes	2D cells + matrix	μm - mm	4% PFA / ETOH 70%	-	-	PMMA/Paraffin / OCT	-	Yes	4 weeks
Cryo	2D cells + matrix + mineralized tissue	μm - mm	Without / 4% PFA	-	-	OCT	-	Yes	1 day
CTscan	3D mineralized tissue	μm - mm	Without / 4% PFA / ETOH 70%	-	-	EPON/PMMA/ Without	-	Yes	1 day - 3 weeks

References

- [1] Moor H. Theory and practice of high pressure freezing. Cryotechniques in biological electron microscopy 1987 (pp. 175-191). Springer, Berlin, Heidelberg
- [2] Hunziker EB, Herrmann W, Schenk RK, Mueller M, Moor H. Cartilage ultrastructure after high pressure freezing, freeze substitution, and low temperature embedding. I. Chondrocyte ultrastructure-implications for the theories of mineralization and vascular invasion. The Journal of cell biology. 1984 Jan;98(1):267-76.
- [3] Hunziker EB, Lippuner K, Shintani N. How best to preserve and reveal the structural intricacies of cartilaginous tissue. Matrix biology. 2014 Oct 1;39:33-43.
- [4] Doyle J. Ageing changes in cartilage from squalus acanthias L. Comparative biochemistry and physiology. 1968 Apr 1;25(1):201-6.
- [5] Mathews MB, Decker L. Comparative studies of water sorption of hyaline cartilage. Biochimica et Biophysica Acta (BBA)-General Subjects. 1977 Mar 29;497(1):151-9.
- [6] Seno N, Anno K, Yaegashi Y, Okuyama T. Microheterogeneity of chondroitin sulfates from various cartilages. Connective tissue research. 1975 Jan 1;3(1):87-96.
- [7] Farrell AP. Encyclopedia of fish physiology: from genome to environment. Academic press; 2011 Jun 1.
- [8] Fox CH, Johnson FB, Whiting J, Roller PP. Formaldehyde fixation. Journal of Histochemistry & Cytochemistry. 1985 Aug;33(8):845-53.
- [9] Hobro AJ, Smith NI. An evaluation of fixation methods: Spatial and compositional cellular changes observed by Raman imaging. Vibrational Spectroscopy. 2017 Jul 1;91:31-45.
- [10] Eltoun I, Fredenburgh J, Myers RB, Grizzle WE. Introduction to the theory and practice of fixation of tissues. Journal of Histotechnology. 2001 Sep 1;24(3):173-90.
- [11] Van der Loos CM. A focus on fixation. Biotechnic & Histochemistry. 2007 Jan 1;82(3):141-54.
- [12] Hayat MA. Glutaraldehyde: role in electron microscopy. Micron and Microscopica Acta. 1986 Jan 1;17(2):115-35.
- [13] Hopwood D. Theoretical and practical aspects of glutaraldehyde fixation. The Histochemical Journal. 1972 Jul 1;4(4):267-303.
- [14] Bachman L. and Mayer E. Physics of water and ice: implications for cryofixation. Cryotechniques in biological electron microscopy. Eds. Steinbrecht RA, Zierold K. Springer Science & Business Media; 2012 Dec 6; 3-34
- [15] Steinbrecht RA, Zierold K, editors. Cryotechniques in biological electron microscopy. Springer Science & Business Media; 2012 Dec 6.
- [16] Bernhard W, Leduc EH. Ultrathin frozen sections: I. Methods and ultrastructural preservation. The Journal of cell biology. 1967 Sep 1;34(3):757-71.
- [17] Boyne AF. A gentle, bounce-free assembly for quick-freezing tissues for electron microscopy: Application to isolated torpedine ray electrocyte stacks. Journal of neuroscience methods. 1979 Dec 1;1(4):353-64.

- [18] Sitte H, Edelmann L, Neumann K. Cryofixation without pretreatment at ambient pressure. *Cryotechniques in biological electron microscopy*. Eds. Steinbrecht RA, Zierold K. Springer Science & Business Media; 2012 Dec 6; 3-34
- [19] Craig EL, Frajola WJ, Greider MH. An embedding technique for electron microscopy using Epon 812. *The Journal of cell biology*. 1962 Jan 1;12(1):190.
- [20] Richardson DS, Lichtman JW. Clarifying tissue clearing. *Cell*. 2015 Jul 16;162(2):246-57.
- [21] Klingberg A, Hasenberg A, Ludwig-Portugall I, Medyukhina A, Männ L, Brenzel A, Engel DR, Figge MT, Kurts C, Gunzer M. Fully automated evaluation of total glomerular number and capillary tuft size in nephritic kidneys using lightsheet microscopy. *Journal of the American Society of Nephrology*. 2017 Feb 1;28(2):452-9.
- [22] Mayrand D, Fradette J. High definition confocal imaging modalities for the characterization of tissue-engineered substitutes. In *Adipose-Derived Stem Cells 2018* (pp. 93-105). Humana Press, New York, NY.
- [23] Rosenberg L. Chemical basis for the histological use of safranin O in the study of articular cartilage. *JBS*. 1971 Jan 1;53(1):69-82.
- [24] Nielsen LF, Moe D, Kirkeby S, Garbarsch C. Sirius red and acid fuchsin staining mechanisms. *Biotechnic & histochemistry*. 1998 Jan 1;73(2):71-7.
- [25] Hyllested JL, Veje K, Ostergaard K. Histochemical studies of the extracellular matrix of human articular cartilage—a review. *Osteoarthritis and cartilage*. 2002 May 1;10(5):333-43.

V | PUBLISHED PAPERS

Paper 1

Co-aligned chondrocytes: Zonal morphological variations and structured arrangement of cell lacunae

Authors:

Júlia Chaumel^{1*}, Merlind Schotte², Joseph J. Bizzarro³, Paul Zaslansky⁴, Peter Fratzl¹, Daniel Baum², Mason N. Dean¹

¹ *Department of Biomaterials, Max Planck Institute of Colloids and Interfaces*

² *Visual Data Analysis Department, Zuse Institute Berlin*

³ *Institute of Marine Sciences, University of California Santa Cruz*

⁴ *Department for Operative and Preventive Dentistry, Universitätsmedizin Berlin*

*Corresponding author

Publication:

This study was published in the journal *Bone* in May 2020, as part of the special issue “*Celebrating John D. Currey’s Contributions to the Science of Bone*” which addresses the topics about bone and cartilage that John found most fascinating.

Publication details: Bone, Volume 134, May 2020, 115264

<https://doi.org/10.1016/j.bone.2020.115264>

Publication link:

<https://www.sciencedirect.com/science/article/abs/pii/S8756328220300442>

This publication cannot be published online on this file, since it is not open access and includes copyrighted material. The publication can be accessed by clicking the publication or doi link.

Image analysis pipeline for segmentation of a biological porosity network, the lacuno-canalicular system in stingray tesseræ

Authors:

Merlind Schotte¹, Júlia Chaumel², Mason N. Dean², Daniel Baum^{1*}

¹ *Visual Data Analysis Department, Zuse Institute Berlin*

² *Department of Biomaterials, Max Planck Institute of Colloids and Interfaces*

*Corresponding author

Publication:

This study was published in the journal *MethodsX* in May 2020, as a method article and, therefore, following a specific paper structure.

Publication details: MethodsX, Volume 7, May 2020, 100905

<https://doi.org/10.1016/j.mex.2020.100905>

Publication link:

<https://www.sciencedirect.com/science/article/pii/S2215016120301242>

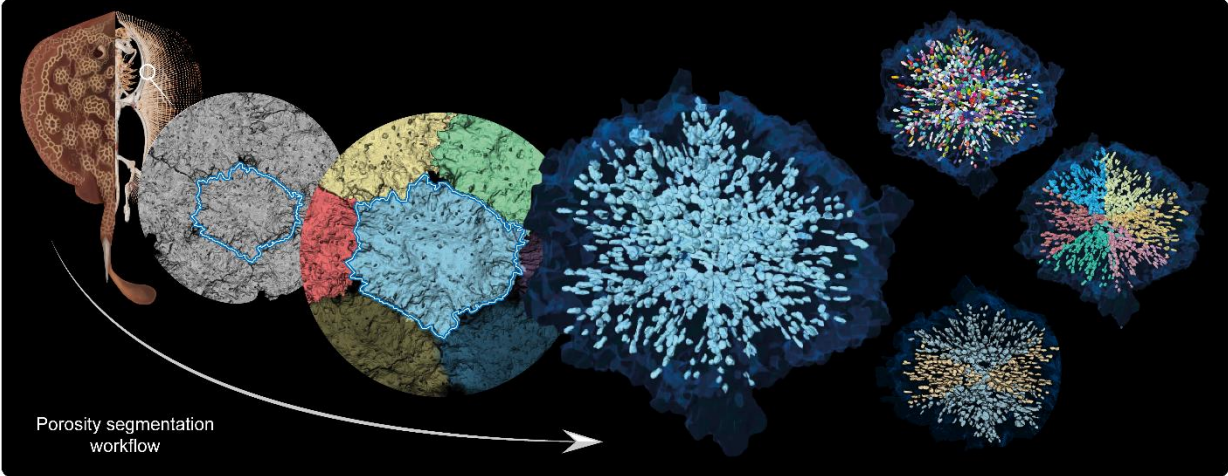
Abstract

A prerequisite for many analysis tasks in modern comparative biology is the segmentation of 3-dimensional (3D) images of the specimens being investigated (e.g. from microCT data). Depending on the specific imaging technique that was used to acquire the images and on the image resolution, different segmentation tools are required. While some standard tools exist that can often be applied for specific subtasks, building whole processing pipelines solely from standard tools is often difficult. Some tasks may even necessitate the implementation of manual interaction tools to achieve a quality that is sufficient for subsequent analysis. In this work, we present a pipeline of segmentation tools that can be used for the semiautomatic segmentation and quantitative analysis of voids in tissue (i.e. internal structural porosity). We use this pipeline to analyze lacuno- canalicular networks in stingray tesserae from 3D images acquired with synchrotron microCT.

- The first step of this pipeline, the segmentation of the tesserae, was performed using standard marker-based watershed segmentation.
- The efficient processing of the next two steps, that is, the segmentation of all lacunae spaces belonging to a specific tessera and the separation of these spaces into individual lacunae required recently developed, novel tools.
- For error correction, we developed an interactive method that allowed us to quickly split lacunae that were accidentally merged, and to merge lacunae that were wrongly split.
- Finally, the tesserae and their corresponding lacunae were subdivided into structural wedges (i.e. specific anatomical regions) using a semi-manual approach.

With this processing pipeline, analysis of a variety of interconnected structural networks (e.g. vascular or lacuno-canalicular networks) can be achieved in a comparatively high-throughput fashion. In our study system, we were able to efficiently segment more than 12,000 lacunae in high-resolution scans of nine tesserae, providing a robust data set for statistical analysis.

Graphical abstract



1. Introduction

Porosity is a characteristic feature of mineralized biological tissues, from the skeletons of corals, sponges and radiolaria to the bone and dentin of vertebrates [1–5] (Fig. 1). These diverse tissues are perforated by canals and cavities of a huge range of size scales, from ostia, medullary cavities and foramina visible to the naked eye down to micron-scale tubules and passages and interstitial nanoscale porosities within the collagen-apatite matrix of teeth and bones. Passages or chambers can communicate to the exterior of the tissue or be bounded and entirely internal, can exhibit relatively uniform geometric properties or a range of constrictions and expansions, can be aligned in simple arrays or in complex and interconnected networks. Internal porosity can play mechanical roles (e.g. reducing weight, aiding buoyancy), but also physiological ones, providing pathways for nerves, vasculature and cell connections. The latter explains why 3D porosity organization and pore size-scale distribution is a vital consideration in tissue engineering scaffolding; see e.g. [4].

The characterization of biological porosities can be greatly challenged by their morphology (e.g. the degree of interconnectedness and linking to the exterior). Here, we describe the design and implementation of a processing pipeline allowing extraction and downstream quantification from microCT data of the lacuno-canalicular network (LCN) of tesserae, porous mineralized tiles that cover the cartilage skeletons of sharks and rays [6–9] (Fig. 1(C)). The overarching goal of the pipeline is to efficiently segment multiple tesserae and their corresponding cell lacunae (several hundred per tessera) to carry out statistically-relevant quantitative analyses on a large scale. The tesseral LCN presents several generally-applicable segmentation challenges: (1) the tesserae are in close contact; (2) the LCN communicates to the exterior of the tesserae (i.e. complicating determination of the ends of passages); (3) the LCN exhibits serial constrictions (canaliculi) and expansions (cell lacunae) that we wished to analyze separately from one another.

The pipeline was developed for a companion study [6], which aimed to characterize the shapes, orientations, and spatial organization of the cell lacunae in tesserae (gaps where cells reside). To achieve this goal, individual cell lacunae had to be separated from one another with high fidelity, requiring us to solve several smaller segmentation problems. First, we had to segment out individual tesserae from the image data. Second, for each tessera, the entire LCN (i.e. all cell lacunae and canaliculi) had to be extracted, from which subsequently the individual cell

lacunae needed to be separated. Finally, in order to allow study of the spatial arrangement and orientation of the cell lacunae with regard to their position in the skeleton (e.g. in association with neighboring tesserae), the cell lacunae needed to be divided into regions called ‘wedges’ [6]. Apart from the last step, these segmentation tasks can be grouped into three broad categories: (1) intensity value-based segmentation; (2) distance-based object separation; (3) cavity segmentation. Some tools that fall into these three categories are reviewed in the following paragraphs.

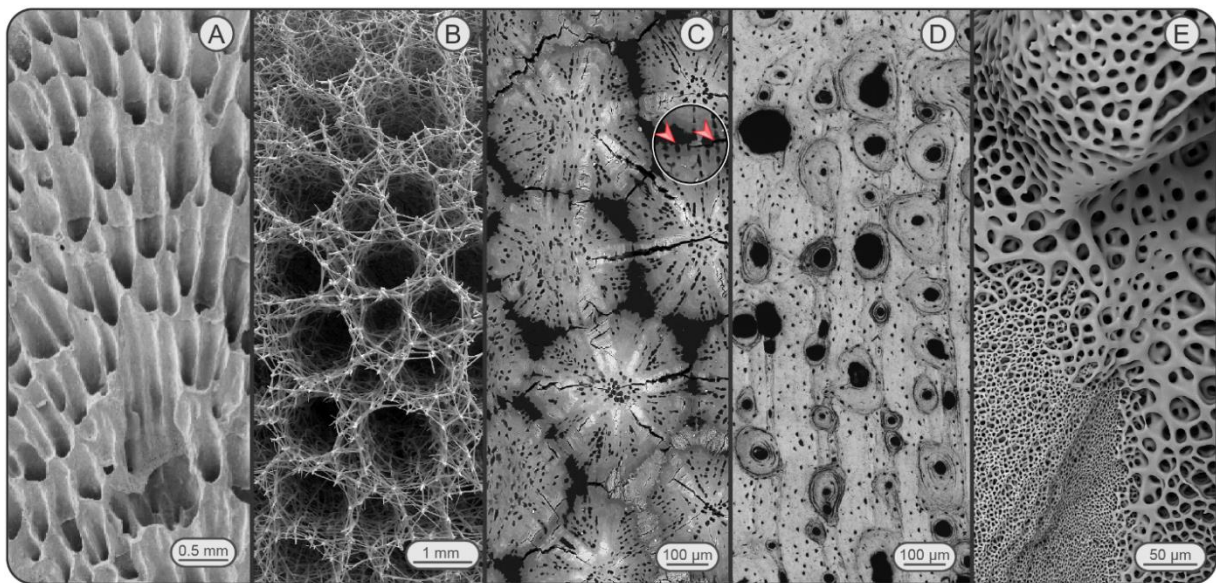


Fig. 1. Porosity in mineralized biological tissues. (A) Sectioned (internal) view of a blue coral skeleton (*Heliopora coerulea*; Helioporacea). (B) Skeletal growth front of a reef-forming glass sponge (*Aphrocallistes vastus*; Hexactinellida). (C) A section through several tesserae from the skeleton of a stingray (*Urobatis halleri*; Chondrichthyes), the study model in the current and companion work [6]. The black gaps between tesserae are unmineralized joints, the small black dots within tesserae are cell lacunae. Note the large sample preparation cracks and the several instances of cell lacunae communicating to the exterior of tesserae (e.g. red arrows) –both situations would pose challenges to traditional segmentation protocols. (D) Osteonal bone from a dog femur (*Canis familiaris*; Carnivora). The larger cavities are vascular channels, the smaller ones peppering the matrix are cell lacunae. (E) The surface of an ossicle from a brittle star (*Ophiopteris papillosa*; Ophiuroidea). Note the large range of sizes and morphologies for porosities, both within and among images. All images are SEM ((C), and (D) from backscatter SEM). (A), (B), and (E) courtesy of James Weaver, (D) courtesy of Ron Shahar.

An important standard tool for intensity value-based segmentation is the watershed algorithm [10]. The basic watershed algorithm starts from local minima and floods the whole image, separating it into as many regions as there are local minima. Segmentation using this method usually results in what is called over-segmentation, because it separates the image in too many regions or segments (i.e. more than the actual number of objects of interest). A typical reason for over-segmentation is noise in the scan data, which can result in many local minima. Such local minima, however, can also be due to small substructural components of the material to be segmented. The hierarchical watershed algorithm [11] was developed to overcome such over-segmentations. It allows merging of neighboring regions according to several criteria. Hierarchical watershed is also similar to the contour-tree segmentation [12] with the major difference being that the latter starts from local maxima instead of local minima as the watershed does. If the number of objects to be segmented in an image is rather small, the marker-based watershed algorithm represents an efficient alternative since it allows the user to specify regions by manually setting a few seeds (starting points). In our processing pipeline, we apply marker-based watershed to segment out the individual tesserae (Section "*Segmentation of cell lacunae*" below).

When objects cannot be separated from one another by considering image intensities alone and are connected by extensions that are substantially narrower than the objects to be separated, distance-based object separation can be applied. The first step is usually to create a binary segmentation containing all objects of interest in the foreground. Then, a *distance transform* [13] is computed on the foreground resulting in an intensity image that can be segmented using the watershed or contour-tree segmentation algorithm. The standard distance transform is the *Euclidean distance transform* [14] that computes for each foreground voxel the shortest distance to any background voxel. One deficiency of this distance transform is its susceptibility to background noise. An alternative distance transform is the more recently developed *random-walk distance transform* [15] that computes for each foreground voxel the average length of all random walks starting at this foreground voxel and ending in any background voxel. This distance transform is much less prone to background noise and, hence, often results in superior segmentations when used in combination with watershed or contour-tree segmentation. In our processing pipeline, we apply the random-walk distance transform together with contour-tree segmentation to separate the individual cell lacunae from one another (Section "*Segmentation of cell lacunae*" below).

Another problem that often arises in image analysis of porosities is the determination of the border of a cavity space of interest to allow its separation from the 'real' background space (i.e. regions external to the scanned object). This problem occurs if the cavity space of an object is connected to the outside of the object, as in the tesserae LCN, where cell network passages connect to the exterior of tesserae [6, 9] (Fig. 1(C)). To solve this problem, the *ambient occlusion algorithm* [16] was developed that computes an intensity field that assigns the degree of occlusion from 'simulated' ambient light to each voxel. In our processing pipeline, we apply this algorithm to separate the tessera cell lacunae space from the background space outside of the tesserae.

2. Specimen preparation and SR- μ CT scanning

Detailed descriptions of sample preparation and scanning protocols are provided in [6]; we provide abridged versions here. Samples of the propterygium (a long, rod-like portion of the skeleton, supporting the wing) were dissected from two adult Haller's round rays (*Urobatis halleri*)—a 19 cm disk width (DW) female and a 21.4 cm DW male. *Urobatis halleri* is an established study system for tessellated cartilage biology, with the majority of recent high-resolution, ultrastructural data coming from this species (e.g. [7, 9, 17–19]). Long strips of tessellated cartilage were excised from skeletal samples, air-dried and affixed upright in micro-centrifuge tubes for subsequent synchrotron experiments.

Tesserae samples were scanned in synchrotron radiation micro-computed tomography (SR- μ CT) at the BAMline, BESSY II synchrotron source, Helmholtz-Zentrum Berlin für Materialien und Energien (HZB) and reconstructed, as described in [6]. The resulting data sets contained several tesserae in close contact, with effective pixel sizes of 876 nm (Fig. 2).

3. Processing pipeline

Here, we describe the processing steps performed to segment tesserae and their cell lacunae, as well as the separation of the tesserae and their cell lacunae into structural wedges (i.e. specific anatomical regions). These steps are the prerequisite to the lacuna morphometric analysis described in the Methods in [6]. All image and geometry processing described in this section was carried out in the visualization software Amira (AmiraZIBEdition 2019.12) [20]. The

Amira modules used for data processing and analysis are detailed below. Whereas most are available in the commercial version of the software, for some steps, we implemented custom Amira modules. These can be obtained upon request from the corresponding author.

The processing pipeline consists of three major steps: (1) the segmentation of all individual tesserae in each data set; (2) the segmentation of individual cell lacunae; and (3) the grouping of cell lacunae according to the tessera wedges. These three steps are described in detail below.

3.1. Segmentation of tesserae

For the segmentation of the input data set (Fig. 2 (A)) into individual tesserae (Fig. 2 (C)), a marker-based watershed transformation was used [10]. This technique involves the manual placement of initial markers in distinct regions (e.g. individual tesserae, joint spaces; Fig. 2 (B)) to act as seeds from which segmentation will begin. This was performed using Amira's segmentation editor, the software's primary segmentation tool. The watershed algorithm expands outward from the markers until the entire data set is segmented, with any remaining regions between tesserae belonging to the background (label/material value = 0) (Fig. 2 (C)). In addition to the markers, we used an 'edge image' generated from the original intensity field. This is a very common approach and serves to guide the algorithm's detection of material boundaries. In the current study, the edge image was generated by using the Watershed tool of Amira's segmentation editor. Edges appear in places with a rapid change of intensity values. As a result, the strength of an edge indicates the likelihood of a material boundary.

From the watershed segmentation result (Fig. 2 (D)), tesserae were extractable as separate data sets, facilitating the downstream segmentation of cell lacunae within individual tesserae. Each label of the watershed segmentation result, however, represented a segmented tessera including all of its internal spaces (i.e. cell lacunae were not yet isolated from the tessera label field) (Fig. 2 (C) and (D)). Furthermore, it is important to note that the lacuno-canalicular passages within tesserae often communicate to the outside (i.e. into the intertesseral joint space; [7]) (some of such cell lacunae are visible in Fig. 3 (B) and (C)). As a result, the borders of this watershed segmentation result did not yet enclose all cell lacunae 'belonging' to a given tessera, but rather partially lacked those lacuno-canalicular passages open to the background, thus requiring additional steps described below.

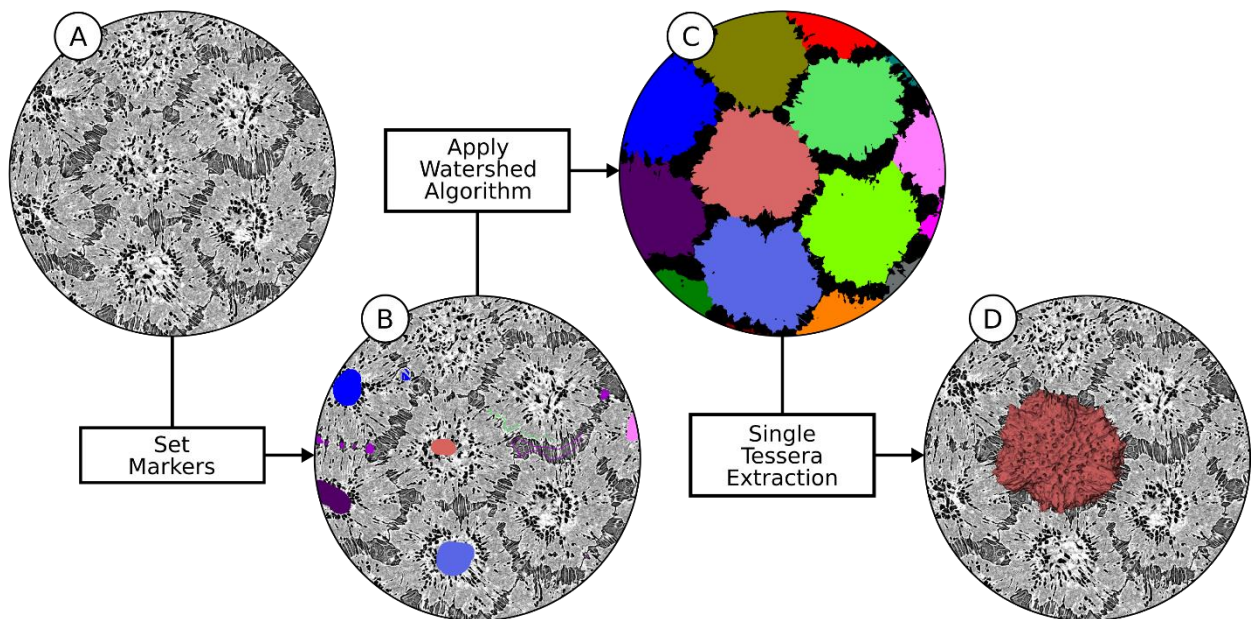


Fig. 2. Pipeline for tesserae segmentation. (A) Input μ CT slice, (B) seed markers, (C) separated tesserae after applying the watershed algorithm, (D) volume rendering of a single tessera. Tesserae shown in (A), (B) and (D) are mineralized and therefore exhibit higher (lighter) intensity values; the joints between tesserae and the cell lacunae inside tesserae are darker.

3.2. Segmentation of cell lacunae

The segmentation of the tesseral LCN and its subsequent division into individual cell lacunae required several steps that are explained in detail below.

3.2.1. Separation of cell lacunae from background

To extract the cell lacunae within a tessera, all voxels representing background unmineralized tissue (i.e. voxels with lower gray values) were first segmented in the original data set using a local threshold, and then stored as a separate label field (Fig. 3 (A)). Subsequently, this background label field was subtracted from each tessera's label field, resulting in a label field with the tessera (mineralized material) as foreground and the tessera's internal spaces (including its cell lacunae) and the area external to the tessera as background (Fig. 3 (B)).

3.2.2. Ambient occlusion field

As stated above, it is challenging to define all cell lacunae (i.e. background voxels) that 'belong' to a tessera, due in particular to those regions where the tessera lacuno-canalicular network is open to the outside [7]. This problem is akin to that of defining the inside/outside borders of

structures with irregular openings (e.g. caves). To avoid 'losing' cell lacunae to the surrounding background, an ambient occlusion scalar field was calculated from the previous result. In this algorithm [16], rays are cast from each background voxel through the label field in all directions. The ratio of the number of rays striking the foreground (i.e. the tessera) to the total number of rays defines the ambient occlusion value (Fig. 3 (C)). In this way, the algorithm allows the identification of background voxels surrounded by foreground voxels (e.g. cell lacunae surrounded by mineralized tissue, but open at one end to the background). By applying a threshold to the resultant ambient occlusion field that accounts for all cell lacunae (i.e. background voxels) belonging to the tessera, a binary cell lacunae label field is generated (Fig. 3 (D)).

3.2.3. Connected components

To divide the single label produced in the previous step containing all lacunae into multiple, individual lacuna labels, the connected components algorithm was applied. This algorithm searches for regions of contiguous voxels in the binary label field, defining each as an individual object (i.e. assigning each to a new label ID). At this point, any isolated cell lacunae (i.e. those not linked to other cell lacunae) were identified as individual objects. However, any multi-lacunae objects (i.e. cell lacunae connected by canaliculi) still required disarticulation (Fig. 3 (E)).

3.2.4. Contour-tree segmentation

The contour-tree segmentation [12] was used for the remaining separation of connected cell lacunae. This algorithm used the random-walk distance transform [15] that, for each voxel of the result of the previous step, calculated the average length of all random walks from this voxel to the background (Fig. 3 (F)). The *Random-Walk Distance Transform* is implemented as a custom Amira module. It takes as input the binary label field of all cell lacunae and outputs a scalar field containing the random-walk distance to the background from each voxel of the cell lacunae. The module does not require any parameter. The *Contour-Tree Segmentation* module takes as input the random-walk distance field and a single parameter, the persistence value, that defines the degree of merging. The contour- tree segmentation using the random-walk distance field takes advantage of the 'string-of-pearls' appearance of objects comprised of multiple cell lacunae connected by canaliculi (i.e. spheroidal objects connected by narrow,

short links; [6, 9]), splitting the multi-lacunae labels at their narrowest points (i.e. their canaliculi). The result is shown in Fig. 3 (G).

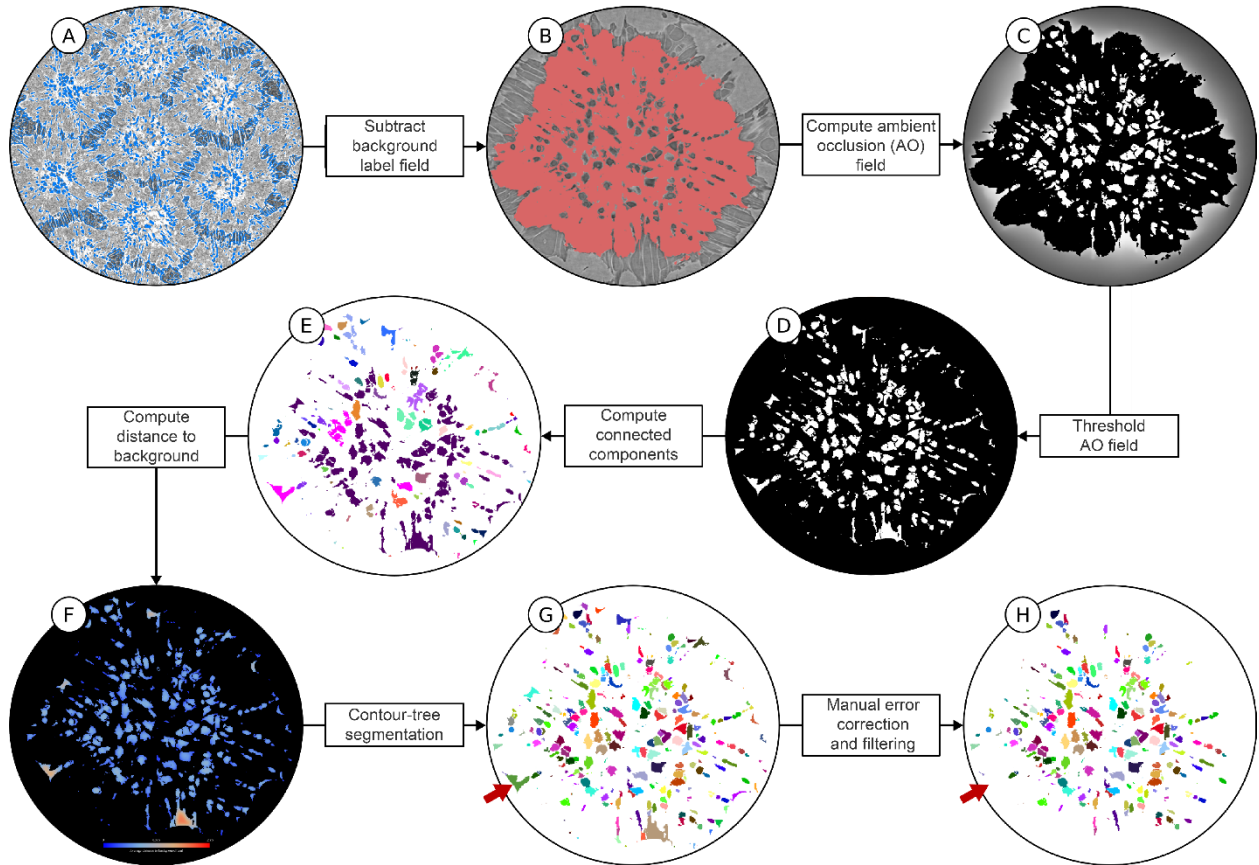


Fig. 3. Segmentation pipeline for cell lacunae. (A) Intratesseral (cell lacunae) and intertesseral space (regions outlined in blue), computed using local thresholding (note, the region is zoomed out relative to images (B)-(H) to show multiple tesserae), (B) single tessera, excluding its cell lacunae, generated by subtracting the label field of (A) from the tessera label generated in the previous tessera segmentation step (see Fig. 2), (C) ambient occlusion (AO) field, (D) binary label field of AO, generated from AO field in (C), (E) separation of disconnected cell lacunae, (F) average length field, (G) contour-tree segmentation, (H) removal of objects incorrectly interpreted as cell lacunae.

3.2.5. Manual error correction and filtering

As a final step, the label field was cleaned and refined by removing objects that had been wrongly interpreted as cell lacunae in the segmentation (Fig. 3 (H)). First, objects with volumes $<70 \mu\text{m}^3$ (far smaller than that of cell lacunae; [6]) were considered as noise and deleted. This was performed in Amira using the *Label Analysis* module followed by application of the *Filter Analysis* module. Additionally, objects considerably larger than cell lacunae were manually removed after being verified as errors by comparison with the raw grayscale data. These were also readily distinguishable from actual cell lacunae by their morphologies, typically being either crack artifacts in the sample or invaginations in the joint face at the tesseral edge (e.g. as indicated by the red arrow in Fig. 3 (G) and (H)). We applied a custom Amira module that allowed us to select and remove such objects by directly picking the labels either on an *Orthoslice* or the *Voxelized Volume Rendering* visualization. Alternatively, a somewhat slower combination of *Arithmetic* module and *Quick Probe* tool could be utilized. Following this, any remaining passages (canaliculi) connecting cell lacunae were removed (i.e. isolating individual cell lacunae). This was achieved using another custom Amira module that allowed one to specify a single label and the number of cell lacunae into which the label should be split. The module again exploited distance-based object separation using the random-walk distance transform and the contour-tree segmentation. First, the random-walk distance transform was computed on the single specified label. Subsequently, the contour-tree segmentation was run and an adequate persistence value was automatically identified that separated the label into the desired number of cell lacunae.

3.3. Subdivision of tesserae cell lacunae into wedge data sets

Previous work on tesserae ultrastructure has demonstrated the presence of large, linear arrays of collagen fibers linking adjacent tesserae, with cell lacunae following the predominant fiber orientation (e.g. [7, 9, 17, 19], Fig. 2(A)). In polarized light microscopy, these fiber arrays appear to converge on the center of tesserae [7, 21–23]. As a result, we hypothesized that cell lacunae orientation is influenced by neighboring tesserae, particularly the further cell lacunae are from the center of their host tessera [6]. In order to investigate this theory—specifically, whether cell lacunae are oriented in a direction perpendicular to the joint face with the nearest neighboring tessera—the cell lacunae label field resulting from the segmentation workflow

(e.g. Fig. 3 (H)) was further subdivided into ‘wedges’ (Fig. 4). These wedges are triangular regions, with their vertices at the tessera center and their bases at the tessera edge (see [6]).

To subdivide the segmented cell lacunae into individual wedges, a semiautomatic custom Amira module, *Tesserae Wedges* , was developed. As input, this module requires the binary label field of a single tessera and its corresponding cell lacunae label field. The center of that label field and its associated local coordinate system can either be computed directly from the module or can be given as optional input. The center of the tessera was calculated from the tessera label field by averaging the position of all voxels belonging to the tessera. The local tessera coordinate system was calculated from the tessera label field via principal component analysis (PCA). From the center point and the first and second principal axes of the PCA, the module created sectioning planes (Fig. 4). The number of planes was set in order to divide each tessera into as many wedges as the tessera had neighbors (e.g. the tessera in Fig. 4 has six neighbors and is divided by six planes); the anatomical justification for this choice is explained in [6]. Wedge sectioning planes could be manually rotated; the sectioning planes were positioned to pass through the tesserae triple junctions—the intersection points of three neighboring tesserae (Fig. 4 (A))—thereby defining the zones of interaction between a tessera of interest and its neighbors. Once the sectioning planes were set, the cell lacunae label field was divided into wedges accordingly (Fig. 4 (B)). For those cell lacunae bisected by a sectioning plane, their wedge assignment was decided by the position of the lacuna center of mass. Lastly, in order to facilitate the wedge-wise analysis of cell lacunae, all cell lacunae in each wedge were extracted into separate data sets (Fig. 4 (D)). Following this step, the coordinate axes for each wedge were calculated and cell lacunae morphology and orientation quantified, as described in the Methods in [6]. Calculation of the cell lacunae morphometric variables was accomplished with a custom analysis module, combining both common Amira analysis variables and additional variables specific to our research questions; see Methods and Table 1 in [6] for more details.

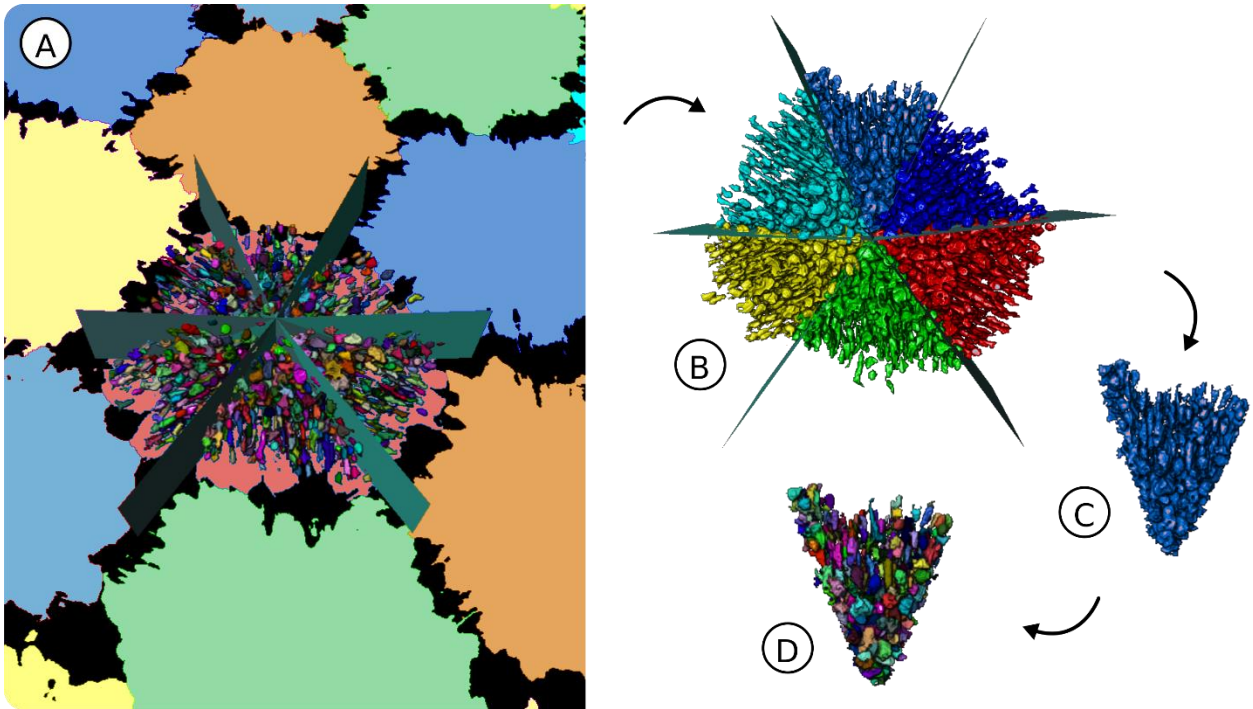


Fig. 4. Subdivision of the lacuna label field. (A) A single tessera and its neighbors, with the focal tessera's segmented cell lacunae subdivided into wedges by planes, (B) division of the entire lacunar data set and assignment into wedges, (C) extraction of one wedge, (D) generation of new (i.e. wedge-specific) lacuna IDs.

4. Conclusions

We have presented an effective segmentation pipeline that makes use of standard segmentation methods like the watershed algorithm, but also uses more advanced, newly developed tools like the ambient occlusion algorithm and the random-walk distance transform. Marker-based watershed segmentation, which we used for the segmentation of the tesserae, is a very powerful tool when the segmentation of a small to medium number of objects is required. For very large numbers of objects (e.g. in the hundreds to thousands), however, the hierarchical watershed algorithm or its kin, the contour-tree segmentation, should be used. We exploited the contour-tree segmentation for the separation of the cell lacunae, which we applied to the result of the random-walk distance transform of the binary cell lacunae segmentation. This new distance transform resulted in a much better initial segmentation compared to using the more traditional Euclidean distance transform, leading to fewer segmentation errors and, thus, drastically reducing the manual work required for error correction. Instead of developing a fully automated segmentation workflow, we favored some degree of manual user control over a completely automated solution that would have required substantially more time for implementation. For example, we used an interactive approach to correct falsely split cell lacunae, rather than spending significant time refining the automated segmentation. Furthermore, instead of implementing a fully automated approach for the subdivision of tesserae into wedges, we used a semiautomatic approach in which the planes separating wedges were manually determined by the user. We believe that such combinations of automated and interactive segmentation methods produce efficient and reliable results for many analysis problems. These considerations are relevant to the segmentation of many complex biological structures, and so are particularly important for investigations of biological porosity and network structure, which rely increasingly on high-throughput analyses of large data sets (e.g. synchrotron microCT and FIB-SEM tomography volumes; see e.g. [5 , 15]).

References

- [1] J.D. Currey, Collagen and the mechanical properties of bone and calcified cartilage, *Collagen: Struct. Mech.* (2008).
- [2] J.D. Currey, R. Shahar, Cavities in the compact bone in tetrapods and fish and their effect on mechanical properties, *J. Struct. Biol.* 183 (2013) 107–122.
- [3] H.A. Lowenstam, S. Weiner, *On Biomineralization*, Oxford University Press, 1989.
- [4] R. Penta, L. Miller, A. Grillo, A. Ramírez-Torres, P. Mascheroni, R. Rodríguez-Ramos, Porosity and diffusion in biological tissues. Recent advances and further perspectives, in: J. Merodio, R. Ogden (Eds.), *Constitutive Modelling of Solid Continua*, Springer International Publishing, Cham, 2020, pp. 311–356 .
- [5] R. Weinkamer, P. Kollmannsberger, P. Fratzl, Towards a connectomic description of the osteocyte lacunocanalicular network in bone, *Curr. Osteoporos. Rep.* 17 (2019) 186–194.
- [6] J. Chaumel, M. Schotte, J.J. Bizzarro, P. Zaslansky, P. Fratzl, D. Baum, M.N. Dean, Co-aligned chondrocytes: zonal morphological variation and structured arrangement of cell lacunae in tessellated cartilage, *Bone* 134 (2020) 115264, doi: 10.1016/j.bone.2020.115264 .
- [7] R. Seidel , K. Lyons , M. Blumer , P. Zaslansky , P. Fratzl , J.C. Weaver , M.N. Dean , Ultrastructural and developmental features of the tessellated endoskeleton of elasmobranchs (sharks and rays), *J. Anat.* 229 (2016) 681–702 .
- [8] R. Seidel , A.K. Jayasankar , R. Shahar , M.N. Dean , The multiscale architectures of fish bone and tessellated cartilage and their relation to function, in: Y. Estrin, Y. Bréchet, J. Dunlop, P. Fratzl (Eds.), *Architected Materials in Nature and Engineering*, 2019, pp. 329–353 .
- [9] M.N. Dean , J.J. Socha , B.K. Hall , A.P. Summers , Canalliculi in the tessellated skeleton of cartilaginous fishes, *J. Appl. Ichthyol.* 26 (2010) 263–267.
- [10] S. Beucher, Use of watersheds in contour detection, in: *Proceedings of the International Workshop on Image Processing, CCETT*, 1979.
- [11] S. Beucher, Watershed, hierarchical segmentation and waterfall algorithm, *Comput. Imaging Vis.* (1994) 69–76, doi: 10.1007/ 978- 94- 011- 1040- 2 _ 10.
- [12] H. Carr, J. Snoeyink, U. Axen, Computing contour trees in all dimensions, *Comput. Geom.* 24 (2003) 75–94.
- [13] M.W. Jones, J.A. Baerentzen, M. Sramek, 3D distance fields: A survey of techniques and applications, *IEEE Trans. Vis. Comput. Graph.* 12 (2006) 581–599.
- [14] P.-E. Danielsson, Euclidean distance mapping, *Comput. Graph. Image Process.* 14 (1980) 227–248.
- [15] D. Baum, J.C. Weaver, I. Zlotnikov, D. Knötel, L. Tomholt, M.N. Dean, High-throughput segmentation of tiled biological structures using random walk distance transforms, *Integr. Comp. Biol.* 59 (2019) 1700–1712.

- [16] D. Baum, J. Titschack, Cavity and pore segmentation in 3D images with ambient occlusion, in: Proceedings of the Eurographics/IEEE VGTC Conference on Visualization, 2016, pp. 113–117.
- [17] M.N. Dean, C.G. Mull, S.N. Gorb, A.P. Summers, Ontogeny of the tessellated skeleton: insight from the skeletal growth of the round stingray *Urobatis halleri*, *J. Anat.* 215 (2009) 227–239.
- [18] R. Seidel, A. Roschger, L. Li, Q. Zhang, J. Yin, T. Yang, J.C. Weaver, P. Fratzl, P. Roschger, M.N. Dean, Mechanical properties of stingray tesserae: High-resolution correlative analysis of mineral density and indentation moduli in tessellated cartilage, *Acta Biomater.* 96 (2019) 421–435.
- [19] R. Seidel, M. Blumer, E.-J. Pechriggl, K. Lyons, B.K. Hall, P. Fratzl, J.C. Weaver, M.N. Dean, Calcified cartilage or bone? Collagens in the tessellated endoskeletons of cartilaginous fish (sharks and rays), *J. Struct. Biol.* 200 (2017) 54–71.
- [20] D. Stalling, M. Westerhoff, H.-C. Hege, Amira: A highly interactive system for visual data analysis, *Vis. Handb.* 38 (2005) 749–767.
- [21] J.G. Clement, Re-examination of the fine structure of endoskeletal mineralization in Chondrichthyans: Implications for growth, ageing and calcium Homeostasis, *Aust. J. Mar. Freshw. Res.* 43 (1992) 157–181.
- [22] W. Bargmann, Zur Kenntnis der Knorpelarchitekturen, *Z. Zellforsch. Microsk. Anat. Histochem.* 29 (1939) 405–424.
- [23] W.J. Schmidt, Über die Verkalkung des Knorpelgewebes der Haie, *Z. Zellforsch. Mikrosk. Anat.* 37 (1952) 377–388.

Autofluorescence imaging of stingray skeletal cartilage: hyperspectral imaging as a tool for histological characterization

Authors:

Júlia Chaumel^{1*}, María Marsal², Adrián Gómez-Sánchez³, Michael Blumer⁴, Emilio José Gualda², Anna De Juan³, Pablo Loza-Alvarez², Mason N. Dean¹

¹ *Department of Biomaterials, Max Planck Institute of Colloids and Interfaces*

² *ICFO – Institute of Photonic Sciences, The Barcelona Institute of Sciences and Technology, Castelldefels, Spain*

³ *Department of Analytical Chemistry, University of Barcelona, Barcelona, Spain*

⁴ *Division of Clinical and Functional Anatomy, Medical University of Innsbruck, Innsbruck, Austria*

*Corresponding author

Publication:

This study was accepted for publication in the journal *Discover Materials* in April 2021. Therefore, the publication details were unavailable at the moment of the submission of the doctoral dissertation.

Abstract

Tessellated cartilage is a distinctive composite tissue forming the bulk of the skeleton of cartilaginous fishes (e.g. sharks and rays), built from unmineralized cartilage covered at the surface by a thin layer of mineralized tiles called tesserae. The finescale structure and composition of elasmobranch tessellated cartilage has largely been investigated with electron microscopy, micro-computed tomography and histology, but many aspects of tissue structure and composition remain uncharacterized. In our study, we demonstrate that the tessellated cartilage of a stingray exhibits a strong and diverse autofluorescence, a native property of the tissue which can be harnessed as an effective label-free imaging technique. The autofluorescence signal was excited using a broad range of wavelengths in confocal and light sheet microscopy, comparing several sample preparations (fresh; demineralized and paraffin-embedded; non-demineralized and plastic-embedded) and imaging the tissue at different scales. Autofluorescence varied with sample preparation with the signal in both plastic- and paraffin-embedded samples strong enough to allow visualization of finescale ($\geq 1 \mu\text{m}$) cellular and matrix structures, such as cell nuclei and current and former mineralization fronts, identifiable by globular mineralized tissue. A defined pericellular matrix (PCM) surrounding chondrocytes was also discernible, described here for the first time in elasmobranchs. The presence of a PCM suggests similarities with mammalian cartilage regarding how chondrocytes interact with their environment, where the PCM acts as a transducer for biomechanical and biochemical signals. A posterior analysis of hyperspectral images by an MCR-ALS unmixing algorithm allowed identification of several distinct fluorescence signatures associated to specific regions in the tissue. Some fluorescence signatures identified could be correlated with collagen type II, the most abundant structural molecule of cartilage. Other fluorescence signatures, however, remained unidentified, spotlighting tissue regions that deserve deeper characterization and suggesting the presence of molecules still unidentified in elasmobranch skeletal cartilage. Our results show that autofluorescence can be a powerful exploratory imaging tool for characterizing less-studied skeletal tissues, such as tessellated cartilage. The images obtained are largely comparable with more commonly used techniques, but without the need for complicated sample preparations or external staining reagents standard in histology and electron microscopy (TEM, SEM).

Keywords: tessellated cartilage, autofluorescence, hyperspectral imaging, confocal microscopy, light sheet microscopy

1. Introduction

Cartilage is a viscoelastic and resilient connective tissue essential to the mechanics and growth of the skeleton of vertebrates. Its gel-like extracellular matrix is composed of water and contains embedded cells (chondrocytes) interspersed within a network of mainly collagen type II fibers and proteoglycans [1, 2]. Variation in the organization, proportion, and composition of extracellular matrix components is reflected in the structural morphology of the tissue, affecting its mechanical properties and its physiological functions [3, 4]. Examinations of cartilage tissue morphology, therefore, have provided great insights into the biomechanics, function and growth of cartilage. Most of this research has focused on mammals, where cartilage (as in most vertebrates) forms the greater part of the embryonic skeleton, providing a tissue scaffold that guides the growth of and eventually gives way to bone [1]. Cartilage is far less predominant in the adult skeleton of most vertebrates, but still performs diverse roles including load-bearing (intervertebral fibrocartilage); shaping of resilient structures like noses, ears and ribs (elastic cartilage); and reduction of frictional forces between bones (articular hyaline cartilage).

Cartilage is, also, far more diverse and ancient than typically appreciated. It is present even in invertebrate taxa [5, 6] and forms an extremely large proportion of the adult skeleton of several fish groups, particularly the clade of sharks and rays (elasmobranch fishes) [7] (Fig. 1). However, the range of functional roles that cartilage plays in the skeletons of these fishes is still unknown. The tissue composition and the cell type of elasmobranch cartilage appear to be similar to the hyaline cartilage in mammalian joints [8–10, 11 and references therein]. However, elasmobranch cartilage performs many functions more akin to those of bone than mammalian hyaline cartilage: providing skeletal shape, body support, and locations for muscle attachment. This multi-functionality is believed to be due to a unique structural feature of elasmobranch cartilage, wherein the skeleton mineralizes only at the surface, forming an ensheathing layer of mineralized tiles called tesserae (Fig. 1B - E).

The mechanical performance of tessellated cartilage is thought to be related largely to the structure and arrangement of its different tissue components, in particular the associations of soft (unmineralized) and hard (mineralized) materials [12–15]. However, the difficulties associated with characterizing the complex structural arrangements of these heterogeneous tissues has limited the definition of clear composition-form-function rules for tessellates

cartilage. In particular, the close association of mineralized and unmineralized tissues, in complex structural arrangements at both large and fine scales, has challenged common visualization techniques, such as conventional microscopy, immuno-histological stainings and electron microscopy [8, 16]. For example, the mineralized matrix of tesserae is perforated by numerous small cavities called lacunae, containing living chondrocytes surrounded by a thin layer of unmineralized matrix, with adjacent lacunae linked by short, matrix-filled passages [17, 18] (Fig.1C - E). This arrangement results in several tissue type transitions over small spatial scales (1-10 μm), also challenging proper fixation and sectioning of these regions. The lateral margins of tesserae also present a heterogeneous mixture of tissues, associated with the joint region between neighbouring tesserae, which comprises a complex combination of unmineralized matrix, fibers and cells [8] (Fig.1E). Additionally, the high water content of the unmineralized cartilage, contrasted with the extremely low water content (high mineral content) of some regions in tesserae (e.g. the hypermineralized 'spokes' reinforcing contact zones; [19]) makes tessellated cartilage prone to differential swelling and cracking during standard fixation and dehydration protocols [12]. Lastly, the scarcity of antibodies and protocols optimized for tissue components (e.g. cell processes, collagen types) in non-model organisms makes the characterization of tessellated cartilage tissue components both time-consuming and costly [20].

Label-free imaging—in other words, not using exogenous fluorophores—has recently proved successful in the study of cartilage composition and structure, using both confocal (linear excitation) and multiphoton (non-linear excitation) microscopy. In label-free imaging, image contrast is provided by the tissue's autofluorescence (AF): the excitation of intrinsic endogenous fluorescent molecules (e.g. coenzymes and amino acids, among others) rather than by the addition of external labeling or contrast agents (e.g. fluorescent or non-fluorescent dyes). These molecules contain aromatic rings with π -bonds, with electrons that react to specific illumination wavelengths, passing to an excited state before decaying to the ground state and emitting energy, including the autofluorescent emission [21]. As tissue AF can be diagnostic for particular tissue components, AF imaging has been demonstrated to be a powerful resource especially in mammalian systems, for evaluating biological substrate structure and composition, from cells to entire organisms, and can provide diagnostic information in a minimally invasive approach (reviewed by [22]). Nonlinear optical microscopy (NLOM) techniques have been particularly successful in the minimally-invasive examination of

cartilage, using only endogenous fluorophores (e.g. flavoproteins, NAD(H)P, collagens and elastin) to characterize the organization and orientation of components within the tissue [23, 24]. NLOM approaches also allow excitation of multiple endogenous fluorophores with a single laser line. By comparison, linear excitation techniques have been less used to study cartilage, although they offer broader excitation and emission spectra than NLOM.

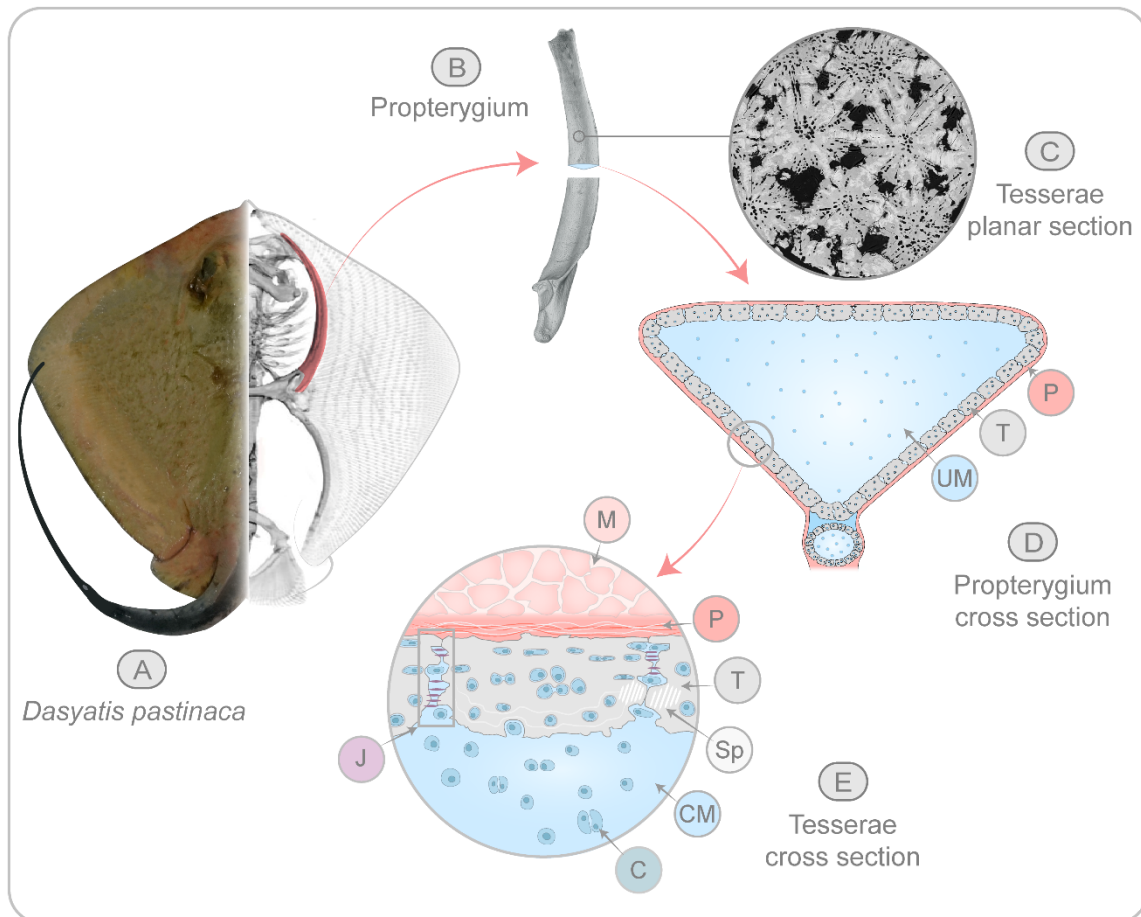


Fig. 1. Tesselated skeleton of sharks and rays (elasmobranchs). **A)** Image of the common stingray *Dasyatis pastinaca* (left) and a microCT scan image of the skeleton (right), with the propterygium highlighted in red. **B)** MicroCT scan of bisected propterygium, showing the inner cartilaginous core (blue) surrounded by the tessellated layer (gray). **C)** Backscatter Scanning Electron Microscopy (BSEM) image of a planar section through multiple tesserae, showing spokes (white streaks) and lacunae (black spaces) within tesserae. **D)** Schema of the propterygium cross section from (B), showing also the outermost perichondrium layer (red). **E)** Schema of zoomed region in (D), showing tesserae in vertical section, sandwiched between the perichondrial layer and the cartilaginous matrix. The single tessera in the center is connected to neighboring tesserae by a joint region (marked with a rectangle). Cells are located within tesserae, the cartilaginous matrix and joint regions. **Abbreviations:** Chondrocytes (C), Cartilaginous matrix (CM), Joint (J), Muscle (M), Perichondrium (P), Spokes (Sp), Tesserae (T)

In this study, we explore the efficacy of linear, one-photon excitation methods in the imaging of tessellated cartilage, examining also whether these effects are altered by standard sample preparation techniques. AF imaging techniques have never been applied as a tool to study this tissue, however there is some evidence that particular regions of tesserae exhibit a characteristic AF [11]. Previous studies have shown that tesserae have distinct and consistent structural features and, thus, can be considered as a useful and repeatable unit of study, particularly since every skeletal cross-section contains multiple sectioned tesserae for examination [18, 25]. Additionally, since tesserae have been shown to grow by accreting mineralized material on all their edges and do not appear to remodel their tissue at all, every tessera contains a permanent structural record of its growth [25–27]. Therefore, using common imaging techniques (e.g. histology, electron microscopy and microCT) and recent ultrastructural characterizations of tesserae as reference, we demonstrate that specific tissue components have consistent and characteristic AF signals, using confocal laser scanning microscopy of thin sections and light sheet microscopy of larger sample blocks providing a more macroscopic perspective. In the process, we explore the potential of AF imaging for ultrastructural examination of elasmobranch skeletal tissue, especially to clarify aspects of fibrous tissue architecture.

2. Materials and Methods

2.1. Specimens and sample preparation

Skeletal samples were collected in May 2019 from two common stingrays (*Dasyatis pastinaca*: Dasyatidae, Batoidea), a male of 21.3 cm disc width (DW) and a female of 32.7 cm DW. Specimens were by-catch captures from trammel net fishery in Alicante and Valencia (Valencian Community, Spain), respectively. Samples were harvested from both specimens less than one hour after death.

We compared tissue autofluorescence (see below) for three sample preparation types that have been used previously in the study of tessellated cartilage (Fig. 2A): (1) “thawed samples”: non-fixed, non-demineralized and non-embedded; (2) “paraffin samples”: fixed, demineralized and paraffin-embedded; and (3) “PMMA samples”: fixed, non-demineralized and embedded in plastic (PMMA). For the thawed samples, the whole head of the second specimen was frozen and sent to the Institute of Photonic Sciences’ facilities (Castelldefels, Spain), where all imaging was performed. Immediately prior to imaging, the head was partially thawed in cool water and a scalpel was used to remove thin slices (~0.5-1.0 mm) of the propterygium (largest skeletal piece supporting the wing). Slices were mounted for confocal imaging on a glass bottom MatTek dish in solidified 1%, low-melting agarose, to maintain position and reduce dehydration.

Samples for paraffin and PMMA were obtained from the first animal specimen. The propterygium was cut in small pieces and fixed with 4% PFA in PBS 0.1 M at the harbor and within 20 minutes of the animal's death to avoid tissue degradation. Samples were kept in the fixative at 4°C overnight and stored in PBS 0.1 M at 4°C before processing for paraffin embedding, PMMA embedding or clearing for SPIM imaging (see next section).

For paraffin embedding, fixed samples were rinsed in PBS, decalcified with ethylenediaminetetraacetic acid (EDTA) at 20 wt-% concentration with pH 7.4 for one week, dehydrated with a graded isopropanol and xylene series, and embedded in paraffin using a routine histological infiltration processor (Miles Scientific Inc., Naperville, IL, USA). Serial vertical sections of 15 µm were made on a HM 355 S microtome (Microm, Walldorf, Germany), and mounted on SuperFrost®Plus slides.

For PMMA (Polymethylmethacrylate) embedding, fixed samples were dehydrated through increasing ethanol concentration (70%, 80%, 96%, 100%), then maintained in xylol for 3 hours, and finally embedded in PMMA (Morphisto Technovit® 9100) using the reagents and protocol provided by the manufacturer. All embedding steps were performed at 4°C. Once the embedding media was polymerized, samples were microtomed in 10 µm slices, deplastified using 2-methoxyethyl acetate, and mounted on DakoFlex® slides.

To compare AF images with those obtained using more traditional methods and to facilitate location of structures of interest, tessellated cartilage samples were also examined using histology and Backscatter Electron Microscopy (BSEM). The sample preparation protocols for each technique can be found in Section 1 of Supplementary Materials.

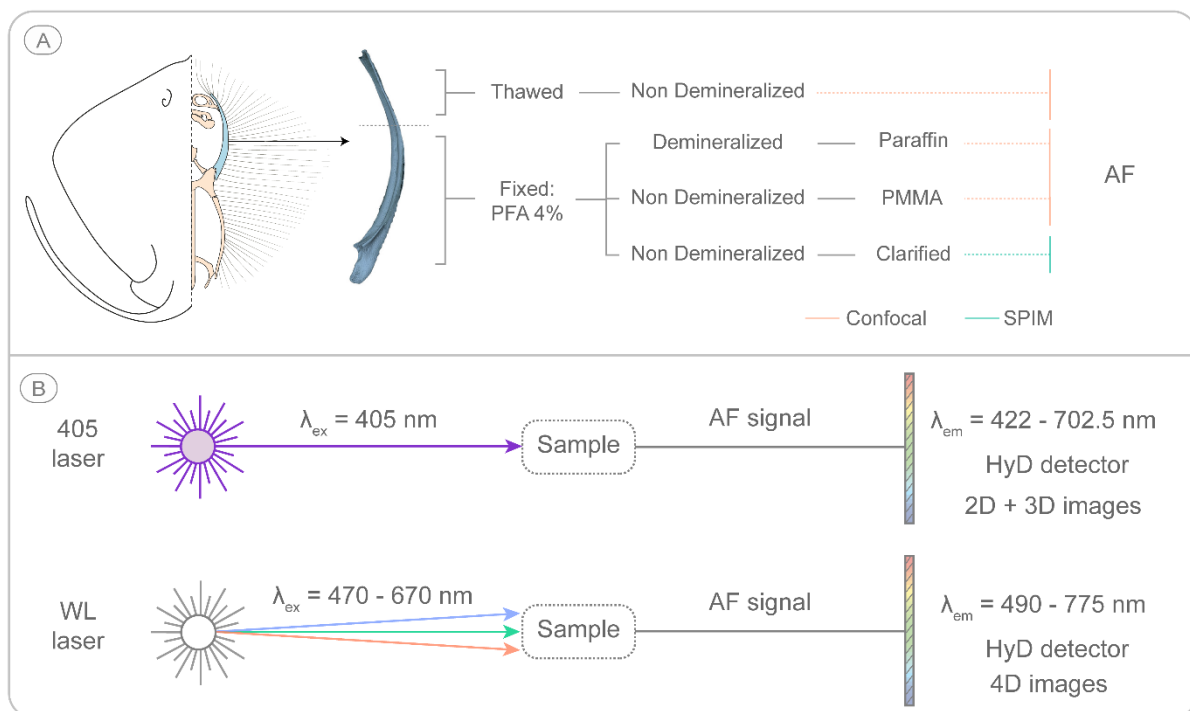


Fig. 2. Scheme of the experimental design. **A)** Different sample preparation methods and microscopes used for their analysis. **B)** Lasers used in the confocal microscope AF analysis. Samples were excited with a 405 nm laser (UV) and White Wavelength Laser (WLL: 470-670 nm, in 10 nm excitation steps). The AF emitted by the samples was collected by detectors with different spectral ranges (listed on the far right), depending on the laser used. 2D and 3D images were generated with the 405 nm laser, whereas 4D images were generated with the WLL (see text for explanation of image types). **Abbreviations:** AF = Autofluorescence signal

2.2. Confocal imaging of thawed, paraffin and PMMA samples

Cartilage samples from all three preparation types described above were examined using a Leica TCS SP8 STED 3x (Leica, Mannheim, Germany) Laser Scanning Confocal Microscope (LSCM) with an HC PL APO CS2 63x/1.40 oil objective. Samples were excited using two lasers and imaged in a wide spectral range that allowed a broad spectral analysis of autofluorescence signal (Fig. 2B). Three types of images (4D, 3D and 2D images) were generated in each imaged region of interest, as described below.

To generate 4D images, samples were excited with the supercontinuum White Light Laser (WLL) in $xy\lambda\lambda$ (lambda-lambda scan) acquisition mode in a range of $\lambda_{ex} = 470$ to 670 nm in 21 excitation steps with 10 nm sampling interval (400Hz scan speed, frame and line accumulations = 1). At each step, fluorescence spectra were collected using a HYD SMD detector in a range of $\lambda_{em} = 490$ to 775 nm in 20 emission steps with a 14.25 nm sampling interval. In this way, we obtained a fluorescence emission hyperspectral image for every excitation step, resulting in a 4D *excitation-emission fluorescence hyperspectral image (EE-HSI)* with two spatial dimensions (x- and y- pixel coordinates) and two spectral dimensions (excitation and emission), where each pixel was associated with a 2D excitation-emission fluorescence landscape (i.e. quantifying the relationship between excitation and emission wavelengths over a broad spectral range) (Supp. Fig. 1B).

Additionally, to generate 3D images, samples were excited with a 405 nm laser in $xy\lambda$ (lambda scan) acquisition mode, with fluorescence spectra collected using a HYD SMD detector in a range of $\lambda_{em} = 422.5$ to 702.5 nm with a 14.74 nm sampling interval (400Hz scan speed, frame and line accumulations = 1). Resulting 3D images had two spatial dimensions (x- and y- pixel coordinates) and one spectral (λ) dimension, with each pixel associated with an emission fluorescence spectrum (i.e. quantifying the autofluorescence produced by the 405 nm laser) (Supp. Fig. 1A).

Lastly, we acquired two types of 2D images as reference images. Firstly, an individual, high-resolution optical image (pixel size = 171 nm) of each region of interest (see below) was acquired using the excitation wavelength found experimentally to produce the strongest AF (405 nm laser with 200Hz scan speed, two frame and line average, 20% intensity) and a wide detector range ($\lambda_{em} = 459$ to 602 nm, with the HYD SMD detector). The resultant image was two-dimensional, with x- and y-pixel coordinates and an integrated global AF value assigned to

each pixel. In order to prevent loss of signal by bleaching and longer dwell-times, analyses were always performed in the following order: WLL lambda-lambda scan, followed by the 405 nm lambda scan, and then 405 nm high-resolution images. Additionally, 2D transmitted light images were acquired simultaneously with the confocal images using the same illumination beam, to ensure that images were in registration.

2D, 3D and 4D images were acquired in three specific regions of interest (ROIs): the tesserae, the joints, and the unmineralized cartilage. Additional 2D, 3D and 4D images were made of the embedding media (paraffin, PMMA) without samples, to determine if these media contributed any AF. We replicated the analyses of each ROI type three times for each sample preparation type (i.e. for PMMA, paraffin and thawed samples, scanning three different tesserae, joints, and unmineralized cartilage regions each).

It was challenging in all sample preparations to find a flat region of interest for high magnification imaging (63x), especially at the interface between tesserae and unmineralized cartilage. Unembedded thawed samples were particularly difficult to prepare and image. As this tissue was not embedded, non-uniform sections were cut manually by razor blade and therefore were not uniform. Also, evaporation of water from the tissue (e.g. the unmineralized cartilage, which has a high water content) caused large shifts in the position and morphology of the tissue, making imaging almost impossible at high magnification. Thus, the images of thawed tissue were only taken at magnification of 10x, with the exception of one tessera sectioned flat enough to be imaged at 63x.

2.3. Analysis of hyperspectral images. Underlying image analysis model and unmixing procedure

Unlike 2D images, where features can be interpreted directly by their global fluorescence intensity, 3D and 4D images require dedicated data treatments by unmixing methods to disentangle the contributions of the distinct fluorescence signatures in a sample. Indeed, natural fluorophores can exist in different concentrations and locations within an analysed tissue, which can result in spatially complex variation and/or mixing (co-localization) of fluorescence signals, often hindering the interpretation of results. The ability to unmix multivariate signals in fluorescence images is particularly important for 3D images and, most

importantly, for 4D images, which have the most potential to detect and distinguish biological regions with distinct fluorescence signatures, due to the wider excitation range used and because differences in both excitation and emission characteristics are considered.

The unmixing algorithm used in this work is Multivariate Curve Resolution-Alternating Least Squares (MCR-ALS), apt for single 3D and 4D images, but also for the treatment of several related images analysed together (multiset analysis) [28, 29]. The results provided by MCR-ALS are distinct fluorescence signatures (emission spectra or excitation/emission fluorescence landscapes for 3D and 4D images, respectively), from either an individual fluorophore (e.g. collagens, elastin, flavins) or a consistent mixture of fluorophores found consistently together (e.g. in a particular tissue type). The resultant distribution maps produced by the MCR-ALS show the spatial distribution of the fluorescence signatures in the 3D/4D source images and therefore their associations with tissues and other biological entities [30]. In this work, all MCR-ALS analyses were performed using in-house implemented routines, programmed in the MATLAB environment (v. 2019) [31]. A detailed description of the function and output of the MCR-ALS is outlined in Section 2 of Supplementary Materials.

2.4. Light sheet microscopy of fixed samples

To examine tessellated cartilage in larger samples without the need for thin sectioning, we also employed light-sheet fluorescence microscopy (LSFM), also known as Single-Plane Illumination microscopy (SPIM) [32], using AF as a contrast mechanism. In contrast to the point-laser illumination of the confocal microscope, SPIM relies on the creation of an illumination plane, with the laser beam shaped into a rectangle and focused in a thin “sheet of light” using a cylindrical lens [32, 33]. The uniqueness of its optical configuration, with uncoupled perpendicular illumination and detection axis, combined with fast camera-based detection, allows acquisition of 3D images of samples at unprecedented speeds.

We analyzed the AF signal of *D. pastinaca* tessellated cartilage using a custom made SPIM microscope [34]. The custom microscope achieves magnifications between 2x and 4x (field of view 6.65x6.65 mm² and 3.33x3.33 mm², respectively), allowing the imaging of samples several millimeters thick. This can be combined with image stitching to allow volumetric imaging of samples several centimeters thick in each linear dimension. In our study, the examined samples

were thick cubes of propterygium (5-6 mm thick), fixed as described in the previous section. To facilitate the imaging of larger sample blocks of tessellated cartilage, samples needed to be clarified (i.e. rendered transparent) to equalize the refractive index throughout the tissue block. No protocols exist for clarification of tessellated cartilage; we used ECI (ethyl cinnamate), which has proved effective for clearing hard tissues in calvaria and long bones [e.g. 35], while also being fast, affordable and non-toxic. For clearing, fixed transverse sections were dehydrated with an ethanol series (pH 9.0) 50%-70%-100% (2X), 12 hours per step, at 4°C. After dehydration, samples were transferred to ECI (W243000 Sigma-Aldrich) and incubated while gently shaking at room temperature until they became transparent. The excitation and emission spectra used in SPIM made it compatible with our analyses made with confocal. Samples were excited with several excitation wavelengths (λ_{ex} = 405, 488 and 561 nm) and the emitted fluorescence collected with filters of 482/25, 520/50 nm and 593 long pass, respectively.

3. Results

3.1. General observations of AF signal

Using AF, it was possible to obtain high resolution optical images of different tissue features of tessellated cartilage, including both mineralized (tesserae) and unmineralized elements (perichondrium, cells, the unmineralized cartilage matrix), although the degree of detail in the images varied with sample preparation (see below). The 405 excitation laser with a broad spectrum of acquired emission wavelengths (459-602 nm) produced the clearest imaging results with the strongest signal, comparable to other techniques commonly used to image tessellated cartilage, such as histology and BSE (Fig. 3).

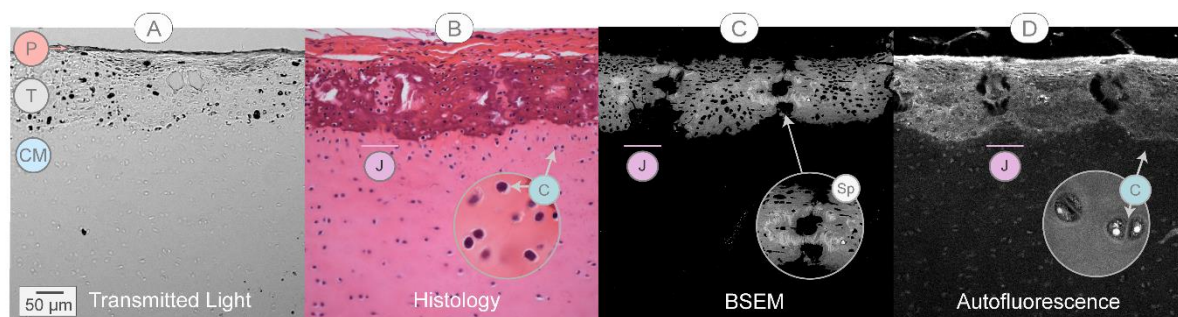


Fig. 3. Comparison of different imaging techniques for tessellated cartilage. A) Image of unstained sample acquired using transmitted light (confocal microscope, 10x objective). B) LM image of a demineralized sample, stained with Hematoxylin – Eosin. The zoomed circles in B and C show chondrocytes in the cartilaginous matrix. C) Backscatter Scanning Electron Microscopy image showing mineral density variation in mineralized regions of the tissue, but no information in non-mineralized areas. The zoomed circle shows a higher magnification of spokes laminae, highly mineralized bands located at the contact region of two tesserae. D) AF image, excited with the 405 nm laser (confocal microscope, 10x objective). All images correspond in scale with A. **Abbreviations** Chondrocytes (C), Cartilaginous matrix (CM), Joint (J), Perichondrium (P), Spokes (Sp)

3.2. Effects of sample preparation

The structures and tissues visible from their AF in tessellated cartilage differed among PMMA samples, paraffin samples, and non-embedded thawed samples (Figs. 4, 5). Examination of the AF signal of the embedding media themselves, showed negligible (PMMA) or no (paraffin) AF, and so did not contribute to tissue AF signals. The discernibility of particular tessellated cartilage features is discussed in detail in the following section, but some general effects of sample preparation are worth noting.

For unembedded thawed samples, the propterygium was thawed a first time to perform a preliminary test of the sectioning and imaging methods, and then a second time months later for the final experimental analysis. The preliminary images showed AF signal in perichondrium, tesserae, and unmineralized cartilage (both cells and matrix) (Fig. 4A [a, d-g], C). In contrast, in the later experimental analysis, only a weak AF signal was visible in the tesserae, being entirely lost in the soft tissues (Fig. 4A [b-c], C).

PMMA samples were non-demineralized and more cleanly sectioned than thawed samples and therefore showed both hard and soft tissues in conditions perhaps closest to their native configurations (Figs. 5 - 7). Tesserae in PMMA samples, however, often exhibited cracks (Figs. 5D; 6A), making it difficult to obtain large, intact regions of the tesserae layer. The cracks were produced during the preparation of the samples, probably during microtome cutting, oven-curing, or mounting of slices. Similar cracking has been seen in several previous studies of tesserae, particularly associated with high mineral density regions (e.g. tesseral spokes; see below) [25]. In contrast, in paraffin samples, demineralization resulted in more intact tesserae, not disrupted by preparation artifacts, yet needless to say, mineralized tissue details were lacking (Fig. 5).

3.3. Observations by individual feature

3.3.1. Tesserae

The tesserae layer could be imaged in all sample preparation methods, with the intensity of the signal always higher than in the unmineralized cartilage (Figs. 4 - 8). However, the visible features and morphology varied. PMMA samples, for example, showed the most clearly defined tesserae morphology and mineralized structures (Figs. 5 - 6). Within the tesserae, a distinct central region delineated by a bright autofluorescent border showed a stronger AF signal than the peripheral region at the margin of tesserae (Figs. 5C - D; 6A). These three AF zones —center, center border and periphery— were also observed in clarified samples imaged with SPIM (Fig. 8), yet were not visible in histology samples (Figs. 3B; 5B). In the central region, cell lacunae were surrounded by wavy, concentric lines in the mineralized matrix (Fig. 6A, D - E). These lines were identified from our histology and BSEM images as Liesegang lines (lines of accretive tissue growth; [25]), and were also observed in other tesserae regions (e.g. just interior to and tracking

the contours of the outer margins of tesserae; Fig. 6C), albeit with lower signal intensity (Fig. 6D - E).

Cells within tesserae are enclosed in lacunae and surrounded by unmineralized matrix, with lacunae connected by small passages (canaliculi). In our examinations, cells within lacunae were clearly visible in PMMA and paraffin samples, however, in contrast with cells in the unmineralized cartilage and joints, appeared more shrunken (e.g. damaged during fixation), and therefore their morphologies could not be properly visualized. Using the AF signal, it was often difficult to distinguish cells from the thin layer of matrix surrounding them, and from the mineralized margins of their lacunar spaces (Fig. 6B). A brighter haze of AF was often seen surrounding and connecting the cells within tesserae (Fig. 6B), but it was unclear whether this corresponded to the unmineralized matrix filling the cavities surrounding and linking cells (lacunae and canaliculi, respectively) or to the mineralized tissue that bordered these cavities, or some combination of the two. Similarly, the interface between tesserae and unmineralized cartilage (i.e. at the lower/chondral margins of tesserae) was difficult to detect in paraffin (demineralized) samples as the two materials had nearly the same gray values in the 405 images (Fig. 6F). In contrast, in PMMA samples, the interface was typically a thin, high-brightness rim marking the mineralization front, which made it easier to distinguish (Fig. 6D - E).

Small autofluorescent globular features ($\sim 1\text{-}2\ \mu\text{m}$) were often visible in PMMA samples at interfacial locations in tesserae: at the border between the central and peripheral regions of tesserae (Fig. 6A), along the interior walls of cell lacunae (Fig. 6B) and surrounding cells that were in the process of being engulfed by tesserae at the interface with the unmineralized matrix (Fig. 6D). These globules corresponded in size and location to mineralized globular features observed in BSE, but were not seen in other techniques where tissue had been demineralized (e.g. paraffin).

3.3.2. Joints

The features of joints (i.e. the structures and tissues between tesserae) were not visible in thawed samples, likely associated with the difficulty of producing samples flat enough for high magnification imaging (Fig. 4A). In PMMA, paraffin and clarified samples, however, the ultrastructures of multiple joint-associated features could be identified using AF (Fig. 5).

Depending on the particular plane in which neighboring tesserae were sectioned, two local morphologies were possible, often with both present in a single joint ROI: (1) the tesserae margins separated by a space containing unmineralized matrix, cells and fibers (Figs. 5F; 6A, 8B) or (2) the tesserae margins in direct contact (Fig. 5G). When tesserae were in direct contact, laminated, highly mineralized features called spokes were visible in PMMA samples, radiating from contact points between neighbouring tesserae [19, 25]. These structures exhibited high AF signal and showed a similar morphology to spokes seen in BSE images (Fig. 5G). In demineralized samples (in both histology and AF of paraffin samples), spokes were only represented by gaps in the tissue where high mineral density laminae had been (Fig. 5C, 5E).

In zones where neighboring tesserae were separated by soft material, cells and fibers connecting tesserae were typically visible. Cells located in the joint space were flattened and arranged in series, passing between neighboring tesserae (Figs. 5E - F; 6A; 8B). In our histology, these cell arrays occupied horizontal gaps between the fiber bundles linking tesserae; using the AF signal, these fibers were often visible as parallel streaks, connecting tesserae and framing cell arrays (Fig. 6A; 8B).

3.3.3. Unmineralized cartilage

The unmineralized cartilage comprises cells embedded in copious amounts of extracellular matrix, as visible in our histological samples (Figs. 3; 5H). This basic tissue arrangement was also visible in AF imaging of all sample preparations, where cells emitted a brighter AF signal than the surrounding matrix (Figs. 3D; 5I - J; 7; 8A, C). Cells in the unmineralized cartilage also appeared more intact than cells within tesserae (see above), allowing observation of some local variation in cell morphology and arrangement across different zones (Fig. 7). In the unmineralized matrix directly beneath tesserae, cells were either well separated or formed twins (closely-associated, isogenous pairs, indicating recent separation by mitosis; Fig. 7D - F). In this zone, the cells exhibited a variety of cross-sectional morphologies, spheroidal (typical of chondrocytes), but also flattened or elongated (Figs. 5I - J; 7F). In contrast, further from the interface with tesserae (i.e. deeper into the unmineralized matrix), cells always presented spheroidal morphologies and often formed isogenous groups (clusters of sister cells) of two or four chondrocytes (Figs. 5H - J; 7D - F; 8C).

Among the sample preparation methods, cells differed in their morphology and the fluorescence signal emitted. In the preliminary analysis of thawed samples, cells emitted a strong AF signal, in comparison to the very low signal of the surrounding matrix (Fig. 4A); both sources of AF were completely lost in the final experimental analysis. Cells in PMMA and paraffin samples exhibited different degrees of shrunkenness, where the cell appeared collapsed away from the walls of its lacuna and surrounded by an empty (black) space [36] (Fig. 7A). Better preserved cells exhibited different appearance and cell structure depending on the sample preparation method. In paraffin samples, these cells were bright ovoids with a darker rounded nucleus and relatively homogeneous cytoplasm (Fig. 7C). In PMMA samples, these cells showed a thin, bright surrounding border and a bright nucleus, but the intracellular compartment had a loose foamy appearance (Fig. 7B, E). Outside the cell, a distinct pericellular region was often visible, typically with a lower grayscale value and different matrix texture (Fig. 7B, E).

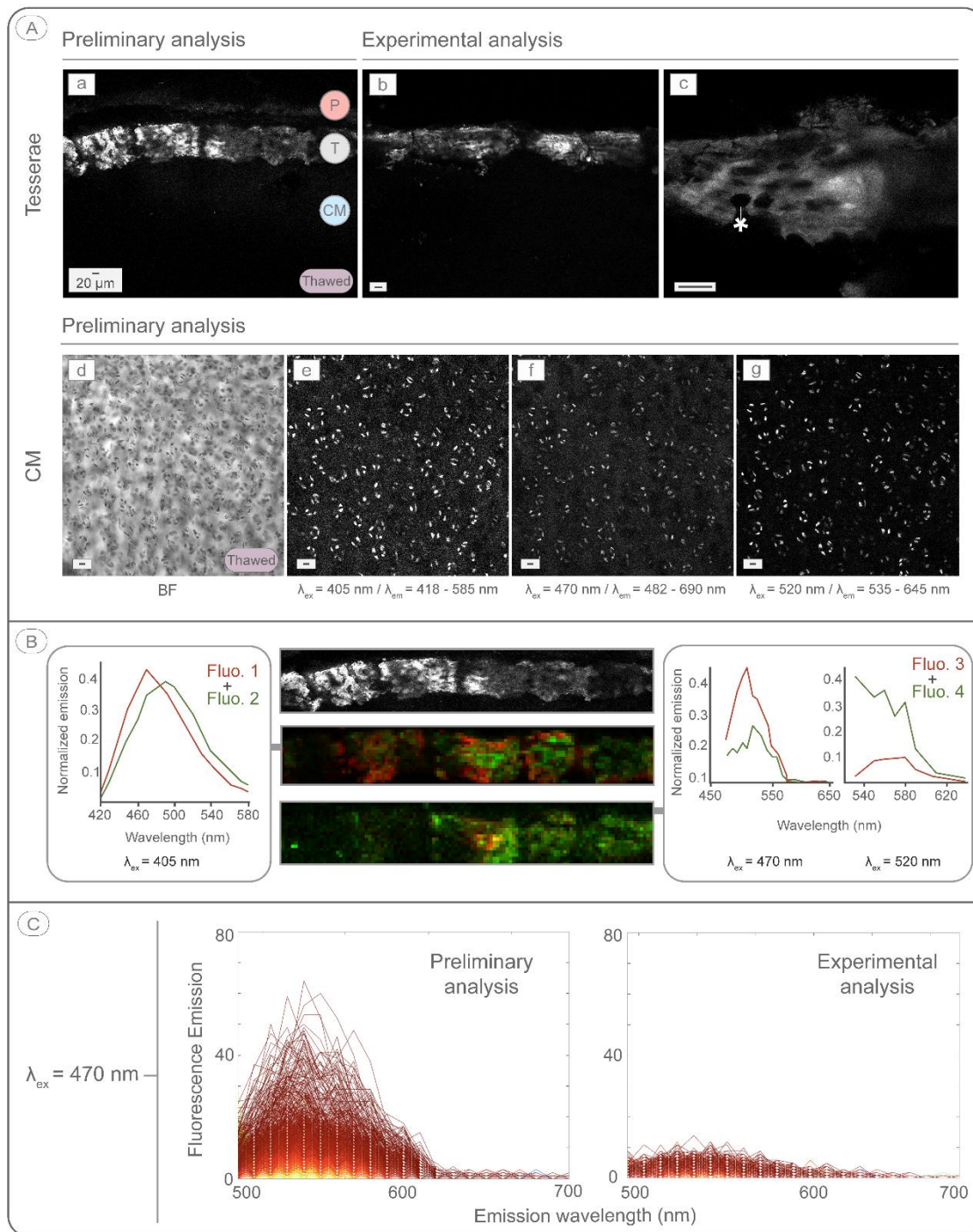


Fig. 4. AF signal of thawed (unfixed) tessellated cartilage. **A**) AF signal of tesserae and cartilaginous matrix (CM) after one freezing-thawing cycle (preliminary analysis) (a, d - g) and two freezing-thawing cycles (experimental analysis) (b,c). CM was imaged first using bright field (d) and then by exciting the AF signal (e-g) using different excitation and emission wavelengths, specified at the bottom of each image. **B**) Results of MCR-ALS analysis of the tesserae from preliminary analysis. Middle images: the location of the different fluorescence signatures in the tesseral layer. Graphs: emission spectra for the observed fluorescence signatures (left: 405 nm excitation; right: 470 and 520 nm excitation wavelengths). **C**) Comparison of AF emission between preliminary and experimental analyses for 470 nm excitation wavelength, showing a clear loss of AF signal after two thawing-freezing cycles. Note: the patchy AF observed in the tesserae is a function of the difficulty of generating planar sections from fresh/thawed tissue. All scale bars = 20 μm . **Abbreviations:** Bright field (BF); Cartilaginous matrix (CM)

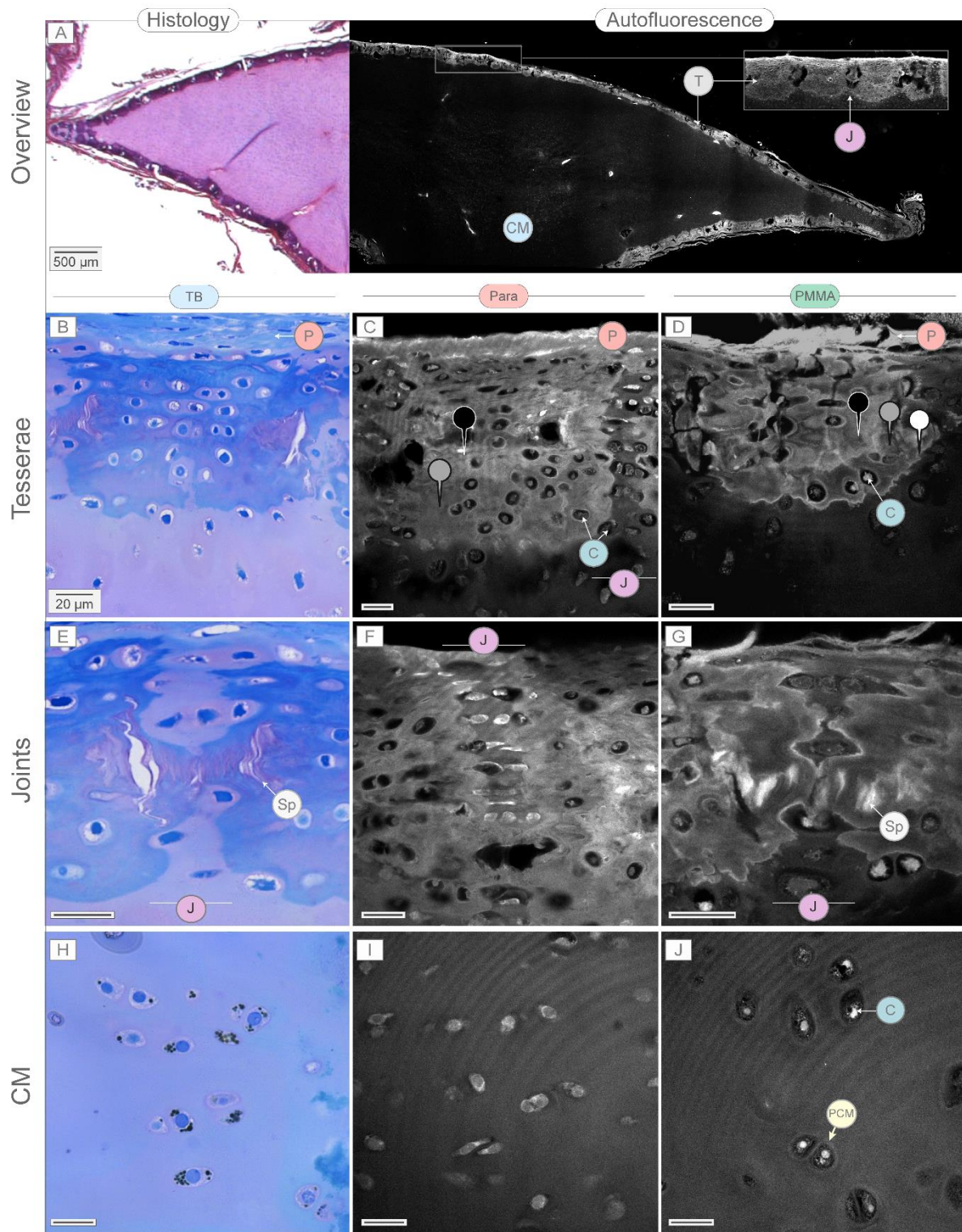


Fig. 5. Comparison of AF images of two sample preparation techniques with histological samples. A) Overview of a propterygium cross-section, stained with hematoxylin-eosin (left) and a non-stained sample imaged with AF (right). The zoomed region shows a closer view of tesserae. Both samples were demineralized and paraffin-embedded. These very large field-of-view images of the entire skeletal cross section are composites, stitched together from multiple 10x images using the built-in Leica Auto Stitching function. B, E, H show regions from decalcified samples, EPON-embedded and stained with toluidine blue. C, F, I show regions from decalcified samples, paraffin-embedded and imaged using AF (ex: 405 nm laser; em: 422 - 702.5 nm). D, G, J show regions from mineralized samples, PMMA

embedded and imaged using AF (ex: 405 nm laser; em: 422 - 702.5 nm). In PMMA, central region (black pushpin), peripheral region (grey pushpin) and outer border (white pushpin) can be distinguished, whereas in paraffin only the central and peripheral region can be seen. Banded patterns observable in some images (e.g. C, I, J) are artifacts generated by the reflection of the light; we verified that these did not affect the MCR analysis and elected not to remove them in post-processing (their removal modified the signal and morphology of imaged tissue structures). All scale bars from B-J = 20 μm . **Abbreviations:** Chondrocytes (C), Cartilaginous matrix (CM), Joint (J), Perichondrium (P), Pericellular matrix (PCM), Spokes (Sp), Toluidine Blue (TB)

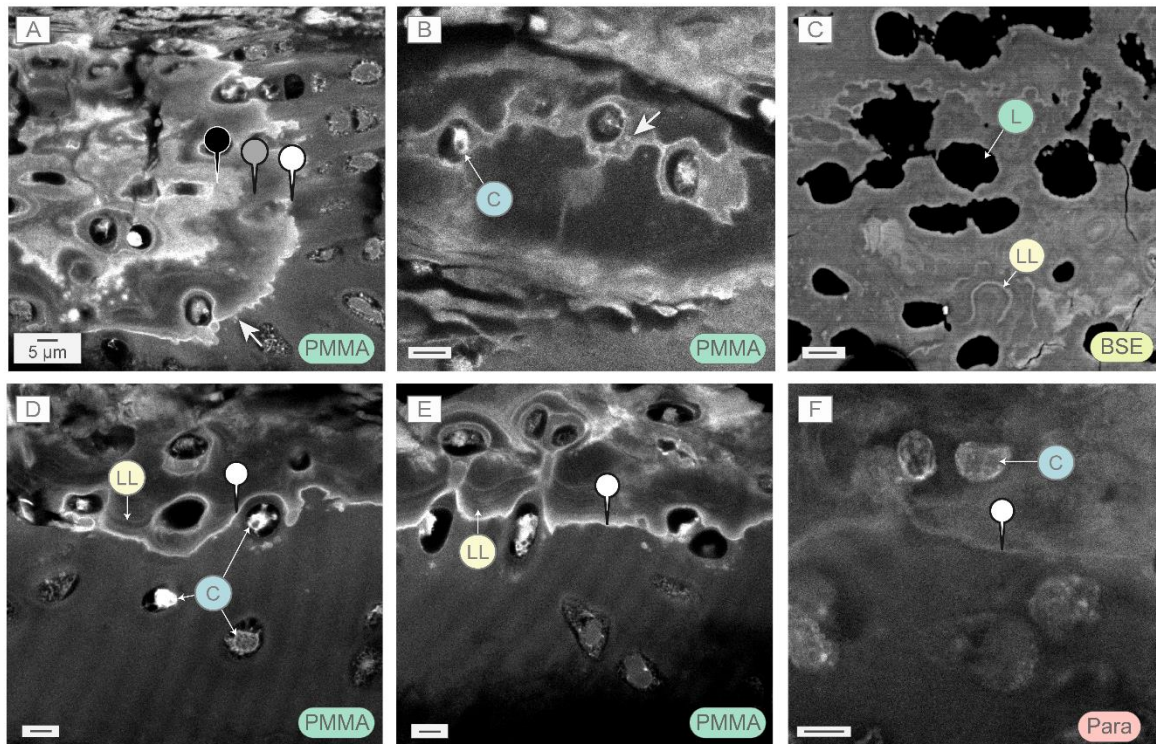


Fig. 6. Several ultrastructural features of tesserae, observable with the AF signal. **A)** A portion of a single tessera (left) and its joint (right). Within the tessera, the peripheral region (grey pushpin) shows a lower AF signal than the central region (black pushpin) and the outer border (white pushpin). Variations in the signal intensity of the central region are observable, such as the globular mineralized features (calcospherites; white arrow in the circle) at the border of the central region and the tessera's outer edge (white arrow). **B)** Cells within lacunar spaces in tesserae. The lacunar spaces presented a brighter signal than the surrounding mineralized tissue. Calcospherites can also be observed within the lacunae space (white arrow). **C)** For comparison with (B), a BSE image of a similar tessera region, but showing only the mineralized tissue; the cells aren't visualized and so lacunae appear empty (note the short canalicular passages connecting adjacent lacunae). Note that finescale features (e.g. Liesegang lines, LL) can be visualized similarly in BSE and with the AF signal. **D-E)** AF images showing the border region between tesserae and unmineralized cartilage matrix. Several features can be observed, such as cells being incorporated into the tesserae, surrounded by calcospherites (white arrow in D), as well as the bright tesseral outer border and LL. **F)** AF image of a similar chondral border region, but from decalcified, paraffin-embedded samples. Note the decreased contrast and less defined structures relative to the mineralized, PMMA-embedded samples. All scale bars = 5 μm . **Abbreviations:** Chondrocytes (C); Backscatter Electron Microscopy (BSE); Lacunae (L); Liesegang lines (LL); Paraffin (Para)

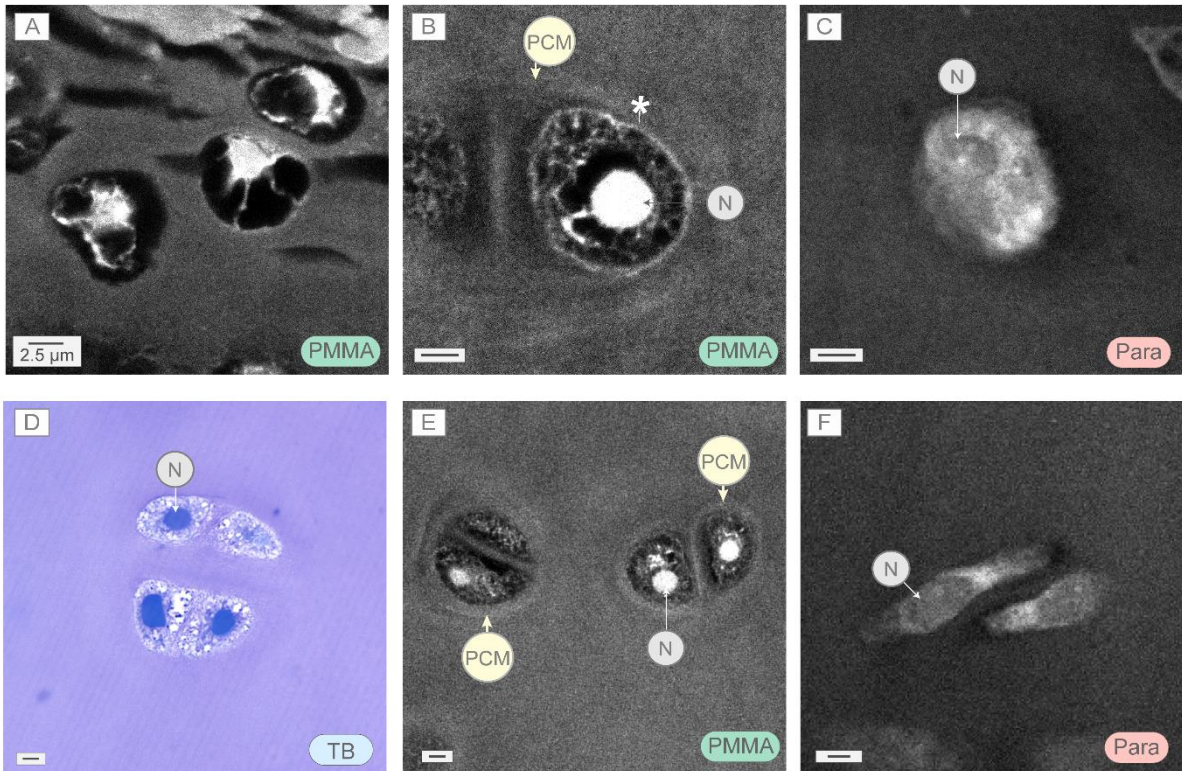


Fig. 7. Chondrocytes from the unmineralized matrix, imaged with AF signal and compared with histological preparations. **A-C** Highlight the appearance of individual chondrocytes, while **D-F** compare the appearance of chondrocyte twins from different sample preparations. **A)** Shrunken chondrocytes, where cells are entirely collapsed within their lacunae. Such chondrocytes were observed in both PMMA-embedded samples (as here) and paraffin-embedded samples. **B)** AF-imaged chondrocyte imaged in PMMA-embedded samples, where the nucleus (N), the cell border (asterisk) and the pericellular matrix (PCM) can be distinguished. **C)** AF-imaged chondrocyte from paraffin-embedded samples, where the nucleus emits a less intense signal than the surrounding cell. **D)** Two pairs of chondrocytes, stained with toluidine blue, where the nucleus and cytoplasm can be appreciated. **E)** Two pairs of chondrocytes in PMMA samples, showing a bright nucleus and a clear PCM surrounding them. **F)** Pair of chondrocytes in a paraffin-embedded section, where the cell and the nucleus present a flat morphology. These morphologies were also seen in PMMA-embedded samples, exclusively located in the cartilaginous matrix directly beneath the tesserae. All scale bars = 2.5 μm. **Abbreviations:** Nucleus (N), Pericellular matrix (PCM); Paraffin (Para), Toluidine Blue (TB)

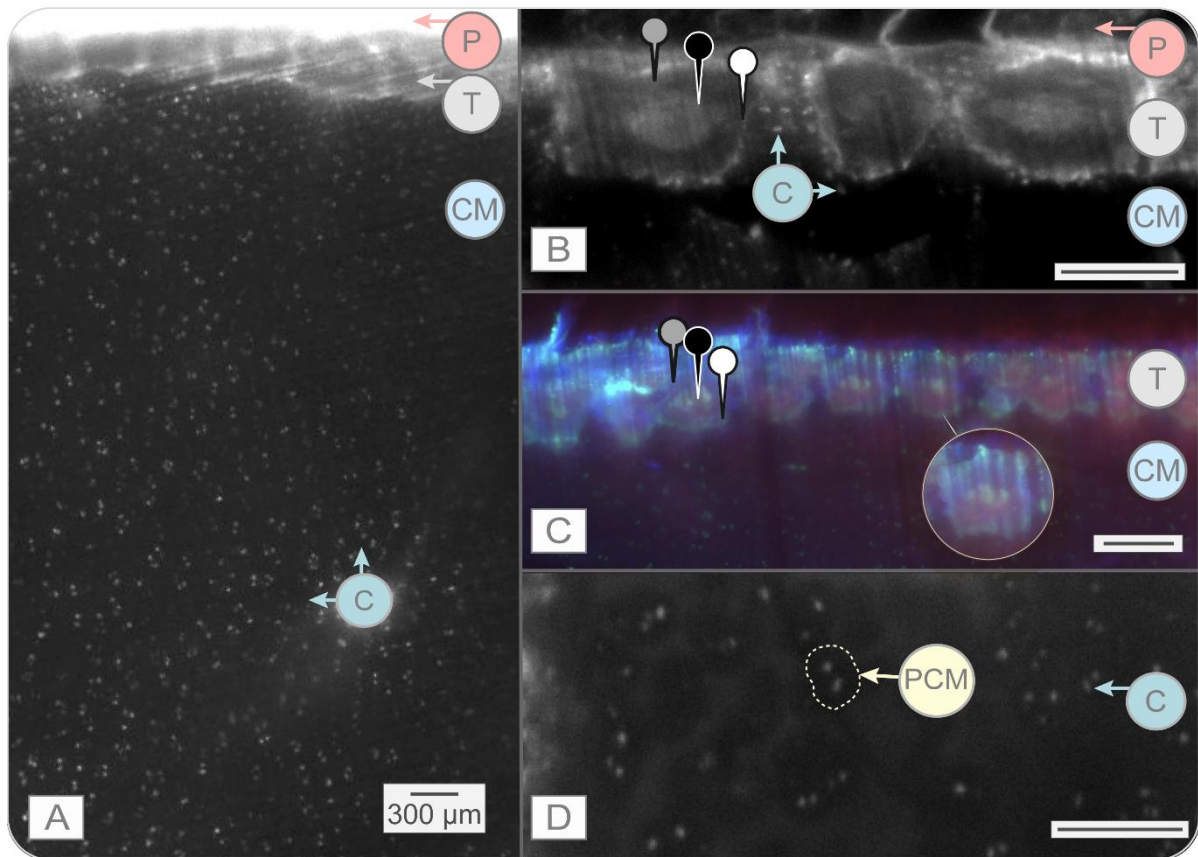


Fig. 8. AF images of tessellated cartilage using SPIM. A) 2D AF image of an excised piece of tessellated cartilage, illustrating the large uncalcified cartilage matrix component relative to the tesserae. B) 2D AF image of several tesserae with intervening joint regions. The three distinct anatomical regions often observed in AF images of tesserae are distinguishable, with the center (black pushpin) and the outer border (white pushpin) presenting brighter signals than the periphery (grey pushpin). Chondrocytes can be appreciated organized in series within the joints. Black and white image settings: $\lambda_{ex}=488\text{ nm}$ / $\lambda_{em}=520/50\text{ nm}$. C) AF image of multiple tesserae in series. The central region and outer border share the same green fluorescence ($\lambda_{ex}=488\text{ nm}$; $\lambda_{em}=520/50\text{ nm}$), which differs from the red fluorescence signal of the peripheral region ($\lambda_{ex}=405\text{ nm}$, $\lambda_{em}=482/25\text{ nm}$), also appreciated in the zoomed tessera (circle). Regions throughout the tissue also show a vague blue AF ($\lambda_{ex}=561\text{ nm}$, $\lambda_{em}=593\text{LP}$), but this did not appear to be associated with specific structures. Chondrocytes in the unmineralized cartilage matrix presented AF with $\lambda_{ex}=488\text{ nm}$ and $\lambda_{em}=520/50\text{ nm}$. D) AF image of the unmineralized cartilage matrix. Groups of chondrocytes can be observed surrounded by a pericellular matrix (PCM), darker than the interstitial extracellular matrix intervening between chondrocyte groups. All scale bars = 300 μm . **Abbreviations:** Chondrocytes (C), Unmineralized cartilage matrix (CM), Pericellular matrix (PCM), Perichondrium (P), Tesserae (T)

3.4. Analysis of hyperspectral images

For both 3D and 4D fluorescence hyperspectral images, three separate multisets were created (one per sample preparation method), formed by combining preprocessed fluorescence images from all ROIs (tesserae, joints and UC) for a given sample preparation method (see Fig. 9 - 11; Suppl. Fig. 1- 4). MCR-ALS was then applied to the 3D and 4D multisets to elucidate the sample constituents present in the analyzed sections of cartilage tissue. The primary parameters and model results of MCR-ALS, as applied to the different multisets analysed, are summarized in Table 1, including the number of images analyzed per multiset, the number of fluorescence signatures resolved by MCR-ALS, and estimates of model quality parameters: lack of fit (LOF) and explained variance. The variance explained by the MCR-ALS models is satisfactory considering the noise level of the spectra analysed. The lower variance explained by 4D images compared with 3D images is explained by the lower signal-to-noise ratio of these data.

The unmixed fluorescence signatures detected in our samples by the MCR-ALS were characterized by distinct pure excitation-emission spectra and distribution in the tissue. To facilitate description and reference in our analysis, we designate the observed unmixed fluorescence signatures “Fluorophores”, however, it is important to note that these AF signatures can be produced either by a single fluorophore (e.g. from elastin or a particular collagen or flavin) or a combination of them. We number the fluorophores arbitrarily for reference (e.g. Fluorophore 1, 2, 3) and in the text below provide general summaries of their excitation/emission ranges; these data are listed in more spectral detail and according to tissue associations, sample preparation and imaging multiset (3D or 4D) in Table 2.

4D images showed a higher number of distinct signatures than 3D images, likely due to the wider excitation range. Regarding the preparation method, PMMA samples showed a higher number of distinct signatures, followed by paraffin. Thawed samples presented a weak AF signal and only preliminary samples exhibited a signal-to-noise ratio that allowed identification of distinct AF signatures.

Table 1. Summary of image multisets analyzed, MCR-ALS model parameters, and primary results (number of unmixed fluorescence signatures resolved). Multisets are organized by image type (3D = 405 nm, 4D = WLL) and sample preparation methodology (paraffin, PMMA or thawed samples), with the number of images comprising each multiset listed and the number of images per ROI in each multiset detailed in parentheses immediately below (in the order: Tesserae/Joint/UC). The number of unmixed fluorescence signatures identified by SVD for each multiset and estimates of model quality parameters (LOF and explained variance) are also listed. No images could be analyzed for the tesserae ROI in the paraffin 4D multiset, since the image settings were not comparable with the other multisets. Tesserae information, however, was available and analyzed from joint ROI images (see Fig. 9). The most relevant ROIs analyzed can be found in Fig. 9 - 11; Supp. Fig. 3 - 4.

Type of image	Embedding medium	Nr. of images	Nr. of unmixed fluorescence signatures	LOF (%)	Explained variance (%)
3D	Paraffin	10 (5/2/3)	1	13.85	98.08
	PMMA	9 (3/3/3)	2	13.62	98.14
	Thawed	1 (1/0/0)	2	8.68	99.25
4D	Paraffin	6 (0/3/3)	3	26.31	93.08
	PMMA	11 (3/3/5)	3	25.39	93.55
	Thawed	3 (1/0/0)	2	24.25	94.12

3.5. Paraffin sample analysis

In paraffin samples, four fluorescence signatures were detected with MCR-ALS, one with 3D images (Fluorophore 1) and three with 4D images (Fluorophore 2, 3 and 4). Fluorophore 1 was excited by the 405 laser (3D multiset: Table 2), observed in the perichondrium, tesserae, joints and cartilage matrix, although with intensity variations across the regions (Fig. 9A). The highest intensities were seen in the perichondrium and within the tesserae.

The tesserae —with this fluorophore, but also others below— presented distinct spatial variation in signal intensity, allowing three distinct tesseral regions to be easily discerned from each other: a center region, a peripheral region surrounding the center concentrically, and a thin edge at the extreme outer border of the tesserae (~1 μm thick). These three regions — center, center border, and periphery— were similar in general appearance to those identified in 2D AF images and SPIM (Fig. 8C; Fig. 9). The AF of the central region and the tesseral outer edge (especially where it bordered the joint region) was more intense than in the peripheral region. In the joints and unmineralized cartilage, this AF signature was weak in the extracellular matrix, but stronger within the cells. Some cells presented local areas of higher intensity, apparently in the cytoplasm.

Fluorophores 2, 3 and 4 (4D fluorescence images) were excited with the WLL in a broad excitation range from 470 to 670 nm. Fluorophore 2 and Fluorophore 3 presented similar excitation-emission profiles, however, the MCR-ALS algorithm could unmix them based on their spectral shape differences (Table 2; Fig. 9B).

Fluorophore 2 was associated with soft tissues, in the extracellular matrices and cells of joints and unmineralized cartilage, but absent in tesserae and perichondrium. The highest signal intensities were seen within the cells of the joints, followed by the cells of the unmineralized cartilage. In the tesserae, some lacunar spaces of the central region also exhibited signals of relatively high intensity.

Fluorophore 3 had a wide distribution, in the perichondrium, the laminae of spokes in tesserae, the cartilage matrix, and in all the cells (except those of the central region in tesserae). Whereas the extracellular matrices of both joints and cartilage display Fluorophore 2, Fluorophore 3 was only located within the cartilage matrix.

Fluorophore 4 was the only fluorescence signature in this multiset located in the mineralized tissue of tesserae: in the border between the central and peripheral regions of the tesserae and in the outer edge surrounding the tesserae. Fluorophore 4 was also located within the cells of all regions (tesserae, joints and unmineralized cartilage). Although Fluorophores 2, 3 and 4 of this multiset were localized in cells, Fluorophore 4 showed the highest cellular AF and was absent in the extracellular matrices of the joints and unmineralized cartilage.

3.6. PMMA sample analysis

In PMMA samples, five fluorescence signatures were detected with MCR-ALS, two in 3D images (Fluorophores 1 and 2) and three in 4D images (Fluorophores 3, 4 and 5). Fluorophores 1 and 2 were excited by the 405 laser, (Table 2; Fig. 10). Fluorophore 1 was homogeneously distributed in the mineralized matrix of the tesserae, and in the extracellular matrix of the joints and unmineralized cartilage, but absent in all cells. Within the tesserae, this fluorescence signature was more intense in the laminae of spokes. The localization within the tissue of this fluorophore correlates with the distribution pattern of Coll2 observed in IHC (Supp. Fig. 5). Fluorophore 2 had an intense signal in the muscles, perichondrium, center region and outer edge of the tesserae and in the cells within the joints and cartilage.

Fluorophores 3, 4 and 5 were excited with the WLL (4D images) in a broad excitation range from 470 to 670 nm (Table 2, Fig. 11). Fluorophore 3 was most intense in muscle, perichondrium, and spokes' laminae, exhibiting lower intensities within the cells and extracellular matrix of the unmineralized cartilage. In the extracellular matrix, this fluorescence signature had a homogeneous distribution, albeit forming higher intensity halos immediately surrounding cells. Fluorophore 3 was lacking in joints and the majority of tesserae cells.

Fluorophore 4 had the highest intensity in muscle. It was also present in the perichondrium, in the border between central and peripheral regions in tesserae, and in the outer edge of tesserae. In the unmineralized cartilage, it was only present within the cells, being completely absent in the extracellular matrix. Fluorophore 5 was most intense in the muscle and perichondrium, in the center, center border and outer edge of the tesserae and, to a lesser degree, in the unmineralized cartilage matrix. A weak signal could be seen within the cells of the unmineralized cartilage, but was absent in the rest of the cells.

Consolidating the information from all fluorescence signatures observed in PMMA samples, it can be noted that the cells differ in signal according to their location: whereas cells of the unmineralized matrix present a combination of Fluorophores 3, 4 and 5, cells of the joints and tesserae exhibit only Fluorophore 4, whereas in cells of the tesserae body zone Fluorophore 3 dominates.

3.7. Thawed samples analysis

For comparison of the AF signals of preliminary and experimental thawed samples, the different instrumental settings (e.g. bandwidth and pixel size) of the two experiments were standardized by binning to unify pixel size and by selecting only common spectral excitation wavelengths (470 and 520 nm). For both of these excitation wavelengths, the AF found in preliminary samples was nearly absent in the experimental thawed samples (Fig. 4C).

In contrast, the MCR-ALS analysis of preliminary thawed samples excited by the 405 nm laser (3D multiset) and by the 470 and 520 nm lasers (4D multiset) allowed tissue features to be distinguished. Following binning of the hyperspectral images by a factor of seven to increase spectral quality (increasing pixel size from 1.06 μm to 7.44 μm), two different fluorescence signatures were detectable, excited by the 405 nm laser (Fig. 4B, Table 2). Fluorophore 1 was generally located in the peripheral region of tesserae, whereas Fluorophore 2 was constrained largely to the central region. In this case, we excited the tissue with individual 470 and 520 nm lasers instead of a broader range, but this was still considered as a single excitation range. With these excitation wavelengths, two fluorescence signatures (Fluorophore 3 and 4) with different emission spectra were associated with each excitation wavelength (Table 2, Figure 4B). Both fluorescence signatures were associated with the tesserae, presenting distinct spatial locations; Fluorophore 3 was generally associated with the peripheral region of the tesserae, whereas the Fluorophore 4 was associated with the central region. The detection of fluorescence signals in thawed samples indicates the presence of natural fluorophores associated with distinct spatial locations of the tissue.

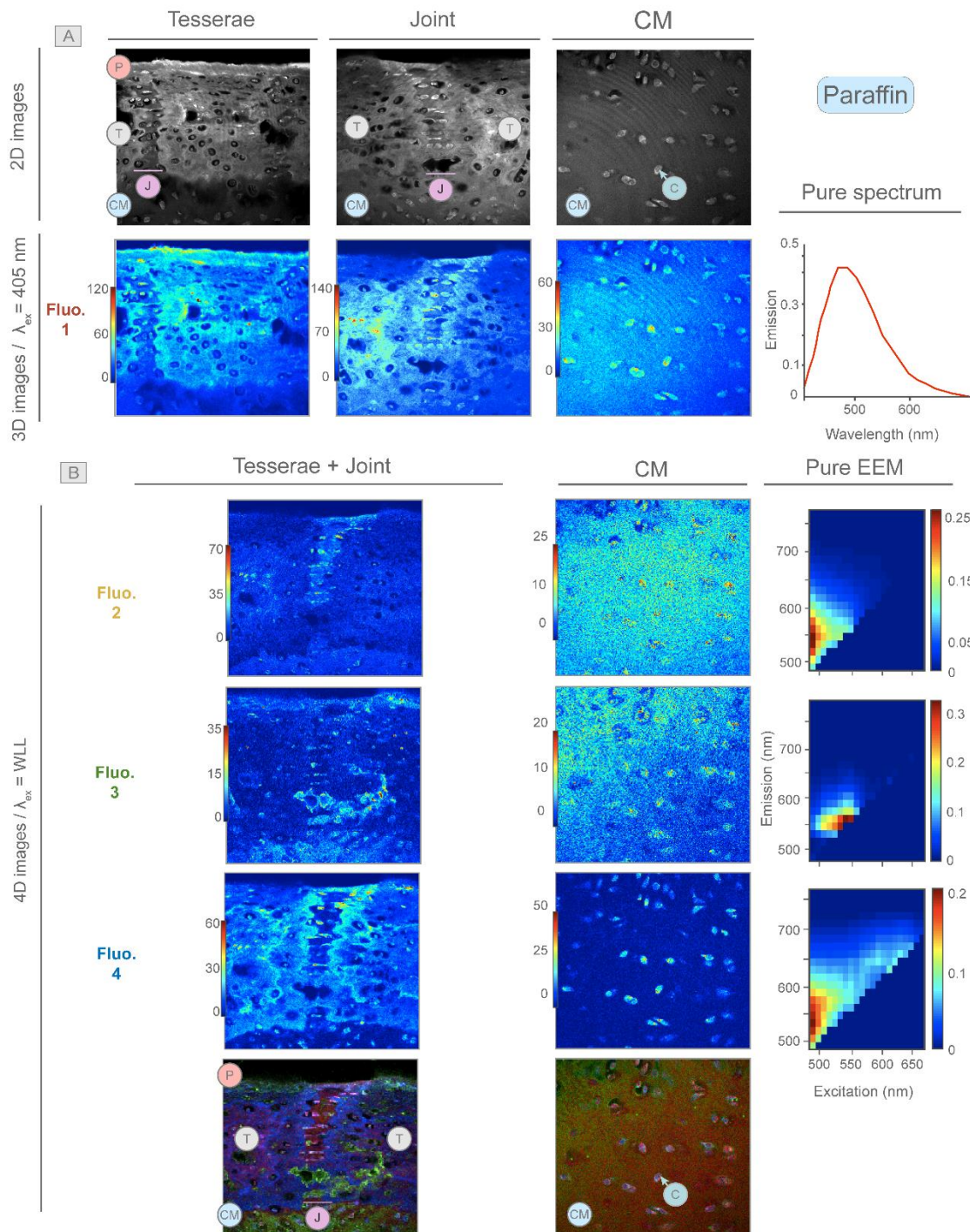


Fig. 9. Distribution maps and EEM of fluorescence signatures detected by MCR-ALS in decalcified, paraffin embedded samples. A) 2D (grayscale) images acquired with 405 nm and wide wavelength emission filter provide reference for overall tissue appearance. The 3D images below show the single detected fluorescence signatures, excited with the 405 nm laser (Fluo. 1). The fluorescence signature's spectral signature is shown to the right. B) 4D images, excited with the WLL, showing three detected fluorescence signatures (Fluo. 2-4); color bars indicate intensity. Merged distribution maps at the bottom overlap all fluorescence signatures in the same image. Excitation-emission (EEM) landscapes for each fluorescence signature are shown to the right. **Abbreviations:** Chondrocytes (C), Unmineralized cartilage matrix (CM), Joints (J), Perichondrium (P), Tesseractae (T)

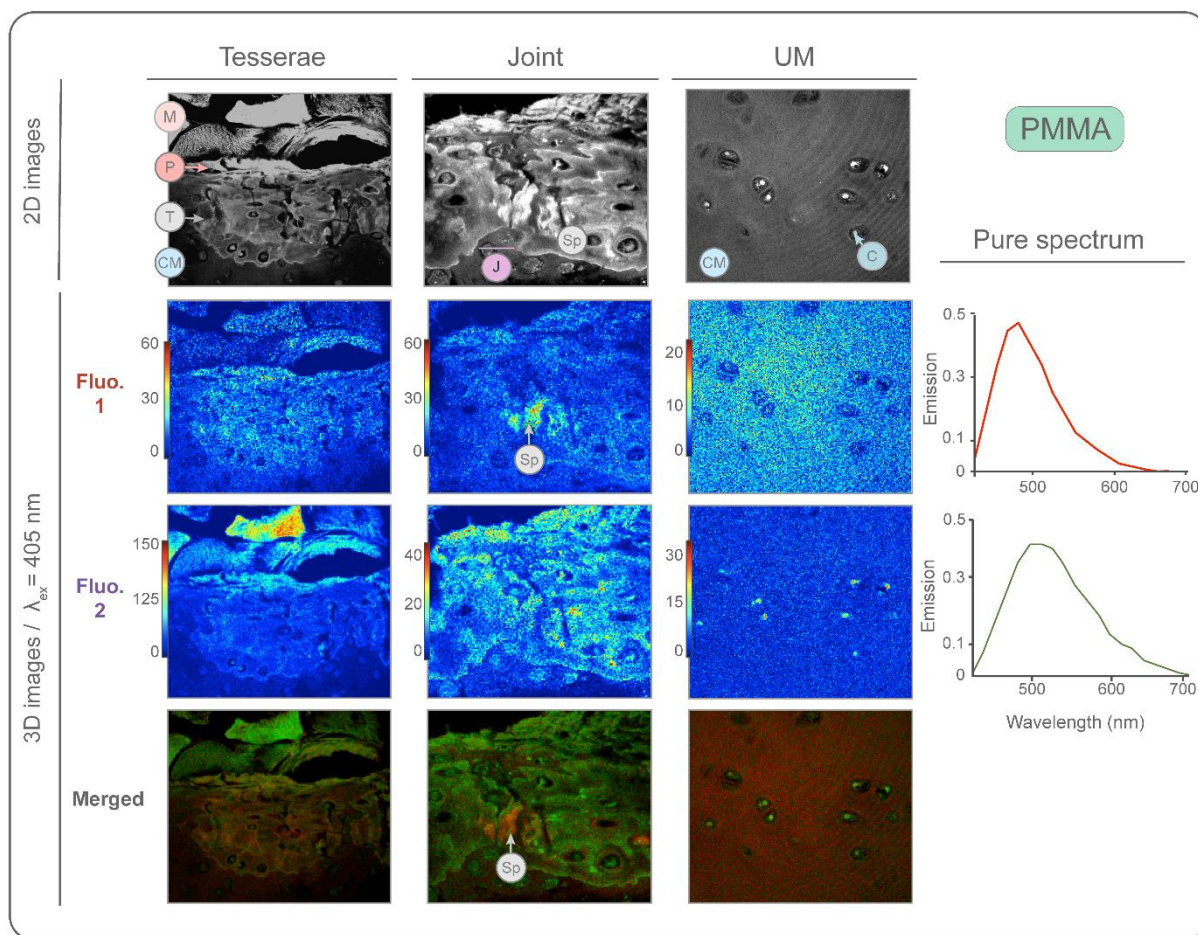


Fig. 10. Distribution maps and pure spectrum of fluorescence signatures detected by MCR-ALS in PMMA samples excited with 405 nm laser. The 2D (grayscale) images (top row) acquired with a 405 nm excitation laser and a wide wavelength emission filter provide reference for overall tissue appearance. The 3D images below show all fluorescence signatures detected with MCR-ALS (Fluo. 1 - 2), with their corresponding spectral signature at the right. Color bars in each image indicate intensity. Merged distribution maps at the bottom overlap both fluorescence signatures in the same image. **Abbreviations:** Chondrocytes (C), Unmineralized cartilage matrix (CM), Joints (J), Perichondrium (P), Tesseractae (T)

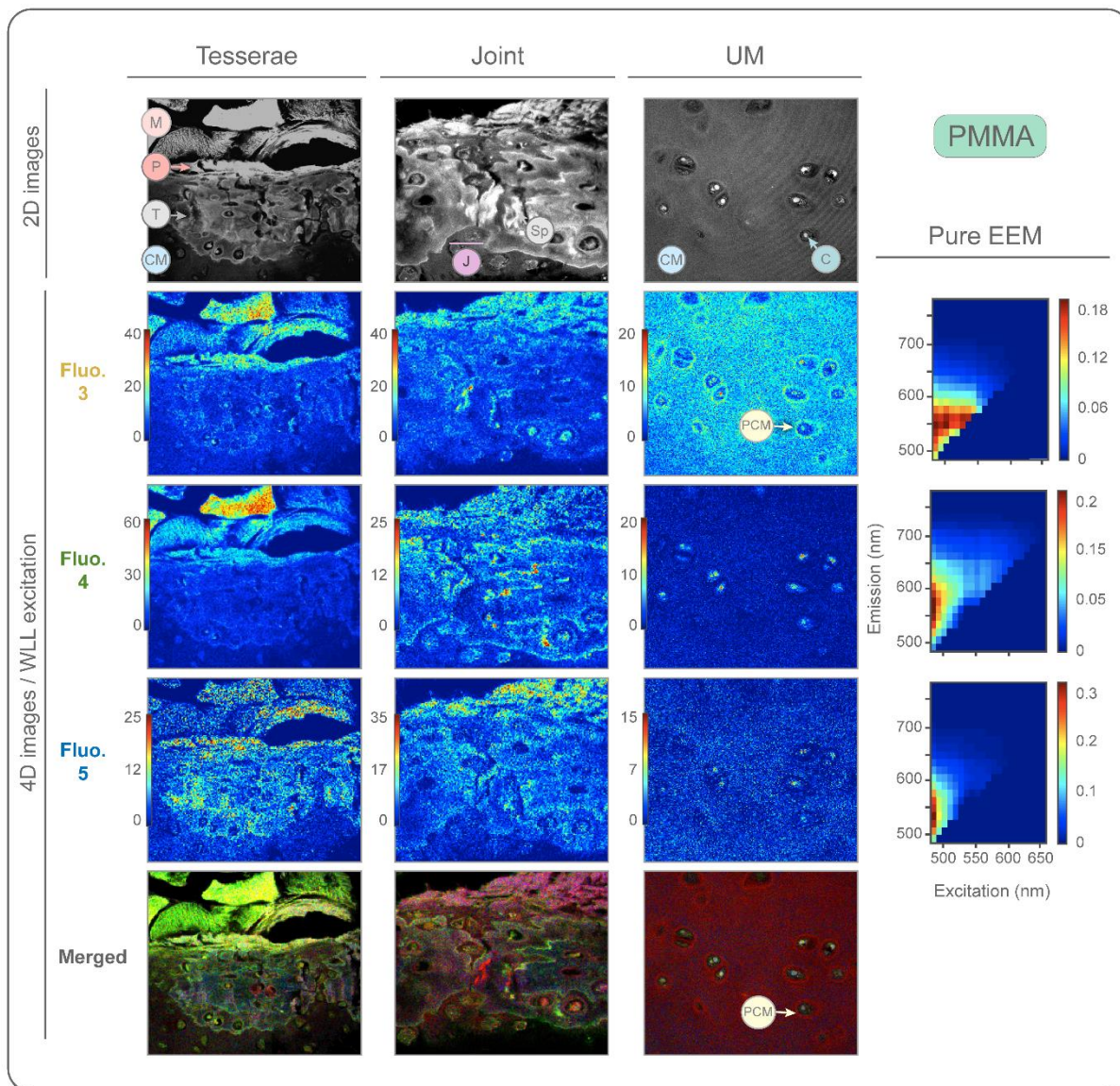











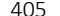

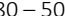
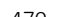





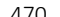

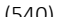



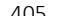
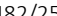


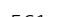



Fig. 11. Distribution maps and EEM of fluorescence signatures detected by MCR-ALS in PMMA samples excited with WLL. The 2D images (grayscale) images (top row) acquired with a 405 nm excitation laser and a wide wavelength emission filter provide reference for overall tissue appearance. The 4D images below show the distribution maps of each fluorescence signatures (Fluo. 3 - 5) identified (color bars indicate intensity). Excitation-emission (EEM) landscapes for each fluorescence signatures are shown to the right. At the bottom, merged distribution maps overlap both fluorescence signatures in the same image. **Abbreviations:** Chondrocytes (C), Unmineralized cartilage matrix (CM), Joints (J), Perichondrium (P), Tesseræ (T)

Table 2. Summary of excitation and emission wavelengths of each fluorescence signature and their tissue associations. Fluorescence signatures (identified with MCR-ALS) were denominated Fluo. 1, 2, 3, etc and are classified by sample preparation (paraffin, PMMA, thawed, or clarified samples) and image type (3D = 405 nm, 4D= WLL, SPIM). The emission and excitation wavelength range and peaks for each fluorescence signature are specified, with the equivalent color code bar illustrated below. The emission ranges listed for SPIM fluorescence signatures represent the emission filters used (see text). The presence of each fluorescence signature in specific tissue structures is annotated in the ‘Distribution’ column, organized by ROIs: Tesserae, Joints and Cartilaginous matrix [CM].

Sample preparation	Image type	Fluorescence signals	λ_{ex} (nm)		λ_{em} (nm)		Distribution
			range	(peak)	range	(peak)	
Paraffin	3D	Fluo. 1	405	-	425 - 700	(480 - 500)	Perichondrium Tesserae: central region + outer edge Joints: cells CM: cells
		Fluo. 2	470 - 570	(470)	475 - 650	(525 - 575)	Joints: matrix + cells CM: matrix + cells
	4D	Fluo. 3	480 - 570	(530 - 560)	500 - 620	(540 - 575)	Perichondrium Tesserae: spokes CM: matrix
		Fluo. 4	470 - 670	(470 - 500)	490 - 700	(500 - 590)	Tesserae: peripheral region + central border CM: cells
PMMA	3D	Fluo. 1	405	-	421 - 680	(480 - 500)	Tesserae: matrix + spokes Joint: matrix CM: matrix
		Fluo. 2	405	-	421 - 700	(495 - 500)	Muscle Perichondrium Tesserae: center region + outer edge Joint: cells CM: cells
	4D	Fluo. 3	470 - 600	(470 - 550)	490 - 640	(500 - 590)	Muscle Perichondrium Tesserae: spokes + cells CM: matrix + cells + PCM

		Fluo. 4	470 - 600 	(470 - 540) 	490 - 670 	(540 - 580) 	Muscle Perichondrium Tesserae: center border + outer edge Joint: cells CM: cells
		Fluo. 5	470 - 570 	(470 - 480) 	490 - 640 	(510 - 560) 	Muscle Perichondrium Tesserae: center + center border + outer edge CM: matrix
3D		Fluo. 1	405 	-	420 - 580 	(460 - 480) 	Tesserae: peripheral region
		Fluo. 2	405 	-	420 - 580 	(480 - 500) 	Tesserae: central region
Thawed	4D		470 	-	(500 - 620) 	(520) 	Tesserae: central region
		Fluo. 3	520 	-	(500 - 620) 	(545 - 580) 	Tesserae: central region
	4D		470 	-	(500 - 620) 	(540) 	Tesserae: peripheral region
		Fluo. 4	520 	-	530 - 640 	(530) 	Tesserae: peripheral region
Clarified	SPIM	Fluo. 1	405 	-	482/25 	-	Tesserae: peripheral region
		Fluo. 2	488 	-	520/50 	-	Perichondrium Tesserae: central region + outer edge Joints: cells CM: cells
		Fluo. 3	561 	-	593LP 	-	Joints: matrix CM: matrix

3.8. Tissue AF imaging at larger scales

In thick samples imaged by SPIM, muscle, cells, tesserae and perichondrium all emitted distinct AF signals, which differed in their excitation and emission wavelengths. The strongest excitation/emission pairings for each tissue are listed in Table 2. The perichondrium was the tissue with the strongest AF (Fluorophore 2; Fig. 8A), and needed to be saturated in image post-processing to allow other features to be visualized.

Tesserae were clearly visible beneath the perichondrium (Fig. 8A - D), exhibiting three spatially distinct regions, similar to those described above for PMMA samples, with distinctive AF wavelengths and intensities. The peripheral region of tesserae showed AF in the 482/25 nm filter window when excited with the 405 nm laser (Fluorophore 1, red in Fig. 8C). This region was encapsulated by a thin outer border delineating the edge of tesserae (~15 - 30 μm), which emitted a very localized AF signal in the 520/50 window (Fluorophore 2, green in Fig. 8C), when illuminated with a 488 nm excitation laser. The center region of tesserae emitted a signal with the same intensity and wavelength as the outer edge, forming a small, hazy autofluorescent region approximately the same cross-sectional shape as the tessera (in vertical and planar sections).

The unmineralized matrix emitted AF in the 593LP window when excited with the 561nm laser (Fluorophore 3 - dark blue in Fig. 8C), with low signal intensity in comparison with the cells and tesserae. However, even with low signal strength, local intensity differences could be appreciated. In particular, individual cells and cell groups were haloed by a zone of AF of lower intensity than that of the bulk cartilaginous matrix. Cells within the cartilaginous matrix and joints exhibited a strong AF (Fluorophore 2), whereas those within tesserae exhibited no visible signal. Although the resolution was not high enough to distinguish cellular form or structures (e.g. nucleus) to any degree, it was possible to visualize the large-scale, 3D arrangements of cells within the unmineralized matrix. For example, cells located directly beneath the tesserae tended to be isolated, yet with increasing distance into the cartilaginous core, tended to be organized into groups of two and then four.

4. Discussion

All major structural components of tessellated cartilage are autofluorescent, sensitive to a broad range of excitation wavelengths (405 - 600 nm). In particular, these components strongly reacted when excited with UV (405 nm), emitting AF with a diversity of tissue-specific green-yellow (i.e. within the 480 - 580 nm range). We show that it is possible to image both soft and hard tissue elements of tessellated cartilage by exciting tissue AF with confocal and SPIM microscopes, resolving tissue components at a broad range of size scales, from millimeter-down to subcellular spatial resolution (1 μm).

4.1. *Effect of preparation methods (PMMA, paraffin and thawed) on AF*

The specific fluorescence signatures we observed —although all within the excitation/emission ranges mentioned in the previous paragraph— were not consistent among the different sample preparations studied, differing in the number of fluorescence signatures detected, their spectral features, and where they were expressed. The reasons for these differences are unclear, but variation in autofluorescence is known to be linked to multiple aspects of sample preparation, as well as tissue composition. For example, the loss of AF in thawed samples could be related to the destructive influence of freezing and thawing on cartilage, which causes disruption of chondrocytes [37, 38] and proteolytic degradation of fibers (e.g. collagens, actin) in the extracellular matrix [39–41]. The AF signatures evident in preliminary thawed samples of tesserae, however, are promising for future research, indicating that neither embedding media nor fluorescent markers are required for the study of this tissue. Cryosectioning of samples will ensure more uniform samples (i.e. resulting in more features in-plane) to facilitate AF imaging in this regard.

With regard to embedded samples, the spectral differences between paraffin and PMMA multisets were not due to fixative effects, as both were fixed following the same protocol. Additionally, although tissue fixation with aldehydes (PFA, glutaraldehyde) can induce tissue AF due to the formation of chemical ring structures, the AF generated by PFA is generally low and hardly detectable with spectroscopy [42, 43]. Paraffin samples presenting fewer fluorophores could be related to the demineralization process. Decalcification using EDTA has been demonstrated to increase AF or produce changes in fluorophores location and/or spectra during mineral removal [44–46]. On the other hand, the capacity for AF from the mineral itself

—carbonated apatite in tesserae, as well as mammalian calcified cartilage and bone [40]— is still under debate, yet several studies showed that it is not autofluorescent [44–49]. It should be noted though that apatite AF has not been investigated at the excitation-emission wavelengths used in this study and should be explored. Additionally, several studies have demonstrated that high temperatures can quench tissue AF and, in our study, paraffin embedding was carried out at higher temperatures (60°C) than PMMA (4°C). Lastly, we are confident that AF differences among preparation types were not due to the embedding media themselves: we verified that both paraffin and PMMA exhibited negligible AF (the latter supported by other studies; e.g. [50, 51]) and moreover, the embedding media were removed from sections prior to imaging.

4.2. Tissue biology insights from AF imaging

Our demonstration of tissue-specific AF in tessellated cartilage opens new opportunities for high-resolution optical imaging and characterization of this tissue. This is particularly true for PMMA samples, which resulted in the highest quality images of tessellated cartilage, with well-defined mineralized and non-mineralized structures (e.g. mineralization fronts, Liesegang lines, spokes, cell nuclei), many not seen in other preparation methods.

4.2.1 Tesserae

The mineralized tissue (tesserae) in stingray cartilage exhibited consistent and strong AF, similar to mammalian calcified cartilage, which exhibits a strong two photon fluorescence signal [52]. Tesserae AF was typically partitioned into three discrete regions: a center region, peripheral region and a narrow border at the outer margin of the tesserae. Curiously, this regional partitioning differs from that typically used to describe tesserae structure, especially in histology, where tesserae are divided into upper “cap” and a lower “body” zones (*sensu* [10]).

In contrast, the three-zone AF we observed in tesserae shows no correspondence with any published histological work that we know of, although some images suggest the center can in fact stain differently than both cap and body (e.g. Fig. 9b in [8]). AF images of tesserae from another stingray species (*Urobatis*: [11]), however, suggest a similar three-zone pattern. In studies of shark species where calcium-binding dyes had been injected to study skeletal growth

[53, 54], fluorescence was also observed in central and outer border regions of tesserae, but attributed to areas of active mineralization and/or material turnover, with AF never considered [11]. For such skeletal age and growth work, our study underlines the importance of characterizing tissue AF to avoid erroneous conclusions, particularly in tissues where growth mechanisms are poorly known. The observations supporting the bipartite (histology-based) and tripartite (AF-based) schemes of tesserae organization argue that both represent real —but different— aspects of tissue composition and architecture.

Whereas differences in collagen and proteoglycan type could, for example, explain cap and body histological staining variation, differences in AF signal must be due to other factors (e.g. density variation of an autofluorescent component), perhaps linked to tesserae development and mineralization (e.g. the growth of tesserae at their margins). For example, the center region exhibits several distinctive characteristics, having comparatively high mineral density [19], association with acid-based stainings [8], and larger and more spherical cells than the remainder of the tessera [18]. We propose that these aspects and the center's AF are also linked to a specific early developmental stage of the skeleton, with the center's AF reflecting the size and shape of tesserae from that ontogenetic stage. Tesserae first form in the unmineralized cartilage, some distance from the perichondrium and not yet in contact with each other [8, 55], gradually increasing in size during ontogeny by accreting mineral on their margins until they come into contact and approach the perichondrium. The ontogenetic transition from isolated tesserae to abutting, perichondrally-associated tesserae therefore correlates with new tissue associations and perhaps the incorporation of different autofluorescent components, and so could be signified by the shift in fluorescence characteristics between the central and peripheral regions.

In contrast, the distinctness of outer border AF relative to that of the periphery could be related to the tesseral edge being an active site of mineralization [9, 25, 26], since mineralization fronts in osteonal bone also show defined autofluorescent bands [47]. In this regard, however, the multiple fluorophores shared between the center and outer border are more difficult to reconcile, as the center is believed to be a mineralization hub only earlier in skeletal development (see above). In the case of the center region, perhaps the AF signal is related to tissue age and degree of mineralization, as in bone [56]. The tissue properties and components at the root of the AF differences among the center, peripheral and outer border regions require

characterization; however, their autofluorescent characteristics and the accretionary growth of tesserae argue these differences are linked to the regions having specific developmental roles and/or representing important turning points in the mineralization of the skeleton.

The potential for AF imaging to inform our understanding of mineralization processes is further supported by the observation of mineralized spheroids in several regions of the tesserae in PMMA samples. These “calcospherites” have been observed by multiple authors at mineralization fronts in elasmobranch skeletons [10, 26, 57–59], but also in mammalian calcified cartilage and bone [60–63], where they are believed to act as accretive building blocks for mineralized tissue. In tessellated cartilage, such calcospherites have been demonstrated predominantly at interfaces between unmineralized cartilage and mineralized tissue, particularly those associated with cells: forming enclosures around chondrocytes in incipient tesserae in young animals or along the chondral border of established tesserae [9, 10, 25, 64]. In our study, AF images highlighted calcospherites in similar locations, but also lining the walls of lacunae in tesserae and additionally at the border between the center and peripheral regions, deeply embedded within the mineralized matrix of tesserae. This visible record of a past mineralization front supports our hypothesis of the autofluorescent center region as a snapshot of a specific developmental period in tesserae, while underlining AF as a useful tool to locate both active and former globular mineralization fronts.

4.2.2. Extracellular matrices

Cartilages are composed of a combination of several organic components (e.g. different collagen types, elastin, glycosaminoglycans), where their variation determines the mechanical properties and function of the tissue [2, 65]. In contrast to mammalian cartilage, the composition of elasmobranch cartilage is not well characterized, with only a few major components identified, such as the primary structural collagens (e.g. Coll1, Coll2). This lack of information is mainly related to the difficulty in identifying tissue components unequivocally, as their identification requires protocols that are either time-consuming/costly (e.g. development of elasmobranch-specific antibodies) or involve steps that can even hamper component identification or ultrastructural investigation (e.g. degradation of surrounding matrices). In comparing our AF data to existing information on tessellated cartilage structure and composition and our own data from other imaging modalities (histology, BSE), we propose

likely sources for some observed fluorophores, particularly those associated with tissues of known collagen composition.

Coll1 and Coll2 are well-known fluorophores in skeletal tissue [2]. In the elasmobranch skeleton, Coll1 is known to be present in both muscles and perichondrium [8]. Among the diverse fluorophores we observed associated with both the perichondrium and muscle (Table 2), the one with the highest intensity is likely associated with Coll1, having also a similar spectral profile of Coll1 in other taxa [4, 63-65] (Fig. 12A). Surprisingly, this fluorophore was also associated with chondrocytes of the unmineralized matrix, which are not known to express Coll1 [66, 67]

Additionally we propose, based on correspondence with immunostained samples, that the two fluorescent signals associated with the extracellular matrix (ECM) of joints and uncalcified cartilage represent or are linked to Coll2 (Fig. 12B). This collagen, in addition to being autofluorescent [41, 68], is indeed a primary component of the ECM of joints, unmineralized cartilage and tesserae [8, 66, 69] (see also Supp. Fig. 5). The specific distribution of these putative “Coll2 fluorophores” raises several interesting points relevant to growth and patterning of tessellated cartilage. First, the relatively homogeneous signal of the two fluorophores, seen throughout the ECM of joints, uncalcified cartilage and tesserae, supports the hypothesis that tesserae arise in and are predominantly composed of Coll2, despite some local variation of other materials (e.g. the mineral in tesserae or the Coll1 Sharpey’s fibers that insert into the cap from the perichondrium). Additionally, the localization of these two fluorophores in the tesserae indicates a potential advantage of AF imaging of tesserae over immunohistochemistry, where Coll2 antibody reactivity in tesserae was only possible after stringent digestion techniques [8]. Lastly, one of the “Coll2 fluorophores” presented an extremely high signal in the laminae of spokes, suggesting the composition of these distinct features, which have otherwise proved challenging to characterize [8, 19]. The factors driving the formation and periodicity of spokes are unknown, but their strong AF signal suggests spoke laminae are formed by packing Coll2 fibrils in particularly high density.

Given the limited data on tessellated cartilage tissue composition, the remaining fluorescence signatures are more difficult to assign to specific tissue components (Fig. 12C - F). In vertebrates, skeletal tissues contain a variety of fluorescent structural proteins and so, additional collagens or proteins like elastin may also be present in tessellated cartilage. Our

results, therefore, offer guides for future targeted characterization of tessellated cartilage structures, whose tissue compositions have yet to be determined.

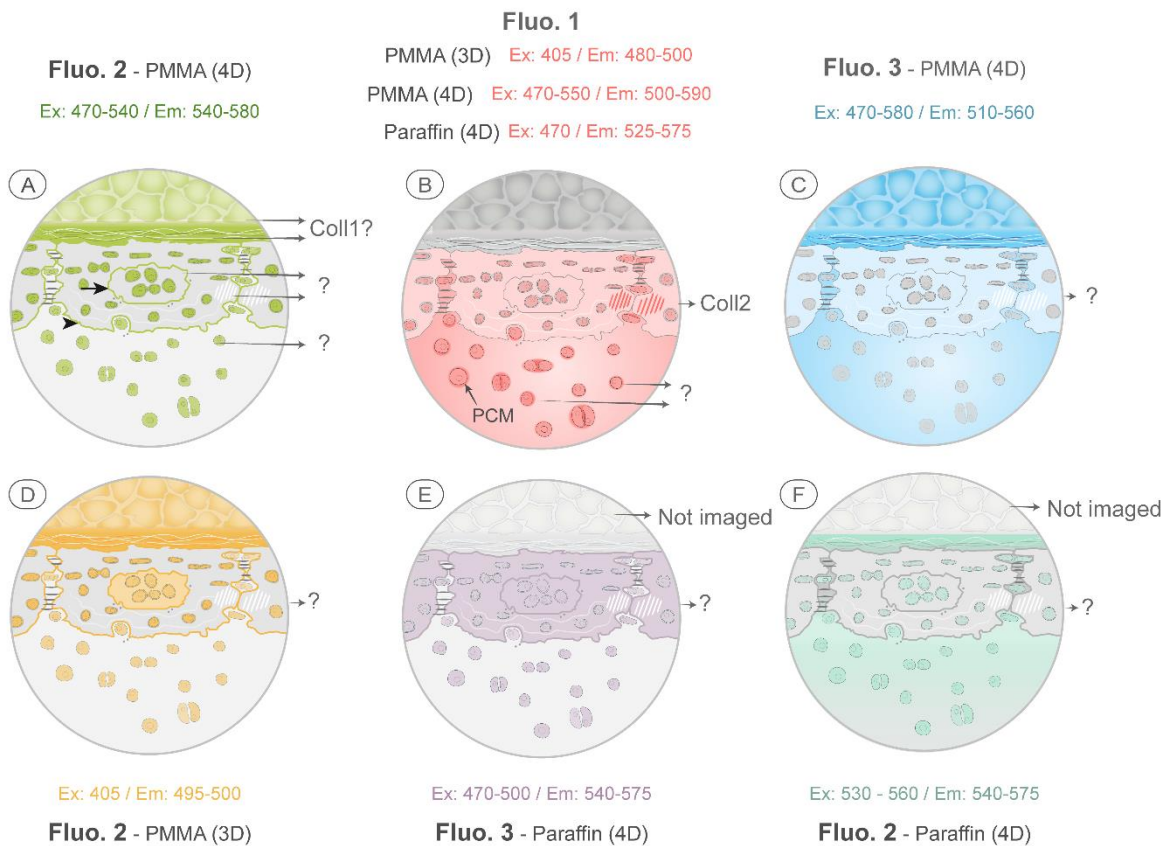


Fig. 12. Summary of tessellated cartilage fluorescence signatures localized, classified according to EEM, tissue location, and potential source. Each fluorescence signature's tissue associations are summarized visually in a color-coded tesserae schematic (see Figure 1). Fluorescence signatures are listed according to assigned numbers from Table 2, their sample preparation, and imaging modality (e.g. Fluo. 2, PMMA, 4D) and excitation (Ex) and emission (Em) values listed are the peak wavelengths associated with the strongest signal for that fluorescence signature. **A)** Fluorescence signatures associated potentially with Coll1 (in perichondrium and muscle). In contrast, the AF source associated with the border of the tesserae center, peripheral regions (arrowhead), the outer tesseral border (arrow) and the cells are unknown. **B)** Several fluorescence signatures likely related with Coll2, based on comparisons with immunostaining. The source of the AF in the pericellular matrix (PCM; Fluo. 1, PMMA, 4D) is unknown (in mammal cartilage, the PCM is comprised of Coll6). **C)** Unknown Fluorescence signatures distributed in muscle, perichondrium tesserae and matrix of joints and unmineralized cartilage, but absent in cells. **D)** Unknown fluorescence signatures observed in muscle, perichondrium, center-periphery border, and the outer margin of tesserae (arrow and arrowhead in A), and within cells. **E)** The source of this fluorescence signature is unknown, found in tesserae and cells. **F)** Unknown fluorescence signature in tesserae and all cells. **Abbreviations:** Pericellular matrix (PCM), Collagen type I (Coll1), Collagen type II (Coll2)

4.2.3. Cells

The AF signal provided information on cellular morphology, for example, demonstrating a clear pericellular matrix (PCM) region, a narrow tissue zone haloing chondrocytes in the unmineralized cartilage. In mammalian cartilage, the PCM acts as an interface between the cells and their environment and is crucial in determining how chondrocytes interact both mechanically and physicochemically with the surrounding matrix [70–72]. A factor in mediating these behaviors is the distinct composition of the PCM which, for example, has a higher proteoglycan content than the surrounding cartilage and is composed uniquely of collagen type VI [73, 74]. Indeed, the proteoglycan aggrecan is considered a potential source of pericellular AF in TPF [75, 76]. Despite its importance in mammalian cartilage, a defined PCM has never been described in elasmobranchs, neither with histology nor electron microscopy. Although we cannot yet identify the source of PCM AF, its defined signal in elasmobranch cartilage suggests it may have distinct compositional, architectural and/or mechanical characteristics, as in mammalian cartilage.

Despite fluorophores having different tissue associations, nearly all fluorophores observed were associated with chondrocytes. Cell AF is typically due to NADH, FAD⁺ (flavins) and lipofuscins (lipopigments), cytoplasmic components with distinct spectral profiles [22, 77–79]. Among these components, flavins are the only ones with a spectral signature located within the spectra used in this study ($\lambda_{em} = 440 - 470 \text{ nm} / \lambda_{ex} = 480 - 540 \text{ nm}$; [22]), whereas the other components are associated with lower wavelengths (<405 nm). Although the source(s) of cellular AF cannot be identified in this study, we note that chondrocytes emitted different signals depending on their location in the tissue. This may be indicative of cells' production of different components and, ultimately, variation in cell function. This hypothesis is supported by the cells in the upper part of the joint emitting a brighter AF signal than other cells, reinforcing the findings of Marconi et al. [67], where joint cells exhibited higher production of Coll2.

5. Conclusions

Tessellated cartilage contains a diversity of fluorophores that emit a native AF signal which, particularly after fixation, embedding and sectioning, is strong enough to image the tissue at a level of detail rivaling backscatter electron microscopy and histology. The AF signal was affected by sample preparation, which should be more deeply explored to clarify how tissue architectures and composition are distorted through common investigation techniques. Images of samples prepared for PMMA showed exceptional preservation of tissue morphology, especially mineralized parts, even allowing identification of active and former mineralization fronts through the localization of calcospherites. AF in tessellated cartilage is mainly emitted in the green - yellow region of the spectrum (480 - 580 nm), excited with a broad range of wavelengths (405 - 600 nm), but reacting most strongly to 405 nm excitation (UV). Several fluorophores could be associated with Coll1 and Coll2, the main structural collagens of tessellated cartilage; the diverse and specific distributions of other unidentified fluorophores, however, suggest the presence of additional collagens and/or other autofluorescent molecules yet to be characterized in elasmobranch cartilage. The localization of the varied fluorescent signatures allowed description of several tissue morphologies, including a novel organizational scheme of three concentric autofluorescent regions in tesserae and a pericellular matrix surrounding chondrocytes. Tissue AF is therefore demonstrated to be a powerful diagnostic tool to image tessellated cartilage that, with further studies and standardized methods, will allow us to generate composition maps without the need of more demanding preparation techniques.

Supplementary Materials

1. Sample preparation for histology, immunohistochemistry and electron microscopy

To compare the images obtained using AF signal with images obtained using more traditional methods and to facilitate location of structures of interest, tessellated cartilage samples were also examined using histology, immunohistochemistry and Backscatter Electron Microscopy (BSEM).

For histology, paraffin sections were stained with haematoxylin and eosin (HE) using a Shandon Varistain 24-4, Histocom (Vienna, Austria) automatic slide stainer. For toluidine blue staining to visualize distribution of proteoglycans, sections fixed with glutaraldehyde 2.5% and PFA 2.5%, were decalcified, EPON-embedded and manually stained.

Immunohistochemistry was performed for collagen type II (Coll2) on demineralized paraffin sections (7 μ m) using the Ventana Discovery XT research platform (Ventana, Strasbourg, France). The samples were previously fixed with 4% PFA during 6 hours. After deparaffinization of the sections, proteolytic induced antigen retrieval with Proteases 3 (Ventana, Strasbourg, France) was performed for 4 minutes. The subsequent protocol comprised incubation with a rabbit anti Coll2 primary antibody (1:200) (catalogue # CL50211AP, Cadarlane, Ontario, Canada) for 60 minutes, followed by incubation with the OmniMap anti-rabbit HRP (horseradish peroxidase) secondary antibody (ready to use) for 32 minutes. Visualization of the antigen-antibody complex was performed with a DAB (diaminobenzidine) detection kit for 8 minutes. Afterwards the sections were counterstained with haematoxylin. The cartilaginous long bones (femur, tibia) of an eight-day-old mouse served as a positive control. A negative control was obtained by substituting the primary antibody with antibody diluent. The negative control yielded no labelling.

For BSEM, samples embedded in PMMA blocks were cut to expose a transverse cross section of the sample and then polished with sandpaper plates of descending grain sizes, ending with the softer polishing plate (0.25 μ m) with diamond spray. Polished samples were imaged with the backscatter electron detector in a Field Emission-Environmental Scanning Electron Microscope (FE-ESEM, FEI Quanta 600F), in environmental mode (low vacuum and without sputtering) and at an accelerating voltage of 15 kV.

2. Analysis of the hyperspectral images

The unmixing algorithm used in this work, the Multivariate Curve Resolution-Alternating Least Squares (MCR-ALS), provides distinct fluorescence signatures formed by an individual fluorophore or by a consistent mixture of fluorophores associated with biological entities such as, for example, tissues (emission spectra or excitation/emission fluorescence landscapes for 3D and 4D images, respectively) and their related distribution maps (i.e. their spatial distribution in the 3D/4D source images) [22]. In fact, MCR-ALS recovers the information associated with the well-known Beer-Lambert law, obeyed by 3D and 4D fluorescence images, where the signal of any pixel spectrum is the concentration-weighted sum of the signal contributions of the pure distinct fluorescence signatures present in that pixel, as expressed in Equation (1). All PCA, MCR-ALS and NMF are methods of bilinear decomposition of data tables, i.e., they describe the variation of the raw data set (spectra in an image for instance) with a small number of component contributions, related to spectral signatures and concentration profiles. They differ in the way the components are calculated. In the case of PCA, components are calculated using the constraint of orthogonality and they cannot be interpreted as meaningful spectra or concentration maps (e.g., some spectra show negative parts). Instead, NMF and MCR-ALS use constraints naturally obeyed by the components to provide spectra and maps. NMF makes non-negativity mandatory to recover maps and spectra, whereas MCR-ALS is a more flexible algorithm that can optionally apply any constraint, for instance non-negativity, but also other conditions related to spatial map properties or spectral shapes. Additionally, MCR-ALS can work with a single image or with image multisets, whereas NMF is usually applied to single images.

MCR-ALS and most unmixing methods are typically applied to data organized into tables or matrices and, therefore, applying them to 3D and 4D images requires reformatting of datasets. With 3D fluorescence images, the initial image cube, sized (x,y,l) is unfolded as shown in Supplementary Figure 1A into a matrix \mathbf{D} , sized $(x \times y, l)$ that contains all pixel spectra stacked one under the other (i.e. each row contains an individual pixel spectrum). In Equation 1, \mathbf{s}_i^T represents the pure spectrum of the i^{th} spectral signature and \mathbf{c}_i the related concentration profile, quantifying the contribution of this signature to the signal of each pixel spectrum. The bilinear model in Equation 1 can be expressed in compact form, as shown in Equation 2 (Supp. Fig. 1A), where \mathbf{S}^T is the matrix that contains the distinct fluorescence signatures of all

fluorophores and the matrix **C** the related concentration profiles. The residuals of the model are expressed by the matrix **E**, which has the same dimensions as **D**. As can be seen in Supplementary Figure 1A, every concentration profile vector \mathbf{c}_i can be refolded into the original 2D image spatial structure to render the distribution map associated with each fluorescence contribution.

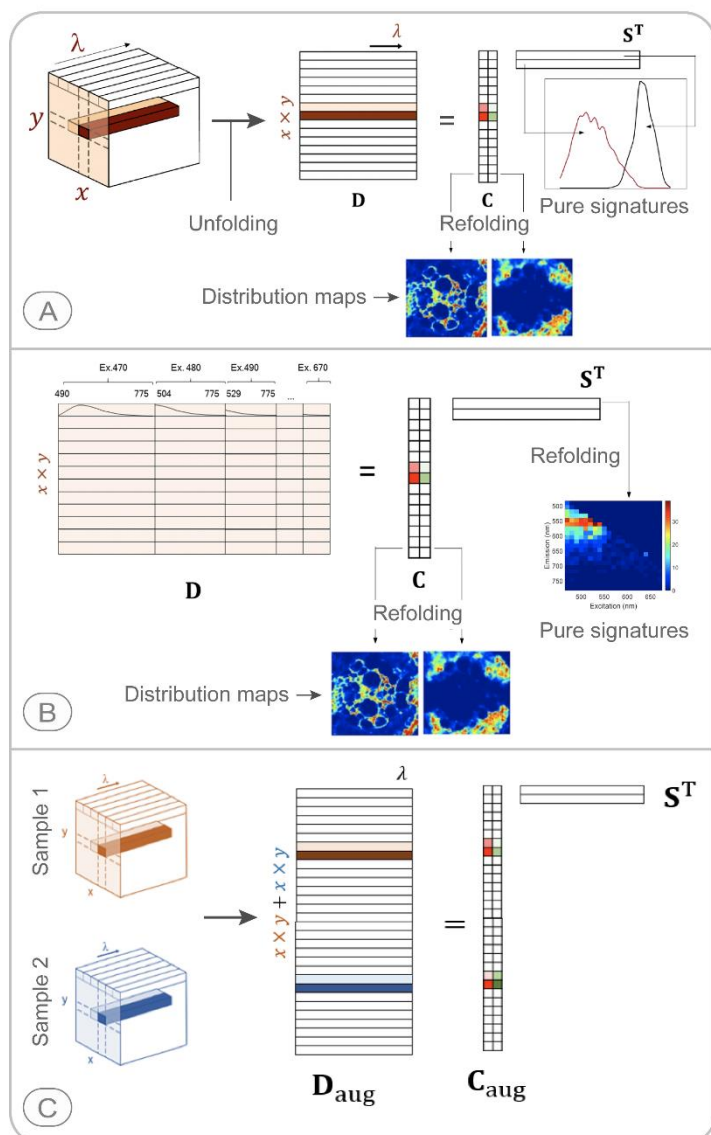
$$\mathbf{D} = \sum_i \mathbf{c}_i \mathbf{s}_i^T + \mathbf{E} \quad \text{Eq. 1}$$

$$\mathbf{D} = \mathbf{C}\mathbf{S}^T + \mathbf{E} \quad \text{Eq. 2}$$

Similarly, 4D fluorescence images can also be expressed as a bilinear model based on the Beer-Lambert. In this case, the 4D hyperspectral image, sized (x, y, l_{ex}, l_{em}) is transformed into a data matrix **D**, sized $(x \times y, l_{ex} \times l_{em})$ by concatenating, in each row of matrix **D**, the emission spectra collected at all tested excitation wavelengths for a particular pixel (Supp. Fig. 1B). As in 3D images, the distribution maps of compounds can be obtained by refolding their related concentration profiles and the pure 2D EEM (excitation-emission) landscapes for each distinct fluorescence signature can be retrieved by refolding the related extended profile in matrix \mathbf{S}^T (Supp. Fig. 1B).

When several images have similar information (e.g. they share some or all the unmixed contributions), a multiset structure can be built by appending the blocks of pixel spectra of the different images one under the other, as shown in Supplementary Figure 3C, to build an augmented data matrix, \mathbf{D}_{aug} . Multiset analyses help MCR-ALS to extract more accurate pure spectra profiles and distribution maps, since more information is added to the model and the profiles recovered satisfy the variation in all images used. Multisets can be built by combining 3D or 4D images, once they are in matrix form, as shown in Supplementary Figure 1C [30]. The only requirement to build a multiset is that the spectral range of the different images be common. The multiset configuration provides a single global bilinear model for all images analyzed together: the model has a single matrix \mathbf{S}^T , containing the distinct fluorescence signatures found in the included images, and an augmented matrix \mathbf{C}_{aug} , which contains concentration profile submatrices linked to the different images analyzed. The concentration profiles of each submatrix in \mathbf{C}_{aug} can be refolded to provide the related distribution maps for

each image analysed. The pure spectra signatures in \mathbf{S}^T are left as such for 3D image multisets, but are refolded into 2D EEM landscapes for 4D multiset images.



For any of the image data configurations described above, MCR-ALS recovers the bilinear model in Equation 2 through an alternating least squares optimization of matrices \mathbf{C} and \mathbf{S}^T under applied constraints (e.g. non-negativity), which help to ensure chemically meaningful concentration profiles and spectral signatures for the sample constituents [80, 81]. Once image datasets are properly configured, the application of MCR-ALS requires an estimation of the number of distinct fluorescence contributions, n , needed to describe the variation in the image dataset \mathbf{D} . This is usually done by Singular Value Decomposition (SVD) [82] although, when in doubt, several MCR models with different numbers of components may be tested and the final

choice can be guided by the model fit and the biological relevance of the retrieved profiles. To begin the iterative optimization, initial estimates of \mathbf{S}^T or \mathbf{C} are required.

Images collected in the same experimental conditions (e.g. all images of ROIs from PMMA-embedded samples acquired with the same spectral range) were combined into different multisets for analysis, as detailed in Table 1. A method based on the SIMPLISMA (simple-to-use interactive self-modelling analysis) algorithm [83] was used to select the n spectra of the image data set \mathbf{D} , which are most dissimilar (i.e., which exhibit the most distinct shapes), to be used as spectral initial estimates. The constraints applied during the optimization were non-negativity in the concentration profiles and pure spectra signatures. Note that, when needed, different constraints can be used for profiles in \mathbf{C} and \mathbf{S}^T and for the related submatrices multiset analysis, in order to adapt to the natural properties of images and spectroscopic techniques.

The iterative optimization was continued until the difference in fit between consecutive iterations was lower than 0.1%. Once this convergence criterion was satisfied, the algorithm stopped, resulting in the final solutions for \mathbf{C} and \mathbf{S}^T . In our study, to assess model fit, two parameters were considered:

the lack of fit

$$LOF (\%) = 100 \times \sqrt{\frac{\sum_{ij} e_{ij}^2}{\sum_{ij} d_{ij}^2}} \quad \text{Eq. 3}$$

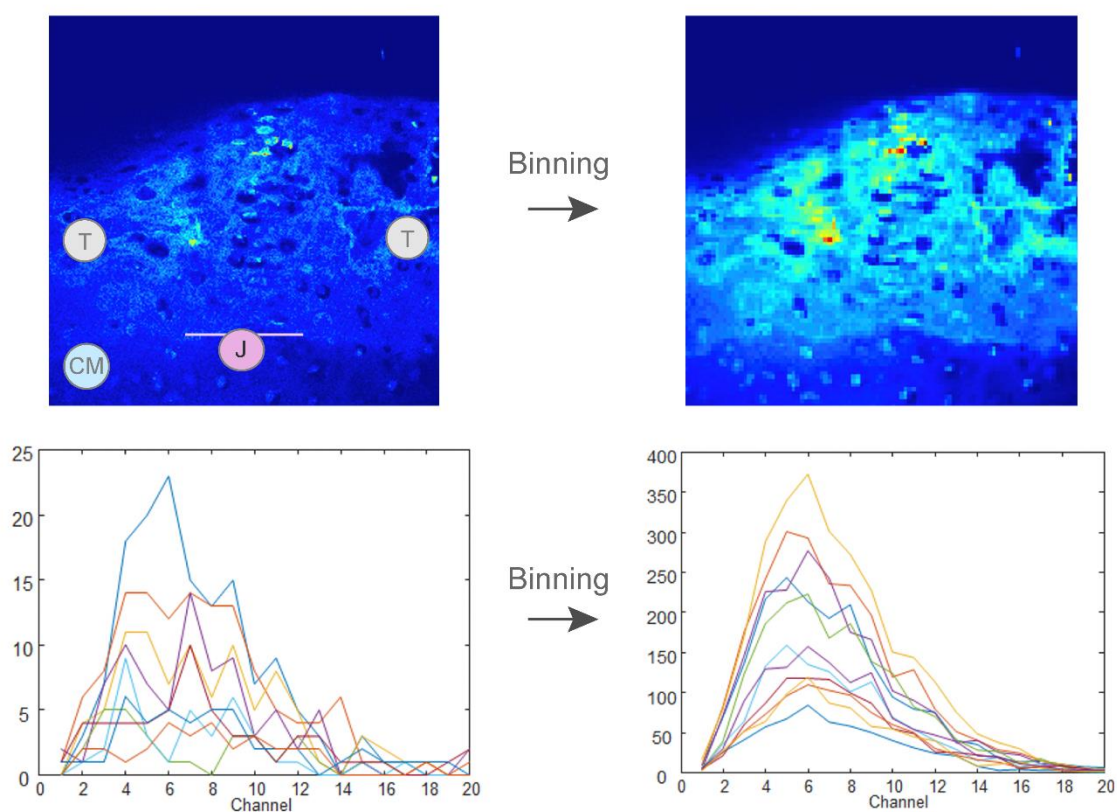
and the variance explained by the model

$$r^2 = 100 \times \left(1 - \frac{\sum_{ij} e_{ij}^2}{\sum_{ij} d_{ij}^2}\right) \quad \text{Eq. 4}$$

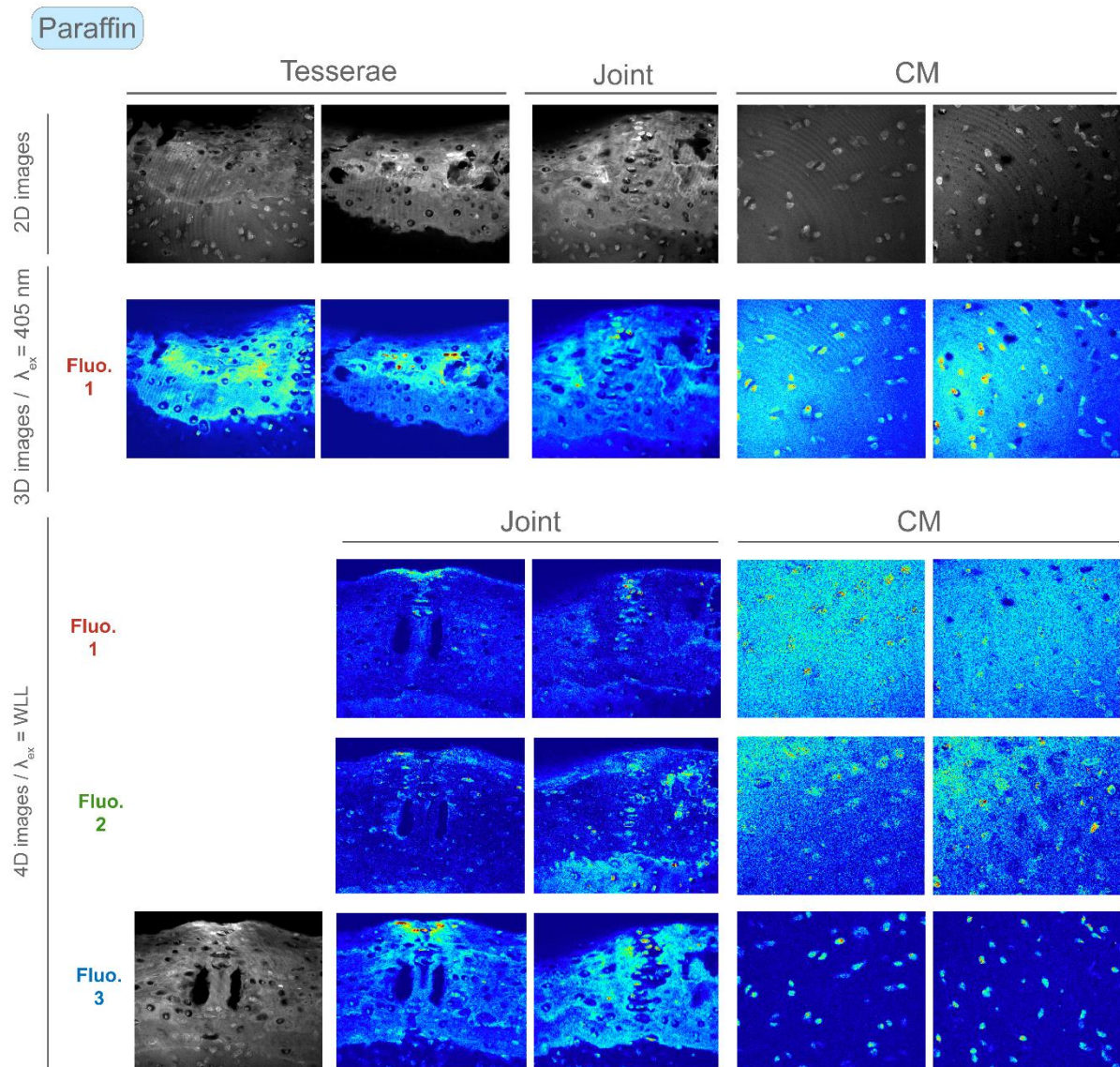
Where d_{ij} refers to the element of the original matrix \mathbf{D} of row i and column j , and e_{ij} refers to the related residual value obtained from the difference between the initial data set \mathbf{D} and the reconstructed matrix by using the bilinear MCR model, \mathbf{CS}^T . Once the final bilinear model formed by \mathbf{C} and \mathbf{S}^T was obtained, the distribution maps were recovered by refolding the

concentration profiles in **C** (as in Supp. Fig. 1A and 1B). Unmodified S^T profiles provided the pure spectral signatures directly for 3D fluorescence images, whereas for 4D images, the 2D EEM pure landscapes was recovered by refolding each of the profiles in S^T (as in Supp. Fig. 1B).

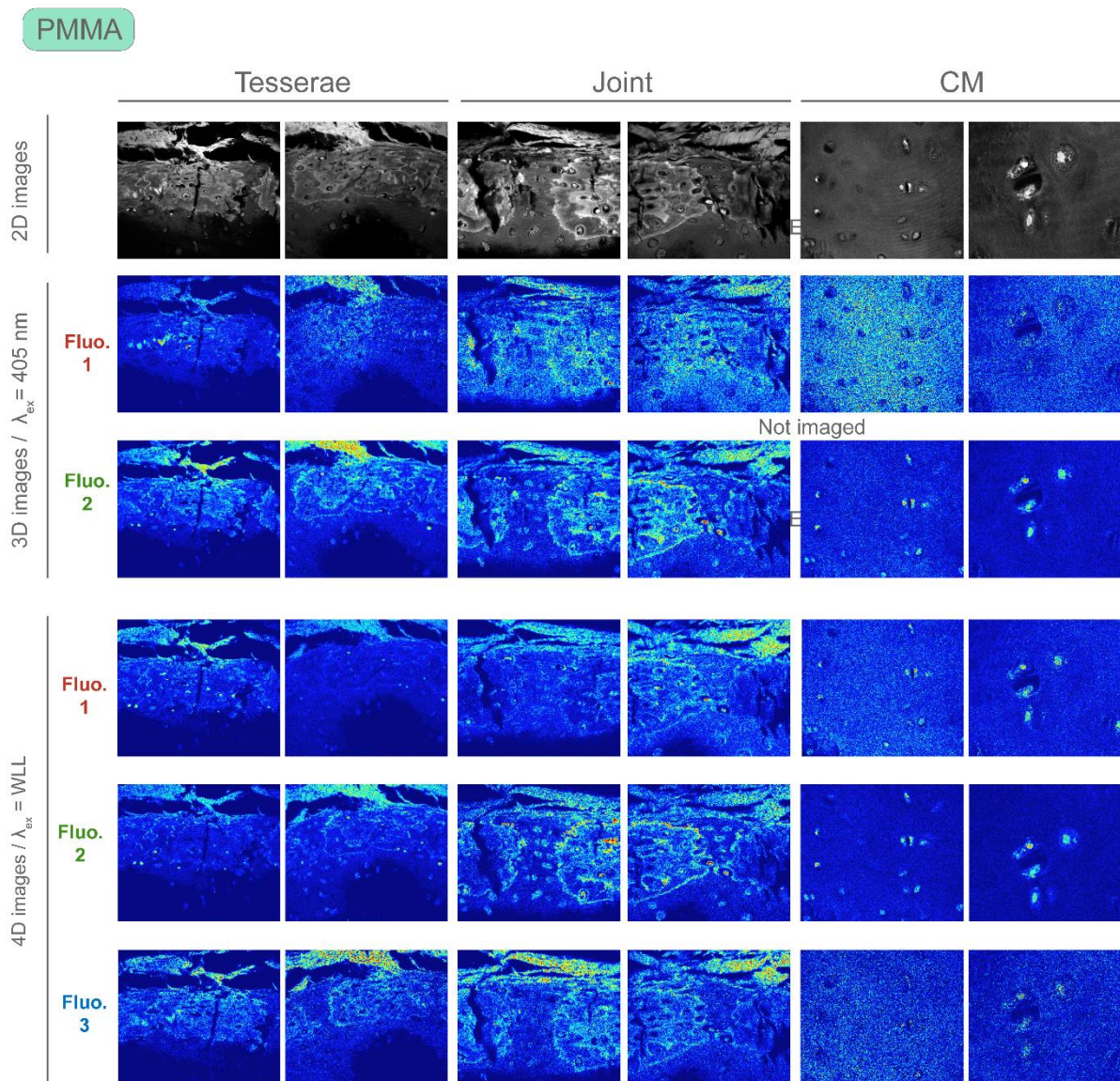
All images were preprocessed before applying the MCR-ALS analysis, by removing spectral zones affected by Rayleigh scattering in 4D images, and by spatial binning fluorescence spectra in both 3D and 4D images. Binning compensated for low per-pixel emission fluorescence due to the high pixel spatial resolution ($0.481 \mu\text{m} \times 0.481 \mu\text{m}$) and the possible low quantum yield of natural fluorophores. To improve the signal quality, spectra of adjacent pixels were summed to create a new larger pixel with a single spectrum of higher intensity and less noise. A 5×5 ($x \times y$) binning was applied, resulting in a pixel size of $2.405 \mu\text{m} \times 2.405 \mu\text{m}$, improving both morphological features and spectral shape (Supp. Fig. 2).



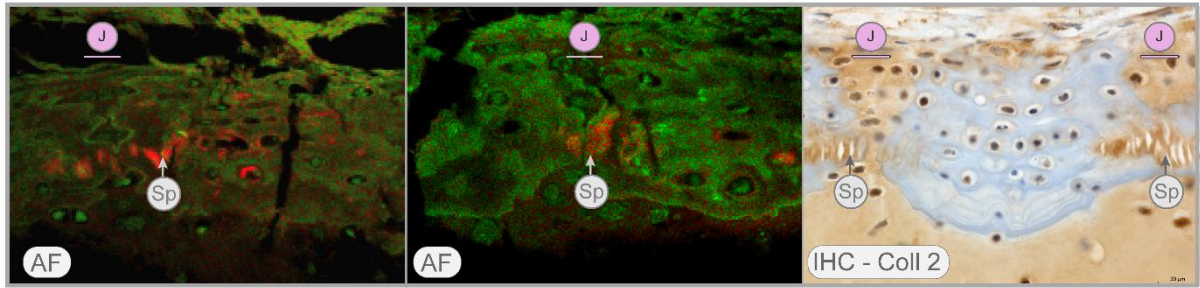
Supp. Fig. 2. Binning effects on images and spectra. On the left, before binning. On the right, after binning. The quality of spectra is increased, while tissue regions are still observable and often more clearly discerned with less noise



Supp. Fig. 3. Distribution maps of fluorescence signatures of decalcified, paraffin-embedded samples for all regions analyzed. The 2D images (grayscale) images (top and bottom of figure) acquired with a 405 nm excitation laser and a wide wavelength emission filter provide reference for overall tissue appearance. 3D images (row 2) show the distribution maps of the fluorescence signature detected when the sample was excited with the 405 nm laser. 4D images (rows 3-5) show the three different fluorescence signatures detected when excited with White Light Laser (WLL), with their corresponding distribution maps. The distribution maps shown here combined with those in Fig. 10, 11 and 12 comprise all paraffin maps included in the MCR-ALS analysis (with the exception of two additional cap zone distribution maps included in the analysis). Fluorescence signatures differ in emission-excitation wavelengths (shown in Fig. 10) and tissue distribution. See Table 2 and Figure 13 for summary



Supp. Fig. 4. Distribution maps of fluorescence signatures of mineralized, PMMA-embedded samples for all regions analyzed. The 2D images (grayscale) images (top row) acquired with a 405 nm excitation laser and a wide wavelength emission filter provide reference for overall tissue appearance. 3D images (rows 2-3) show the distribution maps of the two fluorescence signatures detected when the sample is excited with the 405 nm laser. 4D images (rows 4-6) show the three different fluorescence signatures detected when excited with a White Light Laser (WLL), with their corresponding distribution maps. Fluorescence signatures differ in emission-excitation wavelengths (shown in Fig. 11) and tissue distribution. See Table 2 and Figure 13 for summary. The distribution maps shown here combined with those in Fig. 10, 11 and 12 comprise all PMMA maps included in the MCR-ALS analysis



Supp. Fig. 5 Comparison of AF and immunohistochemistry (IHC) techniques showing collagen type II in tessellated cartilage. In AF images of tesserae (left and central images: Fluo. 1, PMMA, Ex: 405), the spokes (Sp), cartilage matrix in intratesseral lacunae, and the bulk unmineralized cartilage matrix (the latter out-of-plane here) exhibit a similar AF (pseudocolored red in the left and center images). With immunohistochemistry from *Raja clavata* (right), we demonstrate that all three of these regions are also positive for Coll2 (brown color), suggesting this is the source of the fluorescence signatures

References

- [1] Hall BK. *Bones and Cartilage: Developmental and Evolutionary Skeletal Biology*. San Diego (California): Elsevier Academic Press; 2005.
- [2] Pawlina W, Ross MH. *Histology: a text and atlas: with correlated cell and molecular biology*. Lippincott Williams & Wilkins; 2018.
- [3] Hall BK, Newman SA. *Cartilage Molecular Aspects*. CRC Press; 1991.
- [4] Bianco P, Cancedda FD, Riminucci M, Cancedda R. Bone formation via cartilage models: the “borderline” chondrocyte. *Matrix Biol*. 1998;17:185–92.
- [5] Cole AG, Hall BK. Cartilage is a metazoan tissue; integrating data from nonvertebrate sources. *Acta Zool*. 2004;85:69–80.
- [6] Zhang G, Cohn MJ. Hagfish and lancelet fibrillar collagens reveal that type II collagen-based cartilage evolved in stem vertebrates. *Proceedings of the National Academy of Sciences*. 2006;103:16829–33.
- [7] Dean MN. Chapter 03052 - Cartilaginous Fish Skeletal Tissues. Elsevier Ltd.; 2017.
- [8] Seidel R, Blumer M, Pechriggl E-J, Lyons K, Hall BK, Fratzl P, et al. Calcified cartilage or bone? Collagens in the tessellated endoskeletons of cartilaginous fish (sharks and rays). *J Struct Biol*. 2017;200:54–71.
- [9] Dean MN, Mull CG, Gorb SN, Summers AP. Ontogeny of the tessellated skeleton: insight from the skeletal growth of the round stingray *Urolophus halleri*. *J Anat*. 2009;215:227–39.
- [10] Kemp N, Westrin SK. Ultrastructure of calcified cartilage in the endoskeletal tesserae of sharks. *J Morphol*. 1979;160:75–101.
- [11] Dean MN, Ekstrom L, Monson-O’Rnan E, Ballantyne J, Witten PE, Riley C, et al. Mineral homeostasis and regulation of mineralization processes in the skeletons of sharks, rays and relatives (Elasmobranchii). *Semin Cell Dev Biol*. 2015;46 C:51–67.
- [12] Jayasankar AK, Seidel R, Hosny A, Weaver JC, Fratzl P, Chen J, et al. Multi-scale modeling and mechanical performance characterization of stingray skeleton-inspired tessellations. *J Mech Phys Solids*. 2020;138:103906.
- [13] Liu X, Dean MN, Youssefpour H, Summers AP, Earthman JC. Stress relaxation behavior of tessellated cartilage from the jaws of blue sharks. *J Mech Behav Biomed Mater*. 2014;29 C:68–80.
- [14] Liu X, Dean MN, Summers AP, Earthman JC. Composite model of the shark’s skeleton in bending: A novel architecture for biomimetic design of functional compression bias. *Mater Sci Eng C*. 2010;30:1077–84.
- [15] Seidel R, Jayasankar AK, Shahar R, Dean MN. The multiscale architectures of fish bone and tessellated cartilage and their relation to function. In: Estrin Y, Bréchet Y, Dunlop J, Fratzl P, editors. *Architected Materials in Nature and Engineering*. 2019. p. 329–53.
- [16] Dean MN, Gorb S, Summers AP. A cryoSEM method for preservation and visualization of calcified shark cartilage (and other stubborn heterogeneous skeletal tissues). *Microsc Today*. 2008;16:48–50.
- [17] Dean MN, Socha JJ, Hall BK, Summers AP. Canaliculi in the tessellated skeleton of cartilaginous fishes. *J Appl Ichthyol*. 2010;26:263–7.

- [18] Chaumel J, Schotte M, Bizzarro JJ, Zaslansky P, Fratzl P, Baum D, et al. Co-aligned chondrocytes: Zonal morphological variation and structured arrangement of cell lacunae in tessellated cartilage. *Bone*. 2020;134:115264.
- [19] Seidel R, Roschger A, Li L, Zhang Q, Yin J, Yang T, et al. Mechanical properties of stingray tesserae: High-resolution correlative analysis of mineral density and indentation moduli in tessellated cartilage. *Acta Biomater*. 2019;In review.
- [20] Debiais-Thibaud M. The Evolution of Endoskeletal Mineralisation in Chondrichthyan Fish. In: Johanson Z, Underwood C, Richter M, editors. *Evolution and Development of Fishes*. Cambridge University Press; 2018. p. 110–25.
- [21] Lakowicz JR. *Principles of Fluorescence Spectroscopy*. Springer Science & Business Media; 2013.
- [22] Croce AC, Bottiroli G. Autofluorescence spectroscopy and imaging: a tool for biomedical research and diagnosis. *Eur J Histochem*. 2014;58:2461.
- [23] Zipfel WR, Williams RM, Christie R, Nikitin AY, Hyman BT, Webb WW. Live tissue intrinsic emission microscopy using multiphoton-excited native fluorescence and second harmonic generation. *Proc Natl Acad Sci U S A*. 2003;100:7075–80.
- [24] Mansfield JC, Peter Winlove C, Moger J, Matcher SJ. Collagen fiber arrangement in normal and diseased cartilage studied by polarization sensitive nonlinear microscopy. *Journal of Biomedical Optics*. 2008;13:044020. doi:10.1117/1.2950318.
- [25] Seidel R, Lyons K, Blumer M, Zaslansky P, Fratzl P, Weaver JC, et al. Ultrastructural and developmental features of the tessellated endoskeleton of elasmobranchs (sharks and rays). *J Anat*. 2016;229:681–702.
- [26] Omelon S, Georgiou J, Variola F, Dean MN. Colocation and role of polyphosphates and alkaline phosphatase in apatite biomineralization of elasmobranch tesserae. *Acta Biomater*. 2014;10:3899–910.
- [27] Ashhurst D. The cartilaginous skeleton of an elasmobranch fish does not heal. *Matrix Biol*. 2004;23:15–22.
- [28] Juan A de, de Juan A. Multivariate curve resolution for hyperspectral image analysis. *Data Handling in Science and Technology*. 2020;:115–50. doi:10.1016/b978-0-444-63977-6.00007-9.
- [29] Juan A de, de Juan A, Piqueras S, Maeder M, Hancewicz T, Duponchel L, et al. Chemometric Tools for Image Analysis. *Infrared and Raman Spectroscopic Imaging*. 2014;:57–110. doi:10.1002/9783527678136.ch2.
- [30] Gómez-Sánchez A, Marro M, Marsal M, Loza-Alvarez P, De Juan A. 3D and 4D image fusion: coping with differences in spectroscopic modes among hyperspectral images. *Analytical Chemistry*. 2020. doi:10.1021/acs.analchem.0c00780.
- [31] Jaumot J, de Juan A, Tauler R. MCR-ALS GUI 2.0: New features and applications. *Chemometrics and Intelligent Laboratory Systems*. 2015;140:1–12. doi:10.1016/j.chemolab.2014.10.003.
- [32] Huisken J, Swoger J, Del Bene F, Wittbrodt J, Stelzer EHK. Optical sectioning deep inside live embryos by selective plane illumination microscopy. *Science*. 2004;305:1007–9.
- [33] Olarte OE, Andilla J, Gualda EJ, Loza-Alvarez P. Light-sheet microscopy: a tutorial. *Adv Opt Photon*, AOP. 2018;10:111–79.

- [34] Stefaniuk M, Gualda EJ, Pawlowska M, Legutko D, Matryba P, Koza P, et al. Light-sheet microscopy imaging of a whole cleared rat brain with Thy1-GFP transgene. *Sci Rep.* 2016;6:28209.
- [35] Klingberg A, Hasenberg A, Ludwig-Portugall I, Medyukhina A, Männ L, Brenzel A, et al. Fully Automated Evaluation of Total Glomerular Number and Capillary Tuft Size in Nephritic Kidneys Using Lightsheet Microscopy. *J Am Soc Nephrol.* 2017;28:452–9.
- [36] Hunziker EB, Lippuner K, Shintani N. How best to preserve and reveal the structural intricacies of cartilaginous tissue. *Matrix Biol.* 2014;39 C:33–43.
- [37] Muldrew K, Hurtig M, Novak K, Schachar N, McGann LE. Localization of freezing injury in articular cartilage. *Cryobiology.* 1994;31:31–8.
- [38] Muldrew K, Novak K, Yang H, Zernicke R, Schachar NS, McGann LE. Cryobiology of articular cartilage: ice morphology and recovery of chondrocytes. *Cryobiology.* 2000;40:102–9.
- [39] Szarko M, Muldrew K, Bertram JE. Freeze-thaw treatment effects on the dynamic mechanical properties of articular cartilage. *BMC Musculoskelet Disord.* 2010;11:231.
- [40] Peters AE, Comerford EJ, Macaulay S, Bates KT, Akhtar R. Micromechanical properties of canine femoral articular cartilage following multiple freeze-thaw cycles. *J Mech Behav Biomed Mater.* 2017;71:114–21.
- [41] Manning HB, Nickdel MB, Yamamoto K, Lagarto JL, Kelly DJ, Talbot CB, et al. Detection of cartilage matrix degradation by autofluorescence lifetime. *Matrix Biol.* 2013;32:32–8.
- [42] Leischner U, Schierloh A, Zieglgänsberger W, Dodt H-U. Formalin-induced fluorescence reveals cell shape and morphology in biological tissue samples. *PLoS One.* 2010;5:e10391.
- [43] Collins JS, Goldsmith TH. Spectral properties of fluorescence induced by glutaraldehyde fixation. *J Histochem Cytochem.* 1981;29:411–4.
- [44] Capasso L, D’Anastasio R, Guarnieri S, Viciano J, Marigliò M. Bone natural autofluorescence and confocal laser scanning microscopy: Preliminary results of a novel useful tool to distinguish between forensic and ancient human skeletal remains. *Forensic Sci Int.* 2017;272:87–96.
- [45] Bachman CH, Ellis EH. Fluorescence of bone. *Nature.* 1965;206:1328–31.
- [46] Valiev RR, Kalugina YN, Cherepanov VN. Theoretical investigation of fluorescence properties of EDTA and DTPA substituted tetraphenylporphyrin molecules. *Spectrochim Acta A Mol Biomol Spectrosc.* 2012;99:122–5.
- [47] Prentice AI. Autofluorescence of bone tissues. *J Clin Pathol.* 1967;20:717–9.
- [48] Armstrong WG, Horsley HJ. Isolation of fluorescent components from ox-bone human dentine and gelatin. *Nature.* 1966;211:981.
- [49] Laifer LI, O’Brien KM, Stetz ML, Gindi GR, Garrand TJ, Deckelbaum LI. Biochemical basis for the difference between normal and atherosclerotic arterial fluorescence. *Circulation.* 1989;80:1893–901.
- [50] Hawkins KR, Yager P. Nonlinear decrease of background fluorescence in polymer thin-films--a survey of materials and how they can complicate fluorescence detection in μ TAS. *Lab Chip.* 2003;3:248–52.

- [51] Araujo GR, Pollmann T, Ulrich A. Photoluminescence response of acrylic (PMMA) and polytetrafluoroethylene (PTFE) to ultraviolet light. *The European Physical Journal C*. 2019;79:653.
- [52] Mansfield JC, Peter Winlove C. A multi-modal multiphoton investigation of microstructure in the deep zone and calcified cartilage. *J Anat*. 2012;220:405–16.
- [53] Boyne PJ. Study of the chronologic development and eruption of teeth in elasmobranchs. *J Dent Res*. 1970;49:556–60.
- [54] Applegate SP. A survey of shark hard parts. In: Gilbert PW, Matthewson RF, Rail DP, editors. *Sharks, Skates and Rays*. 1967. p. 37–67.
- [55] Eames BF, Allen N, Young J, Kaplan A, Helms JA, Schneider RA. Skeletogenesis in the swell shark *Cephaloscyllium ventriosum*. *J Anat*. 2007;210:542–54.
- [56] Fauch L, Palander A, Dekker H, Schulten EA, Koistinen A, Kullaa A, et al. Narrowband-autofluorescence imaging for bone analysis. *Biomed Opt Express*. 2019;10:2367–82.
- [57] Ørvig T. Histologic studies of Placoderms and fossil Elasmobranchs. I: The endoskeleton, with remarks on the hard tissues of lower vertebrates in general. *Arkiv för Zoologi*. 1951;2:321–454.
- [58] Seidel R, Blumer M, Zaslansky P, Knötel D, Huber DR, Weaver JC, et al. Ultrastructural, material and crystallographic description of endophytic masses - A possible damage response in shark and ray tessellated calcified cartilage. *J Struct Biol*. 2017;198:5–18.
- [59] Takagi M, Parmley RT, Denys FR, Yagasaki H, Toda Y. Ultrastructural cytochemistry of proteoglycans associated with calcification of shark cartilage. *Anat Rec*. 1984;208:149–58.
- [60] Gorski JP. Biomineralization of bone: a fresh view of the roles of non-collagenous proteins. *Front Biosci*. 2011;16:2598–621.
- [61] Omelon SJ, Grynopas MD. Relationships between Polyphosphate Chemistry, Biochemistry and Apatite Biomineralization. *Chem Rev*. 2008;108:4694–715.
- [62] Reznikov N, Steele JAM, Fratzl P, Stevens MM. A materials science vision of extracellular matrix mineralization. *Nature Reviews Materials*. 2016;1:16041.
- [63] Ali SY, Yousuf Ali S, Wisby A. Mitochondrial granules of chondrocytes in cryosections of growth cartilage. *American Journal of Anatomy*. 1975;144:243–8. doi:10.1002/aja.1001440209.
- [64] Peignoux-Deville J, Lallier F, Vidal B. Evidence for the presence of osseous tissue in dogfish vertebrae. *Cell Tissue Res*. 1982;222:605–14.
- [65] Hall BK. *Bones and Cartilage*. Academic Press; 2014.
- [66] Enault S, Muñoz DN, Silva WTAF, Borday-Birraux V, Bonade M, Oulion S, et al. Molecular footprinting of skeletal tissues in the catshark *Scyliorhinus canicula* and the clawed frog *Xenopus tropicalis* identifies conserved and derived features of vertebrate calcification. *Front Genet*. 2015;6:1–14.
- [67] Marconi A, Hancock-Ronemus A, Andrew Gillis J. Adult chondrogenesis and spontaneous cartilage repair in the skate, *Leucoraja erinacea*. *eLife*. 2020;9. doi:10.7554/elife.53414.
- [68] Makarov MS, Storozheva MV, Borovkova NV. Collagen Fiber Autofluorescence Level in Evaluating the Biological Properties of Tissue Grafts. *Современные технологии в медицине*. 2017;9 2 (eng).

<https://cyberleninka.ru/article/n/collagen-fiber-autofluorescence-level-in-evaluating-the-biological-properties-of-tissue-grafts>. Accessed 22 Jul 2020.

- [69] Egerbacher M, Helmreich M, Mayrhofer E, Böck P. Mineralisation of the hyaline cartilage in the small-spotted dogfish *Scyliorhinus canicula* L. *Scr Med* . 2006;79:199–212.
- [70] Guilak F, Alexopoulos LG, Upton ML, Youn I, Choi JB, Cao L, et al. The pericellular matrix as a transducer of biomechanical and biochemical signals in articular cartilage. *Ann N Y Acad Sci*. 2006;1068:498–512.
- [71] Poole CA, Flint MH, Beaumont BW. Chondrons in cartilage: ultrastructural analysis of the pericellular microenvironment in adult human articular cartilages. *J Orthop Res*. 1987;5:509–22.
- [72] Chen C, Tambe DT, Deng L, Yang L. Biomechanical properties and mechanobiology of the articular chondrocyte. *Am J Physiol Cell Physiol*. 2013;305:C1202–8.
- [73] Wilusz RE, Sanchez-Adams J, Guilak F. The structure and function of the pericellular matrix of articular cartilage. *Matrix Biol*. 2014;39 C:25–32.
- [74] Poole CA, Ayad S, Gilbert RT. Chondrons from articular cartilage. V. Immunohistochemical evaluation of type VI collagen organisation in isolated chondrons by light, confocal and electron microscopy. *J Cell Sci*. 1992;103 (Pt 4):1101–10.
- [75] Mansfield JC, Peter Winlove C, Knapp K, Matcher SJ. Imaging articular cartilage using second harmonic generation microscopy. *Multiphoton Microscopy in the Biomedical Sciences VI*. 2006. doi:10.1117/12.643830.
- [76] Yeh AT, Hammer-Wilson MJ, Van Sickle DC, Benton HP, Zoumi A, Tromberg BJ, et al. Nonlinear optical microscopy of articular cartilage. *Osteoarthritis Cartilage*. 2005;13:345–52.
- [77] Surre J, Saint-Ruf C, Collin V, Orenca S, Ramjeet M, Matic I. Strong increase in the autofluorescence of cells signals struggle for survival. *Scientific Reports*. 2018;8. doi:10.1038/s41598-018-30623-2.
- [78] Jahn K, Buschmann V, Hille C. Simultaneous Fluorescence and Phosphorescence Lifetime Imaging Microscopy in Living Cells. *Scientific Reports*. 2015;5. doi:10.1038/srep14334.
- [79] Andersson, Andersson, Baechi, Hoechl, Richter. Autofluorescence of living cells. *Journal of Microscopy*. 2002;191:1–7. doi:10.1046/j.1365-2818.1998.00347.x.
- [80] Tauler R. Multivariate curve resolution applied to second order data. *Chemometrics Intellig Lab Syst*. 1995;30:133–46.
- [81] Tauler R, Maeder M, de Juan A. Multiset Data Analysis: Extended Multivariate Curve Resolution. *Comprehensive Chemometrics*. 2020;:305–36. doi:10.1016/b978-0-12-409547-2.14702-x.
- [82] Golub GH, Van Loan CF. *Matrix Computations*. JHU Press; 2012.
- [83] Windig W, Guilment J. Interactive self-modeling mixture analysis. *Anal Chem*. 1991;63:1425–32.

VI | DISCUSSION

Studies of biological structures rely on imaging techniques to measure and characterize different physiological parameters of tissues, cells and molecules. As a consequence, the development of imaging techniques is often directly correlated with progress and questions in the biological sciences, allowing new insights into tissue organization and cell function. In the last century, in the study of skeletal biology, imaging techniques have mainly been applied to extensively-studied model organisms (e.g. mouse, zebrafish, fruit flies), with the resulting knowledge of biological phenomena then extrapolated to other organisms [1]. However, organisms are highly diverse, the sum-result of phylogenetic history and the evolution of adaptations to survive in different environments; therefore, the information obtained from model organisms is not always accurate to describe other taxa. For example, despite being used for a host of medical research, the skeletal tissues of mice are by no means directly applicable to humans, nor average for vertebrates [2,3]. The broader applicability of fruit flies and zebrafish as models can be similarly challenged. That is not to say these models are without value, rather that proper context (e.g. in phylogeny, ecology) is necessary for interpretation. In order to study a broader range of organisms and their different adaptations to their environments, new imaging techniques and mindsets are required, that are not only geared toward imaging biology in its native state in ways that are minimally invasive/destructive, but also not tethered to assumptions and fluorophores derived from and for model species. However, as emerging techniques are often based on a broad range of physical and chemical principles and biological context is vital for interpretation and direction, multi-disciplinary collaborations between diverse scientists is paramount, requiring cooperation among biologists, computational scientists, physicists, chemists, mathematicians and engineers.

In this dissertation, through a collaboration with scientists from different backgrounds, two label-free imaging techniques were optimized to image and characterize elasmobranch skeletal cartilage, leading to new information about tissue and cellular structures, composition and organization, in 2D and 3D. In the following discussion, the advances and future applications of the optimized techniques are described, followed by the discussion of the significant discoveries in elasmobranch skeletal biology in this dissertation and how these are determinant for the understanding of cartilage biology, the diversity of cartilage in vertebrates and skeletal evolution.

1. Advances in cartilage imaging techniques

Two label-free imaging techniques and analysis workflows were optimized to characterize elasmobranch skeletal cartilage: 1) high-resolution synchrotron microCT (SR- μ CT) imaging combined with a morphometric analysis using an Amira custom workflow and 2) autofluorescence imaging and tissue characterization using a hyperspectral image analysis algorithm (MCR-ALS). Both techniques provided advancements in elasmobranch skeletal cartilage imaging, especially regarding non-mineralized structures such as cells and cartilage matrix, which are commonly challenging to characterize and image due to the difficulty posed by sample processing. As such, to facilitate our imaging goals, this dissertation also developed and refined a series of sample preparation protocols geared toward elasmobranch cartilage imaging.

Fixation is the first and one of the most crucial steps to prepare the tissue for imaging and characterization. In elasmobranch cartilage, cells happened to be especially difficult to preserve, even more than their counterparts in other species, like mammalian chondrocytes. During the doctoral period, we developed fixation protocols to optimize cellular and matrix preservation, which is usually challenging in field-work conditions. However, to preserve cellular morphology and ultrastructure, it is necessary to work with laboratory animals under controlled conditions, as it is the only way to correctly perform crucial fixation steps, such as keeping post-mortem times short, using freshly prepared fixatives and use of laboratory equipment. The presented results represent the best cartilage and cell ultrastructure and morphology data obtained for elasmobranch cartilage to date, which allowed a battery of studies at different scales (from nm to μ m), including ultrastructure imaging in electron microscopy and comparison with mammalian chondrocytes. However, although fixation conditions and steps were similar to those used to preserve the cell ultrastructure in mammals, the obtained cellular ultrastructure is still sub-optimal, with most cells exhibiting a distorted appearance, especially for those living within the tesserae. This indicates that different factors may be influencing the fixation of cells in elasmobranch cartilage and, although these factors are still unknown, it could be argued that they may be related to differences in pH between elasmobranch and mammals; elasmobranchs have a more basic pH (7.45 - 7.82) than mammals (7.38 - 7.44), due to the different plasma concentration of carbon dioxide [4]. Additionally, the osmolality of elasmobranch tissues and body fluids is considerably different from that of

mammals (e.g. containing large amounts of urea and methylamines), which should also influence solute behavior during tissue fixation [5,6,7]. These persistent challenges to tissue fixation, in fact, are representative of our limited knowledge of tissue structure and composition and that there are surely profound differences with mammalian tissues that remain to be characterized. Further studies need to focus on developing protocols optimized more specifically for elasmobranch tissue fixation, which is usually not considered as a crucial step in most studies in elasmobranch research, which often erroneously assume the tissue will behave like mammalian cartilage.

In fact, in previously published work, tesserae cells always present a shrunken appearance [8,9,10], making the characterization of their morphological aspects and ultrastructure impossible. As a result, tesserae cells are less known than other components of the tessellated skeleton, despite being probably essential units of tesserae biomechanics, mineralization and function. To sort out the preservation handicap, we developed a label-free imaging technique to study tessellated cartilage cells that does not require a well-preserved tissue, using, instead, the lacunae (spaces where cells reside) morphology as a proxy to characterize the morphology, orientation and organization of the tesserae cells [11,12]. Lacunae were imaged using SR- μ CT, obtaining 3D images of several tesserae with a high contrast between denser materials (mineralized) and less dense materials (lacunae spaces). The custom workflow we developed and applied in Amira for quantitative and statistical analysis [12] offers a standardized protocol to analyze tesserae datasets, which can be used to compare lacunae organization and orientation from different skeletal elements, species and ages. The information obtained from these comparisons can be used to analyze tesserae ultrastructure across different body regions and developmental stages, to build broader hypotheses of cellular roles in mineralization, development and biomechanics. Until now, there has been no exploration of regional variation in tessellated cartilage (e.g. how mineralized and unmineralized tissues vary throughout the skeleton, according to skeletal shape or role); our technique makes this more tractable, by facilitating high-throughput analysis of morphology. Also, our workflow can be used to study other species and porosities in the tissues of other taxonomic groups, being highly valuable for delicate samples like museum specimens since it is a label-free and non-destructive technique that does not require well-fixed samples (e.g. samples that have lost their soft tissues like fossils, and less-well preserved samples such as, for example, the myriad museum specimens preserved in formalin and ethanol). Our workflow therefore helps to advance morphological

research in general, at a variety of scales, by facilitating anatomical analyses of physiologically-relevant structural features in large digital datasets (e.g. from synchrotron tomography or lab-based microCT). As more and more organismal CT scan data is made freely available online, through museum digitization services and web-based scan databases (e.g. OVert, MorphoSource), such workflows have increasing utility.

Despite SR- μ CT being a convenient technique to image the tesserae cells indirectly, it is not suitable to directly image non-mineralized structures (e.g. cells, matrix) with enough contrast for their characterization. Usually, in elasmobranch skeletal cartilage, non-mineralized structures are imaged using techniques such as classical histology or immunohistochemistry, which require external reagents to highlight specific components. To avoid the use of external reagents, we optimized a label-free imaging technique based on detecting the autofluorescence signal of the tissue [13]. Despite tissue fluorescence being a key tool in determining animal age and growth studies (through the use of fluorescent markers to label growing tissues; [14]), the native fluorescence of tessellated cartilage had never been characterized, although there were hints in the literature that it might be autofluorescent [4]. The images resulting from Paper 3 show that the tissue indeed has a rich inherent fluorescence, strong enough to visualize well defined structure of both mineralized and non-mineralized components, structures that usually are challenging to image simultaneously and rather require a combination of different techniques catering to each tissue phase, such as SEM (mineralized tissues) and histology (unmineralized tissues). The possibility to image both structures using one single technique offers the advantage of studying the tissue as a single complex composite, analyzing the interactions and arrangement of all structures in the same image and at different scales (from μm to cm).

In addition, as the autofluorescence signal is an intrinsic property of the molecules, it is not necessary to know the tissue components (or target molecules) beforehand, as is the case with immunohistochemistry or *in situ* hybridization, where targeted probes need to be used. Therefore, autofluorescence is a powerful tool to localize species-specific tissue components and the structures they can form (e.g. matrix, canals), while also acting as an exploratory tool. For example, in our study, we identified a pervasive but unknown autofluorescent component located in the cartilage matrix of elasmobranchs, different from the Col2 known to pattern the majority of the matrix [13]. Although this component remains unidentified, it may be an

elasmobranch-specific molecule forming the cartilage matrix, similar to myxinin and lamprin, species-specific structural proteins forming the cartilage matrix of hagfishes and lampreys, respectively [15,16,17]. This demonstrates that autofluorescence signal is a useful technique to spotlight unexpected features in tissues by not being tied to image a specific fluorophore. Lastly, as the images were obtained using the intrinsic autofluorescence of the tissue, this technique is not limited to image elasmobranch skeletal cartilage, being suitable to image any tissue as long as it has autofluorescent components. This approach can be highly useful for studies that require a comparative study among different species, especially those including non-model organisms whose non-mineralized tissues cannot be properly imaged using conventional staining techniques. As studies like Paper 3 allow the elucidation of specific spectral signatures for tissue components, increase in the use of autofluorescence as an imaging tool in non-model organisms can lead to the building of a rich database or 'look-up table' for spectral properties and the tissues associated with them (resources common for techniques like Raman spectroscopy or FTIR), valuable as both a diagnostic and exploratory tool.

2. Advances in cartilage biology

The preparation, imaging and analysis techniques used were demonstrated to be efficient and accurate to study elasmobranch skeletal cartilage, providing new information about cartilage structure, composition, cell biology and biomechanics. In this way, the results obtained indicated that the two primary structural components of the elasmobranch skeleton —the tesserae and the unmineralized matrix— differ in tissue composition and cell morphology and organization, an observation that demonstrates how evolution can play with the basic cartilage model to adapt the tissue for novel functional roles.

Tesserae are a distinct skeletal structure of elasmobranchs, having a peculiar tissue organization and material composition that is believed to play a crucial role in skeletal biomechanics by making the skeleton stiff and flexible at the same time [18,19]. Among other particularities, such as their organization based on polygonal tiles joined together [20,21], the cellular organization also appears to be a distinct adaptation of the elasmobranch group. These cells have been described by several authors as chondrocytes (e.g. [8,10,20]); however, while

they are in appearance similar to chondrocytes, their organization within the tesserae suggest that the cellular origin, lifespan and function during both mineralization and within the tesserae may differ from what is known for chondrocytes in other vertebrates. As such, the data from this dissertation suggest that elasmobranch chondrocytes differ from other vertebrate chondrocytes in several aspects.

First, elasmobranch chondrocytes survive the mineralization process without any variation in their morphology, volume and density (i.e. they do not appear to be altered by the mineralization of the surrounding matrix). Once they have been enclosed in the tesserae, the variation in their morphology and orientation depends on their position within the tesserae, suggesting the tissues they arose in (perichondrium or unmineralized cartilage) may dictate their shape and perhaps function in tesserae (see below; Paper 1; [11]).

Second, the chondrocyte lacunae are connected by small passages (canaliculi) forming a lacuno-canalicular network (LCN) [11, 22]. The function of the chondrocyte LCN in tessellated cartilage remains unknown, however, a similar network is seen linking osteocytes (bone cells) in bone which, like chondrocytes in elasmobranchs, survive surrounded by mineralized matrix enclosed in lacunae [23,24]. The fact that two different cell types have a similar organization in mineralized tissues suggests that the LCN is an analogous adaptation for the cells to survive – and perhaps communicate– within mineralized tissues, likely allowing nutrient transport from the surrounding, non-mineralized regions. In addition to maintaining living cells, many other adaptations have been attributed to LCN in bone such as mechanosensing, bone remodeling, communication with other organs and endocrine functions [23,25,26,27]. This broad range of adaptations in the osteocytes LCN can give insights into potential functions of tesserae cells and, although none of these functions have yet been attributed to the LCN of elasmobranch chondrocytes, the results of Paper 1 [11] —showing cell arrangements linked to the tesseral loading environment [19] and converging on each tessera's population of central cells— support the elasmobranch LCN having some role in mechanosensing. Additionally, if indeed the elasmobranch LCN can be shown to be involved in the cycling and exchange of mineralization ions (i.e. local breaking down and building up of tesserae), this would argue that chondrocytes, like osteocytes, are capable of tissue remodeling, pointing to an ancient functional convergence in the biology of skeletal tissue cells.

Third, we found that chondrocytes present different morphologies and orientations depending on their location within tesserae, which can be correlated with the morphology of cells in the surrounding tissues. This is apparently the result of the accretionary growth of tesserae resulting in nearby cells being incorporated into the mineralized tissue [8,10,28]. Specifically, round cells from the tesserae body zone were previously located in the unmineralized cartilage matrix (where chondrocytes are round), flat cells from the cap zone were previously located in the perichondrium, and elongated cells from the radial zone were previously located in the intertesseral joint. It has been demonstrated that the cells in each of these surrounding tissues express different genes, indicating different cell function. For example, the cells in the unmineralized cartilage matrix behave (in principle) as “common” (mammalian) chondrocytes synthesizing Col2 and GAGs [29,30]. In contrast, the cells in the perichondrium appear to be involved in more diverse functions, suggesting the presence of multiple cell types. For example, some perichondrial cells appear to be immature chondrocytes that give way to mature chondrocytes of the unmineralized matrix [30], while others appear to produce Col1 [31], a function mainly related with fibroblasts that maintain the perichondrial matrix in mammalian skeletons [16,32]. The function of intertesseral joint cells is more uncertain. Marconi et al. [30] suggested that these cells correspond to newborn chondrocytes from the perichondrium that, to reach the unmineralized matrix, migrate through the joints. However, this theory is not compatible with the way that these cells are organized: rather than being randomly distributed through the joint matrix, as might be expected for migrating cells, joint cells are disposed discretely in rows, enclosed between parallel fibers that connect two tesserae [10]. Based on this organization, we suggest that these cells act as biomechanical sensors, being aligned to the principal axes of the forces and sharing loads between tesserae. Analyzing the genetic expression of joint cells during tesserae development (e.g. before and after tesserae grow into contact) would provide support for this hypothesis.

The demonstrated diversity of chondrocyte function indicates that tesserae are composed of cells that differed in function before they were enclosed within tesserae. Once elasmobranch chondrocytes are enclosed in tesserae, their function is unknown, but two possibilities seem reasonable: First, when the chondrocytes are enclosed in tesserae, the cells do not change their previous function, which could mean that cells with different functions are coordinated within tesserae via canaliculi communication. In this way, tesserae would represent multi-functional organs (like bones) characterized by several cell types, with their diverse cellular capacity built

by 'recruiting' cells from other tissues. Alternatively (or, perhaps, in addition) elasmobranch chondrocytes could change and align their roles once they are enclosed in tesserae, which would mean that the cells maintain different morphologies, but converge on similar function. The possibility of chondrocytes changing their function once they are enclosed in a mineralized matrix is also seen during bone development (endochondral ossification) where some chondrocytes, instead of dying, transdifferentiate into osteocytes [33,34]. If a similar transdifferentiation occurs in elasmobranch tesserae cells, it could indicate that mineralization in elasmobranchs is also a trigger for a shift in function. Fine scale evaluation of cell gene products, morphology and composition across mineralization fronts (e.g. taking advantage of the tissue preparation and label-free imaging approaches developed in this dissertation) would help to clarify whether there is any cascade of cellular alterations during mineralization in tesserae, perhaps echoing some of the shifts known for chondrocytes in mammalian growth plates. Whether tesseral cells show shifts in function or not, the demonstrated variation in cells in tessellated cartilage (and the differences in function suggested by their varying autofluorescence signatures) support the notion that referring to these cells simply as "chondrocytes" may be limiting or even inaccurate.

Variations in cellular morphology can also be related to skeletal developmental stages. For example, the cells located in the central area of the tesserae (central cells) differ in morphology from the other cells in tesserae and cells in the surrounding tissues (e.g. perichondrium, cartilage matrix): tesserae central cells form clusters, are rounder and larger than other tesserae cells, and the surrounding mineralized matrix has a distinct autofluorescence signal. These features suggest that the central area of tesserae may be a print of the first developmental stages of the skeleton, when tesserae first appear and start growing [13]. During these embryonic stages, the cartilage matrix is characterized by a high cellular density, with the cells organized in twins due to the high cell division [35]; therefore, the organization of round and large cells in clusters appears to be a consequence of tesserae having formed (and first incorporated cells) during those stages. As such, the distinct autofluorescence signal may also be indicative of a specific cartilage matrix composition at this stage, perhaps related with skeletal demands during embryonic development or matrix factors involved in initial tesseral formation. Although it is still unclear how the composition of the cartilaginous matrix varies across ontogeny in elasmobranchs, the characterization of cartilage matrix composition and organization at different developmental stages will shed light on different mechanical functions

through development, while also perhaps providing clues to the hallmarks of ageing in elasmobranch cartilage, which are yet unstudied. Since elasmobranch cartilage persists for far longer than human cartilage, this knowledge could also have important implications for cartilage treatments of degenerative pathologies like osteoarthritis.

The fact that the central cells were enclosed during the first developmental stages and maintain a similar morphology raises important biological questions. First, to maintain those cells at the deepest point within tesserae, in order to transport nutrients and metabolic waste products, there should be a fluid transport between the cells and nutrient sources (e.g. blood vessels) outside of the tesserae. This may be performed by the LCN, which can act as a transport conduit between cells and the environment surrounding tesserae (although the flow and exchange of matrix components through the tesserae LCN has yet to be shown or simulated). Second, the fact that central cells maintain the same structure as in the young skeleton indicates the inability of these cells to divide and be replaced once encased in mineral. These cells offer therefore interesting opportunities to investigate if they suffer any ultrastructure variations across their lifespan as a result of their anatomical 'isolation'. Lastly, the fixed location of central cells in tesserae also makes them useful developmental models to compare with younger cells arrayed more peripherally. Given that some elasmobranchs can live for more than 400 years (the Greenland shark; [36]), further studies could use elasmobranchs to explore chondrocyte senescence, using the consistent cellular arrayment in tesserae to untangle how chondrocytes vary in ultrastructure and function across (even extreme) lifespans.

Lastly, the round morphology and clustering organization obtained as a consequence of being encapsulated during an early developmental stage, may have crucial implications on tesserae biomechanics. In bone, osteocytes with round morphologies can receive mechanical forces isotropically and respond with chemical signaling [37]. Like osteocytes, chondrocytes are mechanosensing cells, where cellular morphology and organization can dictate the cell's (and its tissue's) ability to respond to its environment, and therefore also provide an indication, via their shape, of the forces experienced by a tissue [37,38,39]. In elasmobranch tesserae, the round morphology and clustering organization of the central cells could therefore indicate that they act as a 'switchboard' in the skeleton, a multi-directional reception and distribution center for forces, with access through the canaliculi network to the other cells from the surrounding tesserae regions (cap, body and radial) and, lastly, crossing the intertesseral joints to reach

neighboring tesserae. In this way, the cellular nodal network in the tessellated layer —involving a combination of canaliculi passages and lacunae spaces— could provide channels to communicate even among separated (non-neighboring) tesserae. Cellular networks have been described in other tissues such as among osteocytes in bone and neurons in the brain, but it never has been attributed to cartilage, which is usually composed of isolated chondrocytes that function independently from one to another (but see [40]). This cell organization may have crucial implications in maintaining tesserae structural integrity in terms of tesserae repair and matrix remodeling, allowing communication and coordination among chondrocytes from different skeletal regions.

The demonstrated diversity of the chondrocytes living within tesserae adds a new dimension to the concept that tesserae are a distinct tissue of elasmobranchs [41,42,43], adapted for skeletal performance at different size scales. Whereas most previous studies have focused on anatomical, structural and material aspects of the mineralized tissue [10,20,28,44], this dissertation's work illustrates that organization and function of tesseral cells should also be considered. Curiously, similarly distinct features have yet to be observed in the unmineralized cartilaginous matrix, which constitutes the bulk of the elasmobranch skeleton. Our autofluorescence data, combined with the results obtained in other studies, showed that the elasmobranch unmineralized cartilage resembles other vertebrate cartilages in terms of matrix composition (based in Col2 and GAGs) and chondrocyte organization, morphology and function [13,28,29,30]. That being said, the fact that the chondrocytes living inside tesserae differ from the chondrocytes of the unmineralized matrix is indicative of the plasticity of these cells in elasmobranch cartilage, where cells of ostensibly the same cell type are able to form and maintain, by modifying cell morphology, organization and function, both non-mineralized and mineralized skeletal structures such as the tesserae and unmineralized cartilage matrix, the various tissues forming vertebrae (fibrous, lamellar and areolar mineralization), and likely also articular joints (unknown cartilage type) [21,45,46,47].

In fact, chondrocytes also appear to exhibit a high and under-appreciated degree of versatility in other vertebrates, forming and maintaining myriad different skeletal tissue structures among different species, but also within the same skeleton. For example, beyond forming and maintaining the entire adult skeleton of lampreys and hagfishes (in addition to chondrichthyes), chondrocytes are responsible for forming and maintaining the embryonic cartilaginous

skeleton during early development; for degrading the cartilage matrix during endochondral ossification (as hypertrophic chondrocytes) to form bony skeletons (fishes and tetrapods); and, in adult skeletons, for forming various cartilaginous structures such as elements of the respiratory system (both terrestrial and aquatic), intervertebral discs, bone-tendon intersections, articulations, noses, ears and ribs (e.g. [16,48,49,50,51,52]). Although chondrocytes (and the tissues they produce) are commonly attributed only to deuterostomes (chordates, echinoderms and hemichordates), a type of cellular cartilage has been also described in five groups of protostomes (annelids, mollusk, brachiopods and arthropods) forming, for example, tentacles, jaws, odontophores, respiratory systems, and complex optic structures (in case of cephalopods) [16,53,54]. This invertebrate cartilage is based on a different collagen type, Collagen A, but is histologically similar to vertebrate cartilage in terms of matrix organization and cell morphology [16,54,55]. Whether the cells building and residing in these “cartilages” are true chondrocytes is uncertain. However, the presence of “chondrocytes” and “cartilages” in such hugely divergent modern taxonomic groups suggests that cartilage evolved multiple times in bilaterians, either through multiple cell lineages converging on the production of cartilage-like tissue or a single ancient cell lineage co-opting a shared gene regulatory network (SoxD/E) that was present in a common ancestor of bilaterians [54,55,56].

In either case, tools for making cartilage —either a cartilage-relevant gene regulatory network or a ‘proto-chondrocyte’— would have preceded the divergence of deuterostomes and protostomes, allowing these systems ~555 million years to adapt and evolve to different lineages’ skeletal pressures, to give rise to the abundant cartilaginous skeletal tissues seen today [55,57]. Further comparative studies of cartilage biology are needed to characterize chondrocyte diversity, and whether their function is encoded genetically or, on the other hand, triggered by the varying environmental factors (e.g. chemical, mechanical) experienced by different taxa. Given that bone and cartilage cells in fishes have been shown to perform roles typically attributed to other cells in mammals [58], it is reasonable and exciting to suppose that there are new cartilage cell lineages, to date classified as chondrocytes purely from appearance, that have functions yet to be described.

References

- [1] Leonelli S, Ankeny RA. What makes a model organism?. *Endeavour*. 2013 Dec 1;37(4):209-12.
- [2] De Jong M, Maina T. Of mice and humans: are they the same?—Implications in cancer translational research. *Journal of Nuclear Medicine*. 2010 Apr 1;51(4):501-4.
- [3] Cole HA, Yuasa M, Hawley G, Cates JM, Nyman JS, Schoenecker JG. Differential development of the distal and proximal femoral epiphysis and physis in mice. *Bone*. 2013 Jan 1;52(1):337-46.
- [4] Dean MN, Ekstrom L, Monsonego-Ornan E, Ballantyne J, Witten PE, Riley C, Habraken W, Omelon S. Mineral homeostasis and regulation of mineralization processes in the skeletons of sharks, rays and relatives (Elasmobranchii). In: *Seminars in Cell & Developmental Biology* 2015 Oct 1 (Vol. 46, pp. 51-67). Academic Press.
- [5] Yancey PH, Somero GN. Methylamine osmoregulatory solutes of elasmobranch fishes counteract urea inhibition of enzymes. *Journal of experimental zoology*. 1980 May;212(2):205-13.
- [6] Ballantyne JS. Jaws: the inside story. The metabolism of elasmobranch fishes. *Comparative Biochemistry and Physiology Part B: Biochemistry and Molecular Biology*. 1997 Dec 1;118(4):703-42.
- [7] Hazon N, Wells A, Pillans RD, Good JP, Anderson WG, Franklin CE. Urea based osmoregulation and endocrine control in elasmobranch fish with special reference to euryhalinity. *Comparative Biochemistry and Physiology Part B: Biochemistry and Molecular Biology*. 2003 Dec 1;136(4):685-700.
- [8] Kemp NE, Westrin SK. Ultrastructure of calcified cartilage in the endoskeletal tesserae of sharks. *Journal of Morphology*. 1979 Apr;160(1):75-101.
- [9] Dean MN, Gorb SN, Summers AP. A cryoSEM method for preservation and visualization of calcified shark cartilage (and other stubborn heterogeneous skeletal tissues). *Microscopy Today*. 2008 Nov;16(6):48-51.
- [10] Seidel R, Blumer M, Pechriggl EJ, Lyons K, Hall BK, Fratzl P, Weaver JC, Dean MN. Calcified cartilage or bone? Collagens in the tessellated endoskeletons of cartilaginous fish (sharks and rays). *Journal of structural biology*. 2017 Oct 1;200(1):54-71.
- [11] Chaumel J, Schotte M, Bizzarro JJ, Zaslansky P, Fratzl P, Baum D, Dean MN. Co-aligned chondrocytes: zonal morphological variation and structured arrangement of cell lacunae in tessellated cartilage. *Bone*. 2020 May 1;134:115264.
- [12] Schotte M, Chaumel J, Dean MN, Baum D. Image analysis pipeline for segmentation of a biological porosity network, the lacuno-canalicular system in stingray tesserae. *MethodsX*. 2020 Jan 1;7:100905.
- [13] Chaumel J, Marsal, M, Gómez-Sánchez A, Blumer M, Gualda EJ, De Juan A, Loza-Alvarez P, Dean MN. Autofluorescence imaging of stingray skeletal cartilage: hyperspectral imaging as a tool for histological characterization. *Discover Materials*. Forthcoming 2021
- [14] Caraguel JM, Barreau T, Brown-Vuillemin S, Iglésias SP. In vivo staining with alizarin for ageing studies on chondrichthyan fishes. *Aquatic Living Resources*. 2020;33:1
- [15] Wright GM, Keeley FW, Youson JH, Babineau DL. Cartilage in the Atlantic hagfish, *Myxine glutinosa*. *American journal of anatomy*. 1984 Apr;169(4):407-24.
- [16] Hall BK. *Bones and cartilage: developmental and evolutionary skeletal biology*. Elsevier; 2005 Jun 20.

- [17] Green EM, Peter Winlove C. The structure and mechanical properties of the proteins of lamprey cartilage. *Biopolymers*. 2015 Apr;103(4):187-202.
- [18] Seidel R, Jayasankar AK, Shahar R, Dean MN. The multiscale architectures of fish bone and tessellated cartilage and their relation to function. In: *Architected materials in nature and engineering 2019* (pp. 329-353). Springer, Cham.
- [19] Jayasankar AK, Seidel R, Hosny A, Weaver JC, Fratzl P, Chen J, Dean MN. Multi-scale modeling and mechanical performance characterization of stingray skeleton-inspired tessellations. *Journal of the Mechanics and Physics of Solids*. 2020 May 1;138:103906.
- [20] Clement JG. Re-examination of the fine structure of endoskeletal mineralization in chondrichthyans: implications for growth, ageing and calcium homeostasis. *Marine and Freshwater Research*. 1992;43(1):157-81.
- [21] Dean MN, Summers AP. Mineralized cartilage in the skeleton of chondrichthyan fishes. *Zoology*. 2006 May 22;109(2):164-8.
- [22] Dean MN, Socha JJ, Hall BK, Summers AP. Canaliculi in the tessellated skeleton of cartilaginous fishes. *Journal of Applied Ichthyology*. 2010 Apr;26(2):263-7.
- [23] Bonewald LF. The amazing osteocyte. *Journal of bone and mineral research*. 2011 Feb;26(2):229-38.
- [24] Weinkamer R, Kollmannsberger P, Fratzl P. Towards a connectomic description of the osteocyte lacunocanalicular network in bone. *Current osteoporosis reports*. 2019 Aug;17(4):186-94.
- [25] Jacobs CR, Temiyasathit S, Castillo AB. Osteocyte mechanobiology and pericellular mechanics. *Annual review of biomedical engineering*. 2010 Aug 15;12:369-400.
- [26] Schaffler MB, Cheung WY, Majeska R, Kennedy O. Osteocytes: master orchestrators of bone. *Calcified tissue international*. 2014 Jan;94(1):5-24.
- [27] Buenzli PR, Sims NA. Quantifying the osteocyte network in the human skeleton. *Bone*. 2015 Jun 1;75:144-50.
- [28] Seidel R, Lyons K, Blumer M, Zaslansky P, Fratzl P, Weaver JC, Dean MN. Ultrastructural and developmental features of the tessellated endoskeleton of elasmobranchs (sharks and rays). *Journal of Anatomy*. 2016 Nov;229(5):681-702.
- [29] Enault S, Muñoz DN, Silva WT, Borday-Birraux V, Bonade M, Oulion S, Ventéo S, Marcellini S, Debais-Thibaud M. Molecular footprinting of skeletal tissues in the catshark *Scyliorhinus canicula* and the clawed frog *Xenopus tropicalis* identifies conserved and derived features of vertebrate calcification. *Frontiers in genetics*. 2015 Sep 15;6:283.
- [30] Marconi A, Hancock-Ronemus A, Gillis JA. Adult chondrogenesis and spontaneous cartilage repair in the skate, *Leucoraja erinacea*. *Elife*. 2020 May 12;9:e53414.
- [31] Egerbacher M, Helmreich M, Mayrhofer E, Böck P. Mineralisation of hyaline cartilage in the small-spotted dogfish *Scyliorhinus canicula* L. *Scripta Medica (BRNO)*. 2006 Aug;79:199-212.
- [32] Mundlos S, Engel H, Michel-Behnke I, Zabel B. Distribution of type I and type II collagen gene expression during the development of human long bones. *Bone*. 1990 Jan 1;11(4):275-9.
- [33] Yang G, Zhu L, Hou N, Lan Y, Wu XM, Zhou B, Teng Y, Yang X. Osteogenic fate of hypertrophic chondrocytes. *Cell research*. 2014 Oct;24(10):1266-9.

- [34] Park J, Gebhardt M, Golovchenko S, Perez-Branguli F, Hattori T, Hartmann C, Zhou X, deCrombrugge B, Stock M, Schneider H, Von Der Mark K. Dual pathways to endochondral osteoblasts: a novel chondrocyte-derived osteoprogenitor cell identified in hypertrophic cartilage. *Biology open*. 2015 May 15;4(5):608-21.
- [35] Dean MN, Mull CG, Gorb SN, Summers AP. Ontogeny of the tessellated skeleton: insight from the skeletal growth of the round stingray *Urobatis halleri*. *Journal of Anatomy*. 2009 Sep;215(3):227-39.
- [36] Nielsen J, Hedeholm RB, Heinemeier J, Bushnell PG, Christiansen JS, Olsen J, Ramsey CB, Brill RW, Simon M, Steffensen KF, Steffensen JF. Eye lens radiocarbon reveals centuries of longevity in the Greenland shark (*Somniosus microcephalus*). *Science*. 2016 Aug 12;353(6300):702-4.
- [37] Vatsa A, Breuls RG, Semeins CM, Salmon PL, Smit TH, Klein-Nulend J. Osteocyte morphology in fibula and calvaria—is there a role for mechanosensing?. *Bone*. 2008 Sep 1;43(3):452-8.
- [38] Kerschnitzki M, Wagermaier W, Roschger P, Seto J, Shahar R, Duda GN, Mundlos S, Fratzl P. The organization of the osteocyte network mirrors the extracellular matrix orientation in bone. *Journal of structural biology*. 2011 Feb 1;173(2):303-11.
- [39] Gauthier R, Langer M, Follet H, Olivier C, Gouttenoire PJ, Helfen L, Rongieras F, Mitton D, Peyrin F. 3D micro structural analysis of human cortical bone in paired femoral diaphysis, femoral neck and radial diaphysis. *Journal of structural biology*. 2018 Nov 1;204(2):182-90.
- [40] Mayan MD, Gago-Fuentes R, Carpintero-Fernandez P, Fernandez-Puente P, Filgueira-Fernandez P, Goyanes N, Valiunas V, Brink PR, Goldberg GS, Blanco FJ. Articular chondrocyte network mediated by gap junctions: role in metabolic cartilage homeostasis. *Annals of the rheumatic diseases*. 2015 Jan 1;74(1):275-84.
- [41] Applegate SP. A survey of shark hard parts. *Sharks, skates and rays*. 1967:37-67.
- [42] Dean MN. Cartilaginous Fish Skeletal Tissues. In: Farrell AP, ed. *Encyclopedia of fish physiology: from genome to environment*. Academic press; 2011 Jun 1.
- [43] Maisey JG. The diversity of tessellated calcification in modern and extinct chondrichthyans. *Revue de Paléobiologie*. 2013;32(2):355-71.
- [44] Atake OJ, Cooper DM, Eames BF. Bone-like features in skate suggest a novel elasmobranch synapomorphy and deep homology of trabecular mineralization patterns. *Acta biomaterialia*. 2019 Jan 15;84:424-36.
- [45] Porter ME, Beltrán JL, Koob TJ, Summers AP. Material properties and biochemical composition of mineralized vertebral cartilage in seven elasmobranch species (Chondrichthyes). *Journal of Experimental Biology*. 2006 Aug 1;209(15):2920-8.
- [46] Sullivan T, Regan F. The characterization, replication and testing of dermal denticles of *Scyliorhinus canicula* for physical mechanisms of biofouling prevention. *Bioinspiration & biomimetics*. 2011 Oct 12;6(4):046001.
- [47] Berio F, Broyon M, Enault S, Pirot N, López-Romero FA, Debais-Thibaud M. Diversity and evolution of mineralised skeletal tissues in chondrichthyans. *Frontiers in Ecology and Evolution*. 2021;9:223.
- [48] Benjamin MI. The cranial cartilages of teleosts and their classification. *Journal of Anatomy*. 1990 Apr;169:153.

- [49] Robson P, Wright GM, Sitarz E, Maiti A, Rawat M, Youson JH, Keeley FW. Characterization of lamprin, an unusual matrix protein from lamprey cartilage. Implications for evolution, structure, and assembly of elastin and other fibrillar proteins. *Journal of Biological Chemistry*. 1993 Jan 15;268(2):1440-7.
- [50] Zhang G, Cohn MJ. Hagfish and lancelet fibrillar collagens reveal that type II collagen-based cartilage evolved in stem vertebrates. *Proceedings of the National Academy of Sciences*. 2006 Nov 7;103(45):16829-33.
- [51] Witten PE, Huysseune A, Hall BK. A practical approach for the identification of the many cartilaginous tissues in teleost fish. *Journal of Applied Ichthyology*. 2010 Apr;26(2):257-62.
- [52] Pawlina W, Ross MH. *Histology: a text and atlas: with correlated cell and molecular biology*. Lippincott Williams & Wilkins; 2018 Dec 7.
- [53] Cole AG, Hall BK. The nature and significance of invertebrate cartilages revisited: distribution and histology of cartilage and cartilage-like tissues within the Metazoa. *Zoology*. 2004 Dec 15;107(4):261-73.
- [54] Tarazona OA, Slota LA, Lopez DH, Zhang G, Cohn MJ. The genetic program for cartilage development has deep homology within Bilateria. *Nature*. 2016 May;533(7601):86-9.
- [55] Gillis JA. *The development and evolution of cartilage*. Elsevier Reference Module in Life Sciences: Developmental Biology. 2018.
- [56] Stone JR, Hall BK. Latent homologues for the neural crest as an evolutionary novelty. *Evolution & Development*. 2004 Mar;6(2):123-9.
- [57] Brunet T, Arendt D. From damage response to action potentials: early evolution of neural and contractile modules in stem eukaryotes. *Philosophical Transactions of the Royal Society B: Biological Sciences*. 2016 Jan 5;371(1685):20150043.
- [58] Ofer L, Dean MN, Zaslansky P, Kult S, Shwartz Y, Zaretsky J, Griess-Fishheimer S, Monsonego-Ornan E, Zelzer E, Shahar R. A novel nonosteocytic regulatory mechanism of bone modeling. *PLoS biology*. 2019 Feb 1;17(2):e3000140.

APPENDIX

Protocols

In the following pages are enclosed all protocols optimized to prepare elasmobranch skeletal cartilage during this dissertation. The protocols that did not required additional steps for this particular tissue are not included.

- Fixatives

1. Ethanol
2. PFA
3. GA

- Embedding:

1. PMMA
2. Clarification

- Histology:

1. Alcian blue
2. Sirius red

- Fluorescent dyes:

1. Green phalloidin + DAPI

- Immunohistochemistry:

1. Sox9

- Electron microscopy

1. Osmium tetroxide + Uranyl Acetate + Lead Citrate

Fixatives

Ethanol

Consecutive steps to fix elasmobranch cartilage using increasing ethanol concentrations:

Concentration	Time
1. 30% ETOH	20 min at RT
2. 50% ETOH	20 min at RT
3. 70% ETOH	20 min at RT
4. 80% ETOH	20 min at RT
5. 90% ETOH	20 min at RT
6. 100% ETOH	20 min at RT

PFA 4%

Consecutive steps to fix elasmobranch cartilage using increasing concentrations of PFA 4% in PBS:

Concentration	Time
1. 4% PFA	6h at RT or overnight at 4°C
2. Wash in PBS	20 min at RT
3. Wash in PBS	20 min at RT
4. Wash in PBS	20 min at RT

2%GA + 2%PFA

Steps to fix elasmobranch cartilage using 2%GA +2%PFA

Concentration	Time
1. 2%GA+ 2%PFA	Until sample embedding

PMMA embedding

1. Fixation

- 4% PFA buffered in PBS – Overnight
- Wash the PFA with PBS x3 during 20 min at RT
- Place the samples in the embedding cassettes pre-labeled in pencil.

2. Dehydration

- ETHO 30% - 1 day at 4°C on the rotator (+10 min vacuum)
- ETHO 30% - 1 day at 4°C on the rotator (+10 min vacuum)
- ETHO 50% - 2 days at 4°C on the rotator (+10 min vacuum)
- ETHO 80% - 2 days at 4°C on the rotator (+10 min vacuum)
- ETHO 95% - 2 days at 4°C on the rotator (+10 min vacuum)
- ETHO 100% - 3 days at 4°C on the rotator (+10 min vacuum)

3. Rhodamine staining (optional)

- Rhodamine/ETOH 1 – 1.5 days at 4°C on the rotator (+10 min vacuum)
- Rhodamine/ETOH 2 – 1.5 days at 4°C on the rotator (+10 min vacuum)

4. Pre-infiltration and polymerization

- Xylol – 3 hours at RT (+10 min vacuum) – under the fume hood (toxic)
- Xylol – 3 hours at RT (+10 min vacuum) – under the fume hood (toxic)
- See before start section
- Pre-infiltration – 3 days at 4°C (+10 min vacuum) – under the fume hood (toxic)
- Infiltration 1 – 3 days at 4°C (+10 min vacuum) – under the fume hood (toxic)
- Infiltration 2 – 4 days at 4°C (+10 min vacuum) – under the fume hood (toxic)
- Embedding – RT (+10 min vacuum) – under the fume hood (toxic)
- Polymerization – 3-4 days at -20°C (freezer)

Specimen polymerisation/embedding protocol - Before start

1. Place the specimens (still inside the embedding cassettes) in a metal tray inside the hood and keep them submerged in PMMA infiltration solution (do not let tissue dry out). Position the specimens in the order you want to embed them and open the lid of the embedding cassettes to facilitate access to the specimen-tissue.

2. Place embedding molds in the plastic container boxes which can fit in the freezer and have a lid. Pre-cool the container+molds inside for about 30min at -20°C. Position the paper label inside the molds in the same order as before. Paper label length should be about 3/4 of the mold perimeter (either 25mm or 25 mm), width no more than 5 mm. Position the label slightly above the specimen (approx.)
3. Prepare forceps, towel paper, cut parafilm squares, all ready to use inside the hood.
4. Pre-cool stock solutions A and B and embedding-molds before start (30 min, -20°C).
 - Prepare polymerisation mixture for 5-10 specimens at a time, depending on how fast you perform.
 - Avoid specimens drying out at all times
 - All steps should be conducted under the fume hood.
5. Pre-cooled stock solutions A should look viscous, transparent and without bubbles. Pre-cooled stock solutions B should look transparent and similar consistency as water.
 - Stock solutions A and B must be mixed while they are still cooled in a graduated cylinder in a 9:1 ratio (e.g. 9 ml stock solution A + 1 ml stock solution B).
 - Bring stock solutions A and B back to the freezer.
 - Double-parafilm the graduated cylinder and mix the solutions by doing oscillating the cylinder very gently to avoid bubble formation.
 - After 2-4 minutes of gentle mixing, the polymerisation solution should look homogenous in a single phase, with slightly yellowish colour. Then, it is ready to use.
6. Place the infiltrated tissue into the embedding-mold in the desired reference position for embedding (e.g. for mouse femur place the knee condyles facing downwards). Avoid changing the position of the embedded sample (avoid rapid movements).
7. Pour carefully the polymerisation mixture to the embedding-molds until the mold is almost (1 mm margin) completely filled to allow enough space for the lid to seal the mold later on.
8. Vacuum 10 min at RT. Bubbles that come to the mold surface can be eliminated with a pipette
9. Check if the sample maintains the correct position. If not, reposition very carefully avoiding bubble formation.
10. Hermetically seal the embedding -mold or insert. Polimerisation will take place at -20°C for 3-4 days. Do not open the containers during polymerisation.

Repeat steps 1-6 for the next batch of specimens.

Preparation of the reagents

Rhodamine solution 0.00417% (w/v)

1. Add 250 ml 100% ETOH in a transparent glass bottle with a stirrer
2. Add 1.25g Rhodamine 6G slowly while stirring
3. Stir for 30 min and top up with 100% ETOH to a final volume of 300 ml

**Store in a dark container at RT until next use*

**Rhodamine solution is toxic for the environment and should be discarded appropriately*



Destabilization of the basic solution – processing the components

Technovit 9100 basic solution can be used when stabilized and unstabilized. The applications of destabilized basic solution guarantees that the results for all immunohistochemical studies are analogous to the paraffin histology.

1. Fill chromatography column with approx. 50 g of Al_2O_3 (active, alkaline, 90)
2. Slowly flow Technovit 9100 basic solution (material number 1) through it. A column filling with Al_2O_3 is able to destabilize. 3-4 liters of basic solution.

The destabilized solution is stable for 4 weeks at +4°C or ½ year at -20°C. Store in glass bottles. With metal lids (duran bottles blue lids are not resistant to destabilized solution).

Pre-infiltration solution

1. Prepare 200 ml of destabilized basic solution with a magnetic stirrer in a volumetric flask (200 ml Erlenmeyer) under the fume hood
2. Add 1 g of Hardener 1 and stir for 30 min
3. Store at +4°C to cool down before use

Pre-infiltration solution is stable at for 2 weeks at +4°C or ½ years at -20°C

Infiltration solution

1. Prepare 200 ml of destabilized basic solution in a volumetric flask (250 ml Erlenmeyer) with a magnetic stirrer under the fume hood
2. While stirring, slowly add 20 g PMMA powder
3. Add destabilized basic solution to reach a final volume of 250 ml
Note: dissolving the PMMA powder will increase the density (and volume) of the solution. If you prepare more than 200 ml, it will take longer to dissolve.
4. Stir for 2 hours until the solution becomes clear under the fume hood
5. Add 1 g of Hardener 1 and stir for 20 min

Pre-infiltration solution is stable at for 2 weeks at +4°C or ½ years at – 20°C

Specimens embedding and polymerization

Stock solution A:

1. Prepare 350 ml of destabilized basic. Solution in a volumetric flask (500 ml Erlenmeyer) with a magnetic stirrer under the fume hood
2. While stirring slowly add 80 g PMMA powder
3. Add destabilized basic solution to reach a total volume of 500 ml
4. Stir for 2 hours until the solution becomes clear
5. Add 3 g of Hardener 1 and stir for about 20 minutes
6. While stirring, slowly add 20 g PMMA powder

Stock solution A is stable at for 2 weeks at +4°C or ½ years at – 20°C

Stock solution B: (prepare fresh each time)

1. Prepare 44 ml of destabilized basic solution in a volumetric flask (50 ml) with a magnetic stirrer under the fume hood
Note: pre-cooling the destabilized basic solution will help to cool down Stock Solution B faster
2. While stirring, add 4 ml of Hardener 2
3. While stirring, add 2 ml of polymerization regulator
4. Allow to dissolve during 2 minutes before use

Material cleaning and disposal

- After use, rinse thoroughly (3-4x) all glassware with 70% EtOH and keep overnight under the fume hood to avoid air contamination in the lab. Next day clean normally (out of the fume hood) or bring to the dishwasher.
- Solution waste should be placed in the PMMA waste bottle in the fume hood to be brought to the special-waste treatment deposit.
- Polymerisation occurs in the range of -2°C to -15°C . For example:
Embedding mold of 25 mm diameter requires 10 ml of polymerisation solution. Embedding mold of 15 mm diameter requires ml of polymerisation solution
- The polymerisation times depend on the polymerization volume and the temperature. The greater the volume of the embedding form, the lower the temperature must be, and the longer it will take.

Clarification protocol for elasmobranch cartilage

1. Fixation

- 4% PFA buffered in PBS – Overnight
- Wash the PFA with PBS x3 during 20 min at RT
- Store the sample at 4°C in PBS before use

**Do not fix the samples with glutaraldehyde, since it is highly autofluorescent.*

2. Dehydration

- ETHO 30% - 12 h at RT
- ETHO 50% - 12 h at RT
- ETHO 70% - 12 h at RT
- ETHO 100% - 12 h at RT

**As we are dehydrating entire skeletal pieces, the dehydration steps take longer than for thin samples.*

3. Clarification with ethyl cinnamate (ECi)

Product: Ethyl cinnamate – W243000 Sigma-Aldrich.

- Transfer the sample in a tube with ECi. The sample should be covered by the reagent
- Incubate while gently shaking at RT until the sample become transparent
- The sample can be maintained in the reagent for months.

**The sample is transparent as long as it is in the reagent. Once it is taken out, it won't be transparent anymore.*

Alcian blue staining for PMMA sections

1. Deplastification

- **2-Mea (A)** – 20 min – Under fume hood
- **2-Mea (B)** – 20 min – Under fume hood
- **2-Mea (C)** – 20 min – Under fume hood
- **100% ETOH (A)** – 2 min – Under fume hood
- **100% ETOH (B)** – 2 min – Under fume hood
- **96% ETOH (A)** – 2 min – lab bench
- **96% ETOH (B)** - 2 min – lab bench
- **80% ETOH (A)** – 2 min – lab bench
- **80% ETOH (B)** - 2 min – lab bench
- **70% ETOH (A)** - 2 min – lab bench
- **70% ETOH (B)** - 2 min – lab bench
- **Distilled water** - 2 min – lab bench

**Safety note: 2-MEA is harmful in contact with skin or if inhaled. Handle only under the fume hood.*

2. Weigert's Hematoxylin staining (15'):

- Prepare working solution fresh every time
- Mix equal volumes of Weigert's Haematoxylin A and B solutions. Calculate the required volume as 0.5-1ml/slide
- Apply on the slides laying. On the staining tray with a Pasteur pipette and incubate for 10 min. Make sure all sections are well covered
- Place slides back in staining rack and wash in running distilled water. Do not expose the sections directly to the running water
- Dip the rack of slides 3-4 times in the jar of Acid/Alcohol (1% HCL in 70% ethanol) to remove hematoxylin excess
- Wash slide-rack in a crystal jar with distilled water for 2-5 min and drain

**Safety note: Weigert's Hematoxylin is flammable and corrosive. Avoid exposure to skin and eyes*

3. Alcian Blue (15')

- Immerse slides in the staining rack in Alcian Blue staining solution for 8 min.
- Wash slides in a crystal jar with distilled water to remove excess of staining
- Rinse slide-rack in running distilled water for 2-3 min and drain

**The sample is transparent as long as it is in the reagent. Once it is taken out, it won't be transparent anymore.*

If we want to combine Alcian blue with Sirius Red, start Sirius Red protocol from here.

4. Mounting

Mounting can be done with Vitroclud (xylol-based), Mowiol (aqueous based) or Vectashield (aqueous based). For xylol-based mounting media, the samples have to be dehydrated by consecutive ethanol steps and infiltrated with xylol to make them soluble with the mounting media. To avoid these steps, however, it is preferable to use the aqueous media which, in addition, avoid photobleaching and are optimal to visualize fluorophores.

Protocol for xylol-based Media (Vidroclud)

- 100% (C) ETOH – 2 min (lab bench)
- 100% (D) ETOH – 2 min (lab bench)
- 100% (E) ETOH – 2 min (lab bench)
- Xylol (A) – 3 min fume hood
- Xylol (B) – 3 min fume hood
- Mount sections using xylol-based mounting media (Vidroclud) in the fume hood

**Safety note: Xylol is highly flammable liquid and vapor. Very harmful to skin and respiratory tract.*

Handle under the fume hood only.

5. Color legend

- Proteoglycans – Blue

**All staining solutions should be placed back into the original bottles, labelled with the solution date.*

**Unless otherwise stated, all procedures are conducted at RT and all reagents are dissolved in distilled water.*

Preparation of the reagents

Weigert's Haematoxylin

- 50% (v/v) Weigert's Haematoxyllin Part A – 5 ml
- 50% (v/v) Weigert's Haematoxylin Part B – 5 ml
- Final volume – 10 ml

**Make fresh every time, 0.5-1ml/ slide to calculate the total volume required. Make sure all sections are fully covered.*

Acid Alcohol – 1% HCL in 70% ETOH

- HCL – 3 ml
- Absolute ETOH – 207.9 ml ~208 ml
- Distilled water – 89 ml
- Final volume – 300 ml

**Return solution to Duran bottle when is not in use*

Alcian Blue (keep up to 4 weeks)

- 0.5 % (v/v) Alcian blue 8GX – 1.5g
- 1% (w/v) Glacial acetic acid – 3 ml
- 99% (v/v) Distilled water – 300 ml
- Final volume – 303 ml

**Prepare solution in an Erlenmeyer flask with a magnetic stirrer, agitate until powder is dissolved and filter before use. Return solution to Duran bottle when is not in use*

Info:

Alcian blue staining can be combined with H&E staining, PAS staining, Sirius Red staining and Van Gieson staining methods.

Sirius red staining for PMMA sections

1. Deplastification

- **2-Mea (A)** – 20 min – Under fume hood
- **2-Mea (B)** – 20 min – Under fume hood
- **2-Mea (C)** – 20 min – Under fume hood
- **100% ETOH (A)** – 2 min – Under fume hood
- **100% ETOH (B)** – 2 min – Under fume hood
- **96% ETOH (A)** – 2 min – lab bench
- **96% ETOH (B)** - 2 min – lab bench
- **80% ETOH (A)** – 2 min – lab bench
- **80% ETOH (B)** - 2 min – lab bench
- **70% ETOH (A)** - 2 min – lab bench
- **70% ETOH (B)** - 2 min – lab bench
- **Distilled water** - 2 min – lab bench

**Safety note: 2-MEA is harmful in contact with skin or if inhaled. Handle only under the fume hood.*

2. Phosphomolybdic acid staining (15'):

- Make up the working solution fresh each time
- Immerse slides in the staining rack in Phosphomolybdic acid staining solution for 15 min
- Dip the slide-rack 3x in a crystal jar with distilled water to remove excess of staining

**Excessive washing is counterproductive as Phosphomolybdic acid prepares the specimen-section for Sirius Red staining (Holde & Isler, 1958)*

3. Sirius Red staining (1h):

- Immerse slides in the staining rack in Sirius Red solution for 45 min. It can be extended up to 60 min if necessary
- Wash slides in a crystal jar with distilled water to remove excess of staining
- Rinse slides in running distilled water for 1-2 min and drain

**Safety note: Picric acid is toxic in contact with skin or if inhaled. Explosion hazard when dry.*

4. Mounting

Mounting can be done with Vitroclud (xylol-based), Mowiol (aqueous based) or Vectashield (aqueous based). For xylol-based mounting media, the samples have to be dehydrated by consecutive ethanol steps and infiltrated with xylol to make them soluble with the mounting media. To avoid these steps, however, it is preferable to use the aqueous media which, in addition, avoid photobleaching and are optimal to visualize fluorophores.

Protocol for xylol-based Media (Vituloclud)

- 100% (C) ETOH – 2 min (lab bench)
- 100% (D) ETOH – 2 min (lab bench)
- 100% (E) ETOH – 2 min (lab bench)
- Xylol (A) – 3 min fume hood
- Xylol (B) – 3 min fume hood
- Mount sections using xylol-based mounting media (Vituloclud) in the fume hood

**Safety note: Xylol is highly flammable liquid and vapor. Very harmful to skin and respiratory tract. Handle under the fume hood only.*

5. Color legend

- Cell Nuclei – Black
- Collagen – Pink/red

*All staining solutions should be placed back into the original bottles, labelled with the solution date.

Preparation of the reagents

Phosphomolybdic acid (last 2-3 days)

- 1% (w/v) Phosphomolybdic acid – 3 g
- 100% (v/v) Distilled water – 300 ml
- Final volume – 300 ml

**Prepare solution directly in a glass jar. Solution should become completely clear (yellow color) few minutes.*

**Return solution to Duran bottle when not in use*

**Safety note: Phosphomolybdic acid causes skin, eye and respiratory irritation*

Sirius red (keep up to 3 weeks)

- 0.1% (w/v) Sirius red – 0.3g
- 33.3% (v/v) Saturated picric acid (toxic) – 100 ml
- 66.6% (v/v) distilled water – 200 ml
- Final volume – 300 ml

**Safety note: Picric acid is toxic, and also explosive when dry*

**Take care when adding water to saturated Picric acid solution with staining powder (i.e. avoid splashing)*

**Prepare solution in an Erlenmeyer flask with a magnetic stirrer, agitate until powder is dissolved and filter before use*

**Return solution to Duran bottle when not in use*

Green phalloidin + DAPI

1. Deplastification

- **2-Mea (A)** – 20 min – Under fume hood
- **2-Mea (B)** – 20 min – Under fume hood
- **2-Mea (C)** – 20 min – Under fume hood
- **100% ETOH (A)** – 2 min – Under fume hood
- **100% ETOH (B)** – 2 min – Under fume hood
- **96% ETOH (A)** – 2 min – lab bench
- **96% ETOH (B)** – 2 min – lab bench
- **80% ETOH (A)** – 2 min – lab bench
- **80% ETOH (B)** – 2 min – lab bench
- **70% ETOH (A)** – 2 min – lab bench
- **70% ETOH (B)** – 2 min – lab bench
- **Distilled water** – 2 min – lab bench

**Safety note: 2-MEA is harmful in contact with skin or if inhaled. Handle only under the fume hood.*

2. Permeabilize the sample

- Wash the sample in PBS+Triton during, at least, 1h at RT

3. Staining with DAPI + Phalloidin

- Staining with Pha (1:100 / 1:250) – 1h at RT in dark conditions (Pha is photosensitive)
- Wash in large volumes with PBSTw (5 min x2)
- Stain with DAPI (1:200) – 5 min at RT in dark conditions
- Wash in large volumes with PBSTw (5min x2)

Prepare **Phalloidin and DAPI** solution

[DAPI] = 1:500 (1 μ L DAPI in 500 μ L PBS).

To prepare the solution, first think how much volume of solution we need. Each sample (slice) needs to be covered with 1 drop of solution (drop \cong 100 μ L). So, if we have 5 samples, we will need 500 μ L.

4. Mounting

Mount with a glass cover using Fluoroshield mounting media

- Add 1 drop of mounting media on the sample, without bubbles
- Cover with the cover slip gently
- Leave the samples dry overnight in a flat surface and protected from light

If we aim to analyze the samples in high resolution microscopes, we have to use coverslips of 1.5 (check in the box).

Sox9 - Immunohistochemistry

This protocol was optimized in demineralized and paraffin embedded samples.

1. Deparaffinize sections:

- Wash in **xylene** – 5 min (3x) – **Under fume hood**.
- Wash in **100% ethanol** – 5 min (1x)
- Wash in **90% ethanol** – 5 min (1x)
- Wash in **70% ethanol** – 5 min (1x)
- Wash in **PBS** – 5 min (3x)

**If we want to stain samples that are already mounted in glass slides and covered with coverslips, the mounting media should be removed. To do so, the samples need to be during, at least, 24h in xylene. If after 24h the coverslip cannot be removed, leave the samples during other 24h more.*

2. Immuno

Rehydrate

- The samples were in ddH₂O, so we put them PBS.
Eg: 1,5 ml PBS + 3 um DAPI + 3 um PH.

Block Solution and Primary Antibody (Sox 9)

- Wash the samples in block solution during, at least, 1h at Room Temperature (the longer the better).
- Incubate the samples with the Primary Antibody (Sox 9) diluted in block solution (1:400) overnight.

1:400 Sox 9: 200 um for embryo + 150 um + 3 slices = 800 um.

800 um of solution, where 2 um will be Sox9 (1:400).

Secondary antibody

- Wash the samples (x2; 5- 10 min) with block solution at Room Temperature.
- Incubate the samples with Secondary Antibody (FITC; 1:500) + DAPI (1:200) at 4°C in dark conditions overnight or 1h at room temperature.
- Wash the samples in large volumes of PBSTw

3. Mounting

Mount with a glass cover using Mowiol and nail polish.

- Add 1 drop of Mowiol on the sample, without bubbles.
- Add 4 drops of nail polish surrounding the sample, to stick the coverslip on the glass-slide.
- Add the glass – slide and fix it adding nail polish at the surroundings.

If we aim to analyze the samples in high resolution microscopes, we have to use coverslips of 1.5 (check in the box).

Preparation of reagents

Blocking buffer solution:

1 PBS + 1 % BSA + SDS 0.02% + Triton 1:1000

- Triton is light sensitive.

20 ml PBS + 20 μ m Triton + 200 μ m SDS + 2 g BSA (solution calculated for Sox9)

Concentrations:

- Sox9 (Primary antibody): 1:400
- Secondary Antibody (FITC): 1:500
- Triton: 1:1000
- DAPI: (1:200).

Calculations:

1.2 ml of block solution + 0.6 μ m DAPI

(it will be 1 μ m cos 0.6 is too small)

200 μ m block sol + Phalloidin
(1:100)

1 ml block sol + 2n antibody (20
 μ m)

We stained some samples with
DAPI + Pha

Controls

- **Negative control:** it is used to check if the secondary antibody works. For that, we treat a “control” slices in the same way than our test slices but without using primary antibody. Doing that we will check if the secondary antibody does not bind in other places than primary antibody.
- **Positive control:** to check if the antibody works. For that, we test it using a tissue / animal that we know the antibody works. In this case, we used an embryo (stage 19 – 22) of Cat shark.

TEM + FIB-SEM sample preparation

1. Fixation

- Keep the postmortem time as short as possible (less than 20 min)
- 2% Glutaraldehyde + 2% PFA buffered in PBS (0.1M) – 24h at RT in a rotator

**The samples can be maintained in the pre-fixative for several weeks. However, make sure that the solution stays clear. If not, change this solution for freshly prepared one.*

**This solution has to be done in PBS.*

2. Post-fixation

Osmium tetroxide preparation:

- Prepare 1% Osmium tetroxide (OsO₄) in distilled water or MiliQ one day after starting the protocol (see page 243).
- To prepare the OsO₄ solution, prepare a glass bottle with MiliQ covered by silver foam (OsO₄ is photosensitive)
- Break the OsO₄ ampullae and immediately place it in the glass bottle with MiliQ and close it. – under the fume hood with the glass closed until the end.
- Place the glass bottle in the rotator during 5 minutes
- Place the glass bottle in the fridge at 4°C overnight

**OsO₄ is highly toxic and volatile. All steps should be done under the fume hood, wearing lab coat, lab goggles and gloves.*

Optional: add 1% Kaliumhexacyanidoferrat to the osmium solution. For fish samples, Michael uses 0.5% OsO₄ + 1% Kaliumhexacyanidoferrat in distilled water.

Post-fixation:

- Wash the sample in PBS (0.1 M) at RT during 20 min (x3)
- Before using OsO₄, shake it during 5 minutes in the ultrasound machine
- Add the OsO₄ in the samples and leave it 24h (or overnight) at 4°C

**The samples should be wrapped in silver foam during all the protocol.*

3. Dehydration

- Wash the samples in MilliQ during 20 min in the rotator (x3). The MilliQ should be clear after the third washing. If not, continue washing until the MilliQ is clear
- 30% acetone – 1-2h at RT in the rotator (x2)
- 40% acetone – 1-2h at RT in the rotator (x2)
- 50% acetone – 1-2h at RT in the rotator (x2)
- 70% acetone – 1-2h at RT in the rotator – samples can be maintained several weeks in the fridge in this solution
- 90% acetone – 1-2h at RT in the rotator (x2)
- 100% acetone – 1h at RT in the rotator (x2)
- Stain with UA during 2 h and wash the samples with 100% acetone during 20 min (x3)
- 100% acetone – overnight at 4°C

**Instead of acetone could be ethanol. If so, after 100% ethanol the samples have to be washed in 100% acetone during 1h at RT in the rotator (x2)*

**For UA preparation, see page 4*

4. Infiltration

EPON resin preparation:

- Resin 8 g
- DDSA 5.34 g
- NMA 3.34 g
- BDMA 0.33 g

** Depending on the quantities needed, this recipe can be cut in half or doubled. See page 244*

- 10% resin in acetone – 2h at RT in the rotator
- 20% resin in acetone – 2h at RT in the rotator
- 30% resin in acetone – 2h at RT in the rotator (or overnight at 4°C)
- 50% resin in acetone – 2h at RT in the rotator
- 70% resin in acetone – 2h at RT in the rotator
- 90% resin in acetone – 2h at RT in the rotator
- 100% resin – 3h at RT in the rotator
- 100% fresh prepared resin – 4°C overnight

5. Embedding

- Prepare fresh resin
- Wash the molds with water and soap and pre-heat them in the oven at 60°C
- Replace the resin with fresh 100% resin and transfer to the molds
- Place the samples to the molds in the desired position. Although the resin is toxic, this step is recommended to be done under the scope, which is outside of the hood.
- Pre-heat the oven at 40°C
- Place the molds with the samples in the oven. First during 2h at 40°C
- Then at 60°C for 2-4 days.

Preparation of the reagents

Osmium tetroxide:

1. Prepare the workspace under the fume hood: clean it using ETHO, cover everything with clean papers, put a special trash for the pipettes/gloves/vials waste (OsO₄ + PFA + UA waste). Keep the liquid waste in Falcon tubes inside the hood until we finish the protocol.
2. Prepare the Osmium solution. Commercially, OsO₄ comes as solid in little glass and closed bottles (ampullae), with a constant weight of 0.25 g. The concentration that we need is 1% OsO₄ in distilled water. For the conversion we need:

$$1\% = \frac{1\text{gr}}{100\text{ml}}$$

So, our formula will be:

$$1\% \text{ --- } 1\text{ gr --- } 100\text{ml}$$

$$0.25\text{ gr ---- } x$$

$$X = (100 * 0.25) / 1 = \mathbf{25\text{ ml}}$$

To get a solution of 1 % OsO₄ we need to dissolve the 0.25 g OsO₄ in 25 ml of distilled water.

3. We put 25 ml of MiliQ or distilled water in a glass bottle. OsO₄ is **photosensitive**, so wrap the bottle with silver foam.
4. Close the hood until the end, keeping just your arms inside (Osmium is toxic and volatile). Break the glass bottle with OsO₄, put all inside the glass bottle (broken bottle, both parts) with Des. Water. And close it quickly to avoid the Osmium volatilize.
5. Label the bottle (date, OsO₄ and buffer we used: des. Water or MiliQ).
6. Leave it in the shaker during 5 minutes.

7. Leave the solution in the fridge.
8. Before using it, shake it during 5 minutes at ultrasound machine.

***Osmium tetroxide toxicity (OsO_4):** Osmium is highly toxic. Low concentrations in air can cause lung congestion, skin damage and severe eye damage. Osmium tetroxide is highly **volatile**, it can be absorbed into the body by inhalation of its vapor, by inhalation of its aerosol and by ingestion.



Acute Toxic



Health Hazard



Environmental Hazard

Uranyl acetate:

Staining medium: 9.9 – 9.8 ml of ANHYDROUS acetone supplemented with 100 – 200 μl of uranyl acetate 20% (**0.2-0.4 % final**). The stock solution of uranyl acetate (UA) is made of 20% UA dissolved in pure methanol, therefore the FSM contains 1% methanol(!!!)

Preparation of 20% UA (weight/volume ratio 50mg in 250ul):

1. Weigh 50 mg UA powder
2. Add 250 μl Methanol to the powder and shake them for ten minutes to dissolve it.

***Uranyl acetate toxicity (UA):** Uranyl acetate is both radioactive and toxic. UA is very toxic if ingested, inhaled as dust or by skin contact if skin is cut or abraded.



Acute Toxic



Health Hazard



Environmental Hazard

